APPLIED COMPUTATIONAL ELECTROMAGNETICS SOCIETY JOURNAL

February 2016
Vol. 31 No. 2
ISSN 1054-4887

The ACES Journal is abstracted in INSPEC, in Engineering Index, DTIC, Science Citation Index Expanded, the Research Alert, and to Current Contents/Engineering, Computing & Technology.

The illustrations on the front cover have been obtained from the research groups at the Department of Electrical Engineering, The University of Mississippi.

EMERITUS EDITORIAL ASSISTANTS

FEBRUARY 2016 REVIEWERS

THE APPLIED COMPUTATIONAL ELECTROMAGNETICS SOCIETY

JOURNAL

Vol. 31 No. 2 February 2016

TABLE OF CONTENTS

Microwave Imaging Using Synthetic Radar Scheme Processing for the Detection of Breast Tumors

Abdullah K. Alqallaf [1], Rabie K. Dib [2], and Samir F. Mahmoud [1]

[1] Electrical Engineering Department, College of Engineering and Petroleum
Kuwait University, Kuwait
Al.qallaf@ku.edu.kw, samirfm2000@yahoo.com

[2] Electronics Engineering Department, College of Technological Studies
Public Authority of Applied Education and Training, Kuwait
rk.dib@paaet.edu.kw

Abstract ─ Microwave imaging of the human breast for detection of possible tumors is studied by applying the method of synthetic radar imaging using both simulation and theoretical results. The breast is modeled as a homogeneous medium having complex dielectric constant, while the tumor is modeled as a small spherical inhomogeneity. A flexible bow-tie antenna excited by a narrow-band pulse illuminates the breast and the reflected field is monitored as the antenna takes a number of discrete positions along the breast surface. The collected data is processed in a synthetic radar scheme to image the interior of the breast. Simulation results for tumor response are obtained and compared with theoretically obtained results. It is shown that a tumor of few millimeter radius, between 3 to 7 mm, can be detected and located with reasonable resolution. It is found that the tumor response increases with the tumor size at a given frequency band in an oscillatory fashion.

Index Terms ─ Breast, microwave imaging, synthetic radar, tumor detection.

I. INTRODUCTION

Microwave imaging of the breast has been of primary interest for few decades. The main purpose is the detection of possible tumors in their early stages. The tumor detection is based on the clear contrast between the complex dielectric constant of the normal breast tissue and the tumor [1-4]. Unlike the X-ray mammography, which is currently the main method of tumor detection, the microwave imaging method enjoys the property of being a nonionizing source of radiation which minimizes the cumulative side-effects to healthy breast tissues and consequently provides safer scanning alternative. In addition, the X-ray mammography has the basic limitation of small contrast between the diseased and normal tissues density, while the microwave imaging method scans in-depth penetration of the breast tissues by applying low power and longer wavelength signals to provide more accurate breast modal at the regular scanning conditions [5-8, 32]. There are mainly two approaches for microwave imaging. In the first approach, the breast is illuminated and the scattered field is used in an inverse scattering algorithm to construct an image of the electrical properties of the breast tissues. However, this inverse problem is considered an ill-conditioned nonlinear one and normally requires intensive computational work [9-11]. This is so due to the heterogeneous nature of the breast medium. However, some initial successful experimental results appear in [12-13]. The second approach is based on synthetic radar imaging that focus waves on small volume that is, in turn, scanned throughout the breast. This approach is also known as 'Confocal Microwave imaging'. This method has been investigated by Hagness and his group [14-17], and by Fear et al. [18-21] who confirm the method by simulation and experiment. A more recent study presents a tomographic based microwave system and signal processing to extract the tumor information from the background information and then to reconstruct the image through confocal method [31]. However, no attempt is made to study the resolution power of tumor location and the dependence of reflection level on tumor size.

In this paper, we introduce a parametric study of the resolution power of the confocal microwave imaging method. We intend to test the effectiveness of the synthetic radar approach for locating tumors using simple antenna driven by narrow band pulse. We also present results on the dependence of the reflection level on the tumor size. Both analytical and simulation results are obtained for assumed tumors of different size and location. We do so by modeling the breast and the illuminating antenna as illustrated in Section 2. Simulation results that include the resolution of tumor detection and the dependence of the reflected signal on

Submitted On: March 13, 2015
Accepted On: February 20, 2016

the tumor size are demonstrated in Section 3. In Section 4, analytical derivation of the response of a spherical tumor is presented. The theoretical results are compared with those obtained by simulations and are followed by concluding remarks.

II. THE BREST MODEL AND THE ANTENNA

Two possible positions for the breast can be used during imaging: the supine position and the prone position. In the supine position the breast is oriented upwards and flattened out, while in the prone position the breast is oriented downwards [17]. Further, it is found that the supine position is more practical for measuring process. Therefore, in this paper, we focus our study in the paper on the supine position. The breast is then modeled as a rectangular box with upper surface coinciding with $Z = 0$ plane as shown in Fig. 1. The width of the breast is taken equal to 20 cm, and the sides are loaded with matched loads. The depth is assumed equal to 15 cm. The breast medium is assumed homogeneous with conductivity σ (S/m) and relative permittivity ε_r. A possible tumor of spherical shape with radius 'a' exists at a depth d, i.e., at $Z = -d$. The tumor has a contrasting conductivity σ_s and relative permittivity ε_{rs}. An antenna is placed with its phase center at the origin of (x,y,z) coordinate system and radiates in the breast medium. The planar antenna lies directly on the breast. A suitable thin layer is placed between the breast surface and the antenna. The material of the layer should electrically match the body so that no reflection occurs at the surface [17]. The center of the spherical tumor lies at ($X = -L$ and $Z = -d$) as shown in Fig. 1. A rotated Cartesian coordinates (x,y,z) has origin at the sphere center. While the relative permittivity ε_r of normal tissues is around 10, that of the tumor is around 50. There is also contrast between the conductivities, being about 0.15 S/m for normal tissue and 0.7 S/m for tumors [17]. The choice of a suitable antenna for breast cancer detection is very crucial matter. The antenna is required to be compact, wide band, low profile, light weight, and flexible enough to be placed directly on the breast.

Recently, several antenna designs for breast cancer detection have been proposed including the dielectric resonator antenna [22-23], the stacked patch antenna [24], the wide slot UWB antenna [25], and the flexible bow-tie [26, 30]. All of these antennas meet the required traits of a breast cancer sensor. We have selected the flexible bow-tie antenna for our investigation since it has the smallest size and it is mechanically flexible to have a good contact with the breast. The antenna geometry and dimensions are chosen as in Fig. 2 and Table 1 to operate around the center frequency of 6 GHz. This frequency is chosen as a compromise between required depth of penetration in the tissues and the tumor location with acceptable resolution. The metal body of the bow-tie is printed on two thin flexible dielectric sheets as suggested in [26, 29] and is fed by a microstrip line as shown in Fig. 2. The total thickness of the two dielectric sheets equals 0.1287 mm. The dielectric sheet is 0.05 mm thick and has a relative permittivity of 4. A matching scheme is designed with the feed line as shown in Fig. 2. The resulting reflection loss $|S_{11}|$, when the antenna is placed on a medium that resembles the breast electrical properties is given in Fig. 3. It is seen that a -10 dB reflection loss or more is secured in the frequency ranges 4.75-6.7 GHz.

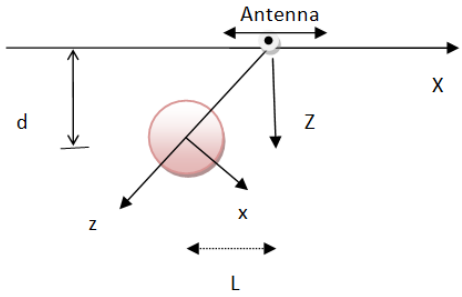

Fig. 1. Model of a spherical tumor of radius 'a' at depth d below the breast upper surface. The antenna lies on the surface at a lateral distance L from the tumor center.

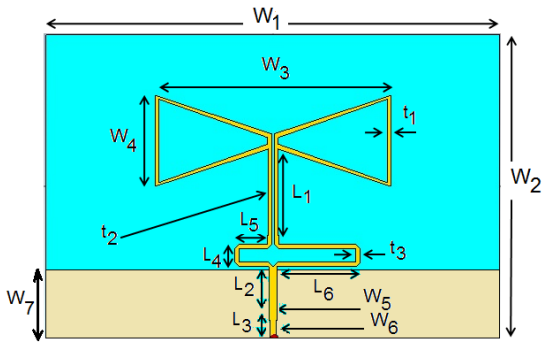

Fig. 2. Bow-tie antenna used for imaging. The antenna dimensions are given in Table 1. The antenna is placed on a medium with the breast-like permittivity.

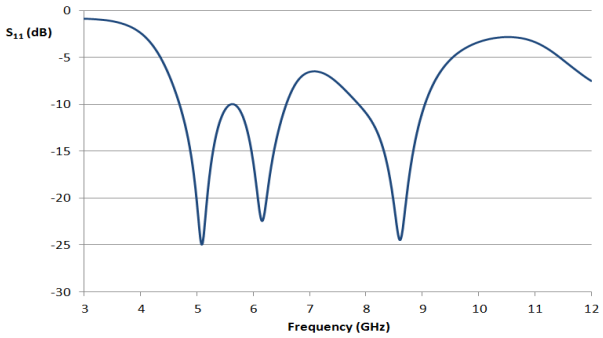

Fig. 3. The reflection $|S_{11}|$, in dB, versus the frequency, in GHz, where the antenna is placed on a medium with the breast-like permittivity.

Table 1: Bow-tie antenna dimensions used for imaging

Parameters	Length in (mm)
W_1	36
W_2	23.2
W_3	18.72
W_4	6.96
W_5	0.65
W_6	0.51
W_7	7.2
L_1	6.12
L_2	4.03
L_3	2.48
L_4	1.53
L_5	2.57
L_6	5.74
t_1	0.23
t_2	0.24
t_3	0.34

III. SIMULATION RESULTS

The antenna is placed on the breast surface and is fed by a pulse that covers a bandwidth of 500 MHz around 6 GHz center frequency. The pulse shape in the time domain is shown in Fig. 4. The pulse bandwidth is less than 10% of the center frequency. Within this narrow bandwidth, the breast electrical parameters can be assumed constants and therefore, one can accurately compensate for the propagation effects in the breast. One can apply the pulse at different discrete center frequencies to obtain multi-frequency images for the tumor.

The voltage waveform picked up by the antenna is monitored for, say, *M* different positions of the antenna as it is displaced along the *X*-axis. To remove the primary pulse and possible reflections from the skin layer of the breast, the average received waveform from the *M* positions is subtracted from each of the received waveforms. The resulting signals represent the scattered field from the tumor inhomogeneity at the *M* antenna positions. The next step is to process the *M* signals so as to synthetically focus the field at an arbitrary point within the breast. This leads to imaging the breast medium. In processing the *M* waveforms, we have to account for the variations of the antenna radiation pattern at the scanned points.

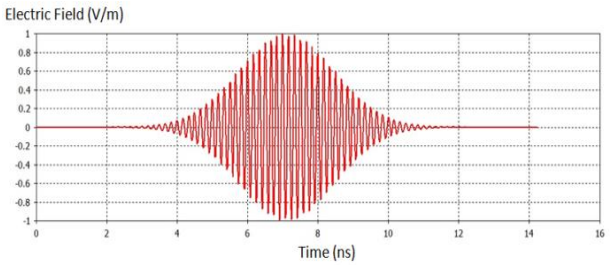

Fig. 4. The feeding pulse shape in the time domain.

The response obtained from a spherical tumor of radius 4 mm in the *X*-*Z* plane is shown is Fig. 5. The tumor is placed at $X = 0$ and $Z = -d = -30$ mm.

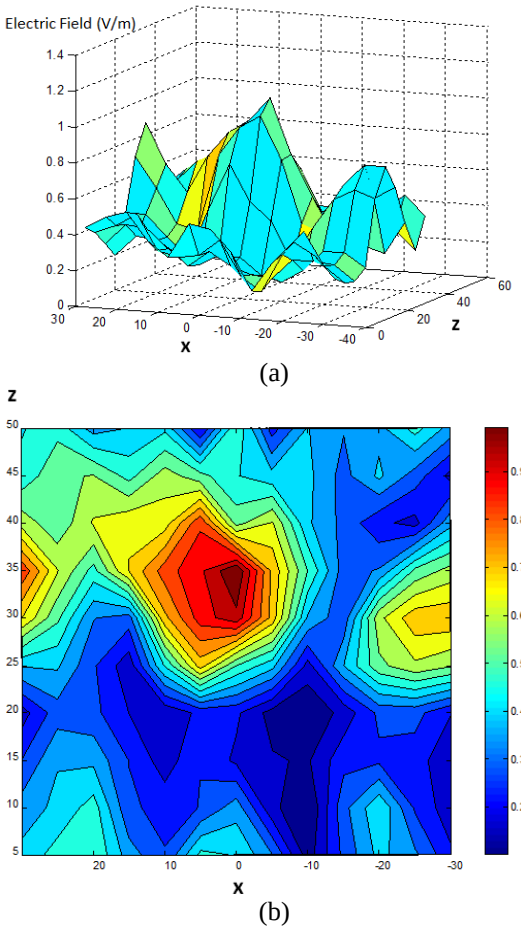

Fig. 5. Reflection response versus observing point on the x-z plane for 4 mm radius tumor: (a) 3-dimensional plot, and (b) contours of constant reflection.

The breast is modeled as a block of width 200 mm, and depth of 100 mm. The response in Fig. 5 (a) is obtained for $M = 17$ positions of the antenna on the $Z = 0$ plane with spacing of 8 mm between positions. The contours of constant response levels are shown in Fig. 5 (b). Figures 6 (a), (b) show the same response as in Fig. 5 (a), (b), except that the tumor radius is increased to 6 mm. It is clear from both figures that there is a clear peak response at the exact position and depth of the tumor. The resolution may be determined by the region where the response is reduced to 50% of the peak value. For the 4 mm tumor, the resolution region covers 20 mm about the *X* position and about 15 mm in the *Z*-direction. This means that two tumors separated horizontally by less than 20 mm or vertically by 15 mm cannot be distinguished and will show as one tumor. It is interesting to study the reflection level as a function of

the tumor radius at a given depth. The normalized reflection response for different tumor sizes at 6 GHz center frequency is presented for d = 30 mm in Fig. 7. It is seen that the response increases with tumor size in an oscillatory fashion. There is a minimum response for tumor radii of 3 mm and 5 mm. These minima will move to other values of tumor radii if the center frequency changes.

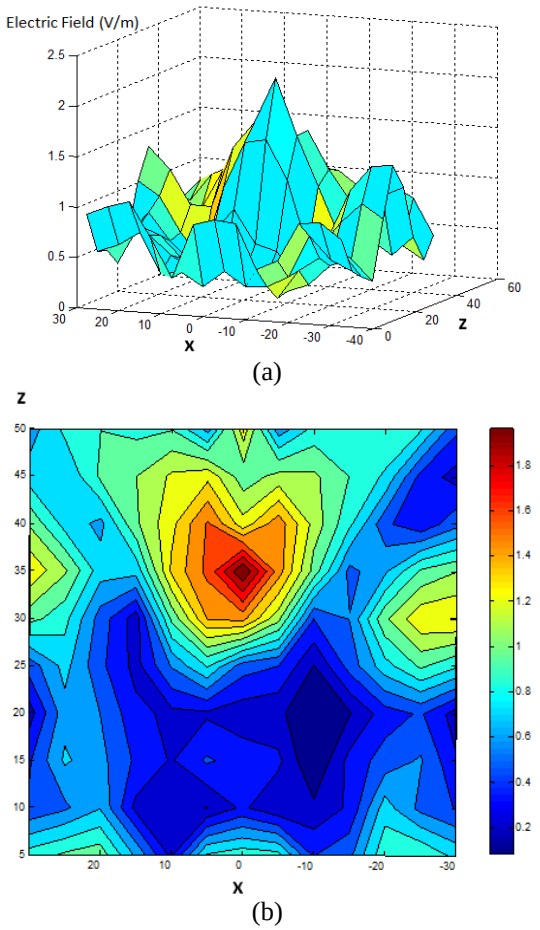

Fig. 6. Reflection response versus observing point on the x-z plane for 6 mm radius tumor: (a) 3-dimensional plot, and (b) contours of constant reflection.

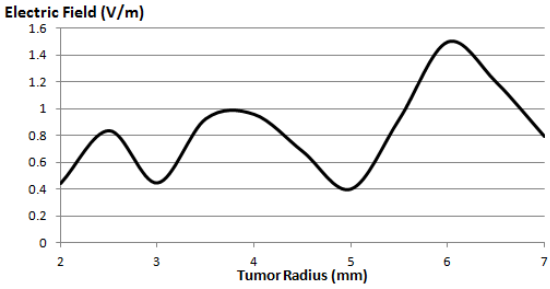

Fig. 7. Simulated reflection response vs. tumor radius (mm) at 6 GHz.

IV. THEORETICAL ANALYSIS

In this section we derive the scattered field from the tumor inhomogeneity. The antenna illuminates the tumor by an incident wave which is generally a spectrum of plane waves. However, we can assume that in the vicinity of the tumor whose dimensions are less than the applied wavelength, the incident wave is a single plane wave directed from the antenna phase center to the tumor center (in the z-direction). Adopting this assumption, we write the incident E and H field as:

$$E_x^i = E_o e^{-jkz} = E_o e^{-jkr\cos\theta}, \quad (1)$$

$$H_y^i = \frac{E_o}{\eta} e^{-jkr\cos\theta}, \quad (2)$$

where a time harmonic field dependence as $exp(j\omega t)$ has been assumed with $j = \sqrt{-1}$ and the complex wave number $k = \omega\sqrt{\mu_0\epsilon_0(\epsilon_r - \frac{j\sigma}{\omega\epsilon_0})}$. The radial coordinate r is measured from the sphere center, and η is the wave impedance in the breast medium. It is useful to obtain the radial fields in order to pursue the analysis to obtain the scattered fields in the spherical coordinate system (r,θ,ϕ). In terms of the spherical wave functions, the incident radial E takes the form:

$$E_r^i = \frac{E_o\cos\phi}{jkr}\sum j^{-n}(2n+1)\hat{J}_n(kr)\frac{\partial}{\partial\theta}P_n^{(1)}(\cos\theta)), \quad (3)$$

here $\hat{j}_n\,(kr)$ is the spherical Bessel function as defined in [28], and $P_n^{(1)}(\cos\,\theta)$ is the associated Legendre polynomial [27]. The radial E in (4) is also derivable from a magnetic vector potential A_r, so that,

$$E_r^i = (j\omega\epsilon)^{-1}\left[\frac{\partial^2}{\partial r^2} + k^2\right]A_r^i = (j\omega\epsilon)^{-1}\,\frac{n(n+1)}{r^2}\,A_r^i.$$

Therefore:

$$A_r^i = \frac{E_o}{\omega\mu}\cos\phi\sum_{n=0}^{\infty}a_n J_n(kr)P_n^{(1)}(\cos\theta), \quad (4)$$

where $a_n = j^{-n}(2n+1)/(n(n+1))$. Treating the radial magnetic field in the same way, we arrive at the incident electric vector potential F_r as [28]:

$$F_r^i = \frac{E_o}{k}\sin\phi\sum_{n=0}^{\infty}a_n J_n(kr)P_n^{(1)}(\cos\theta). \quad (5)$$

The scattered fields have similar form except that $\hat{j}_n(kr)$ is replaced by the spherical Hankel function $\hat{H}_n(kr)$. The total external field to the sphere (incident + scattered) is given by:

$$A_r^{ex} = \frac{E_o}{\omega\mu}\cos\phi\sum_{n=0}^{\infty}(a_n J_n(kr) + b_n\hat{H}_n(kr)P_n^{(1)}(\cos\theta)$$
$$F_r^{ex} = \frac{E_o}{k}\sin\phi\sum_{n=0}^{\infty}(a_n J_n(kr) + c_n\hat{H}_n(kr)P_n^{(1)}(\cos\theta) \quad (6)$$

where b_n and c_n coefficients are, so far, unknown to be determined from the boundary conditions at the spherical

surface. The next step towards the determination of the fields everywhere is to write down the internal fields inside the spherical tumor, namely:

$$A_r^{in} = \frac{E_o}{\omega\mu}\cos\phi\sum_{n=1}^{\infty} d_n J_n(k_s r)P_n^{(1)}(\cos\theta)$$
$$F_r^{ex} = \frac{E_o}{k_s}\sin\phi\sum_{n=1}^{\infty} e_n J_n(k_s r)P_n^{(1)}(\cos\theta) \quad , \quad (7)$$

where again d_n and e_n are unknown coefficients. Note that k_s is the wave number in the spherical tumor. Namely, $k_s = \omega\sqrt{\mu_0\epsilon_0(\epsilon_{rs} - \frac{j\sigma_s}{\omega\epsilon_0})}$.

Now, we are ready to apply the boundary conditions requiring the continuity of the $\theta$and ϕ–field components at the spherical surface. This leads to the determination of the scattered field coefficients b_n and c_n as given in the Appendix.

The scattered E_θ component in the external region is given by:

$$E_\theta^S(r,\theta) = \frac{-E_o}{kr}cos\emptyset\left[\begin{matrix}\sum_{n=1}^{N} c_n\widehat{H}_n(kr)\frac{P_n'(cos\theta)}{sin\theta} \\ +jb_n\widehat{H}_n'(kr)\frac{\partial P_n'(cos\theta)}{\partial\theta}\end{matrix}\right]. \quad (8)$$

The summation term is truncated after N terms, where N depends on the tumor size. Numerical calculations show that N = 5 gives acceptable convergence up to tumor radius of 7 mm at 6 GHz applied frequency. The scattered field at the transmitting antenna is equal to: $E_\theta(r_1,\pi)\,(-\frac{d}{r_1})$, where $r_1 = \sqrt{d^2 + L^2}$ and we have assumed that the antenna major polarization is along X' direction.

Next, signal processing is applied to realize focusing on the tumor for M positions of the antenna at $L = i\Delta$; i=0, 1, 2 … (M -1). The net signal for the M positions of the antenna is:

$$E_{total} = \sum_{i=0}^{M-1}\,[E_\theta(r_1,\pi)\,(-\tfrac{d}{r_1})]\,\exp[+2jkr_1]. \quad (9)$$

As an example we plot (11) versus the tumor radius 'a' in mm for an applied frequency of 6 GHz, and depth d = 30 mm in Fig. 8. The antenna is positioned in 17 equidistant positions with spacing Δ = 10 mm. The field is normalized relative to the incident E. It is noted that the response tends to increase with the tumor radius, but in an oscillatory manner. The theoretical result is compared with simulation in the same figure, and it is seen that there is a reasonable agreement. We have to bear in mind that the theoretical curve is computed for a single applied frequency (6 GHz), while the simulation curve is done for a band of frequency (5.75 – 6.25 GHz). In order to study the effect of varying the applied frequency, the tumor response is plotted versus the frequency between 5-7.5 GHz at three different tumor radii in Fig. 9. It is seen that depending on the tumor radius, there is an optimum frequency for tumor detection. For example a tumor of 3 mm radius is not detectable at f~6.1 GHz while it is well detected at f~7.0 GHz. On the other hand, the optimum frequency for detecting a tumor of 6 mm radius is f~6.2 GHz. We thus conclude the importance of imaging the breast by several narrow band pulses of distinct center frequencies.

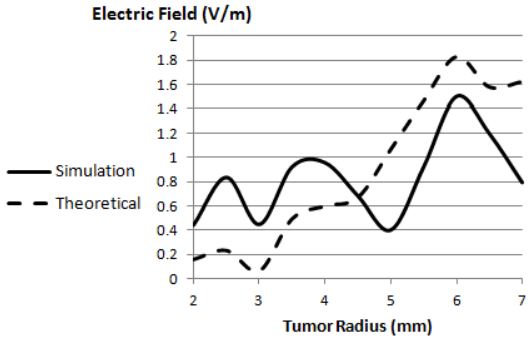

Fig. 8. Simulation and theoretical normalized reflection response vs. tumor radius (mm) at 6 GHz.

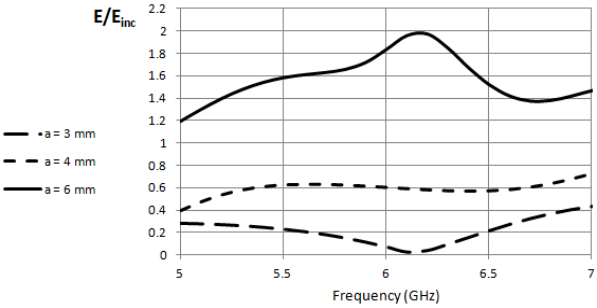

Fig. 9. Theoretical reflection response for three different tumor radii a = 3, 4, and 6 mm vs. center.

V. CONCLUSION

In this paper we have presented a study of microwave imaging of the human breast for possible tumor detection by applying the method of synthetic radar imaging. Both analytical and simulation results are presented for assumed tumors of different size and location. The breast is modeled as a homogeneous medium having complex dielectric constant, while the tumor is modeled as a small spherical inhomogeneity. The breast is illuminated by a microwave pulse of narrow bandwidth through a bow-tie antenna and the reflected field is monitored as the antenna is positioned at a number of discrete positions along the breast surface. Signal processing is applied to the collected data to focus the wave at different points to scan the whole breast. It has been demonstrated that a spherical tumor of few millimeter radius can be detected with reasonable resolution using a pulse of 6 GHz center frequency and 0.5 GHz bandwidth. The response of a tumor generally increases with its size, but in an oscillatory manner. The simulation results are supported by analytical results

where a reasonably good agreement is observed. Our study also shows that the optimum frequencies for detecting tumors depend on the tumors' radii. Finally, it is recommended that images should be taken at few distinct frequencies in the range 5-7 GHz in order to detect tumors of different sizes.

VI. APPENDIX

The coefficients b_n and c_n in (8) are obtained from the boundary conditions at the spherical surface $r=a$ as:

$$b_n / a_n = [\bar{\eta}_s R_{ns} J_n(ka) - J_n^{'}(ka)] / [\hat{H}_n^{'}(ka) - \bar{\eta}_s R_{ns} \hat{H}(ka)], \quad \text{(A1)}$$

$$c_n / a_n = [\bar{k}_s R_{ns} \hat{J}_n(ka) - \hat{J}_n^{'}(ka)] / [\hat{H}^{'}(ka) - \bar{k}_s R_{ns} \hat{H}(ka)], \quad \text{(A2)}$$

where the dash on the Bessel and Hankel spherical functions denotes differentiation with respect to the argument,

$$\bar{\eta}_s = \eta_s/\eta, \ \overline{k_s} = \frac{k_s}{k}, \text{ and } R_{ns} = \hat{J}_n^{'}(k_s a)/\hat{H}_n^{'}(k_s a).$$

ACKNOWLEDGMENT

This work was supported by Kuwait University Research Grant No. [RE02/12].

REFERENCES

[1] A. J. Surowiec, S. S. Stuchly, J. R. Barr, and A. Swarup, "Dielectric properties of breast carcinoma and the surrounding tissues," *IEEE Trans. Biomed. Eng.*, vol. BME-35, pp. 257-263, Apr. 1988.

[2] W. T. Joines, Y. Zhang, C. Li, and R. L. Jirtle, "The measured electrical properties of normal and malignant human tissues from 50 to 900 MHz," *Med. Phys.*, vol. 21, pp. 547-550, Apr. 1994.

[3] S. S. Chaudhary, R. K. Mishra, A. Swarup, and J. M. Thomas, "Dielectric properties of normal and malignant human breast tissues at radiowave and microwave frequencies," *Indian J. Biochem. Biophys.*, vol. 21, pp. 76-79, Feb. 1984.

[4] S. C. Hagness, K. M. Leininger, J. H. Booske, and M. Okoniewski, "Dielectric characterization of human breast tissue at microwave frequencies," *Presented at the 2nd World Congr. Microwave and Radio Frequency Processing*, Orlando, FL, Apr. 2000.

[5] M. Brown, F. Houn, E. Sickles, and L. Kessler, "Screening mammography in community practice," *Amer. J. Roentgen.*, vol. 165, pp. 1373-1377, Dec. 1995.

[6] P. T. Huynh, A. M. Jarolimek, and S. Daye, "The false-negative mammogram," *Radiograph.*, vol. 18, no. 5, pp. 1137-1154, 1998.

[7] J. G. Elmore, M. B. Barton, V. M. Moceri, S. Polk, P. J. Arena, and S. W. Fletcher, "Ten-year risk of false positive screening mammograms and clinical breast examinations," *New Eng. J. Med.*, vol. 338, no. 16, pp. 1089-1096, 1998.

[8] V. P. Jackson, R. E. Hendrick, S. A. Feig, and D. B. Kopans, "Imaging of the radiographically dense breast," *Radiology*, vol. 188, pp. 297-301, Aug. 1993.

[9] S. Caorsi, G. L. Gragnani, and M. P. Pastorino, "Reconstruction of dielectric permittivity distributions in arbitrary 2-D inhomogeneous biological bodies by a multiview microwave numerical method," *IEEE Trans. Med. Imag.*, vol. 12, pp. 232-239, June 1993.

[10] A. E. Souvorov, A. E. Bulyshev, S. Y. Semenov, R. H. Svenson, A. G. Nazarov, Y. E. Sizov, and G. P. Tatsis, "Microwave tomography: a two-dimensional Newton iterative scheme," *IEEE Trans. Microwave Theory Tech.*, vol. 46, pp. 1654-1659, Nov. 1998.

[11] M. Bertero, M. Miyakawa, P. Boccacci, F. Conte, K. Orikasa, and M. Furutani, "Image restoration in chirp-pulse microwave CT (CP-MCT)," *IEEE Trans. Biomed. Eng.*, vol. 47, pp. 690-699, May 2000.

[12] P. M. Meaney, K. D. Paulsen, J. T. Chang, M. W. Fanning, and A. Hartov, "Nonactive antenna compensation for fixed-array microwave imaging–Part II: imaging results," *IEEE Trans. Med. Imag.*, vol. 18, pp. 508-518, June 1999.

[13] P. M. Meaney, M. W. Fanning, D. Li, S. P. Poplack, and K. D. Paulsen, "A clinical prototype for active microwave imaging of the breast," *IEEE Trans. Microwave Theory Tech.*, vol. 48, pp. 1841-1853, Nov. 2000.

[14] S. C. Hagness, A. Taflove, and J. E. Bridges, "Two-dimensional FDTD analysis of a pulsed microwave confocal system for breast cancer detection: fixed-focus and antenna-array sensors," *IEEE Trans. Biomed. Eng.*, vol. 45, pp. 1470-1479, Dec. 1998.

[15] S. C. Hagness, A. Taflove, and J. E. Bridges, "Wideband ultra low reverberation antenna for biological sensing," *Electron. Lett.*, vol. 33, no. 19, pp. 1594-1595, 1997.

[16] S. C. Hagness, A. Taflove, and J. E. Bridges, "Three-dimensional FDTD analysis of a pulsed microwave confocal system for breast cancer detection: design of an antenna-array element," *IEEE Trans. Antennas Propagat.*, vol. 47, pp. 783-791, May 1999.

[17] X. Li and S. C. Hagness, "A confocal microwave imaging algorithm for breast cancer detection," *IEEE Microwave Wireless Comp. Lett.*, vol. 11, pp. 130-132, Mar. 2001.

[18] E. Fear and M. Stuchly, "Microwave system for breast tumor detection," *IEEE Microwave Guided Wave Lett.*, vol. 9, pp. 470-472, Nov. 1999.

[19] E. C. Fear and M. A. Stuchly, "Microwave detection of breast cancer," *IEEE Trans. Microwave Theory Tech.*, vol. 48, pp. 1854-1863, Nov. 2000.
[20] E. C. Fear and M. A. Stuchly, "Microwave detection of breast tumors: comparison of skin subtraction algorithms," *Proc. SPIE*, vol. 4129, pp. 207-217, 2000.
[21] E. C. Fear, X. Li, S. C. Hagness, and M. A. Stuchly, "Confocal microwave imaging for breast cancer detection: localization of tumors in three dimensions," *IEEE Transactions on Biomedical Engineering*, vol. 49, no. 8, Aug. 2002.
[22] W. Huang and A. A. Kishk, "Compact wideband multi-layer cylindrical dielectric resonator antennas," *IEE Proc. Microw. Antennas Propag.*, vol. 1, no. 4, pp. 998-1005, 2007.
[23] W. Huang and A. A. Kishk, "Compact dielectric resonator antenna for microwave breast cancer detection," *IET Microwave, Antennas & Propagation*, vol. 3, iss. 4, pp. 638-644, 2009.
[24] R. Nilavalan, I. J. Craddock, A. Preece, J. Leendertz, and R. Benjamin, "Wideband microstrip patch antenna design for breast cancer detection," *IET Microw. Propag.*, vol. 1, no. 2, pp. 277-281, 2007.
[25] D. Gibbins, M. Klemm, I. J. Craddock, J. A. Leendertz, A. Preece, and R. Benjamin, "A comparison of a wide-slot and a stacked patch antenna for the purpose of breast cancer detection," *IEEE Transactions on Antennas and Propagation*, vol. 58, no. 3, pp. 665-674, 2010.
[26] A. C. Durgun, C. A. Balanis, C. R. Birtcher, and D. A. Allee, "Design, simulation, fabrication and testing of flexible bow-tie antennas," *IEEE Trans. on Antennas and Propagat.*, vol. 59, no. 12, 2011.
[27] M. Abramowitz and I. A. Stegun, ed., *Handbook of Mathematical Functions*, Chapter 10 by H. Antosiewice, Dover Publications, Inc., New York, 1970.
[28] R. F. Harrington, *Time Harmonic Electromagnetic Fields*, Chapter 6, McGraw Hill, 1961.
[29] A. A. Eldek, A. Z. Elsherbeni, and C. E. Smith, "Wideband modified printed bow-tie antenna with single and dual polarization for C and X-band applications," *IEEE Transaction on Antennas and Propagations*, vol. 53, no. 9, pp. 3067-3072, Sep. 2005.
[30] E. Porter, G. Walls, Y. Zhou, M. Popovic, and J. D. Schwartz, "A flexible broadband antenna and transmission line network for a wearable microwave breast cancer detection system," *Progress In Electromagnetics Research Letters*, vol. 49, pp. 111-118, Oct. 2014.
[31] Z. Wang, E. G. Lim, Y. Tang, and M. Leach, "Medical applications of microwave imaging," *The Scientific World Journal*, vol. 2014, 2014.
[32] P. K. Singh, S. K. Tripathi, R. Sharma, and A. Kumar, "Design & simulation of microstrip antenna for cancer diagnosis," *International Journal of Scientific & Engineering Research*, vol. 4, iss. 11, pp. 1821-1824, Nov. 2013.

Abdullah K. Alqallaf is an Assistant Professor with the Department of Electrical Engineering at the Kuwait University. He received the B.S. and M.S. degrees in Electrical Engineering from Kuwait University in 1996 and 1999, respectively, and the Ph.D. degree in Electrical Engineering from the University of Minnesota – Twin Cities, St. Paul, MN, in 2009. Alqallaf's research interests are Microwave Imaging Techniques, Multimedia Signal Processing, Communication, Bioinformatics and Medical Image Analysis. Alqallaf is an IEEE Board Member - Professional Activities - Kuwait section.

Rabie K. Dib is an Instructor with the Electronics Engineering Dept., College of Technological Studies at Public Authority of Applied Education and Training, Kuwait. He received the B.S. and M.S. degrees in Electrical Engineering from Kuwait University in 1999 and 2002, respectively. Dib's research interests are Electromagnetics, Communication, Antenna Design, Microwave Imaging Techniques and Analysis.

Samir F. Mahmoud is a Professor with the Department of Electrical Engineering at the Kuwait University. He received the B.S. in Electrical Engineering from the Electronic Engineering Dept., Cairo University, Egypt in 1964. He received the M.Sc. and Ph.D. degrees in the Electrical Engineering Department, Queen's University, Kingston, Ontario, Canada in 1970 and 1973, respectively. He was a Visiting Research Fellow at the Cooperative Institute for Research in Environmental Sciences (CIRES), Boulder, CO, doing research on Communication in Tunnels during the academic year 1973-1974. He spent two sabbatical years, 1980-1982, between Queen Mary College, London and the British Aerospace, Stevenage, where he was involved in design of antennas for satellite communication. Recently, he has visited several places including Interuniversity Micro-Electronics

Centre (IMEC), Leuven, Belgium and spent a sabbatical leave at Queen's University and the Royal Military College, Kingston, Ontario, Canada in 2001-2002. His research activities have been in the areas of antennas, geophysics, tunnel communication, and e.m wave interaction with composite materials. Mahmoud is a Fellow of IET and one of the recipients of the best IEEE/MTT paper for 2003.

Probe Position Errors Corrected Near-Field – Far-Field Transformation with Spherical Scanning

F. D'Agostino, F. Ferrara, C. Gennarelli, R. Guerriero, and M. Migliozzi

Dipartimento di Ingegneria Industriale
University of Salerno, via Giovanni Paolo II, 132 - 84084 Fisciano, Italy
fdagostino@unisa.it, flferrara@unisa.it, cgennarelli@unisa.it, rguerriero@unisa.it, mmigliozzi@unisa.it

Abstract ─ Two effective approaches to correct known positioning errors in a near-field – far-field (NF–FF) transformation with spherical scan for electrically long antennas are proposed and validated numerically and experimentally. They rely on a nonredundant sampling representation of the voltage acquired by the probe, obtained by assuming that the antenna under test is enclosed in a cylinder ended in two half-spheres. The former approach exploits the singular value decomposition method, to retrieve the NF data at the points fixed by the sampling representation from the acquired irregularly spaced ones, and can be used when the nonuniformly spaced samples lie on nonuniform parallels. The latter employs an iterative technique, which can be adopted even if such a hypothesis is not satisfied, but requires the existence of a one-to-one correspondence associating at each uniform sampling point, the nearest nonuniform one. Once the uniform samples have been recovered, the NF data needed by the classical spherical NF–FF transformation are efficiently evaluated via an optimal sampling interpolation algorithm.

Index Terms ─ Antenna measurements, nonredundant sampling representations, probe positioning errors compensation, spherical near-field – far-field transformation.

I. INTRODUCTION

Among the techniques which allow the evaluation of the antenna far field from measurements performed in the near-field region, the near-field – far-field (NF–FF) transformation with spherical scanning is the most interesting one, due to its unique features to allow the full reconstruction of the radiation pattern and to avoid the errors related to the truncation of the measurement surface. Therefore, it has attracted a considerable attention in the last four decades [1-15]. In fact, the first work dealing with a NF–FF transformation with spherical scanning based on the spherical wave expansion (SWE) was the Ph.D. dissertation thesis of Jensen [1], published later in a more complete form in the paper [2], wherein a proper transmission formula for the probe correction was derived. An efficient fast Fourier transform scheme to evaluate the SWE coefficients of the antenna under test (AUT) was then developed by Wacker [3], that also proposed the use of a probe with a pattern azimuthal dependence of the first order. Further improvements in the numerical efficiency were achieved in [4,5]. A comprehensive book [6], which deals with the theoretical as well as practical aspects of the classical probe-compensated NF–FF transformation with spherical scanning, was published by Hansen. Alternative probe-corrected formulas were derived in [7,8] by expressing the probe output in terms of the spatial derivatives of the incident field. Recently, the probe correction has been generalized to higher-order probes [9,10], thus allowing the characterization of wideband antennas without changing the probe.

The classical spherical NF–FF transformation [6] has been modified in [11], by taking into account the spatial bandlimitation properties of radiated electromagnetic (EM) fields [16]. In particular, the highest spherical wave to be considered has been fixed by these properties and the number of data on the parallels has resulted to be decreasing towards the poles. In this framework, the application of the nonredundant sampling representations of radiated EM fields [17,18] has allowed the development of effective NF–FF transformations with spherical scanning [11-14], which usually require a number of NF data remarkably lower than that needed by the classical one [6]. As a matter of fact, the NF data required by this last are accurately retrieved by interpolating a minimum set of measurements via optimal sampling interpolation (OSI) expansions. A remarkable measurement time saving can be so obtained making these nonredundant transformations more and more appealing, since today such a time is very much greater than the computational one needed to perform the transformation. This result relies on the fact that, according to the abovementioned representations, the EM fields radiated by antennas, enclosed in a convex domain bounded by a rotational surface Σ and observed on a surface M with the same rotational symmetry, can be very well approximated by spatially band-limited functions when a proper phase

Submitted On: July 2, 2015
Accepted On: November 3, 2015

factor is singled out from the field expression and proper parameterizations are adopted to describe M [17]. Since the voltage acquired by a nondirective probe has the same effective spatial bandwidth of the field radiated by the AUT, these representations can be applied to the voltage too. In particular, an elongated antenna has been considered as enclosed in a prolate ellipsoid [11,12] or in a rounded cylinder (a cylinder ended in two half-spheres) [13,14], whereas an oblate ellipsoid [11,12] or a double bowl (a surface formed by two circular bowls with the same aperture diameter, but with bending radii which can be different for a better fitting of the AUT geometry) [13,14] have been employed to model a quasi-planar antenna.

An alternative sampling technique for reducing the needed NF data has been developed in [15]. It makes use of a proper decision threshold to adaptively concentrate the acquisition on the strongly changing NF regions, while skipping the sampling points from the smoothly varying ones.

It must be stressed that the errors due to an imprecise control of the positioning systems and their finite resolution do not allow the exact placing of the probe at the points fixed by the sampling representation, even if their location can be accurately determined by optical devices. Therefore, it is very important to develop an effective algorithm for an accurate and stable reconstruction of the NF data needed by the NF–FF transformation from the irregularly spaced ones. To this end, an approach based on the conjugate gradient iteration method and exploiting the unequally spaced fast Fourier transform [19,20] has been developed for compensating the positioning errors in the classical NF–FF transformations with planar [21] and spherical [22] scannings. Unfortunately, such an approach is not tailored to the aforementioned nonredundant NF–FF transformations. A viable and convenient strategy [23] is to retrieve the uniform samples from the irregularly spaced (nonuniform) ones and then reconstruct the needed NF data via an accurate and stable OSI expansion. In this context, two different approaches have been proposed. The former is based on an iterative technique, which converges only if it is possible to build a biunique correspondence associating at each uniform sampling point the nearest nonuniform one, and has been applied to the reconstruction of the uniform samples in plane-rectangular [23], cylindrical and spherical grids [24]. The latter relies on the singular value decomposition (SVD) method, does not exhibit the above limitation and has been applied to the uniform samples reconstruction in planar [25,26] and cylindrical [27] geometries. It allows to exploit the data redundancy to increase the algorithm stability, but can be conveniently applied only if the uniform samples recovery can be reduced to the solution of two independent one-dimensional problems. At last, both the approaches have been applied and numerically compared in [28] with reference to the positioning errors compensation in the nonredundant spherical NF–FF transformation based on the prolate ellipsoidal AUT modelling.

The aim of this paper is to validate numerically and experimentally the application of these two approaches to the NF–FF transformation with spherical scanning for long antennas [13] using the rounded cylinder modelling (Fig. 1). The experimental tests have been carried out in the Antenna Characterization Lab of the University of Salerno, provided with a roll over azimuth spherical NF facility supplied by MI Technologies.

The nonredundant sampling representation on the scanning sphere for the voltage measured by the probe, obtained by modelling the AUT with a rounded cylinder, is summarized in Section 2. The two approaches to compensate known positioning errors are then presented in Section 3, and numerically and experimentally validated in Sections 4 and 5, respectively. Finally, the conclusions are drawn in Section 6.

II. NONREDUNDANT SAMPLING REPRESENTATION ON A SPHERE

Let us consider an electrically long AUT, enclosed in a convex domain $\mathcal{D}$ bounded by a surface Σ with rotational symmetry, a nondirective probe scanning a sphere of radius d in the antenna NF region, and adopt the spherical coordinate system (r, ϑ, φ) for denoting an observation point P (Fig. 1). Since the voltage measured by this type of probe has the same effective spatial bandwidth of the field radiated by the AUT, the nonredundant representations of EM fields [17] can be applied to obtain an effective sampling representation of it. Accordingly, it is convenient to adopt an optimal parameter ξ to describe each of the curves C (meridians and parallels) representing the sphere and to introduce the "reduced voltage":

$$\tilde{V}(\xi) = V(\xi) \mathrm{e}^{\mathrm{j}\gamma(\xi)}, \tag{1}$$

where $V(\xi)$ is the voltage V_1 or V_2 measured by the probe or by the rated probe, and $\gamma(\xi)$ is a proper phase function to be determined. The error, occurring when $\tilde{V}(\xi)$ is approximated by a bandlimited function, becomes negligible as the bandwidth exceeds a critical value W_ξ [17] and can be effectively controlled by considering approximating functions with bandwidth $\chi' W_\xi$, where $\chi' > 1$ is the enlargement bandwidth factor, slightly greater than unity for electrically large antennas. As shown in [13], an effective modelling for an elongated antenna is obtained by assuming a rounded cylinder as surface Σ enclosing it, namely, a cylinder of height h' ended in two half-spheres of radius a' (see Figs. 1 and 2).

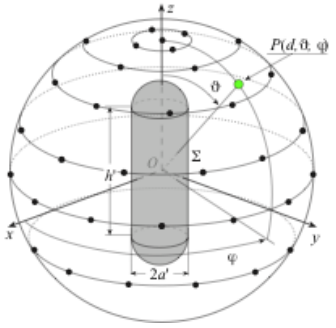

Fig. 1. Spherical scanning for a long antenna.

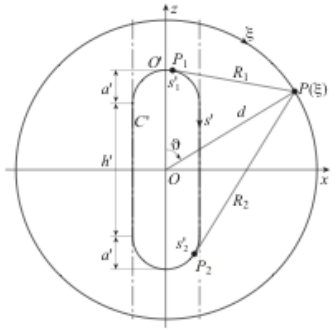

Fig. 2. Relevant to the rounded cylinder modelling.

When considering a meridian, the bandwidth W_ξ, the parameterization ξ and the corresponding phase function γ are [13,17]:

$$W_\xi = \beta \ell' / 2\pi, \tag{2}$$

$$\gamma = (\beta/2)\left[R_1 + R_2 + s_1' - s_2'\right], \tag{3}$$

$$\xi = (\pi/\ell')\left[R_1 - R_2 + s_1' + s_2'\right], \tag{4}$$

where β is the wavenmumber, $\ell' = 2(h' + \pi a')$ is the length of the intersection curve C' between the meridian plane through the observation point P and Σ, $R_{1,2}$ are the distances from P to the two tangency points $P_{1,2}$ between the cone of vertex at P and C', and $s_{1,2}'$ are their curvilinear abscissae (see Fig. 2). The explicit expressions of $R_{1,2}$ and $s_{1,2}'$, which change depending on the location of the points $P_{1,2}$, have been determined in [13] and are reported below for reader's convenience. In particular, three cases occur when ϑ varies in the angular range [0, π] (see Fig. 2).

For $0 \le \vartheta \le \sin^{-1}(a'/d)$, it results:

$$R_1 = \sqrt{(d\sin\vartheta)^2 + (d\cos\vartheta - h'/2)^2 - a'^2}, \tag{5}$$

$$s_1' = a'\sin^{-1}\left(\frac{a'd\sin\vartheta + R_1(h'/2 - d\cos\vartheta)}{R_1^2 + a'^2}\right), \tag{6}$$

$$s_2' = a'\sin^{-1}\left(\frac{a'd\sin\vartheta - R_2(h'/2 - d\cos\vartheta)}{R_2^2 + a'^2}\right), \tag{7}$$

and $R_2 = R_1$.

For $\sin^{-1}(a'/d) < \vartheta \le \pi - \sin^{-1}(a'/d)$, R_1 and s_1' are given by (5) and (6), while:

$$R_2 = \sqrt{(d\sin\vartheta)^2 + (d\cos\vartheta + h'/2)^2 - a'^2}, \tag{8}$$

$$s_2' = h' + a'\left[\pi - \sin^{-1}\left(\frac{a'd\sin\vartheta + R_2(h'/2 + d\cos\vartheta)}{R_2^2 + a'^2}\right)\right]. \tag{9}$$

Finally, when $\pi - \sin^{-1}(a'/d) < \vartheta \le \pi$, R_2 and s_2' are again given by (8) and (9), whereas:

$$R_1 = \sqrt{(d\sin\vartheta)^2 + (d\cos\vartheta + h'/2)^2 - a'^2}, \tag{10}$$

$$s_1' = h' + a'\left[\frac{\pi}{2} - \sin^{-1}\left(\frac{R_1 d\sin\vartheta + a'(h'/2 + d\cos\vartheta)}{R_1^2 + a'^2}\right)\right], \tag{11}$$

when C is a parallel, the phase function is constant and it is convenient to use the azimuthal angle φ as parameter. The related bandwidth W_φ is given [13,17] by:

$$W_\varphi = \frac{\beta}{2}\max_{z'}(R^+ - R^-) = \frac{\beta}{2}\max_{z'}\left(\sqrt{(z-z')^2 + (\rho + \rho'(z'))^2} - \sqrt{(z-z')^2 + (\rho - \rho'(z'))^2}\right), \tag{12}$$

wherein $\rho = d\sin\vartheta$, $\rho'(z')$ is the equation of Σ in cylindrical coordinates and the maximum is achieved [13] at:

$$z' = \begin{cases} z & |z| \le h'/2 \\ \left[\dfrac{h'}{2} + \dfrac{(|z| - h'/2)\ a'^2}{(d\sin\vartheta)^2 + (|z| - h'/2)^2}\right]\mathrm{sgn}(z) & |z| > h'/2 \end{cases}, \tag{13}$$

$\mathrm{sgn}(\cdot)$ being the sign function.

According to the above results, the reduced voltage at P on the meridian at φ can be efficiently reconstructed by means of the OSI expansion [13]:

$$\tilde{V}(\xi(\vartheta), \varphi) = \sum_{n=n_0-q+1}^{n_0+q} \tilde{V}(\xi_n, \varphi)\, G\left(\xi, \xi_n, \bar{\xi}, N, N''\right), \tag{14}$$

where $n_0 = \mathrm{Int}(\xi/\Delta\xi)$, $2q$ is the number of retained intermediate samples $\tilde{V}(\xi_n, \varphi)$, i.e., the reduced voltages at the intersection points between the sampling parallels and the meridian passing through P:

$$G\left(\xi, \xi_n, \bar{\xi}, N, N''\right) = \Omega_N\left(\xi - \xi_n, \bar{\xi}\right) D_{N''}(\xi - \xi_n), \tag{15}$$

$$\xi_n = n\Delta\xi = 2\pi n/(2N''+1);\ N'' = \mathrm{Int}(\chi N') + 1, \tag{16}$$

$$N' = \mathrm{Int}(\chi' W_\xi) + 1;\ N = N'' - N';\ \bar{\xi} = q\Delta\xi, \tag{17}$$

χ being an oversampling factor controlling the truncation error [17] and Int(x) denoting the integer part of x. In (15),

$$D_{N''}(\xi)=\frac{\sin[(2N''+1)\xi/2]}{(2N''+1)\sin(\xi/2)}, \quad (18)$$

$$\Omega_N(\xi,\bar{\xi})=\frac{T_N\left[2\cos^2(\xi/2)/\cos^2(\bar{\xi}/2)-1\right]}{T_N\left[2/\cos^2(\bar{\xi}/2)-1\right]}, \quad (19)$$

are the Dirichlet and Tschebyscheff sampling functions [17], $T_N(\vartheta)$ being the Tschebyscheff polynomial of degree N. The intermediate samples are given by [13]:

$$\tilde{V}(\xi_n,\varphi)=\sum_{m=m_0-p+1}^{m_0+p}\tilde{V}(\xi_n,\varphi_{m,n})G(\varphi,\varphi_{m,n},\bar{\varphi},M_n,M_n''), \quad (20)$$

wherein $m_0=\mathrm{Int}(\varphi/\Delta\varphi_n)$, $2p$ is the retained samples number, $\tilde{V}(\xi_n,\varphi_{m,n})$ are the reduced voltage samples on the parallel fixed by ξ_n, and

$$\varphi_{m,n}=m\Delta\varphi_n=2\pi m/(2M_n''+1);\ M_n''=\mathrm{Int}(\chi M_n')+1, \quad (21)$$

$$M_n'=\mathrm{Int}\left[\chi^* W_\varphi(\xi_n)\right]+1;\ \ M_n=M_n''-M_n', \quad (22)$$

$$\chi^*=1+(\chi'-1)\left[\sin\vartheta(\xi_n)\right]^{-2/3};\ \bar{\varphi}=p\Delta\varphi_n. \quad (23)$$

The accurate reconstruction of the voltages V_1 and V_2 at any point on the sphere can be then obtained by matching the OSI expansions (14) and (20).

III. FROM NONUNIFORM TO UNIFORM SAMPLES

Two different approaches to correct known positioning errors are presented in this section by highlighting their advantages and limitations. These approaches are then numerically and experimentally validated in Sections 4 and 5, respectively.

A. The SVD-based approach

Let us suppose that, apart the sample at the pole $\vartheta=0$, the irregularly spaced samples lie on parallels not uniformly distributed on the scanning sphere, which represents a realistic hypothesis in a spherical NF facility, when the NF data are acquired by scanning along parallels as it is required to exploit the possibility to reduce the number of NF data on the noncentral parallels, offered by the previous nonredundant representation. In this case, the uniform samples recovery reduces to the solution of two independent one-dimensional problems.

The uniform $2M_k''+1$ samples on a nonuniform parallel at $\vartheta(\eta_k)$ are recovered as follows. Given a sequence of $J_k \geq 2M_k''+1$ nonuniform sampling points (η_k,ϕ_j) on such a parallel, the related reduced voltages $\tilde{V}(\eta_k,\phi_j)$ can be expressed in terms of the uniform ones by means of (20), thus getting a linear system which can be rewritten in the matrix form:

$$\underline{\underline{A}}\,\underline{x}=\underline{b}, \quad (24)$$

where $\underline{x}$ is the vector of the unknown uniform samples $\tilde{V}(\eta_k,\varphi_{m,k})$, $\underline{b}$ is that of the known nonuniform ones $\tilde{V}(\eta_k,\phi_j)$, and $\underline{\underline{A}}$ is a $J_k\times(2M_k''+1)$ matrix, whose elements:

$$a_{jm}=G\left(\phi_j,\varphi_{m,k},\bar{\varphi}_k,M_k,M_k''\right), \quad (25)$$

are the weight functions of the OSI expansion, where $\varphi_{m,k}=m\Delta\varphi_k=2m\pi/(2M_k''+1)$ and $\bar{\varphi}_k=p\Delta\varphi_k$. It is useful to note that, for a fixed row j, the elements a_{jm} are zero if the index m is external to the range $[m_0(\phi_j)-p+1,\ m_0(\phi_j)+p]$. The SVD method is then applied to get the best least square approximated solution of (24). After this step, the OSI expansion (20), where the samples $\tilde{V}(\eta_k,\varphi_{m,k})$ take the role of the $\tilde{V}(\xi_n,\varphi_{m,n})$ ones, is employed to determine the intermediate samples $\tilde{V}(\eta_k,\varphi)$ at the intersection points between the nonuniform parallels and the meridian through P. Since these samples are again irregularly spaced, the voltage at P can be found by first recovering the uniformly distributed intermediate samples $\tilde{V}(\xi_n,\varphi)$ again via SVD and then interpolating them by means of the OSI expansion (14).

Both the distances between each nonuniform parallel and the related uniform one and those between the nonuniform sampling points and the associated uniform ones on the nonuniform parallels have been assumed less than one half of the corresponding uniform spacing to avoid a strong ill-conditioning of the related linear systems.

It must be stressed that it is convenient to retrieve the same number N_φ of uniform samples on each nonuniform parallel to minimize the computational effort. In fact, in such a case, these samples are aligned along the meridians and, accordingly, the number of systems to be solved is minimum. Obviously, the number N_φ is that corresponding to the equator, wherein the azimuthal bandwidth W_φ attains its maximum value. Once the uniform samples have been determined, the data needed by the standard NF–FF transformation [6] can be evaluated by means of the OSI expansions (14) and (20), this last properly modified to account for the redundancy in φ.

The SVD-based approach could be still used when the irregularly spaced samples no longer lie on parallels, but the dimension of the involved matrix would become very large, thus requiring a huge computational effort. Accordingly, in such a case, it is more convenient [28] to resort to the iterative technique, which will be described in the next subsection.

B. The iterative approach

Let us now suppose that, save for the sample at the pole $\vartheta = 0$, all the others are irregularly spaced on the scanning sphere. Moreover, let us assume that the nonuniform samples distribution is such that it is possible to build a biunique correspondence between each uniform sampling point and the "nearest" nonuniform one. By expressing the reduced voltage at each nonuniform sampling point $(\eta_k, \phi_{j,k})$ as a function of the unknown values at the nearest uniform ones $(\xi_n, \varphi_{m,n})$ by means of the OSI expansions (14) and (20), we obtain:

$$\tilde{V}(\eta_k, \phi_{j,k}) = \sum_{n=n_0-q+1}^{n_0+q} \left\{ G(\eta_k, \xi_n, \bar{\xi}, N, N'') \cdot \sum_{m=m_0-p+1}^{m_0+p} \tilde{V}(\xi_n, \varphi_{m,n})\, G(\phi_{j,k}, \varphi_{m,n}, \bar{\varphi}, M_n, M_n'') \right\}. \quad (26)$$

The resulting linear system can be rewritten in the form $\underline{\underline{A}}\,\underline{x} = \underline{b}$, where b is the vector of the known nonuniform samples $\tilde{V}(\eta_k, \phi_{j,k})$, $\underline{x}$ is that of the unknown uniform ones $\tilde{V}(\xi_n, \varphi_{m,n})$, and $\underline{\underline{A}}$ is a sparse banded matrix of sizes $Q \times Q$, wherein Q is the overall number of uniform/nonuniform samples. By splitting the matrix $\underline{\underline{A}}$ into its diagonal part $\underline{\underline{A}}_D$ and nondiagonal one $\underline{\underline{\Delta}}$, multiplying both members of the system by $\underline{\underline{A}}_D^{-1}$ and rearranging the terms, the following iterative procedure results:

$$\underline{x}^{(\nu)} = \underline{\underline{A}}_D^{-1}\underline{b} - \underline{\underline{A}}_D^{-1}\underline{\underline{\Delta}}\,\underline{x}^{(\nu-1)} = \underline{x}^{(0)} - \underline{\underline{A}}_D^{-1}\underline{\underline{\Delta}}\,\underline{x}^{(\nu-1)}, \quad (27)$$

$\underline{x}^{(\nu)}$ being the uniform samples vector estimated at the νth step. The necessary conditions for the convergence of the procedure are surely fulfulled in the assumed hypothesis on the nonuniform samples distribution. In fact, the modulus of each element on the principal diagonal of $\underline{\underline{A}}$ results to be not zero and greater than those of the other elements on the same row and column. In explicit form, Eq. (27) becomes:

$$\tilde{V}^{(\nu)}(\xi_n, \varphi_{m,n}) = \frac{1}{G(\eta_n, \xi_n, \bar{\xi}, N, N'')\, G(\phi_{m,n}, \varphi_{m,n}, \bar{\varphi}, M_n, M_n'')} \cdot \left\{ \tilde{V}(\eta_n, \phi_{m,n}) - \sum_{\substack{\ell=\ell_0-q+1 \\ (\ell \neq n)}}^{\ell_0+q} \sum_{\substack{i=i_0-p+1 \\ \wedge\ (i \neq m)}}^{i_0+p} G(\eta_n, \xi_\ell, \bar{\xi}, N, N'') \cdot G(\phi_{m,n}, \varphi_{i,\ell}, \bar{\varphi}, M_\ell, M_\ell'')\, \tilde{V}^{(\nu-1)}(\xi_\ell, \varphi_{i,\ell}) \right\}. \quad (28)$$

Once the regularly spaced samples have been recovered, the NF data needed by the standard NF–FF transformation [6] can be determined via the OSI expansions (14) and (20).

IV. SIMULATION RESULTS

Some numerical results, which assess the effectiveness of the described approaches to correct known positioning errors in the NF–FF transformation with spherical scanning using the rounded cylinder modelling of the antenna, are shown in this section. The simulations, which complete the preliminary ones reported in [29], are relevant to a uniform planar array of elementary Huygens sources polarized along the z axis, spaced by 0.5λ (λ being the wavelength), which cover a zone in the plane $y = 0$, formed by a rectangle ended in two half-circles. The sizes of the rectangle are: $2a' = 14\lambda$ and $h' = 40\lambda$. The scanning sphere has radius $d = 35\lambda$ and an open-ended circular waveguide, having radius 0.338λ, is chosen as probe.

The first set of simulations (from Fig. 3 to Fig. 6) is relevant to the case of irregularly distributed samples lying on parallels nonuniformly spaced on the scan sphere, so that the reconstruction of the uniform samples can be split into the solution of two independent one-dimensional problems. The nonuniform samples have been generated by imposing that the distances in ξ and φ between each nonuniform parallel and the related uniform one and those between the nonuniform sampling points and the associated uniform ones on the nonuniform parallels are random variables uniformly distributed in $(-\Delta\xi/2, \Delta\xi/2)$ and $(-\Delta\varphi_k/2, \Delta\varphi_k/2)$, which is a pessimistic hypothesis in an actual scanning system. Figures 3 and 4 show the reconstruction of the amplitude of the rotated probe voltage V_2 on the meridians at $\varphi = 0°$ and $\varphi = 90°$, respectively. As can be seen, the reconstruction is everywhere accurate, thus assessing the accuracy of the approach. For completeness, the reconstruction of the phase of V_2 on the meridian $\varphi = 90°$ is also reported in Fig. 5. To assess in a more quantitative way the algorithm performances, the mean-square errors in the reconstruction of the uniform samples of V_2 have been evaluated. They are normalized to the voltage maximum value on the sphere and have been obtained by comparing the recovered and the exact uniform samples. Figure 6 shows these errors for $\chi = 1.15, 1.20, 1.25$, $\chi' = 1.20$ and $p = q$ ranging from 2 to 12. Practical identical results, non-reported here to save space, have been obtained by applying the iterative algorithm to the same set of irregularly spaced NF data, which fulfils also its applicability conditions.

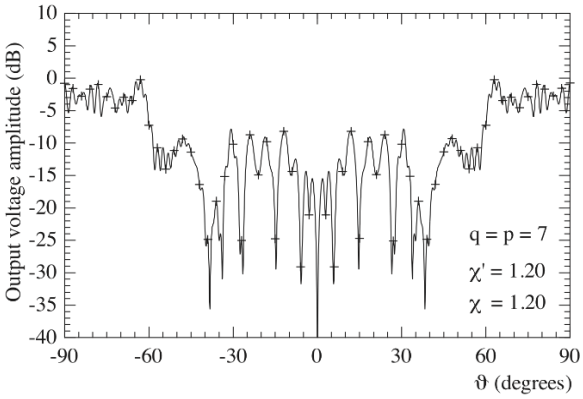

Fig. 3. Amplitude of V_2 on the meridian at $\varphi = 0°$. Solid line: exact. Crosses: reconstructed from nonuniform samples via the SVD-based algorithm.

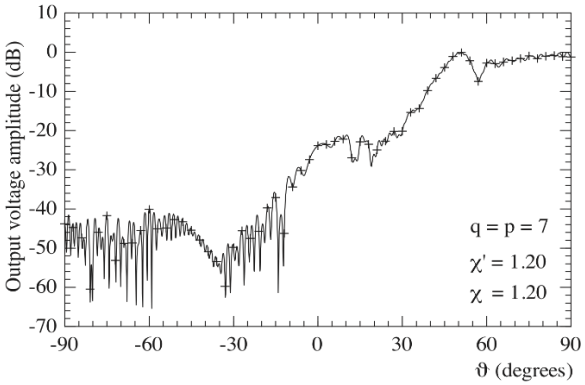

Fig. 4. Amplitude of V_2 on the meridian at $\varphi = 90°$. Solid line: exact. Crosses: reconstructed from nonuniform samples via the SVD-based algorithm.

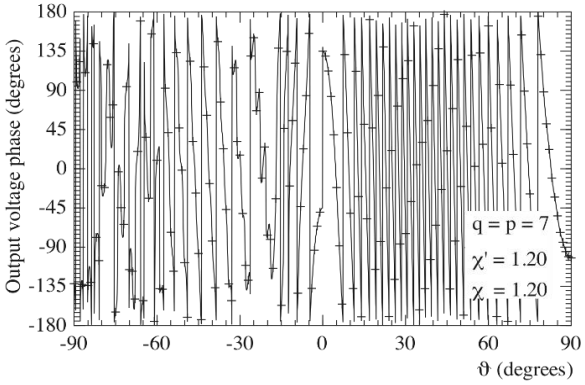

Fig. 5. Phase of V_2 on the meridian at $\varphi = 90°$. Solid line: exact. Crosses: reconstructed from nonuniform samples via the SVD-based algorithm.

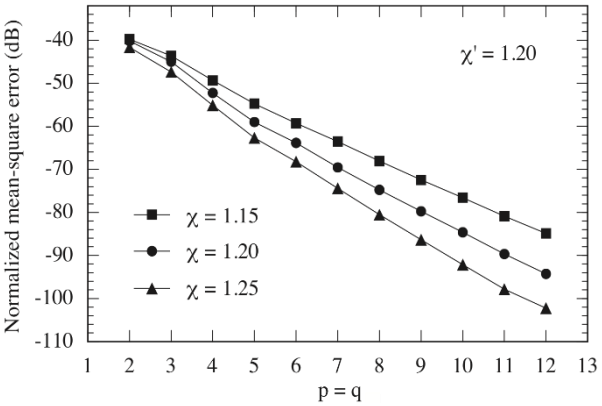

Fig. 6. Normalized mean-square errors in the reconstruction of the uniform samples of V_2 via the SVD-based algorithm.

The second set of numerical tests refers to the case of samples irregularly spaced on the sphere, which do not lie on parallels. In such a situation, it is more convenient, from the computational point of view, to employ the iterative algorithm, which requires the existence of a biunique correspondence between the uniform and nonuniform samples, that associates at each uniform sampling point the nearest irregular one. Therefore, the nonuniform samples have been generated in such a way that the displacements in ξ and φ between each nonuniform sampling point and the corresponding uniform one are random variables uniformly distributed in $(-\Delta\xi/3, \Delta\xi/3)$ and $(-\Delta\varphi_n/3, \Delta\varphi_n/3)$. To assess the effectiveness of the iterative algorithm, the normalized mean-square errors in the reconstruction of the uniform samples of V_2 have been evaluated. They are shown in Table 1 as function of the number of iterations ν and retained samples number $p = q$. As can be seen, these errors decrease on increasing ν and $p = q$. Moreover, just few iterations are enough to ensure the convergence of the iterative scheme.

Once the regularly spaced (uniform) samples have been retrieved by applying the SVD-based approach or the iterative one, depending on the considered nonuniform samples distribution, they have to be interpolated to reconstruct the NF data required by the classical spherical NF–FF transformation. Figures 7 and 8 show the comparison between the exact far field patterns in the principal planes and those obtained from the former set of irregularly spaced samples via the SVD-based algorithm and from the latter by applying the iterative approach. As can be seen, a very good reconstruction results.

Table 1: Normalized mean-square errors in the reconstruction of the uniform samples of V_2 versus the number of iterations and the retained samples number

p = q \ # iterations (ν)	0	1	2	3	4	5	6	7	8	9	10
3	-33.08	-46.24	-48.50	-48.53	-48.53	-48.53	-48.53	-48.53	-48.53	-48.53	-48.53
4	-32.96	-48.72	-54.64	-54.94	-54.95	-54.95	-54.95	-54.95	-54.95	-54.95	-54.95
5	-32.89	-49.31	-60.10	-61.25	-61.26	-61.26	-61.26	-61.26	-61.26	-61.26	-61.26
6	-32.87	-49.28	-63.15	-66.41	-66.51	-66.51	-66.52	-66.52	-66.52	-66.52	-66.52
7	-32.87	-49.21	-64.60	-71.48	-71.88	-71.89	-71.89	-71.89	-71.89	-71.89	-71.89
8	-32.86	-49.12	-65.06	-75.95	-77.28	-77.31	-77.31	-77.31	-77.31	-77.31	-77.31
9	-32.86	-49.04	-65.07	-78.72	-82.16	-82.31	-82.31	-82.31	-82.31	-82.31	-82.31
10	-32.85	-48.96	-64.99	-80.14	-86.98	-87.38	-87.39	-87.39	-87.39	-87.39	-87.39
11	-32.84	-48.90	-64.87	-80.62	-91.11	-92.39	-92.42	-92.42	-92.42	-92.42	-92.42
12	-32.84	-48.84	-64.76	-80.65	-94.12	-97.07	-97.16	-97.17	-97.17	-97.17	-97.17

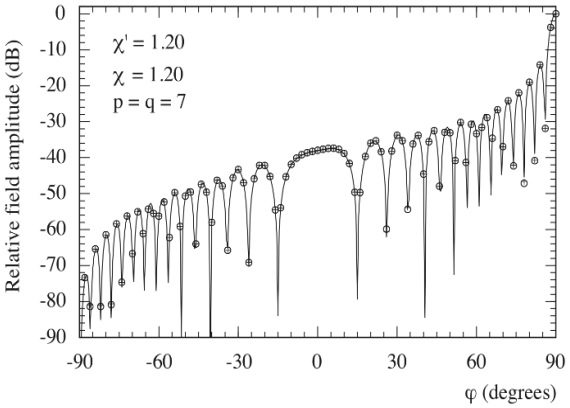

Fig. 7. H-plane pattern. Solid line: exact. Crosses: reconstructed from nonuniform samples (first set) via the SVD-based algorithm. Circles: reconstructed from nonuniform samples (second set) via the iterative approach.

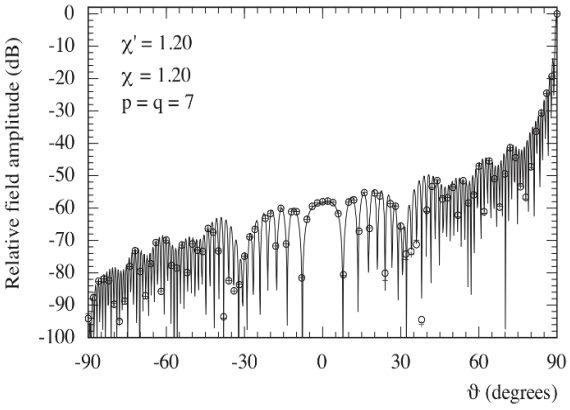

Fig. 8. E-plane pattern. Solid line: exact. Crosses: reconstructed from nonuniform samples (first set) via the SVD-based algorithm. Circles: reconstructed from nonuniform samples (second set) via the iterative approach.

It must be stressed that the reconstructions would be severely compromised without using these positioning errors compensation techniques, see, for instance, Fig. 9, which shows the corresponding reconstructed E-plane pattern, obtained from the second set of irregularly spaced NF data without using the iterative approach.

It can be interesting to compare the number of the used nonuniform NF data (19 489) with those (130 562) needed by the classical NF–FF transformation with spherical scanning [6].

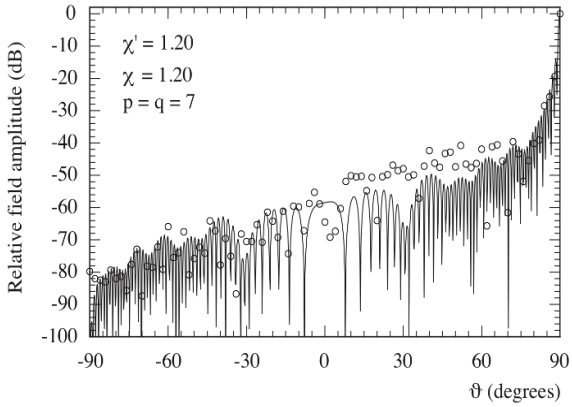

Fig. 9. E-plane pattern. Solid line: exact. Circles: reconstructed from nonuniform samples (second set) without using the iterative approach.

V. EXPERIMENTAL RESULTS

The described techniques have been experimentally tested in the anechoic chamber of the Antenna Characterization Lab of the University of Salerno, wherein a roll (φ axis) over azimuth (ϑ axis) spherical NF facility, supplied by MI Technologies, is available. The chamber, $8\text{m}\times5\text{m}\times4\text{m}$ sized, is covered with pyramidal absorbers which ensure a wall reflectivity lower than –40 dB. The measurements are

carried out by means of a vector network analyzer. The reported experimental results refer to a X-band resonant slotted waveguide array made by PROCOM A/S, which works at 10.4 GHz and has been realized by cutting 12 round-ended slots on both the broad walls of a WR-90 rectangular waveguide and soldering two cylinders on its narrow walls (see Fig. 10). Such an antenna has been modelled by a rounded cylinder with $h' = 28.27$ cm, $a' = 2.60$ cm and mounted in such a way that the broad walls are parallel to the plane $y = 0$ and its axis is coincident with the z one (Fig. 1). The probe voltages have been collected by an open-ended WR-90 waveguide on a sphere with radius $d = 45.20$ cm.

The first set of figures (from Fig. 11 to Fig. 16) is relevant to the case of the irregularly spaced sampling points lying on parallels of the scanning sphere. The NF data have been collected in such a way that the distances between each nonuniform parallel and the related uniform one and between the nonuniform sampling points and the uniform ones on the nonuniform parallels are random variables uniformly distributed in $(-\Delta\xi/2, \Delta\xi/2)$ and $(-\Delta\varphi_k/2, \Delta\varphi_k/2)$, respectively. The amplitude and phase of the probe voltage V_1 on the meridian at $\varphi = 0°$, recovered via the SVD-based approach, are compared in Figs. 11 and 12 with those directly measured on the same meridian. As can be seen, the reconstructions are very accurate, in spite of the severe values of the positioning errors.

The overall effectiveness of the SVD-based technique is assessed by comparing the FF patterns in the principal planes E and H (Figs. 13 and 14) reconstructed from the nonuniform NF data with those (references) obtained from the NF data directly acquired on the classical spherical grid. In both the cases, the MI Technologies' software MI-3000, implementing the classical spherical NF–FF transformation [6], has been used to obtain the FF reconstructions. The FF pattern reconstruction in the cut plane at $\varphi = 90°$ is then shown in Fig. 15. Also the FF reconstructions result to be very accurate, thus confirming the effectiveness of the approach. Practical identical results (non-reported for space saving) have been obtained by applying the iterative approach to the same set of nonuniform NF data, which satisfies also its applicability conditions. It is useful to note that the number of used samples is 836, remarkably less than that (5 100) required by the standard NF–FF transformation [6]. At last, the FF pattern in the cut plane at $\varphi = 90°$, reconstructed from the collected irregularly spaced NF data without using the SVD-based approach, is shown in Fig. 16. As can be seen, this FF reconstruction is severely compromised as compared with those achieved by using the proposed techniques, thus further confirming their capability to effectively compensate known positioning errors. The remaining figures (from Fig. 17 to Fig. 20) are relevant to the case of sampling points irregularly spaced on the sphere which do not lie on parallels and, therefore, only the iterative technique can be conveniently applied. The nonuniform samples have been acquired in such a way that the displacements in ξ and φ between the position of each nonuniform sample and that of the associated uniform one are random variables uniformly distributed in $(-\Delta\xi/3, \Delta\xi/3)$ and $(-\Delta\varphi_n/3, \Delta\varphi_n/3)$. The amplitude and phase of the voltage V_1 on the meridian at $\varphi = 0°$ recovered by using 10 iterations are compared in Figs. 17 and 18 with those directly measured on the same meridian. It must be stressed that such a number of iterations ensures the convergence of the algorithm with very low errors. At last, the overall effectiveness of the iterative technique is confirmed by the E-plane and H-plane pattern reconstructions reported in Figs. 19 and 20.

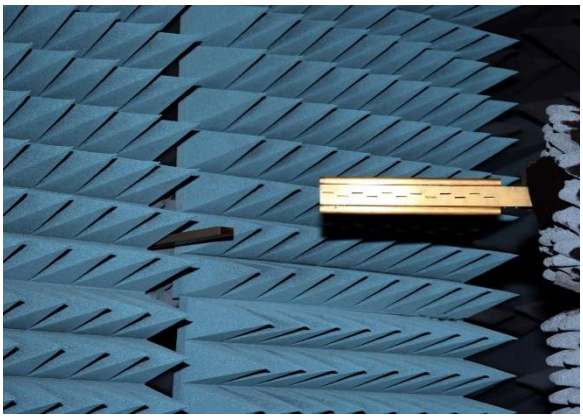

Fig. 10. Photo of the X-band resonant slotted waveguide array.

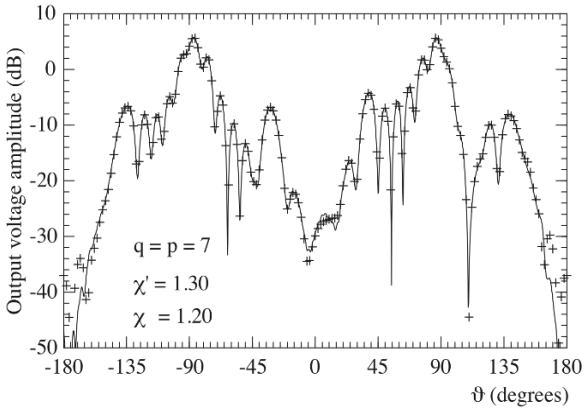

Fig. 11. Amplitude of V_1 on the meridian at $\varphi = 0°$. Solid line: measured. Crosses: reconstructed from nonuniform NF data via the SVD-based algorithm.

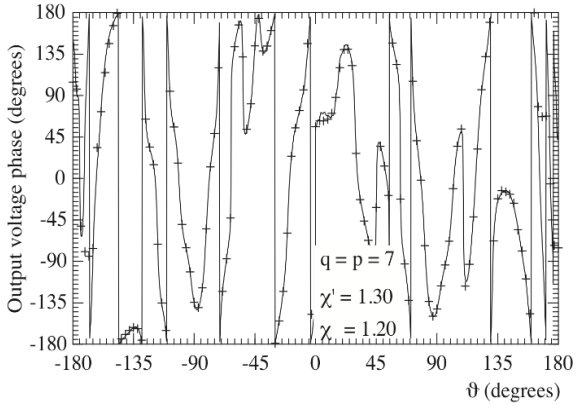

Fig. 12. Phase of V_1 on the meridian at $\varphi = 0°$. Solid line: measured. Crosses: reconstructed from nonuniform NF data via the SVD-based algorithm.

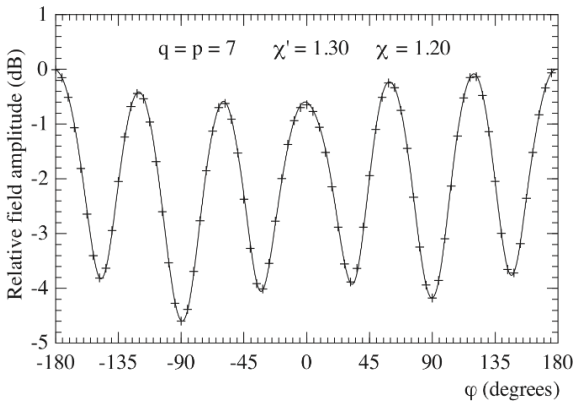

Fig. 13. E-plane ($\vartheta = 90°$) pattern. Solid line: reference. Crosses: reconstructed from nonuniform NF data via the SVD-based algorithm.

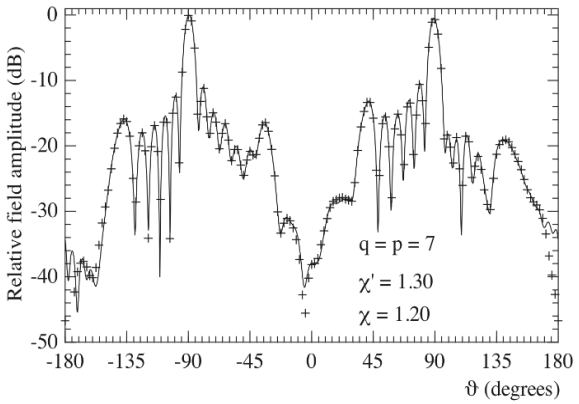

Fig. 14. H-plane ($\varphi = 0°$) pattern. Solid line: reference. Crosses: reconstructed from nonuniform NF data via the SVD-based algorithm.

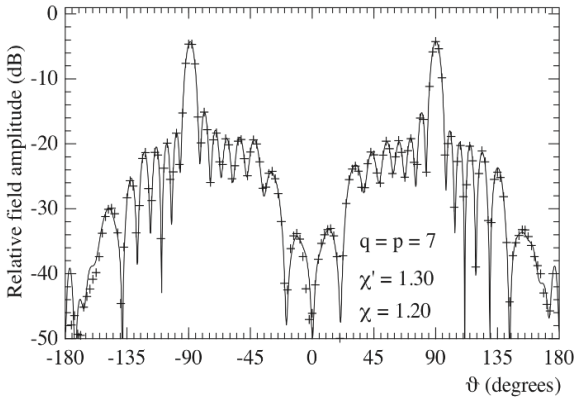

Fig. 15. FF pattern in the cut plane at $\varphi = 90°$. Solid line: reference. Crosses: reconstructed from nonuniform NF data via the SVD-based algorithm.

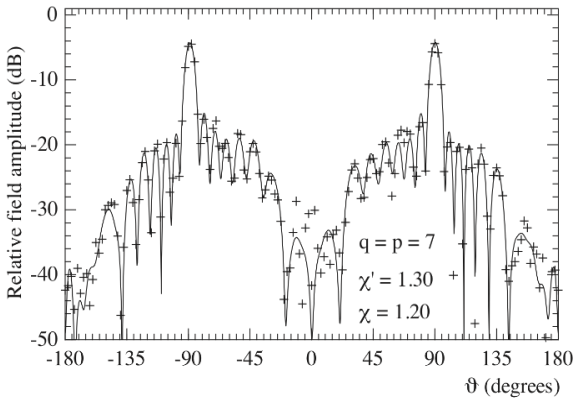

Fig. 16. FF pattern in the cut plane at $\varphi = 90°$. Solid line: reference. Crosses: reconstructed from nonuniform NF data without using the SVD-based algorithm.

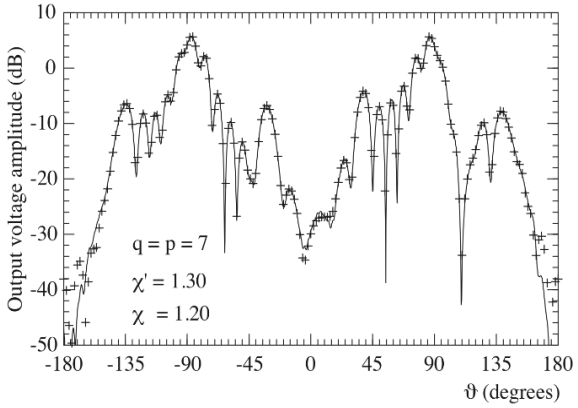

Fig. 17. Amplitude of the voltage V_1 on the meridian at $\varphi = 0°$. Solid line: measured. Crosses: reconstructed from nonuniform NF data via the iterative algorithm.

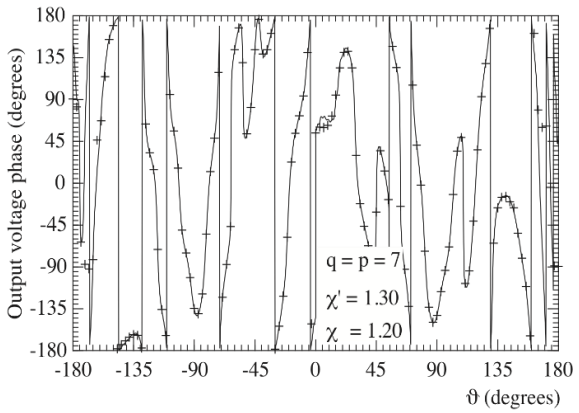

Fig. 18. Phase of V_1 on the meridian at $\varphi = 0°$. Solid line: measured. Crosses: reconstructed from nonuniform NF data via the iterative algorithm.

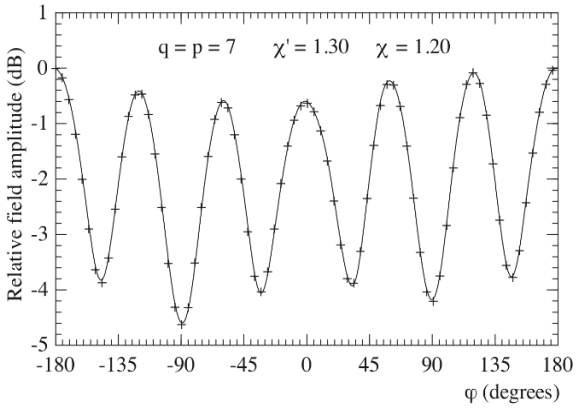

Fig. 19. E-plane ($\vartheta = 90°$) pattern. Solid line: reference. Crosses: reconstructed from nonuniform NF data via the iterative algorithm.

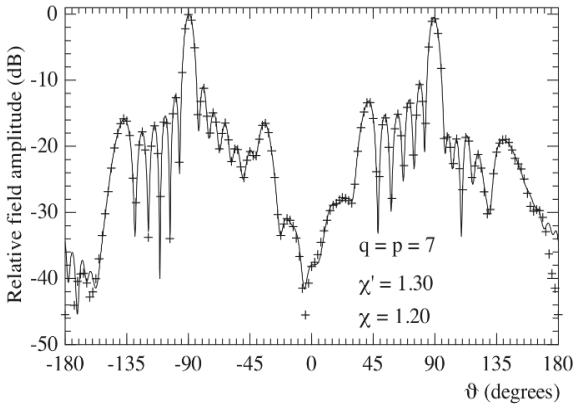

Fig. 20. H-plane ($\varphi = 0°$) pattern. Solid line: reference. Crosses: reconstructed from nonuniform NF data via the iterative algorithm.

VI. CONCLUSION

In this paper, two different efficient techniques, which allow the correction of known positioning errors in the nonredundant spherical NF–FF transformation using the rounded cylinder modelling, have been presented. Both the techniques retrieve the nonredundant uniform NF samples at the points fixed by the sampling representation from the acquired irregularly distributed ones. Then, these retrieved samples are efficiently interpolated via an OSI algorithm to accurately reconstruct the NF data required to perform the classical spherical NF–FF transformation. In order to recover the uniform samples, the former technique makes use of the SVD method and can be profitably employed when the nonuniform samples lie on parallels, so that the uniform samples recovery can be reduced to the solution of two independent one-dimensional problems. The latter adopts an iterative scheme, which does not require the fulfillment of such a hypothesis, but can be applied only if there is a biunique correspondence between each uniform sampling point and the nearest nonuniform one. Some numerical and experimental results assessing the effectiveness of both the techniques, even in presence of large and pessimistic positioning errors in an actual scan, have been shown.

REFERENCES

[1] F. Jensen, *Electromagnetic Near-Field–Far-Field Correlations, Ph.D. Dissertation*, Tech. Univ. of Denmark, Rep. LD15, 1970.

[2] F. Jensen, "On the probe compensation for near-field measurements on a sphere," *Archiv Elektr. Übertr*., vol. 29, pp. 306-308, 1975.

[3] P. F. Wacker, "Non-planar near-field measurements: spherical scanning," *NBSIR 75-809*, Boulder, CO, USA, 1975.

[4] F. H. Larsen, "Probe correction of spherical near-field measurements," *Electr. Lett*., vol. 13, pp. 393-395, July 1977.

[5] F. H. Larsen, *Probe-Corrected Spherical Near-Field Antenna Measurements, Ph.D. Dissertation*, Tech. Univ. of Denmark, Rep. LD36, 1980.

[6] J. Hald, J. E. Hansen, F. Jensen, and F. H. Larsen, *Spherical Near-Field Antenna Measurements*, J. E. Hansen Ed., IEE Electromagnetic Waves Series, Peter Peregrinus, London, UK, 1998.

[7] A. D. Yaghjian, "Simplified approach to probe-corrected spherical near-field scanning," *Electr. Lett*., vol. 20, pp. 195-196, Mar. 1984.

[8] A. D. Yaghjian and R. C. Wittmann, "The receiving antenna as a linear differential operator: application to spherical near-field measurements,"

IEEE Trans. Antennas Prop., vol. AP-33, pp. 1175-1185, 1985.

[9] T. Laitinen, S. Pivnenko, J. M. Nielsen, and O. Breinbjerg, "Theory and practice of the FFT/matrix inversion technique for probe-corrected spherical near-field antenna measurements with high-order probes," *IEEE Trans. Antennas Prop*., vol. 58, pp. 2623-2631, Aug. 2010.

[10] T. B. Hansen, "Numerical investigation of the system-matrix method for higher-order probe correction in spherical near-field antenna measurements," *Int. Jour. Antennas Prop*., vol. 2012, ID 493705, 8 pages, 2012.

[11] O. M. Bucci, F. D'Agostino, C. Gennarelli, G. Riccio, and C. Savarese, "Data reduction in the NF–FF transformation technique with spherical scanning," *Jour. Electr. Waves Appl*., vol. 15, pp. 755-775, 2001.

[12] F. D'Agostino, F. Ferrara, C. Gennarelli, R. Guerriero, and M. Migliozzi, "Non-redundant spherical NF – FF transformations using ellipsoidal antenna modeling: experimental assessments," *IEEE Antennas Prop. Magaz*., vol. 55, pp. 166-175, 2013.

[13] F. D'Agostino, F. Ferrara, C. Gennarelli, R. Guerriero, and M. Migliozzi, "Effective antenna modellings for NF–FF transformations with spherical scanning using the minimum number of data," *Int. Jour. Antennas Prop*., vol. 2011, ID 936781, 11 pages, 2011.

[14] F. D'Agostino, F. Ferrara, C. Gennarelli, R. Guerriero, and M. Migliozzi, "Experimental testing of nonredundant near-field to far-field transformations with spherical scanning using flexible modellings for nonvolumetric antennas," *Int. Jour. Antennas Prop*., vol. 2013, ID 517934, 10 pages, 2013.

[15] M. A. Qureshi, C. H. Schmidt, and T. F. Eibert, "Adaptive sampling in spherical and cylindrical near-field antenna measurements," *IEEE Antennas Prop. Magaz*., vol. 55, pp. 243-249, Feb. 2013.

[16] O. M. Bucci and G. Franceschetti, "On the spatial bandwidth of scattered fields," *IEEE Trans. Antennas Prop*., vol. AP-35, pp. 1445-1455, Dec. 1987.

[17] O. M. Bucci, C. Gennarelli, and C. Savarese, "Representation of electromagnetic fields over arbitrary surfaces by a finite and non redundant number of samples," *IEEE Trans. Antennas Prop*., vol. 46, pp. 351-359, Mar. 1998.

[18] O. M. Bucci and C. Gennarelli, "Application of nonredundant sampling representations of electromagnetic fields to NF-FF transformation techniques," *Int. Jour. Antennas Prop*., vol. 2012, ID 319856, 14 pages, 2012.

[19] A. Dutt and V. Rohklin, "Fast Fourier transforms for nonequispaced data," *Proc. SIAM Jour. Scient. Comp.*, vol. 14, pp. 1369-1393, 1993.

[20] G. Beylkin, "On the fast Fourier transform of functions with singularities," *Appl. Comp. Harmonic Analysis*, vol. 2, pp. 363-381, 1995.

[21] R. C. Wittmann, B. K. Alpert, and M. H. Francis, "Near-field antenna measurements using nonideal measurement locations," *IEEE Trans. Antennas Prop*., vol. 46, pp. 716-722, May 1998.

[22] R. C. Wittmann, B. K. Alpert, and M. H. Francis, "Near-field, spherical-scanning antenna measurements with nonideal probe locations," *IEEE Trans. Antennas Prop*., vol. 52, pp. 2184-2186, Aug. 2004.

[23] O. M. Bucci, C. Gennarelli, and C. Savarese, "Interpolation of electromagnetic radiated fields over a plane from nonuniform samples," *IEEE Trans. Antennas Prop*., vol. 41, pp. 1501-1508, Nov. 1993.

[24] O. M. Bucci, C. Gennarelli, G. Riccio, and C. Savarese, "Electromagnetic fields interpolation from nonuniform samples over spherical and cylindrical surfaces," *IEE Proc. Microw. Antennas Prop*., vol. 141, pp. 77-84, Apr. 1994.

[25] F. Ferrara, C. Gennarelli, G. Riccio, and C. Savarese, "Far field reconstruction from nonuniform plane-polar data: a SVD based approach," *Electromagnetics*, vol. 23, pp. 417-429, 2003.

[26] F. D'Agostino, F. Ferrara, C. Gennarelli, R. Guerriero, M. Migliozzi, and G. Riccio, "A singular value decomposition based approach for far-field reconstruction from irregularly spaced planar wide-mesh scanning data," *Microw. Opt. Tech. Lett*., vol. 49, pp. 1768-1772, July 2007.

[27] F. Ferrara, C. Gennarelli, G. Riccio, and C. Savarese, "NF–FF transformation with cylindrical scanning from nonuniformly distributed data," *Microw. Opt. Tech. Lett*., vol. 39, pp. 4-8, Oct. 2003.

[28] F. D'Agostino, F. Ferrara, C. Gennarelli, R. Guerriero, and M. Migliozzi, "Two techniques for compensating the probe positioning errors in the spherical NF–FF transformation for elongated antennas," *The Open Elect. Electr. Eng. Jour*., vol. 5, pp. 29-36, 2011.

[29] F. D'Agostino, F. Ferrara, C. Gennarelli, R. Guerriero, M. Migliozzi, and D. Spagnuolo, "Compensation of the probe positioning errors in the spherical NF–FF transformation for elongated antennas," *Proc. of ICEAA'11*, pp. 255-258, Turin, Sept. 2011.

Francesco D'Agostino was born near Salerno (Italy) in 1965. He received the Laurea degree in Electronic Engineering from the University of Salerno in 1994, where in 2001 he received the Ph.D. degree in Information Engineering. From 2002 to 2005 he was Assistant Professor at the Engineering Faculty of the University of Salerno where in October 2005, he was appointed Associate Professor of Electromagnetics and joined the Department of Industrial Engineering, where he is currently working. His research activity includes application of sampling techniques to electromagnetics and to innovative NF–FF transformations, diffraction problems radar cross section evaluations, Electromagnetic Compatibility. In this area, D'Agostino has co-authored 4 books and over 150 scientific papers, published in peer-reviewed international journals and conference proceedings. He is a regular Reviewer for several journals and conferences and has chaired some international events and conferences. D'Agostino is a Member of AMTA, EurAAP, and IEEE.

Flaminio Ferrara was born near Salerno, Italy, in 1972. He received the Laurea degree in Electronic Engineering from the University of Salerno in 1999. Since the same year, he has been with the Research Group in Applied Electromagnetics at the University of Salerno. He received the Ph.D. degree in Information Engineering at the same University, where he is presently an Assistant Professor of Electromagnetic Fields. His interests include: application of sampling techniques to the efficient reconstruction of electromagnetic fields and to NF–FF transformation techniques; monostatic radar cross section evaluations of corner reflectors. Ferrara is co-author of more than 180 scientific papers, mainly in international journals and conference proceedings. He is a Member of the IEEE society.

Claudio Gennarelli was born in Avellino, Italy, in 1953. He received the Laurea degree (*summa cum laude*) in Electronic Engineering from the University of Naples, Italy, in 1978. From 1978 to 1983, he worked with the Research Group in Electromagnetics at the Electronic Engineering Department of the University "Federico II" of Naples. In 1983, he became Assistant Professor at the Istituto Universitario Navale (IUN), Naples. In 1987, he was appointed Associate Professor of Antennas, formerly at the Engineering Faculty of Ancona University and subsequently at the Engineering Faculty of Salerno University. In 1999, he has been appointed Full Professor at the same University. The main topics of his scientific activity are: reflector antennas analysis, antenna measurements, diffraction problems, radar cross section evaluations, scattering from surface impedances, application of sampling techniques to electromagnetics and to NF–FF transformations. Gennarelli is co-author of more than 360 scientific papers, mainly in international journals and conference proceedings. In particular, he is co-author of four books on NF–FF Transformation Techniques. He is a Senior Member of the IEEE and Member of the Editorial board of the Open Electrical and Electronic Engineering Journal and of the International Journal of Antennas and Propagation.

Rocco Guerriero received the Laurea degree in Electronic Engineering and the Ph.D. degree in Information Engineering from the University of Salerno in 2003 and 2007, respectively. Since 2003, he has been with the Reaserch Group in Applied Electromagnetics of University of Salerno, where he is currently an Assistant Professor of Electromagnetic Fields. His interests include: application of sampling techniques to the efficient reconstruction of electromagnetic fields and to near-field-far-field transformation techniques; antenna measurements; inversion of ill-posed electromagnetic problems; analysis of microstrip reflectarrays; diffraction problems. Guerriero is co-author of more than 135 scientific papers, mainly in international journals and conference proceedings. Since 2015, he is a Member of IEEE.

Massimo Migliozzi received the Laurea degree in Electronic Engineering from the University of Salerno, in 1999. He received the Ph.D. degree in Information Engineering at the same University, where at the present time he is a Research fellow in Electromagnetic Fields. His scientific interests include: application of sampling techniques to the efficient reconstruction of electromagnetic fields and to NF–FF transformation techniques; antenna measurements; electromagnetic compatibility; antenna design; diffraction problems. Migliozzi is co-author of about 100 scientific papers, mainly in international journals and conference proceedings.

Dissipation Factor and Permittivity Estimation of Dielectric Substrates Using a Single Microstrip Line Measurement

Ricardo Gonçalves [1], Roberto Magueta [1], Pedro Pinho [2], and Nuno B. Carvalho [1]

[1] DETI, Instituto de Telecomunicações
Universidade de Aveiro, 3810-193 Aveiro, Portugal
rmrgoncalves@ua.pt, rlm@ua.pt, nbcarvalho@ua.pt

[2] Instituto de Telecomunicações
Instituto Superior de Engenharia de Lisboa, 1959-007 Lisboa, Portugal
ppinho@deetc.isel.pt

Abstract ─ The knowledge of the dielectric properties of materials, for the design of several components and circuits at high frequencies, is mandatory. In this paper, we present a simple method for the estimation of the dissipation factor (loss tangent) of dielectric materials based on the reflection measurement of a single microstrip line, which is applied to some common known materials, such as FR-4 and Rogers RO3010 laminates. The obtained results match well with the data on the literature for the considered materials.

Index Terms ─ Dielectric characterization, loss factor estimation, microwaves, permittivity estimation.

I. INTRODUCTION

Adaptability and integration of electronic systems is a major concern for current design engineers. In order to promote these, even at high frequencies, new solutions are constantly being proposed. One of those, is the use of alternative substrate materials [1,2].

Common substrates, used for the design of antennas and circuits for RF applications, can be replaced by other materials, that are, most of the times, easily available and preferably less expensive and ecofriendly; like plastic, fabrics, paper, or ceramics.

A very clear example is RFID (radio frequency identification) which is responsible for an increased diversity of the electronics printing techniques. It's being extensively used in many different kinds of applications and is one of the most promising bets for the development of the Internet of Things concept [3]. RFID systems operating in the HF (high frequency) band have been designed upon paper and plastic surfaces for mass production and implementation at the lowest costs possible. However, this has been done due to the low frequency of operation and simplicity of the system design. When the application envisioned is operating at UHF (ultra high frequency) or microwave frequencies there are more limitations and constraints to consider when designing the system.

According to [4], printed antennas and transmission lines have dimensions directly related to the wavelength, and hence the frequency of the desired system. The wavelength is dependent on the permittivity and permeability of the propagation medium. Therefore, in order to efficiently design a printed antenna or RF circuit, the electrical properties: relative permittivity (ε_r); relative permeability (μ_r); and the dissipation factor, also known as loss tangent (tan δ), of the substrate must be known.

The information regarding these parameters is commonly found on the laminate's datasheets, but this does not happen for common materials not intended for electronic applications (e.g., fabrics, ceramics, paper, or plastic). So when designing RF circuitry using such materials, characterization in terms of permittivity and losses must be performed. In many cases, the substrates are dielectric non-magnetic materials; therefore, the relative permeability is unitary.

Permittivity and loss estimation is an old research subject and there's extensive literature regarding several methods to characterize different kinds of materials that can be found in reviews [5], application notes [6] and books [7]. In many of these methods, specific equipment is required, and might not be available in every lab.

The simplest methods available that allow the estimation of the permittivity, require the measurement of the scattering parameters of microstrip lines, such as presented in [8,9]. In these proposals, the dielectric under test is used as the substrate for the microstrip lines. Two different lines, with different lengths are required, for which the exact lengths and widths must be known with high precision. Other possibility is presented in [10], using a similar approach based on two lines with different lengths, but in which the material under test is placed above the lines, as a superstrate.

Submitted On: August 7, 2015
Accepted On: December 6, 2015

In this paper, we propose a method that only requires a single measurement of the reflection coefficient of an open-ended microstrip line, for the estimation of the permittivity and dissipation factor of the line substrate. The dissipation factor estimation proposed is the actual novelty. It is shown, that the proposed method can achieve better estimations when compared to other common methods, and does not require any prior knowledge of the conductivity, or other sources of losses, in the line. Since the permittivity is required for the calculation of the dissipation factor, we show the steps based on transmission line theory and microstrip line theory that allow the estimation of its value.

This paper is organized as follows. In the following section we present the steps for the permittivity and loss estimation based on reflection of microstrip lines method. In Section III we explain the experimental setup and present the results for permittivity and loss tangent obtained through measurements of different dielectric samples; namely, FR-4, Plastic and a Rogers RT5880. Finally, Section IV contains the uncertainty analysis of the proposed method, and Section V presents the conclusions.*Z*

II. PERMITTIVITY AND DISSIPATION FACTOR ESTIMATION: THEORY

Microstrip lines are simpler to design and fabricate when compared to coplanar or striplines. Especially if we consider creating such lines in a material that doesn't have electrodeposited conductors and where such processes are very hard and costly to apply.

As mentioned in the previous section, there are other approaches to characterize dielectric materials that can be made with microstrip lines. However, it requires the development of two lines, with different lengths, in which, the lengths, width and the height of the substrate must be known with high precision. Any error present in this dimensions can lead to large errors in the permittivity estimation. Especially an error in the width of the lines or in the length difference between them. By using a single microstrip line we avoid this sources of errors.

In order to determine the dissipation factor of a given material, its permittivity value is needed. Therefore, if not accessible in references, one must first assess its value. In the following subsection we describe a way to calculate it based on the measurement of a single microstrip line. It is derived from the known transmission line and microstrip line theory. In Subsection B, we present the techniques to determine the dissipation factor along with our novel approach.

A. Permittivity estimation with a microstrip line

If we terminate a transmission line with an open-circuit ($Z_L=\infty$) then, according to [4], the impedance seen at the entrance of the line along l is:

$$Z_{in} = \frac{Z_0}{\tanh(\alpha l + j\beta l)}, \tag{1}$$

being Z_0 the characteristic impedance of the line and α and β the propagation attenuation and phase constant. Considering $\beta = 2\pi/\lambda$ and $l = \lambda_r/2$, where λ_r is the wavelength at the line resonance, then we have $\beta l = \pi f/f_r$. If we replace this into (1), separate the real from the imaginary part, and consider the input impedance at one fourth of the resonant frequency ($\beta l = \pi/4$), then (1) becomes:

$$Z_{in} = Z_0 \left\{ \frac{2\tanh(\alpha l)}{1+\tanh^2(\alpha l)} - j\frac{1-\tanh^2(\alpha l)}{1+\tanh^2(\alpha l)} \right\}. \tag{2}$$

If we assume the losses are positive (which is correct for the majority of materials), and considering $Z_{in} = R - jX$, we can say:

$$\tanh(\alpha l) = -\frac{X}{R} + \sqrt{\left(\frac{X}{R}\right)^2 + 1}, \tag{3a}$$

$$Z_0 = X\frac{1+\tanh^2(\alpha l)}{1-\tanh^2(\alpha l)} = R\frac{1+\tanh^2(\alpha l)}{2\tanh(\alpha l)}. \tag{3b}$$

This process to determine the characteristic impedance of the line is rather simple, since we just have to measure the input impedance of the line at one fourth of the first resonant frequency, which can be done simply with a network analyzer. With that impedance value we can calculate (3a) and then determine the characteristic impedance with (3b).

With the knowledge of the characteristic impedance of the line we can relate it to the effective permittivity of the substrate. For a microstrip line, according to [11], we have:

$$\varepsilon_{eff} = \left(\frac{60}{Z_0} \ln\left(\frac{8h}{W} + \frac{W}{4h} \right) \right)^2, \tag{4a}$$

$$\varepsilon_{eff} = \left(\frac{120\pi}{Z_0} \frac{1}{\frac{W}{h} + 1.393 + 0.667\ln\left(\frac{W}{h} + 1.444\right)} \right)^2, \tag{4b}$$

where (4a) should be used when $W/h \leq 1$, and (4b) when otherwise. Being W the width of the microstrip line and h the height of the substrate. These can be solved for the relative permittivity of the substrate as:

$$\varepsilon_r = \frac{2\varepsilon_{eff} + \frac{1}{\sqrt{1+12h/W}} - 1}{1 + \frac{1}{\sqrt{1+12h/W}}}. \tag{5}$$

B. Dissipation factor estimation with a microstrip line

The dissipation factor, also known as loss tangent ($\tan\delta$), of a dielectric material in a microstrip line

substrate, can be related, according to [4], to the attenuation of the dielectric material (α_d) as:

$$\tan\delta = \frac{\alpha_d \sqrt{\varepsilon_{eff}}(\varepsilon_r - 1)}{\pi\varepsilon_r(\varepsilon_{eff} - 1)}\frac{c}{f}. \quad (6)$$

The total attenuation applied to the propagation is characterized by the sum of the dielectric, conductor, radiation and leakage losses. In order to determine the losses from the dielectric the total loss and the contribution from each of the other sources must be known. The total attenuation can be determined from the input impedance measurement as shown in (3a) or by:

$$\alpha = -\frac{\ln(|T|)}{l}, \quad (7)$$

where T is the transmission parameter which is determined according to the NRW (Nicolson-Ross-Wier) method [12,13]. The conductor losses can be calculated using empiric closed form expressions as shown in [14]. However, these expressions are empirical, meaning they're dissociated from what actually is being measured and are frequency independent. Since the losses from the dielectric change with frequency, a small error in the calculation of the conductor losses can lead to a large error in the overall result. Besides, it is very hard to account the contribution from radiation and leakage losses. Even though leakage can be negligible and radiation is more significant for high microwave and/or millimeter wave frequencies. Therefore, we developed an iterative method to calculate the dissipation factors that does not require knowledge of the radiation, conductor or leakage losses and still provides reasonable estimations.

Considering a lossless line, with perfect conductors and a lossless substrate, terminated in an open circuit, then the input impedance measured at the resonant frequency of the line is infinite. However, when considering the losses, either from the conductor or dielectric, the input impedance decreases as the losses rise.

Using ADS Momentum EM simulator, we designed several lines with different lengths and widths and changed the characteristics of the substrate material. Some of the simulated lines and the corresponding impedance values obtained are presented in Table 1. Where z_{in} is the normalized input impedance, at the resonant frequency, when considering perfect conductors (the only source of considerable loss is from the dielectric). While z_c is the normalized input impedance, considering also the conductor losses.

It is noticeable from the presented values, that there is a decrease in the input impedance as the losses increase. Besides, there is a direct proportionality between the characteristic impedance of the lines and the input impedance at resonance. We can see this tendency in Fig. 1, where the variation of the characteristic impedance of several lines with their input impedance at resonance, considering tan δ = 0.01, is depicted. Moreover, it is also shown a possible linearization of this relation, as:

$$z_{in} = 1.95Z_0 - 27.4, \quad (8)$$

and since the loss tangent is inversely proportional to this input impedance, we reach:

$$\tan\delta = \frac{0.0195Z_0 - 0.274}{z_{in}}. \quad (9)$$

This expressions can give a first estimation of the loss tangent. However, it only takes into account the dielectric loss. In order to consider the remaining sources of losses in the microstrip line, for the correct calculation of the dissipation factor, we consider a normalized impedance z_m that tends towards z_{in} as the conductivity increases, which can be also devised by the results on Table 1. We approximate this relationship according to expression (10):

$$z_m = z_{in}\left(1 - Ke^{\frac{Z_0 W}{\tau}}\right)^{-1}. \quad (10)$$

So by knowing the characteristic impedance of the line, the width of the line and the factors K and τ, one can determine an equivalent input impedance z_m and then determine a more accurate estimation of the loss tangent with (9) by replacing z_{in} with z_m. To reach the correct factors K and τ, we can rearrange (10) in order to get a relation between K, τ and Z_0W, being W expressed in millimeters, as:

$$Z_0 W = -\tau \ln\left(1 - \frac{z_m}{z_{in}}\right) + \tau \ln K, \quad (11)$$

since z_m is the input impedance considering all the losses, which will tend towards z_{in} as the conductivity increases, one can calculate the K and τ factors for different loss tangents and different conductivity values. By doing so, we reached the values presented in Table 2.

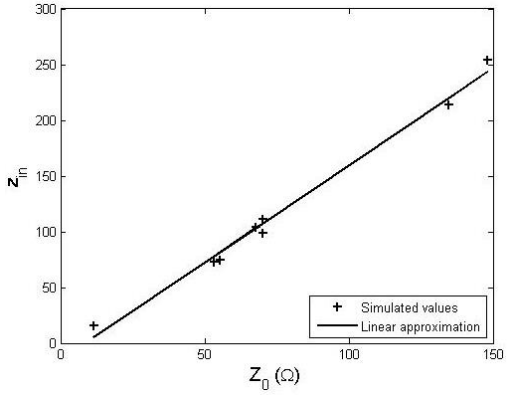

Fig. 1. Relation between the characteristic impedance of microstrip lines and the input impedance at resonance for perfect conductor lines.

Table 1: Input impedance of microstrip line simulations using ADS Momentum for different substrate materials

Line Properties	tan δ	z_{in} (Ω)	σ (S/m)	z_c (Ω)
Line 1 Z0 = 11.53 W = 2 mm h = 0.1 mm ε_r = 2	0.01	15.55	1.0E6	3.03
			10.0E6	5.87
			60.0E6	9.01
	0.03	5.15	1.0E6	2.20
			10.0E6	3.35
			60.0E6	4.17
	0.05	3.07	1.0E6	1.73
			10.0E6	2.34
			60.0E6	2.70
Line 2 Z0 = 53.23 W = 1 mm h = 1 mm ε_r = 8	0.01	72.77	1.0E6	30.43
			10.0E6	46.99
			60.0E6	58.28
	0.03	24.20	1.0E6	16.62
			10.0E6	20.51
			60.0E6	22.42
	0.05	14.49	1.0E6	11.42
			10.0E6	13.10
			60.0E6	13.84
Line 3 Z0 = 70.18 W = 2 mm h = 1 mm ε_r = 1.8	0.01	110.94	1.0E6	60.39
			10.0E6	47.28
			60.0E6	48.91
	0.03	36.77	1.0E6	28.50
			10.0E6	33.09
			60.0E6	35.08
	0.05	21.93	1.0E6	18.94
			10.0E6	20.67
			60.0E6	21.38
Line 4 Z0 = 148.13 W = 1 mm h = 3 mm ε_r = 2	0.01	254.03	1.0E6	137.74
			10.0E6	190.75
			60.0E6	221.63
	0.03	84.09	1.0E6	65.18
			10.0E6	75.63
			60.0E6	80.19
	0.05	50.29	1.0E6	43.29
			10.0E6	47.28
			60.0E6	48.91

Table 2: Calculated K and τ factors for different simulated microstrip lines

tan δ	σ (MS/m)	τ	K
0.01	1.0	210.63	0.858
	10.0	141.62	0.673
	60.0	118.54	0.426
0.03	1.0	139.59	0.600
	10.0	114.82	0.349
	60.0	105.18	0.185
0.05	1.0	125.45	0.436
	10.0	109.28	0.228
	60.0	103.62	0.114

According to these values, we can see that there is an inverse linear relation of K and τ with the square root of the conductivity as depicted in Figs. 2 and 3.

Based on these results, we can write K and τ in the form:

$$K = \frac{a_K}{\sqrt{\sigma_a}} + b_K, \tag{11a}$$

$$\tau = \frac{a_\tau}{\sqrt{\sigma_a}} + b_\tau, \tag{11b}$$

where σ_a is an educated guess of the conductivity value and the factors a_τ, a_K, b_τ and b_K, are obtained from a linearization that relates to the loss tangent as follows:

$$a_K = -2.105\tan\delta + 0.475, \tag{12a}$$

$$b_K = \frac{0.0644}{\sqrt{\tan\delta}} - 0.203, \tag{12b}$$

$$a_\tau = -1991.0\tan\delta + 115.6, \tag{12c}$$

$$b_\tau = \frac{1.097}{\sqrt{\tan\delta}} + 95.53, \tag{12d}$$

Since these factors depend on the loss tangent itself, we need an iterative method in order to solve this problem.

The algorithm is described as follows: We start by calculating a first approximation to the loss tangent with (9), after that we can calculate the K and τ factors that allow the calculation of (10). Using that new estimated impedance we can recalculate the loss tangent with (9), by replacing z_{in} with z_m.

A good approximation for the loss factor is achieved usually after four iterations. The convergence graphic is shown in Fig. 4.

A comparison about the estimation of the loss tangent with three different methods is shown in Fig. 5. These results are obtained from simulation for dielectrics with different losses (0.01, 0.02 and 0.005).

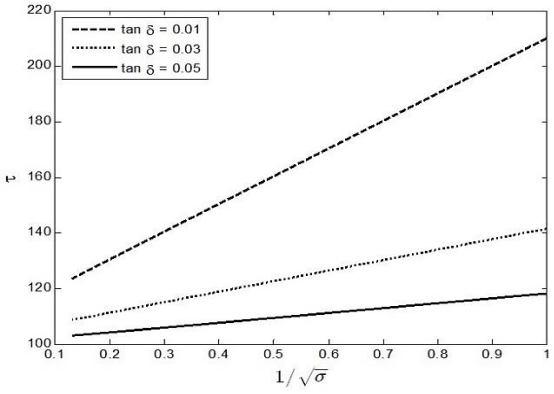

Fig. 2. Relation between the τ coefficient and the conductivity of the line conductors for different loss tangent values.

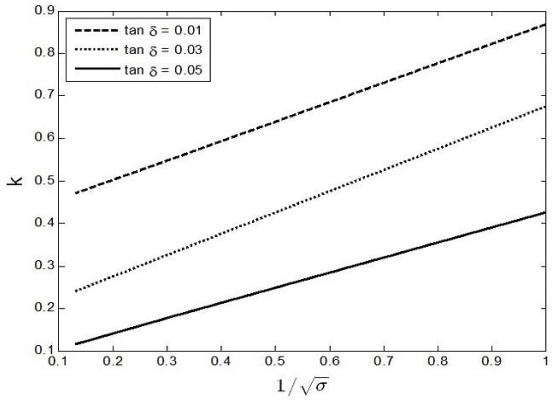

Fig. 3. Relation between the *K* coefficient and the conductivity of the line conductors for different loss tangent values.

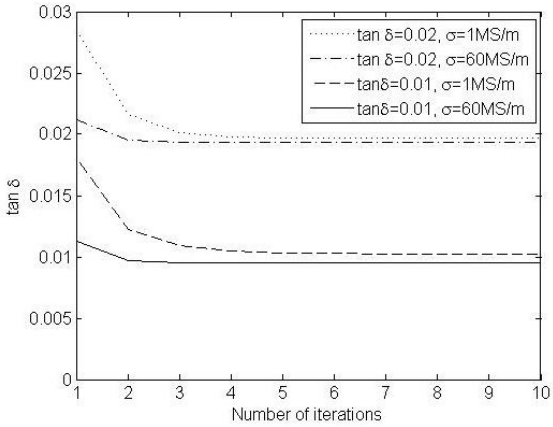

Fig. 4. Convergence of the dissipation factor determination method with the number of iterations, for different conductivities and dielectrics losses.

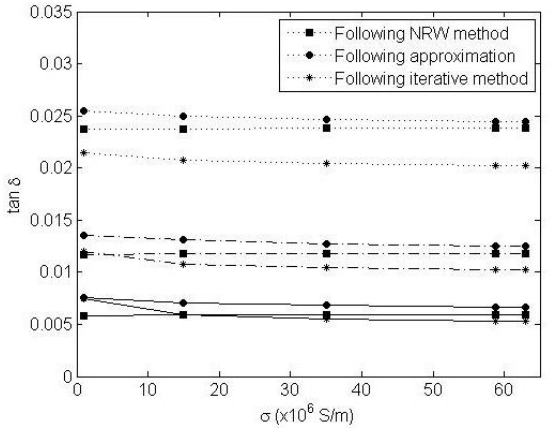

Fig. 5. Loss tangent determination for different loss dielectrics with NRW method, approximation (3a) and the iterative method.

From the results in Fig. 4 we can see that, independently of the loss tangent or the conductivity losses, the method converges for a very reasonable value after the fourth iteration. Moreover, even for very different conductor loss values, the method converges for a very approximate dielectric loss; therefore, showcasing low dependence on this parameter. This means that even if the conductivity value is not precise, one can reach accurate dielectric loss values.

It is clear, from the results depicted in Fig. 5, that the iterative method proposed leads to better estimations of the loss tangent, independently of the dielectric or conductor losses, when compared to other estimation methods.

III. PERMITTIVITY AND DISSIPATION FACTOR ESTIMATION: MEASUREMENTS

To ensure the accuracy of the results obtained by applying the previously described expressions, we tried to characterize three different dielectric substrates, from low to higher permittivity and different losses. The three dielectrics used are presented in Fig. 6.

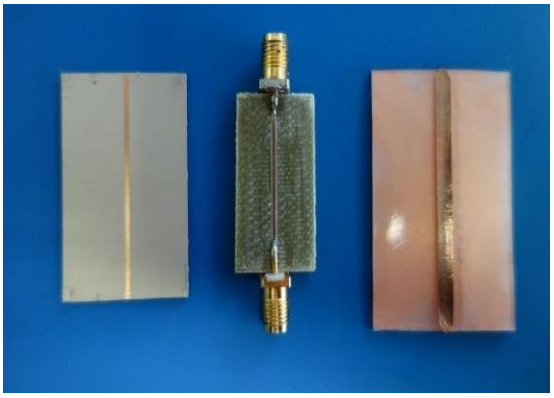

Fig. 6. Picture of the transmission lines tested. From left to right: Rogers RT6010 substrate, FR-4 substrate and LDPE (low density polyethylene) substrate.

There is no special considerations to take for the microstrip line dimensions. However, one thing to keep in mind which might help to achieve better results, is to have a ratio of the width of the line (*W*) to the height of the substrate (*h*) such that avoids being in the border intervals as referenced for the calculations of (4).

As we can see from Table 3, we used different ratios for the line, so that the calculations would fall into the different intervals for each.

The microstrip lines on the Rogers and the FR-4 substrates were etched traditionally, using a milling process. For the plastic, since these had no conductor electrodeposited in it, we used copper tape for the conductive parts of the lines.

Table 3: Dielectric substrate samples physical dimensions

Material	L (cm)	H (mm)	W (mm)	Ws (mm)
FR-4	3.96	1.59	0.8	18
Rogers RT6010	4.42	0.635	1.0	26
LDPE	4.60	1.00	1.16	31

The first step to extract the permittivity is therefore to measure the input impedance of the line with an open circuit in the end. Ensuring that the line is ended in an open circuit is important, connecting an open circuit load from the VNA calibration kit is a way to ensure it. Leaving an open terminated line or an SMA connector does not guarantee an open circuit for the frequency band in consideration, which leads to errors in the loss determination.

To calculate the permittivity of the considered lines first we need to measure the characteristic impedance of the line, which is the real part of the measured the input impedance at one fourth of the resonant frequency. With the input impedance value we can use expression (3) in order to calculate the characteristic impedance of the line. With the characteristic impedance of the lines we use expression (4) to extract ε_{eff}. In order to obtain better results we can consider the effective width of the lines (W_e), as described in [11]. With the effective permittivity we can then calculate the relative permittivity of the substrate with (5).

As for the loss tangent determination the iterative method as described in the previous section should be used. The method stops when the variation of the value between iterations is very small or when you reach a negative value, in which case, the current and previous values should be discarded and second to last value obtained is the one considered the closest to the loss tangent of the dielectric under test.

The results obtained for the considered lines based on the measurements and calculations described, yield the results presented in Table 4.

Table 4: Estimated values of the three sample dielectric slabs based on the proposed method and reference values from literature

Sample	Z_0 (Ω)	ε_r	Ref. ε_r	tan δ	Ref. tan δ
FR-4	93.3	4.29	4.30 – 4.70	0.018	0.025
Rogers RT6010	36.9	10.15	10.20	0.003	0.0023
LDPE	84.8	2.30	2.20 – 2.35	0.07	0.001

Comparing the obtained values for the permittivity and the dissipation factor with the reported values in the materials datasheets we can see a good agreement. However, these values are only relative references since the frequencies and methods used to characterize such materials differ. Besides, it is known, as stated earlier, that these parameters are dependent on frequency and temperature. Therefore, it is expected to observe some differences regarding the estimated values.

IV. UNCERTAINTY ANALYSIS

Although the results reported in the previous section match closely with reported values in the materials datasheets, the reliability of the characterization method must be assessed. In order to do so, we did a set of measurements to the same microstrip lines and verified the error and variation obtained for the permittivity and the loss tangent.

Every measurement is susceptible to errors and therefore it is important to assess the sources of possible mismatches than can occur during measurement that lead to errors in the results. The method proposed here has a few sources which can introduce errors. Those are the measurement of the physical dimensions of the microstrip line, the error occurring from the uncertainty of the VNA, the use of SMA connectors or a test fixture for transmission lines and the added losses from corrosion of the material.

The contribution of some of these sources of error are nearly impossible to separate from the others; therefore, in this section we show the results obtained from several measurements performed to the microstrip lines and analyze the variations of each main parameter that occur in order to certify the robustness of the method.

It is depicted in Figs. 7 and 8 the probability functions, obtained from the measurements of the three dielectric samples, for the permittivity and loss tangents.

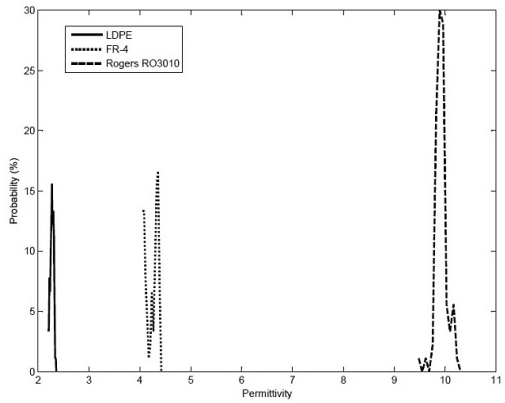

Fig. 7. Probability function of the microstrip lines substrate permittivity (ε_r).

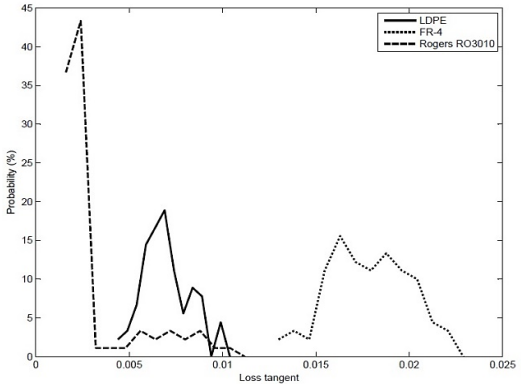

Fig. 8. Probability function of the microstrip lines substrate loss tangent (tan δ).

The uncertainty is characterized by the standard deviation observed in a probability function obtained from a large set of measurements performed under the same conditions. Table 5 resumes the mean values and uncertainty values obtained for the different parameters for each of the dielectric slabs.

Table 5: Mean values and uncertainty obtained in the measurement of the different dielectric sample materials

Sample		f_0 (MHz)	Z_0 (Ω)	ε_r	tan δ
FR-4	$\overline{X}$	1453	93.32	4.32	0.019
	$\overline{U}$	6.91	1.13	0.12	0.002
Rogers RT3010	$\overline{X}$	1152	36.89	10.16	0.003
	$\overline{U}$	65.4	0.48	0.28	0.002
LDPE	$\overline{X}$	1344	84.80	2.30	0.007
	$\overline{U}$	1.82	0.40	0.027	0.0012

From the results obtained we can see that the estimation of the permittivity of the LDPE and FR4 are rather accurate, with obtained values in close relation to the reported in the manufacturer datasheet. The estimation of the RT6010 has shown the highest deviation from the documented values, since we obtained estimations for permittivity ranging from 9.8 to 10.8, with the highest incidence around 10 while the manufacturer reports a permittivity of 10.2 to 10.8. It is therefore clear, that although the method shows reliable results for low and medium permittivity materials, it may provide worst estimations for high permittivity low loss materials.

V. CONCLUSION

The method for permittivity estimation proposed here is quite simple to apply and is obtained directly from the equations that characterize printed transmission lines. It is less expensive when compared to other methods which require specific equipment. However, it is only suitable for the measurement of thin dielectrics, since it requires a microstrip line with the test dielectric as substrate.

Although the input impedance should be calculated at a fourth of the resonant frequency, this method allows the calculation of the permittivity at multiple frequencies. Multiples of half of the resonant frequency should be avoided since these will not provide any reasonable value. Still, one must take into account that the losses and therefore the error increases with frequency.

The proposed iterative method for the estimation of the dissipation factor presents better estimations than other commonly used methods at the cost of requiring more calculations. Still, it is shown that the method usually converges after few iterations.

The main drawback of this method is the error, especially in the estimation of higher permittivity low loss dielectrics. Still, the obtained results agree fairly with values reported in datasheets of the considered dielectrics and also with simulation results for printed transmission lines. This means that it can be used to obtain a rough first estimation of an uncharacterized dielectric material that might be used as a substrate for RF circuitry.

As a final remark we can say that the robustness of the method increases if the mean value of multiple measurements on lines with the same substrate is used.

ACKNOWLEDGMENT

The authors acknowledge the Portuguese FCT/MCTES for financing the Ph.D. grant SFRH/BD/91249/2012, the project CREATION EXCL/EEI-TEL/0067/2012 and the project UID/EEA/50008/2013.

REFERENCES

[1] R. Salvado, C. Loss, R. Gonçalves, and P. Pinho, "Textile materials for the design of wearable antennas: a survey," *Sensors 2012*, 12, 15841-15857, 2012.

[2] R. Goncalves, S. Rima, R. Magueta, A. Collado, P. Pinho, N. B. Carvalho, and A. Georgiadis, "RFID tags on cork stoppers for bottle identification," *IEEE MTT-S Int. Microwave Symp. Dig.*, Tampa Bay, FL, 2014.

[3] L. Roselli, N. B. Carvalho, F. Alimenti, P. Mezzanotte, G. Orecchini, M. Virili, C. Mariotti, R. Goncalves, and P. Pinho, "Smart surfaces: large area electronics systems for internet of things enabled by energy harvesting," *Proc. of the IEEE*, vol. 102, no. 11, pp. 1723,1746, Nov. 2014.

[4] D. M. Pozar, *Microwave Engineering*, 4th ed., John Wiley & Sons, Inc., 2012.

[5] J. Baker-Jarvis, R. G. Geyer, J. H. Grosvenor, Jr., M. D. Janezic, C. A. Jones, B. Riddle, C. M. Weil, and J. Krupka, "Dielectric characterization of low-loss materials a comparison of techniques," *IEEE Trans. Dielectrics Electrical Insulation*, vol. 5, no. 4, pp. 571-577, Aug. 1998.

[6] K. C. Yaw, "Measurement of dielectric material properties: application note," *Rhode & Schwarz*, 04.2012-RAC-0607-0019_1_5E, 2012.
[7] L. Chen, C. K. Ong, V. V. Varadan, and V. K. Varadan, *Microwave Electronics: Measurement and Materials Characterization*, John Wiley & Sons, Inc., 2004.
[8] M. Q. Lee and S. Nam, "An accurate broadband measurement of substrate dielectric constant," *IEEE Microw. Guided Wave Lett.*, vol. 6, pp. 168-170, 1996.
[9] S F. Declercq, H. Rogier, and C. Hertleer, "Permittivity and loss tangent characterization for garment antennas based on a new matrix paencil two line method," *IEEE Trans. Antennas Propagat*., vol. 56, pp. 2548-2554, 2008.
[10] J. Roelvink, S. Trabelsi, and S. O. Nelson, "A planar transmission-line sensor for measuring the microwave permittivity of liquid and semisolid biological materials," *IEEE Trans. Instrum. Meas*., vol. 62, no. 11, pp. 2974-2982, Nov. 2013.
[11] B. C. Wadell, *Transmission Line Design Handbook*, Artech House, Inc., 1991.
[12] A. Nicolson and G. Ross, "Measurement of the intrinsic properties of materials by time domain techniques," *IEEE Trans. Instrum. Meas*., vol. 19, no. 4, pp. 377-382, Nov. 1970.
[13] W. B. Weir, "Automatic measurement of complex dielectric constant and permeability at microwave frequencies," *Proc. of the IEEE*, vol. 62, no. 1, pp. 33-36, Jan. 1974.
[14] R. A. Pucel, D. J. Massé, and C. P. Hartwig, "Losses in microstrip," *IEEE Trans. Microw. Theory Tech*., vol. 16, pp. 342-350, 1968.

Ricardo Gonçalves was born in Lisbon, Portugal, in 1988. He received the B.Sc. and M.Sc. degrees in Electronics and Telecommunications Engineering from the Instituto Superior de Engenharia de Lisboa, Lisbon, in 2010 and 2012, respectively. He is currently working toward the Ph.D. in Electrical Engineering at the University of Aveiro. He is a Researcher at the Instituto de Telecomunicações, Aveiro, Portugal.

His main research interests include wireless power transfer systems, radio-frequency identification (RFID), and wireless passive sensor networks. He is a Student Member of the IEEE MTT-S and AP-S societies and a Member and Founder of the MTT-S Student Branch at the University of Aveiro. He is also a Student Member of the ACES society.

Roberto Magueta received his M.Sc. degree in Electronics and Telecommunications Engineering from University of Aveiro, Portugal, in 2013. After which he joined Instituto de Telecomunicações, Aveiro, as a Researcher in the project RadioVoip - Smart Antenna for Maritime Communications. He is currently working towards is Ph.D., his thesis is focused on transmitter and receiver designs for future mm-wave and massive MIMO based Wireless Systems.

Pedro Pinho was born in Vale de Cambra, Portugal, in 1974. He received the Licenciado and M.Sc. degrees in Electrical and Telecommunications Engineering and the Ph.D. degree in Electrical Engineering from the University of Aveiro, Aveiro, Portugal, in 1997, 2000 and 2004, respectively.

He is currently a Professor Adjunto at the Department of Electrical Telecommunications and Computers Engineering, Instituto Superior de Engenharia de Lisboa, Lisbon, Portugal, and a Researcher at the Instituto de Telecomunicações, in Aveiro, since 1997. His current research interests are in antennas for location systems, reconfigurable antennas, and antenna design for passive sensors in nonconventional materials.

Nuno Borges Carvalho was born in Luanda, Angola, in 1972. He received the Diploma and Doctoral degrees in Electronics and Telecommunications Engineering from the University of Aveiro, Aveiro, Portugal, in 1995 and 2000, respectively. He is a Full Professor at the Universidade de Aveiro, Aveiro, Portugal and a Senior Research Scientist with the Instituto de Telecomunicaçõess (IT), in Aveiro, where he coordinates the Radio Systems Group.

He has co-authored over 200 papers in journals and conferences and two books. He co-holds four patents. His main research interests include wireless power transmission, nonlinear distortion analysis in microwave/ wireless circuits and systems, and measurement of nonlinear phenomena. He has recently been involved in the design of dedicated radios and systems for newly emerging wireless technologies.

Borges Carvalho is an IEEE Fellow and the Chair of the IEEE MTT-11 Technical Committee. He is a Member of IEEE MTT-20, MTT-24, and MTT-26. He is an Associate Editor for the IEEE Transactions on Microwave Theory and Techniques, IEEE Microwave Magazine, Cambridge Journal on Wireless Power Transmission and the Chair of the URSI–Portugal Metrology Group.

Improvements in DNA Biosensors Using Joint Split Ring Resonators Coupled with Thin Film Microstrip Line

Mohammad Abdolrazzaghi [1*], Ali Abdolali [2], and Soheil Hashemy [2]

[1] Electrical and Computer Engineering Department
University of Alberta, Edmonton, Alberta, T6G 2V4, Canada

[2] Department of Electrical Engineering
Iran University of Science and Technology (IUST), Tehran, 1684613114, Iran

Abstract ─ Detecting the presence of materials in biomedical science using THz sensors, especially thin DNA strands, needs considerably sensitive sensors. Connection of unit cells in new frequency selective surface (FSS) structure, coupled with transmission line is introduced so that not only helps to miniaturize in sensing applications through THz frequency range, but also has steeper flanks in transitions, thus leads us to have higher sensitivities. All of the results are taken out from resonant frequencies related to reflection (s_{11}), a new property used instead of transmission loss (s_{21}), which is measurable using THz spectrometers. The effect of analyte thickness and dielectric properties of load on frequency response is explained. This approach is a new way in recognizing very small amounts of material even with rather low dielectric constants.

Index Terms ─ DNA detection, metamaterials, sensitivity improvement, THz biosensors.

I. INTRODUCTION

Pendry et al. [1], in 1999, following Veselago's idea of metamaterials [2], suggested split ring resonators (SRRs) theoretically as being feasible devices that show magnetic response from nonmagnetic conducting materials in microwave region. Smith et al. in 2001 demonstrated the possibility of SRRs using periodic lattice of long metallic wires and double split ring resonators (DSRR) [3]. Excitation of DSRRs with electric fields outside, can bring about LC–resonances, identified by Linden et al. [4] for TE and electric (plasmon) resonances for TM radiation [2], [4], [5].

High quality factor of such structures, lately persuaded researchers to utilize SRRs as sensing devices. The change in resonant frequencies of SRRs after being loaded with biological materials of different dielectric constants, is the main idea; as the rapid transition of frequency response paves the way for identification of small amounts of tissues. Therefore, recently, thin-film sensing using frequency selective structures (FSS) are widespread.

Feasibility of SRRs as being bio sensing devices has been confirmed in the previous works [5], [6], [7]. In these thin-film sensors frequency of resonance and sensitivity are two important factors to consider both in simulation and in practice. Main problem of the proposed structures, are higher resonant frequencies and lower sensitivities [8]. We introduce a new back-to-back structure that meet both needs, and is useful in identifying minute amounts of biological tissues namely DNA strands, with promising results. All results of the simulations are obtained using CST Microwave Studio with perfectly matched layer (PML) boundary condition. Besides, the evolution process of the structure is explained. Knowing that thickness is another important factor in recognizing the type of material, the effect of load thickness on resonant frequency is illustrated and frequency response of the sensor after being loaded with dielectrics of diverse thicknesses are presented. Fitting with a Gaussian function presented at the end of the article helps to find intermediate corresponding fr according to desired thickness.

II. METHODS

Interaction of the applied field with metal molecules makes induced currents that result in resonances [2]. In this paper, we used TE illumination, which makes a path for electrons to flow as current along a loop. The fields produced from the induced currents will have constructive or destructive effect on each other as the wave passes through or reflects from the FSS, and finally makes a resonance in reflection at frequency:

$$f_r = \frac{1}{2\pi\sqrt{LC}}, \quad (1)$$

where L stands for inductance of the metal, and C is the capacitance between edges of metals whether in free space or inside substrate. It is clear that the frequency is

Submitted On: February 24, 2015
Accepted On: December 27, 2015

inversely proportional to the size (dimension) of the SRR [9].

Dimensions of the structure are derived from observing several demands such as working in THz region as biosensor, small size and simplicity of the structure. Input impedance of thin film microstrip depends on the strip width and substrate height, which is determined uncontrollably due to the resonant frequency and the quality factor of the sensor. According to loading effects of SRRs on microstrip, the input impedance of the sensor is obtained as 220 Ω at resonant frequency, using CST simulations. In order to match such device, we need a transmission line (TML) with characteristic impedance $Z_0 = \sqrt{Z_{in} Z_{out}}$, where Z_{in} equals the standard input impedance for measurement, and Z_{out} is the input impedance of loaded thin film microstrip line. Another way of matching the TML is to use interdigital capacitor [10]. As a result, we came up with what is shown in Fig. 1.

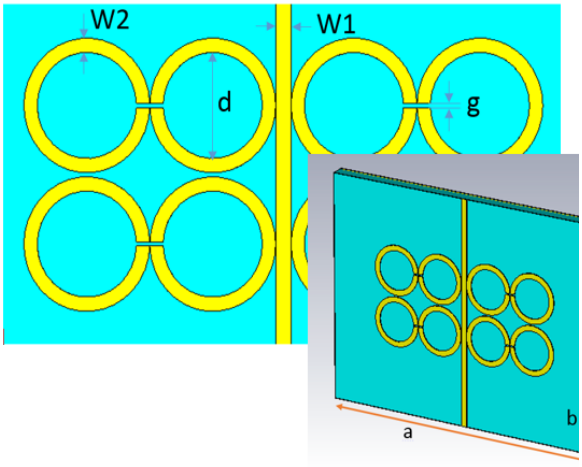

Fig. 1. Dimensions of the structure, a = 400 um, b = 300 um, w1 = 8 um, w2 = 7 um, d = 52 um, g = 2 um and the aluminum metal of thickness 1 um is over and under 18 um thick silicon (loss free) substrate of ε_r = 11.9.

Surface current of the structure after being illuminated through waveguide port at resonant frequency is shown in Fig. 2. It is clear that the density of current is more in the middle of transmission line due to the greatest amount of its interaction with the surrounding media.

In this work, single-stranded deoxyribonucleic acid (ss-DNA) and complementary deoxyribonucleic acid (c-DNA) are the biological elements to be detected and the single SRR for the transducer which converts chemical change into electrical signal. The principle of such biosensor lies in shifting of resonant frequencies due to changes of L or C. Changing the capacitance between the FSS edges, is an easy task as it needs to introduce other materials to the sensor. We implemented the design using the proposed idea by adding generally biological tissues that impose appreciable change on sensor's effective dielectric constant, as well as resonances occur at different frequencies according to the Equation (1). After such simulations, we will have a rich database of f_r and corresponding external situation. In order to distinguish the surrounding environment using the sensor, we need to use the database in reverse manner by ANN, SVM machines, Fuzzy Logic or etc.

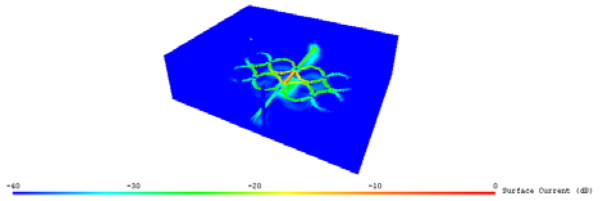

Fig. 2. The surface current of the structure in exposure to the external field at resonant frequency.

III. RESULTS AND DISCUSSION

Selection of the substrate and the FSS metal was due to their THz properties. As Silicon does not show appreciable loss in terahertz, especially lower frequencies, we chose it as loss-free to neglect its effect in our simulations [11]. Gold as the metal that has great capabilities in reacting to biological tissues, more importantly DNA, was suitable for our later diagnosis procedures.

Figure 3 shows the frequency response of the sensor during its configuration process. First of all, having just one SRR gives a deep resonance at 443 GHz; although it is a good one, but for minimization and technical reasons we need to lower the resonant frequency. Therefore, we proceeded in adding extra SRRs to see the differences. Second graph shows a back-to-back structure on one side of the transmission line, the resonances are not satisfactory; whereas, duplicating the latter on the other side makes third frequency response, and having another row yields the final deep and much lower resonant frequency, almost 55% lower than first one. It shows how more resonators can couple with each other as well as possible to have a strong resonance.

Reduction factors finally gave a resonance at 194.6 GHz with reasonably depth of -21.11 dB reflection. In observation of the structures for its Q factor, we noticed that the higher the input impedance, the better the quality factor, that's why we chose the sensor's input impedance to be 220 ohms. After all, the final design has a quality factor of almost $Q = \frac{fr}{\Delta f} = 121$ that is quite suitable for sensing applications. Some prohibiting probabilities should be avoided, as mentioned below. An important factor is that keeping

the resonators just 2 um away from the transmission line, totally worsens the response, as shown in Fig. 3. It shows that connecting the rings to each other and to the transmission line, makes higher possibility of coupling and an increase in L, so besides other reported structures, here "connection" works. On the other hand, connecting two rows of SRRs degrades the result as nothing has been gained from the scratch. The coupling effect through a higher electric field concentration between the SRR rows (in close distance), helps us to reduce the resonances in great amounts. Whilst, their connection interfere with the induced opposite currents on face-to-face edges of SRRs so that current flows cancel each at the intersection. As mentioned above several considerations should be taken into account in reaching desired function as a good sample of the prospective biosensors.

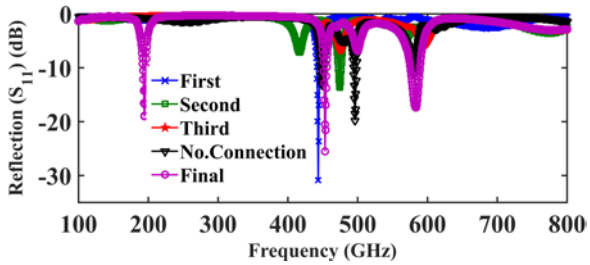

Fig. 3. The frequency response of the structure during different stages of evolution.

We show that the thickness of the analyte inside the gaps of the structure, affects the resonant frequency as well. Suppose that sides of each unit cell (dotted region in inset of Fig. 4) make a capacitance when considered in front of each other, as shown in Fig. 4, as very small sizes of the elements makes it possible to assume semi-TEM fields in the region, the following analysis becomes accurate. The analyte (shown in green color) of thickness t_x fills the gap ($0 < t_x < t$). If we take the edges as parallelization of infinite simple plates of such capacitor, we can calculate the total capacitance after introduction of analytes. As the gap is so small and is quasi-static condition, we have following relationships for capacitance of regions filled with dielectric (Equation (2)), and free space (Equation (3)) regions:

$$C_1 = \epsilon_0 \epsilon_r \frac{t_x b}{d}, \tag{2}$$

$$C_2 = \epsilon_0 \frac{(t - t_x) b}{d}, \tag{3}$$

$$C_{total} = C_1 + C_2 = \epsilon_0 \frac{b}{d}(t + (\epsilon_r - 1)t_x). \tag{4}$$

From Equation (4), it is evident that for a specified dielectric constant, the more thick the analyte, the more capacitance we get. Therefore, frequency of LC-resonance is lower according to the following relationship:

$$\frac{df_r}{f_r} = -\frac{1}{2}\frac{dC}{C} = -\frac{1}{2}\frac{(\epsilon_r - 1)\,\mathrm{d}\,t_x}{t + (\epsilon_r - 1)t_x} \tag{5}$$

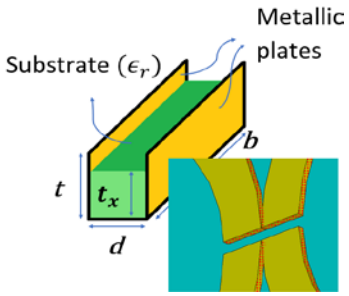

Fig. 4. Filled capacitor, schematic of dotted area in inset.

Infinite number of such capacitances hand in hand to make the total C, required for resonance. Thus in Fig. 6, frequency response of the structure is represented for fixed thickness of 1 um (filling the free space over substrate) and different dielectric permittivity ranging from 5 to 35. It is clear that increasing the dielectric constant itself, lowers the resonant frequency because of change in C, as is represented in Equation (1). Table 1, which shows sensitivity of the sensor can be understood using the change in resonant frequency with respect to change of the dielectric constant through a wide range of No Load (no analyte mounted) to Full Load (with 1 um thick biomaterial with distinctive permittivity) status.

High shift of almost average 2.1% (4.1 GHz) per ϵ_r especially in lower dielectric constants represents its high sensitivity and this property guarantees a reliable tool in sensing.

In Fig. 5, the same feature is examined after changing the thickness of the analyte incrementally. It shows that the design is capable of distinguishing the differences among medium with ϵ_r = 10, and various thicknesses. After fitting the data shown in Fig. 5 with a Gaussian function, according to the following equation:

$$f_r(t) = 1.45e16e^{-\left(\frac{t+254.3}{44.03}\right)^2} + 130.4e^{-\left(\frac{t+32.17}{191.8}\right)^2}. \tag{6}$$

We can determine resonant frequency of the structure in intermediate thickness range, as shown in Fig. 7. The diagram shows that the biosensor is able to work with thicker materials up to 23 um before saturation.

Finally, to check the sensitivity of the biosensor in identification of very small amounts of analytes such as DNA in biology, we examine the sensor with 0.01 and 0.2 um of DNA strands (ϵ_r = 3.2). Table 2 shows the results, frequency shifts of 1.42 GHz and 2.16 GHz for t = 0.01 um and t = 0.1 um respectively, brings about

totally measurable 4.84 dB and 10.7 dB changes in S_{11} depth respectively, for reflection at resonant frequency of unloaded microstrip.

Table 1: The sensitivity of the design according to the load

Dielectric Constant	Change of f_r for Change of ε_r (GHz)	Percentage of Change of f_r for Change of ε_r (%)
No Load-5	20.5	10.5
No Load-10	37.2	19.1
No Load-15	49.5	25.35
No Load-20	59.2	30.4
No Load-25	66.25	34
No Load-30	74.7	38.4
No Load-35	75.95	38.85

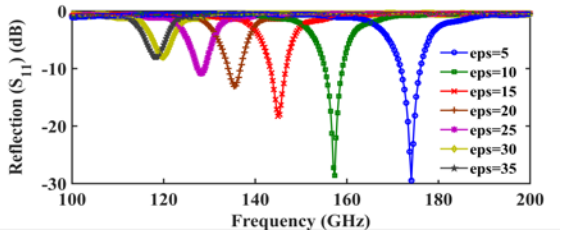

Fig. 5. Resonant frequency shifting according to different dielectric constants of the load with analyte thickness of 1 um.

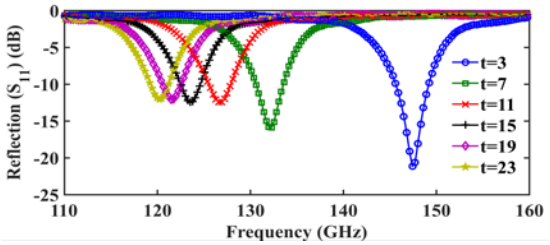

Fig. 6. Frequency response of the structure loaded with homogeneous materials of dielectric constant of 10 and various thicknesses (um).

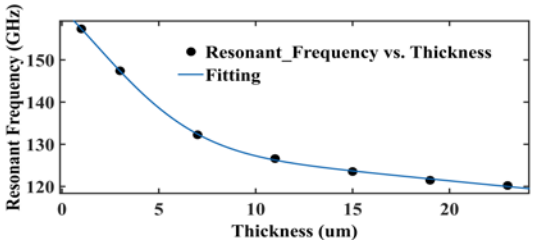

Fig. 7. Fitting of the resonant frequencies according to changes in thickness.

Table 2: Resonant frequencies of loaded microstrip and relevant s_{11}

Thickness of DNA (um)	Resonant frequency (GHz)	Return Loss at unloaded *fr* (dB)
No Load	194.65	-21.11
t = 0.1	193.23	-16.27
t = 0.2	192.49	-11.04

IV. PRACTICAL NOTES IN DNA STABILIZATION AND MEASUREMENT

We need to immobilize the DNA strands on the silicon substrate in order to measure the resonant frequencies. At first, it is needed to cover the silicon substrate with thin film of carbon to prevent its oxidation in contact with air (formation of amorphous silica layer); otherwise, DNA coupling will be impossible. Therefore, a special pretreatment is needed for subsequent reaction with organic particles, which could be achieved by a reaction of the prepared Si(111) surface with unsaturated ω-functionalized alkenes in the presence of UV irradiation. Figure 8 shows complete procedure for DNA coupling into Si [13], [14], [15].

The process will start with bonding just one strand of DNA on the silicon between the gold slots according to the method aforementioned. Then the sample with DNA strands will be introduced to the structure. The single strands will find their complementary parts in the liquid, and form helix DNA strands or hybridized [12]. Addition of extra strands, enable us to detect new resonant frequency. The change will inform us about the quality and quantity of the present DNA in the liquid. The effect of the added immobilizer to the sensor is not included in the simulations while it will have negligible constant effect on all the conclusions [13], [14].

One of specific usages of the FSS biosensor is diagnosing Leukemia (cancer of blood characterized by mutations in DNA) in its first stages, when the disease has not progressed so much. In the critical period, usual procedures are not able to detect the existence of the cancer simply because of the amount of abnormal tissues in the body are not enough to be distinguished, while it can be halted during the evolution, if detection would be available. The accuracy of the sensory structure, as its diagnosis is related to the interactions of single DNA strands with their complementary ones (DNA hybridization) and the strands will connect only to their pairs and nothing irrelevant, is totally reliable.

This paper introduced the mechanism of such biosensor referring to simulations with CST Microwave Studio, while optoelectronic measurements are capable of verifying the results and the type of measurement setup connection is illustrated in [16] as the structure abovementioned is a thin film microstrip line (TFMSL).

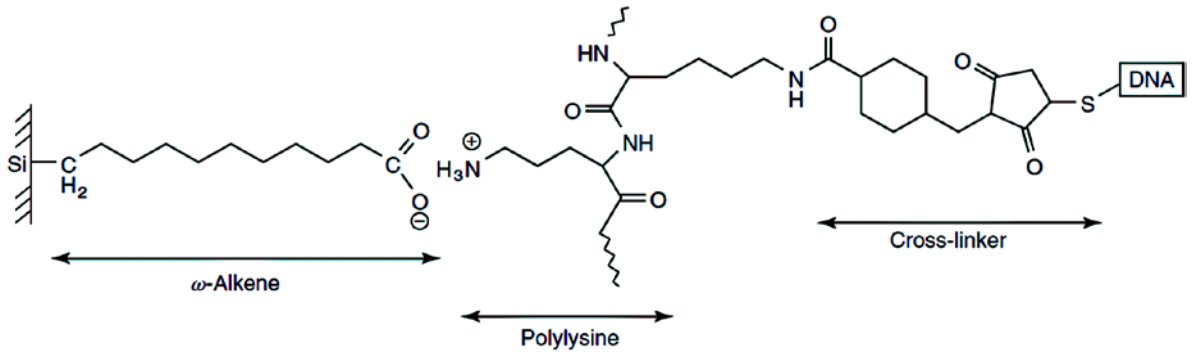

Fig. 8. Scheme for the preparation of a modified Si(111) surface. In the first step, a layer of alkenyl acid is linked to the surface by covalent attachment. Subsequently, a polylysine layer is electrostatically bound to the carboxylic activated surface and finally the DNA is coupled to the surface in a reaction mediated by cross link (sulfosuccinimidyl 4-(N-maleimidomethyl)-cyclohexane-1-carboxylate) [13], [14].

V. CONCLUSIONS

We represented a new design for sensing different kinds of biological tissues with high sensitivity and great quality factor of Q = 121.56 that is gained after introducing new ideas of joining extracted from the SRRs. A complete configuration process of the structure is analyzed using promising frequency responses. Besides, we demonstrated the reflection of loading the sensor with 1 um thick analyte of $\varepsilon_r = 5-35$. The fitting plot helps us to interpolate other responses. The effect of thickness on the resonant frequency is explained clearly. A resonance at 194.6 GHz with -21.11 dB reflection and Q = 121 is gained, and after loading the structure with homogenous materials, an average of 2.1% change in frequency due to unit change in permittivity is observed. We examine the sensor in identification of vary small amount of DNA strands (thickness = 0.01 um, ϵ_r = 3.2) and got quite satisfactory results.

REFERENCES

[1] J. Pendry, A. Holden, D. Robbins, and W. Stewart, "Magnetism from conductors and enhanced nonlinear phenomena," *IEEE Trans. Microwave Theory & Tech.*, vol. 47, no. 12, pp. 2075-2084, Nov. 1999.

[2] V. G. Veselago, "The electrodynamics of substances with simultaneously negative values of permittivity and permeability," *Sov. Phys. Uspekhi*, vol. 10, 1968.

[3] D. R. Smith, W. J. Padilla, D. C. Vier, S. C. Nemat-Nasser, and S. Schultz, "Composite medium with simultaneously negative permeability and permittivity," *Phys. Rev. Lett.*, vol. 84, no. 18. pp. 4184-4187, May 2000.

[4] S. Linden, C. Enkrich, M. Wegener, J. Zhou, T. Koschny, and C. M. Soukoulis, "Magnetic response of metamaterials at 100 THz," *Science*, 306(5700), pp. 1351-1361, 2004.

[5] V. M. Shalaev, "Optical negative index metamaterials," *Nat. Photonics*, vol. 1, no. 1, pp. 41-48, 2007.

[6] H. J. Lee and J. G. Yook, "Biosensing using split-ring resonators at microwave regime," *Appl. Phys. Lett.*, vol. 92, pp. 254103-1-3, June 2008.

[7] H. S. Lee, H. J. Lee, H. H. Choi, J. G. Yook, and K. H. Yoo, "Carbon-nanotube-resonator-based biosensors," *Small*, vol. x, no. x, pp. 1-5, Sep. 2008.

[8] H. J. Lee, et al., "DNA sensing based on single element planar double split-ring resonator," *Microwave Symposium Digest, 2009, MTT'09, IEEE MTT-S International, IEEE*, 2009.

[9] S. Linden, C. Enkrich, G. Dolling, M. W. Klein, J. Zhou, T. Koschny, C. M. Soukoulis, S. Burger, F. Schmidt, and M. Wegener, "Photonic metamaterials: magnetism at optical frequencies," *IEEE J. Sel. Top. Quantum Electron.*, vol. 12, no. 6, pp. 1097-1105, 2006.

[10] M. Ali, A. Kachouri, and M. Samet, "Novel method for planar microstrip antenna matching impedance," *arXiv preprint arXiv:1006.0856*, 2010.

[11] Y. Kadoya, M. Onuma, S. Yanagi, T. Ohkubo, N. Sato, and J. Kitagawa, "THz, wave propagation on strip lines," *Devices, Properties, and Applications Japan Radio Engineering*, vol. 17, no. 2, 2008.

[12] Y. Okahata, Y. Matsunobu, K. Ijiro, M. Mukae, A. Murakami, and K. Makino, "Hybridization of nucleic acids immobilized on a silicon crystal microbalance," *J. Am. Chem. Soc.*, vol. 114, no. 21, pp. 8299-8300, 1992

[13] C. Wittmann and C. Marquette, *DNA Immobilization*, This article was published in the Encyclopedia of Analytical Chemistry in 2012 by John Wiley & Sons, Ltd.

[14] J. F. O'Hara, et al., "Thin-film sensing with terahertz split-ring resonators," *Conference on Lasers and Electro-Optics*, Optical Society of America, 2008.

[15] A. del Campo and I. J. Bruce, *Substrate Patterning and Activation Strategies for DNA Chip Fabrication*, in Topics in Current Chemistry 260 – Immobilization of DNA on Chips I, ed. C. Wittmann, Springer-Verlag, Berlin Heidelberg, 77-111, 2005.

[16] H.-M. Heiliger, M. Nagel, H. G. Roskos, H. Kurz, F. Schnieder, and W. Heinrich, "Thin-film microstrip lines for mm and sub-mm-wave on-chip interconnects," *in IEEE MTT-S Int. Microwave Symp. Dig*., pp. 421-424, 1997.

Muhammad Abdorrazzaghi was born in Marand, Iran, in February, 1991. He has received his bachelor's degree at Electrical Engineering Department of Iran University of Science and Technology (IUST). His research interest includes: metamaterial, biosensors, THz, bioelectromagnetics, wave propagation in inhomogeneous medium, scattering and inverse scattering, metamaterial inspired sensors. He is currently pursuing his Ph.D. at University of Alberta, Canada.

Ali Abdolali was born in Tehran, Iran, on May 3, 1974. He received the B.Sc. degree from University of Tehran, and the M.Sc. degree from University of Tarbiat Modares, Tehran, and the Ph.D. degree from the Iran University of Science and Technology (IUST), Tehran, all in Electrical Engineering, in 1998, 2000, and 2010, respectively. In 2010, he joined the Department of Electrical Engineering, Iran University of Science and Technology, Tehran, Iran, where he is an Assistant Professor of Electromagnetic Engineering. His research interests include electromagnetic wave scattering, radar cross section (RCS) & RCSR, radar absorbing materials (RAM), cloaking, metamaterials, wave propagation in complex media (anisotropic, inhomogeneous, dispersive media), frequency selective surfaces (FSS), bioelectromagnetics (BEM). He has authored or co-authored over 60 papers in international journals & conferences.

Soheil Hashemi was born in Tehran, Iran, on May 13, 1987. He received the B.Sc. and M.Sc. degrees from the University of Tehran in Electrical engineering, in 2010 and 2012 respectively. He is studying the Ph.D. degree at the Iran University of Science and Technology (IUST), Tehran in Electrical Engineering, Fields and Waves. His research interests include bioelectromagnetics (BEM), electromagnetic wave scattering, cloaking, metamaterials, wave propagation in complex media, frequency selective surfaces (FSS) and antennas.

New Compact Dual Bandpass Filter Using Coupled Double-Ring Resonators and DGS-Technique

A. Boutejdar [1], N. M. Eltabit [2], A. A. Ibrahim [3], E. P. Burte [1], and M. A. Abdalla [4]

[1] Department of Electrical Engineering
German Research Foundation DFG, Braunschweig, 32108, Germany
boutejdar69@gmail.com, Edmund.burte@ovgu.de

[2] Department of Mathematics
University of Magdeburg, Magdeburg, 38102, Germany
nurieltab@yahoo.com

[3] Faculty of Engineering
El-Minia University, El-Minia, Egypt
ahmedabel_monem@mu.edu.eg

[4] Electronic Engineering Department
MTC College Cairo, Egypt
maaabdalla@ieee.org

Abstract ─ This paper presents a design of dual-band bandpass filter using novel ring resonator and H-defected ground. The bandpass filter is designed optimized and realized using mixed coupled microstrip double ring resonators and two electrically coupled H-cells DGS resonators, which are etched in background of the structure. Using this new ring structure leads to generate a selective bandpass filter with two isolated passbands. The measurement results show that the optimized filter has two passbands, the first band from 1.6 GHz to 2 GHz and the other from 3.6 GHz to 5.5 GHz. The proposed structure occupies an area of ($0.45\lambda g \times 0.35\lambda g$) with $\lambda g = 0.044$ m. The simulated and experimented results show good agreement and validate the proposed approach.

Index Terms ─ Coupled resonators, defected ground structure (DGS), double-ring resonators, dual-band bandpass filter.

I. INTRODUCTION

Recently, defected ground structures (DGS) and electromagnetic band gap (EBG) structures have drawn a great interest in microwave and millimeter wave applications because of their numerous advantages like significant size compactness and undesired harmonic suppression and their using in mobile communication systems and in various applications of microwave technology. DGS can be etched periodically or non-periodically cascaded shapes in ground of a planar transmission line. DGS caused disturbance in a shield current distribution in the metallic ground plane. This disturbance leads change of characteristics of a transmission line such as line capacitance and inductance. Thus, DGS elements are equivalent to the LC circuit [1]. Compact filters which use DGS structures as main block of resonators are investigated [2], [3] and antennas [4], [5]. To meet the requirements in modern microwave engineering and mobile communication systems, much effort has been made in the past years to develop a variety of the compact bandpass filter with sharp and deep rejection outside the passband by generating transmission zeros or attenuation poles [6-8]. The DGS-technique presents one of the very successful solutions to achieve significant size compactness and to suppress the undesired periodicity effect [9], [10].

With recent development in wireless communication systems, dual-band filters have been needed for many dual-band operation systems. A dual-band bandpass filter was implemented by a cascade connection of two single-band filters [11]. However, this approach not only increases the overall size of the filter, but also requires extra impedance matching networks. Defected ground structure is also used to achieve dual-band filter [12], [13].

In this paper, a new type of dual bandpass filter using microstrip coupled double-ring resonators and

Submitted On: January 15, 2015
Accepted On: December 6, 2015

defected ground structure technique is designed, fabricated, and measured. In order to tune the desired transmission zeros which determine the sharpness of the transitions of the stop domain, the slot between the internal-arms of the ring resonator and the position of the 50 Ω microstrip feeds are optimized.

The proposed filter shows two passbands from 1.6 GHz to 2.0 GHz and from 3.6 GHz to 5.5 GHz. The out-band rejection between both passbands is better than 20 dB from 2.2 GHz to 3.3 GHz. The two passbands of the filter at 1.8 GHz center frequency with 22.2% fractional bandwidth (FBW) and at 4.5 GHz center frequency with 42.2 % fractional bandwidth at -3 dB have been implemented for the applications of L- and C-band communication systems respectively. The proposed filter is fabricated and measured. The CST software was employed in the full wave simulations. Finally, the measured results exhibit good agreement with the simulations. The out-band rejection is better than 20 dB up to 10 GHz.

II. CHARACTERISTICS OF THE NEW DOUPLE RING RESONATOR

The configuration of the double-ring resonator is shown in Fig. 1. It consists of a small interior ring, which is connected to a wide exterior ring. The new double-ring resonator can be presented as LC resonator, in which the arms present the inductance and the slot the capacitor. The proposed resonator acts as a dual resonator of different circumstances. Hence, the proposed resonator can behave as a dual bandstop filter. By loading this resonator with the microstrip line, the whole structure acts as a dual bandstop filter. The frequency response of the filter can be adjusted. The lower frequency stopband is mainly controlled by the larger loop dimensions, whereas the higher frequency is controlled by the smaller loop. To examine the proposed dual-band resonator response, it has been examined for different small loop gap (s) so that the return loss and the insertion are demonstrated in Fig. 2.

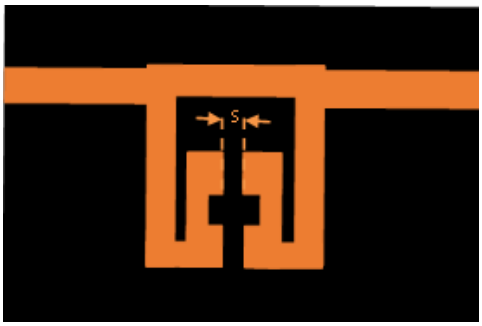

Fig. 1. The 2-D layout of the double microstrip ring resnator.

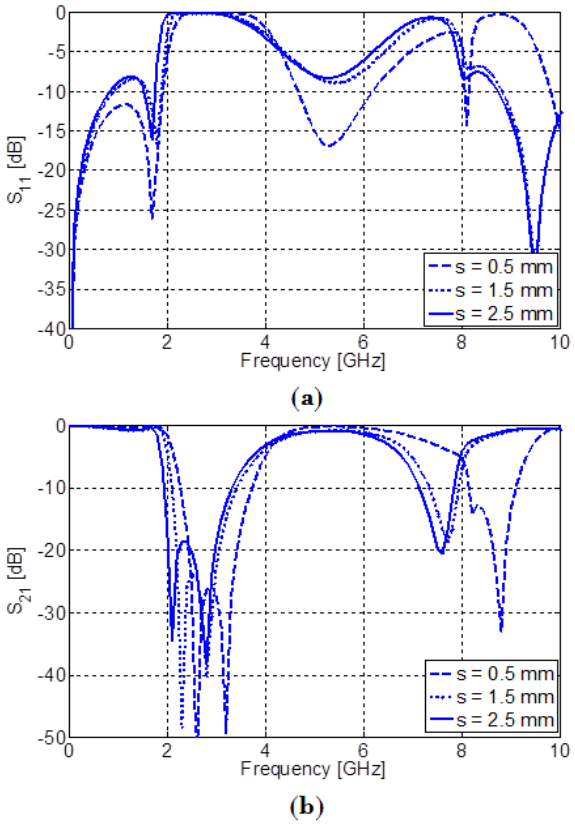

Fig. 2. Parametric study of the double microstrip ring resonator at different value of (s): (a) return loss, and (b) insertion loss.

Based on the several proposed resonator structures and their analysis in our published papers [1], [9], [10], the equivalent circuit of the investigated microstrip resonator, corresponds to a parallel LC circuit. The values of the L and C can be calculated as following:

$$C = \frac{5 f_c}{\pi Z_0 \left(f_0^2 - f_c^2 \right)}, \tag{1}$$

$$L = \frac{250}{C_p (\pi f_0)^2}. \tag{2}$$

By increasing S from 0.5 mm to 2.5 mm, it is clear that the structure has dual-bands. The first stopband is from 2 GHz to 4 GHz and is not affected by changing (s). On the other hand, a second stopband which is approximately from 6 GHz to 8 GHz for S = 1.5 mm and 2.5 mm. However, by decreasing the distance (s) to 0.5 mm, this stopband can be shifted up to be from 8 GHz to 9 GHz. In effect, we can say the propose resonator introduces a LPF from 0 to 2 GHz along with bandpass filter. These results confirm that by controlling each loop individually, a dual bandstop filter can be obtained. The filter performance can be

further investigated by plotting the electric field at different frequencies as shown in Fig. 3.

As shown in the figure, two passband filed profile (from port 1 to port 2) is clear at 1.8 GHz and 5 GHz in Fig. 3 (a) and Fig. 3 (b), respectively. At 2.3 GHz, a total reflection (stopband) field concentration at the input as illustrated in Fig. 3(c).

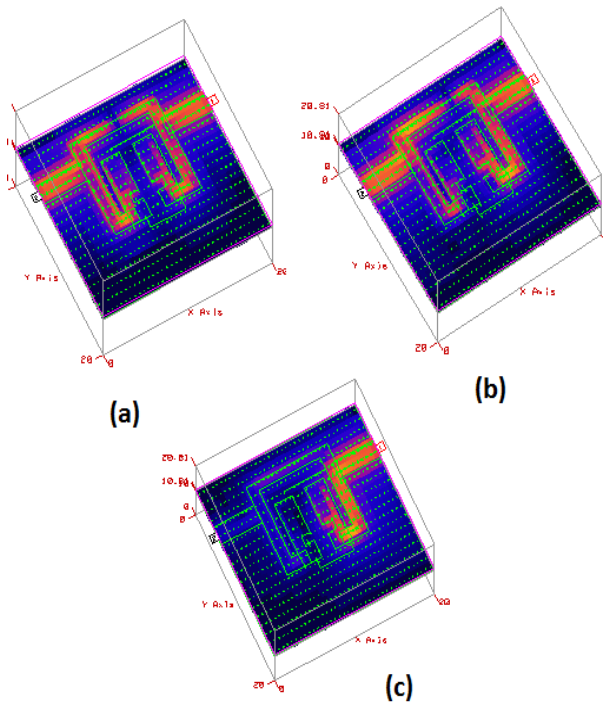

Fig. 3. Elcetric field distribution results in the double microstrip ring resnator: (a) passband at 1.8 GHz, (b) passband at 5 GHz, and (c) reject band at 2.3 GHz.

III. SIMULATETED RESULTS AND DISCUSSIONS

The dual-band performance in our reported filter can be introduced by coupling the before designed dual-band resonator to be as shown in Fig. 4. This structure acts as a coupled line bandpass filter with two possible bandpass. The first band is around 2 GHz due to the first resonator loop, whereas the second one is around 6 GHz as a result of the second resonator loop.

To enhance the attenuation between the two passbands, a two pairs of H-DGS cells are etched under feed lines. The H-DGS is functioned as a notch stopband pass filter. By adjusting its center frequency to be around 2.5 GHz, this can improve stopband rejection after the first passband without affecting the center frequency and insertion loss of basic filter passbands. To confirm our design methodology, the proposed filter as in Fig. 4, is simulated and its scattering parameters are shown in Fig. 5 which confirms the dual passband filter performance at 2 GHz and 6 GHz with 2.5 GHz attenuation up to 50 dB.

Fig. 4. 3-D model of the proposed dual-band bandpass filter.

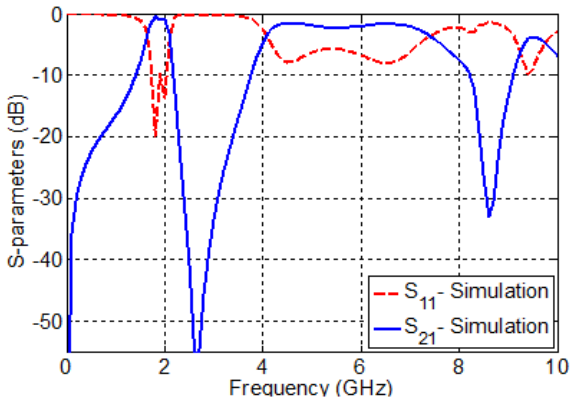

Fig. 5. The simulated S-parameters results of the proposed dual-band bandpass filter.

The function of the introduced H-DGS is examined by comparing the field profile at 1.8 GHz and 2.5 GHz as shown in Fig. 6. It is quite clear that at 1.8 GHz, the passband field is from port 1 to port 2. On the other hand, at 2.5 GHz, the field can reach the middle of the filter and dies there where the H-DGS is inserted. From the results shown in Fig. 5, we can claim that the second passband has a poor passband compared to the first one. This can be as a result of the position of the feeding transmission line as shown in Fig. 7. The filter scattering parameters magnitudes are examined for different (t) values and its insertion loss and return loss are depicted in Fig. 8. As shown in the figure, the first passband is not affected by changing the value of (t). On the other hand, the second passband insertion loss level can be enhanced by changing the value of (t). For t = 0, the first passband has almost 0 dB insertion loss and the second passband demonstrates almost flat insertion loss with a 1 dB average value.

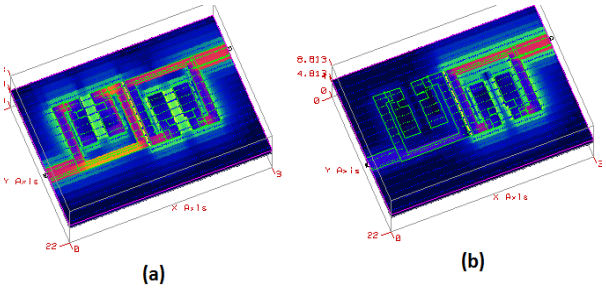

Fig. 6. Elcetric field distribution results in the proposed dual-band bandpass filter: (a) passband at 1.8 GHz, and (b) reject band at 2.5 GHz.

Fig. 7. 2-D layout of the proposed dual-band bandpass filter at different value of (t).

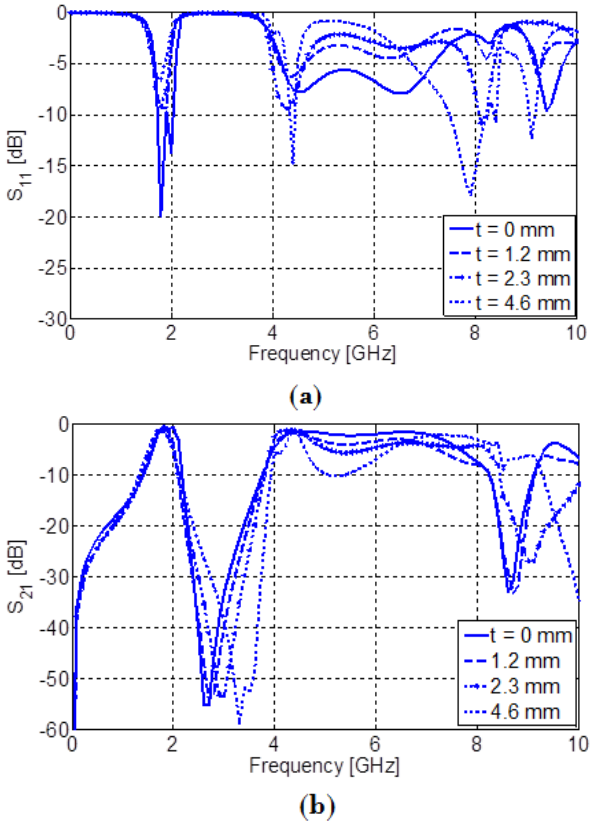

Fig. 8. Parametric study of the proposed dual-band bandpass filter at different value of (t): (a) return loss, and (b) insertion loss.

IV. EXPEREMENTAL RESULTS

The proposed dual-band bandpass filter has been fabricated using substrate Rogers RO4003 with dielectric constant of 3.38, a thickness of 0.813 mm and a dielectric loss tangent (δ) = 0.0027. The feeding microstrip line width is equal to 2 mm to have a characteristic impedance of 50 Ω.

The photograph of the fabricated dual-band filter is illustrated in Fig. 9. From Fig. 9 (a) is the top view of the proposed filter, it is clear that the filter consists of two mixed coupled microstrip double-ring resonators. On the other hand, from Fig. 9 (b), it is obvious that there are two electrically coupled H-cells DGS resonators, which is used to enhance the stopband rejection of the filter.

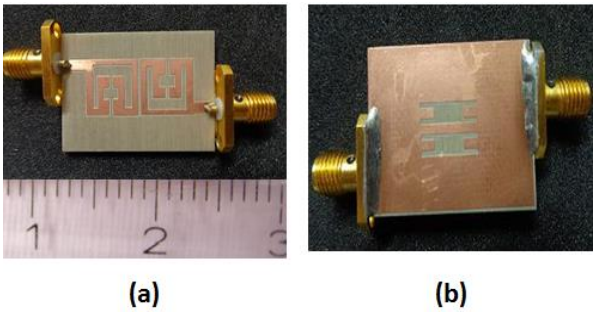

Fig. 9. Photograph of the fabricated dual-band bandpass filter: (a) top view, and (b) bottom view.

The fabricated filter is tested and measured using HP8722D network analyzer and the results are demonstrated in Fig. 10. From Fig. 10, it is seen that from the insertion loss result the proposed filter has dual frequency band from 1.6 GHz to 2 GHz and the other from 3.6 GHz to 5.5 GHz. The filter has high stopband rejection from 2.3 GHz to 3.5 GHz, this stopband is achieved using the H-Shaped DGS resonators.

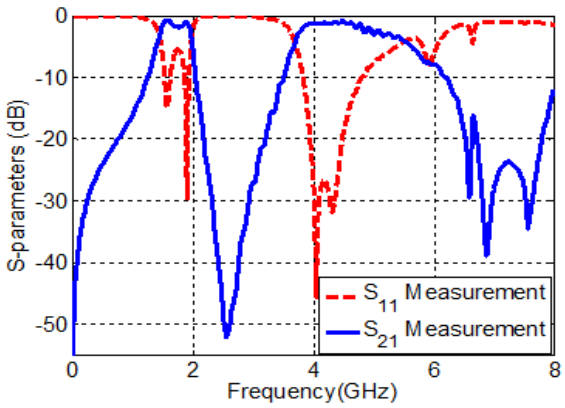

Fig. 10. Measured S-parameters of the proposed dual-band bandpass filter.

Finally it is claimed that there is good agreement achieved between the simulated and measured results. However, there is slightly deviation between the simulated and experimental results which can be observed. This can be caused by the usual connectors and manufacturing errors or by the undesired DGS radiations.

V. CONCLUSION

A design of dual-band bandpass filter using ring resonator and H-defected ground has been introduced. The optimized bandpass filter is designed and realized using mixed coupled microstrip double-ring resonators and two electrically coupled H-cells DGS resonators. The final two pole Chebyshev DGS microstrip filter obtained has been simulated and fabricated. Two passbands from 1.6 GHz to 2.0 GHz L-band applications and from 3.6 GHz to 5.5 GHz C-band applications have been achieved. The out-band rejection between both passbands is better than 20 dB from 2.2 GHz to 3.3 GHz. The proposed structure occupies an area of ($0.45\lambda g \times 0.35\lambda g$) with $\lambda g = 0.044$ m. Good agreement between the simulated and measured results has been achieved.

ACKNOWLEDGMENT

This work was financially supported by the Deutsche Foschungsgemeinschaft (DFG). The authors wish to thank the German Research Foundation for making this project possible and to thank Eng. Sonja Boutejdar for her substantial help and steadfast moral support.

REFERENCES

[1] A. Boutejdar, A. Darwish, and A. Omar, "Design and improvement of compact half-wavelength band pass filter employing overlapped slotted ground structure (SGS) and multilayer technique," *ACES Journal - The Applied Computational Electromagnetics Society*, vol. 28, no. 8, 2013.

[2] L. Yang, Y. Hongchun, W. Yawei, and X. Shaoqiu, "Ultra-wideband bandpass filter based on parallel-coupled microstrip lines and defected ground structure," *ACES Journal - The Applied Computational Electromagnetics Society*, vol. 28, no. 1, 2013.

[3] A. Boutejdar, "Design of broad-stop band low pass filter using a novel quasi-Yagi-DGS-resonators and metal box-technique," *Microwave and Optical Technology Letters*, vol. 56, no. 3, pp. 523-528, 2014.

[4] B. Wu, B. Li, and C. H. Liang, "Design of lowpass filter using a novel split-ring resonator defected ground structure," *Microwave and Optical Technology Letters*, vol. 49, pp. 288-291, 2007.

[5] A. Boutejdar, A. Elsherbini, A. Balalem, J. Machac, and A. Omar, "Design of new DGS hairpin microstrip bandpass filter using coupling matrix method," *PIERS Proceedings Prague*, Czech Republic, Aug. 2007.

[6] M. A. Abdalla and A. A. Ibrahim, "Compact and closely spaced meta-material MIMO antenna with high isolation for wireless applications," *IEEE Wireless Propagation Letter*, vol. 12, pp. 1452-1455, 2013.

[7] A. Boutejdar, M. Makkey, A. Elsherbini, and A. Omar "Design of compact stop-band extended microstrip low-pass filters by employing mutual coupled square shaped defected ground structures," *Microw. Opt. Technol. Lett.*, vol. 50, iss. 4, pp. 1107-1111, Apr. 2008.

[8] X. Wang, B. Wang, H. Zhang, and K. J. Chen, "A tunable bandstop resonator based on a compact slotted ground structure," *IEEE Trans. Microw. Theory Tech.*, vol. 55, no. 9, pp. 1912-1917, Sep. 2007.

[9] M. Al Sharkawy, A. Boutejdar, F. Alhefnawi, and O. Luxor, "Improvement of compactness of lowpass/ bandpass filter using a new electromagnetic coupled crescent defected ground structure (DGS) resonators," *ACES Journal - The Applied Computational Electromagnetics Society*, vol. 25, no. 9, 2010.

[10] A. Boutejdar, M. Challal, and A. Azrar," A novel band-stop filter using octagonal-shaped patterned ground structures along with interdigital and compensated capacitors," *ACES Journal - The Applied Computational Electromagnetics Society*, vol. 26, no. 4, 2011.

[11] A. Faraghi, M. Azarmanesh, and M. Ojaroudi, "Small microstrip low-pass filter by using novel defected ground structure for UWB applications," *ACES Journal - The Applied Computational Electromagnetics Society*, vol. 28, no. 4, 2013.

[12] L.-C. Tsai and C.-W. Huse, "Dual-band bandpass filters using equal-length coupled-serial-shunted lines and Z-transform techniques," *IEEE Trans. Microw. Theory Tech.*, vol. 52, no. 4, pp. 1111-1117, 2004.

[13] X.-H. Wang and B.-Z. Wang, "Compact broadband dual-band bandpass filters using slotted ground structures," *Progress in Electromagnetics Research, PIER*, vol. 82, pp. 151-166, 2008.

Ahmed Boutejdar was born in Souk El-Arbaa du Gharb, Marocco. He received the Diploma (Licence) in Mathematics, Physics and Chemistry from Morocco in 1994 and in Technische Hochschule Köthen in 1997. From 1995 to 1997 Preparatory Year of German Language and Preparatory Year of Engineering High School in köthen, Germany. B.Sc. and Dipl.-Eng. Degree with summa cum laude in Electrical Engineering, Communication, and Microwave Engineering from Otto-von-Guericke University of Magdeburg, Germany in 2002 and 2004 respectively, and he received his Ph.D. degree with summa cum laude in 2010 from the Department of Communication and High Frequency-Technique from the University of Magdeburg. His research interests include the design and analysis of microstrip filters, design and modeling of microstrip UWB-antennas, reconfigurable patch-antennas, DMS-filters/antennas and tunable DGS-DMS-filters using MEMS-technology and magnetics electromagnetic field theory.

Boutejdar has authored over 140 papers in technical journals and international conferences. His papers have more than 480 citations with Scopus h-index of 13 and has presented 30 articles in the international scientific congresses. He is serving as Reviewer and as a Technical Committee Member of several prestigious international journals and for Peer International Conference on Microwave and Millimeter Wave Technology. He is Reviewer of the IEEE Microwave and Wireless Components Letters (MWCL). He is Reviewer of the IEEE Transaction on Electromagnetic Compatibility (IEEE EMC). He is Reviewer of Applied Computational Electromagnetics Society Journal (ACES). He is Reviewer of the Journal of Microwaves, Optoelectronics and Electromagnetic Applications (JMOe). He is Reviewer of the Progress in Electromagnetics Research Symposium (PIERS). He is Reviewer of the Recent Patents on Electrical Engineering-journal (EENG).

Ahmed A. Ibrahim was born in 1986. He received the B.Sc. degree, with grade of very good, in Electrical Engineering from the Electronic and Communication Engineering Department, Elminia University, Elminia, Egypt in 2007. He was awarded the M.Sc. degree in Electronic and Communication Engineering from Elminia University in 2011 and the Ph.D. degree from Electronic and Communication Engineering from Elminia University in 2014.

Edmund P. Burte was born in Bayreuth, Germany. He received the M.Sc. (Mathematics & Physics) and Doktor-Ing. degrees in Material Science in 1979, and 1984, respectively. From October 1984 to June 1988 he was Head of Laboratory and Debuty Head of the department of the business unit development of the Semikron International in Nuremberg, Germany. From July 1988 to December 1998 he headed the Department Technology of the Fraunhofer-Institute for Integrated Circuits, Semiconductor Devices, Erlangen, Germany. Burte is a Full Professor for Semiconductor Technology at the Otto-von-Guericke University Magdeburg, Germany since April 1998

Nuri M. Mohamed was born in Sebha. He received the B.S. degree in Statistics form the Sebha University Faculty of Science and the M.S. and doctorate degrees from Otto-von-Guericke University of Magdeburg, Germany; from 2004 to 2011. Currently he is taking a German Course Level C1 in Jop.

Mahmoud A. Abdalla was born in 1973. He received the B.Sc. and M.Sc. degrees in Electrical Engineering from the Electronic Engineering Department, Military Technical College, Cairo, Egypt in 1995 and 2000 respectively, and the Ph.D. degree from Microwave and Communication Group, School of Electrical Engineering, Manchester University, UK, in 2008.

Resonant and Radiation Characteristics of Rectangular Microstrip Patch Antenna on Suspended-Composite Substrates

S. Bedra [1] and T. Fortaki [2]

[1] Department of Industrial Engineering
University of Khenchela, Khenchela, 40004, Algeria
bedra_sami@yahoo.fr

[2] Department of Electronics
Batna 2 University, Batna, 05000, Algeria

Abstract ─ In this paper, the resonance and radiation characteristics of rectangular microstrip patch printed on suspended and composite substrates are investigated theoretically. The analysis approach is based on the spectral-domain method of moments in conjunction with the stationary phase method. The complex resonant frequency of the microstrip antenna on suspended and composite substrates is studied with sinusoidal functions as basis functions, which show fast numerical convergence. Using a matrix representation of each layer, the far-field pattern of the suspended-composite configuration is efficiently determined by the (TM, TE) representation. The validity of the solution is tested by comparison of the computed results with experimental data. Finally, numerical results for the effects of suspended and composite substrates on the resonant frequency and half-power bandwidth are also presented.

Index Terms ─ Full-wave analysis, Galerkin method, microstrip patch, radiation pattern, suspended and composite layers.

I. INTRODUCTION

Due to their low profile, low weight, low cost and its ability of conforming to curve surfaces, conformal microstrip structures have witnessed enormous growth in the past few years [1-3]. Presently, there are many other government and commercial applications, such as mobile radio and wireless communications that have similar specifications. To meet these requirements, microstrip antennas can be used [4-5]. Since the bandwidth of microstrip antenna frequencies is very narrow [6], it is important to develop accurate algorithms for computation of those resonant frequencies [7].

The resonant frequency value of a microstrip patch antenna depends on the structural parameters and it is evident that if the resonant frequency is to be changed, a new antenna is needed. In order to achieve tunable resonant frequency characteristic, an adjustable air gap layer can be inserted between the ground plane and substrate, resulting in a two-layer structure. Using the magnetic wall cavity model, some efforts have been made to analyze microstrip antennas on suspended substrates [3, 8-10]. By means of an adjustable air gap, bandwidth enhancement is possible as a result of the lowered equivalent permittivity and the increased thickness of the structure. Therefore, a new structure having tunable properties is obtained for which a new resonant frequency formulation is required. The suspended substrate patch antenna is a special type of a patch antenna on the composite substrate [5]. In the previous literature, several researches have studied the characteristics of rectangular microstrip patch antenna with and without air gap [8-13]. Among them [9] theoretically and experimentally studied the effect of suspended substrate of the resonant frequency, but the effect of suspended substrate on the bandwidth of rectangular microstrip patch antenna was not investigated, also no results for the effects of the air gap on the radiation pattern were reported.

This paper, presents the extended spectral domain approach to study the effects of composite and suspended substrates on the resonant characteristics and radiation patterns of rectangular microstrip patch antenna.

II. PROBLEM FORMULATION

The rectangular microstrip patch antenna considered in this work is shown in Fig. 1. The antenna substrate consist of two dielectric layers (region I and II), having dielectric constant ε_{r1} and thickness d_1, and ε_{r2} and thickness d_2 respectively, and permeability μ_0 with optical axis normal to the patch. The region III is characterized by free space permeability μ_0 and permittivity ε_0. All fields and currents are time harmonic with $e^{j\omega t}$ time dependence suppressed. To simplify the analysis, the antenna feed will not be considered. The

Submitted On: October 28, 2013
Accepted On: February 24, 2016

rectangular patch is embedded in the stratification at the interface plane $z = z_p$. The transverse fields inside the composite substrate, can be obtained via the inverse vector Fourier transform as [7]:

$$\tilde{\mathbf{E}}(\mathbf{k}_s,z)=\begin{bmatrix}E_x(\mathbf{k}_s,z)\\E_y(\mathbf{k}_s,z)\end{bmatrix} = \frac{1}{4\pi^2}\int_{-\infty}^{+\infty}\int_{-\infty}^{+\infty}\bar{\mathbf{F}}(\mathbf{k}_s).\mathbf{e}(\mathbf{k}_s,z)\,dk_x\,dk_y, \quad (1)$$

$$\tilde{\mathbf{H}}(\mathbf{k}_s,z)=\begin{bmatrix}H_y(\mathbf{k}_s,z)\\-H_x(\mathbf{k}_s,z)\end{bmatrix} = \frac{1}{4\pi^2}\int_{-\infty}^{+\infty}\int_{-\infty}^{+\infty}\bar{\mathbf{F}}(\mathbf{k}_s).\mathbf{h}(\mathbf{k}_s,z)\,dk_x\,dk_y, \quad (2)$$

where $\bar{\mathbf{F}}(\mathbf{k}_s)$ is the kernel of the vector Fourier transform [7], and the superscripts *e* and *h* denote the *TM* and *TE* waves, respectively, and $\mathbf{k}_s = \hat{x}k_x + \hat{y}ky$ is the transverse vector wavenumber and $k_s = |\mathbf{k}_s|$:

$$\bar{\mathbf{F}}(\mathbf{k}_s)=\frac{1}{k_s}\begin{bmatrix}k_x & k_y\\k_y & -k_x\end{bmatrix}=\bar{\mathbf{F}}^{-1}(k_s), \quad (3)$$

$$\mathbf{e}(\mathbf{k}_s,z)=\begin{bmatrix}e^e(\mathbf{k}_s,z)\\e^h(\mathbf{k}_s,z)\end{bmatrix}=\bar{\mathbf{F}}(\mathbf{k}_s).\tilde{\mathbf{E}}(\mathbf{k}_s,z), \quad (4)$$

$$\mathbf{h}(\mathbf{k}_s,z)=\begin{bmatrix}h^e(\mathbf{k}_s,z)\\h^h(\mathbf{k}_s,z)\end{bmatrix}=\bar{\mathbf{F}}(\mathbf{k}_s)\cdot\tilde{\mathbf{H}}(\mathbf{k}_s,z). \quad (5)$$

The relation which related the currents $\bar{\mathbf{j}}(\mathbf{k}_s)$ on the conducting patch to the electric field in the corresponding interface ($z = z_p$) is given by:

$$\mathbf{e}(\mathbf{k}_s,z_p)=\bar{\mathbf{G}}(\mathbf{k}_s).\bar{\mathbf{j}}(\mathbf{k}_s), \quad (6)$$

where $\bar{\mathbf{G}}(\mathbf{k}_s)$ is the spectral dyadic Green's function in (TM, TE) representation, it is given by [7]:

$$\bar{\mathbf{G}}(\mathbf{k}_s)=diag\left[G^e,G^h\right]. \quad (7)$$

In the coordinate system (x, y) the dyadic Green's function $\bar{\mathbf{Q}}(\mathbf{k}_s)$ is defined by [7]:

$$\tilde{\mathbf{E}}=(\mathbf{k}_s,z_P)=\bar{\mathbf{Q}}(\mathbf{k}_s).\tilde{\mathbf{J}}(\mathbf{k}_s) = \begin{bmatrix}Q_{xx} & Q_{xy}\\Q_{yx} & Q_{yy}\end{bmatrix}.\tilde{\mathbf{J}}(\mathbf{k}_s). \quad (8)$$

Next, the Equation (8) is multiplied by $\tilde{\mathbf{F}}(\mathbf{k}_s)$. Thus, Equation (6) becomes:

$$\tilde{\mathbf{E}}(\mathbf{k}_s,z_P)=\bar{\mathbf{F}}(\mathbf{k}_s).\bar{\mathbf{G}}(\mathbf{k}_s).\bar{\mathbf{F}}(\mathbf{k}_s).\tilde{\mathbf{J}}(\mathbf{k}_s). \quad (9)$$

Comparing (8) with (9), we obtain the following relation between $\bar{\mathbf{Q}}(\mathbf{k}_s)$ and $\bar{\mathbf{G}}(\mathbf{k}_s)$:

$$\bar{\mathbf{Q}}(\mathbf{k}_s)=\bar{\mathbf{F}}(\mathbf{k}_s).\bar{\mathbf{G}}(\mathbf{k}_s).\bar{\mathbf{F}}(\mathbf{k}_s). \quad (10)$$

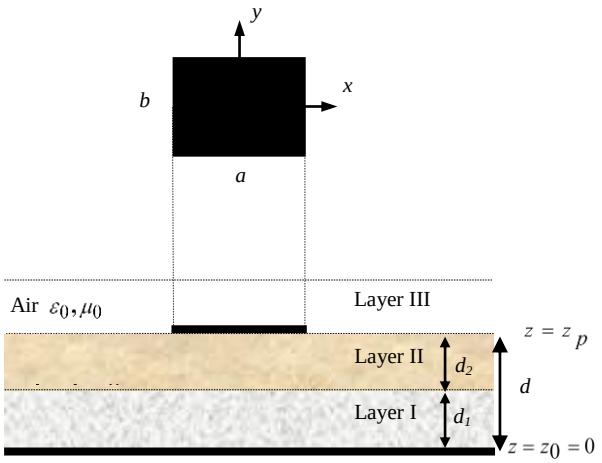

Fig. 1. Geometry of rectangular microstrip patch on suspended-composite substrates.

Now that we have the necessary Green's function, it is relatively straightforward to formulate the moment method solution for the antenna characteristics. The transverse electric field can be obtained from (8) via the inverse Fourier transform:

$$\mathbf{E}(x,y,z_p)=\frac{1}{4\pi^2}\int_{-\infty}^{+\infty}\int_{-\infty}^{+\infty}\bar{\mathbf{Q}}(\mathbf{k}_s)\cdot\tilde{\mathbf{J}}(\mathbf{k}_s)e^{(ik_xx+ik_yy)}dk_xdk_y. \quad (11)$$

Enforcement of the boundary condition requiring the transverse electric field of (11) to vanish on the perfectly conducting patch yields the sought integral equation:

$$\int_{-\infty}^{+\infty}\int_{-\infty}^{+\infty}\bar{\mathbf{Q}}(\mathbf{k}_s).\tilde{\mathbf{J}}(\mathbf{k}_s)e^{(ik_xx+ik_yy)}dk_xdk_y=\mathbf{0}. \quad (12)$$

The Galerkin moment method is implemented in the Fourier transform domain to reduce the integral Equation (12) to a matrix equation. The surface current J on the patch is expanded into a finite series of known basis function J_{xk} and J_{ym}:

$$\mathbf{J}(x,y)=\sum_{k=1}^{K}a_k\begin{bmatrix}J_{xk}(x,y)\\0\end{bmatrix}+\sum_{m=1}^{M}b_m\begin{bmatrix}0\\J_{ym}(x,y)\end{bmatrix}, \quad (13)$$

where a_k and b_m are the mode expansion coefficients to be sought. Substituting the Fourier transform of (13) into (12). Next, the resulting equation is tested by the same set of basis functions that was used in the expansion of the patch current. Thus, the integral Equation (12) is discretized into the matrix equation:

$$\begin{bmatrix} \left(\overline{\mathbf{Z}}^{11}\right)_{K\times K} & \left(\overline{\mathbf{Z}}^{12}\right)_{K\times M} \\ \left(\overline{\mathbf{Z}}^{21}\right)_{M\times K} & \left(\overline{\mathbf{Z}}^{22}\right)_{M\times M} \end{bmatrix} \cdot \begin{bmatrix} (\mathbf{a})_{K\times 1} \\ (\mathbf{b})_{M\times 1} \end{bmatrix} = \mathbf{0}, \quad (14)$$

where

$$\left(\overline{\mathbf{Z}}^{11}\right)_{qk} = \int_{-\infty}^{+\infty}\int_{-\infty}^{+\infty} Q_{xx}\, \tilde{J}_{x\,q}(-\mathbf{k}_s)\tilde{J}_{x\,k}(\mathbf{k}_s)\, dk_x dk_y, \quad (15)$$

$$\left(\overline{\mathbf{Z}}^{12}\right)_{qm} = \int_{-\infty}^{+\infty}\int_{-\infty}^{+\infty} Q_{xy}\, \tilde{J}_{x\,q}(-\mathbf{k}_s)\tilde{J}_{y\,m}(\mathbf{k}_s)\, dk_x dk_y, \quad (16)$$

$$\left(\overline{\mathbf{Z}}^{21}\right)_{lk} = \int_{-\infty}^{+\infty}\int_{-\infty}^{+\infty} Q_{yx}\, \tilde{J}_{y\,l}(-\mathbf{k}_s)\tilde{J}_{x\,k}(\mathbf{k}_s)\, dk_x dk_y, \quad (17)$$

$$\left(\overline{\mathbf{Z}}^{22}\right)_{lm} = \int_{-\infty}^{+\infty}\int_{-\infty}^{+\infty} Q_{yy}\, \tilde{J}_{y\,l}(-\mathbf{k}_s)\tilde{J}_{y\,m}(\mathbf{k}_s)\, dk_x dk_y. \quad (18)$$

The existence of non-trivial solution of (14) requires that:

$$\det(\overline{\mathbf{Z}}(f)) = 0, \quad (19)$$

where $\overline{\mathbf{Z}}$ is the matrix in (14). Equation (19) is the characteristic equation for the complex resonant frequency $f = f_r + \mathrm{i}f_i$ of the generalized microstrip structure illustrated in Fig. 1. f_r is the resonant frequency and $2f_i/f_r$ is the half-power bandwidth of the structure.

Once the complex resonant frequency is determined, the eigenvector corresponding to the minimal eigenvalue of the impedance matrix gives the coefficients of the current on the rectangular patch. The current density is thus obtained in numerical form. This current density can be used for computing the radiation electric field in the region $z \geq d$ of Fig. 1. Using the stationary phase method [7], we can obtain the far-field pattern function on the upper air half-space of Fig. 1 in terms of the transverse electric field at the plane $z = d$ as follows:

$$\begin{bmatrix} \mathbf{E}_{\theta'}(r',\theta',\phi') \\ \mathbf{E}_{\phi'}(r',\theta',\phi') \end{bmatrix} = \mathrm{i}k_0 \frac{e^{-\mathrm{i}k_0 r'}}{2\pi r'} \underbrace{\begin{bmatrix} -1 & 0 \\ 0 & \cos\theta' \end{bmatrix}}_{\mathbf{e}(\mathbf{k}_s, d)}, \quad (20)$$

where $\{r', \theta', \phi'\}$ is a local set of spherical coordinates defined with respect to the Cartesian system $\{x' \equiv x, y' \equiv y, z' \equiv z\}$ with an origin placed at the plane $z = d$ of Fig. 1.

III. RESULTS AND DISCUSSION

In this section, typical numerical results for the resonant frequencies, bandwidth and radiation patterns of rectangular patch on composite, suspended and single substrates. Although the full-wave analysis described in the previous section can give results for several resonant modes [7], only results for the TM01 mode are suggested in this paper. In order to determine the most appropriate suggestion given in the literature, we compared our computed values of the resonant frequencies and half power bandwidth of rectangular patch on single substrate with the theoretical and experimental results reported by another scientists, all which are given in Table 1 and 2. The convergence of the extended formulation of the spectral domain approach is checked by comparing our results with experimental and theoretical data available in open literature. These comparisons show that an extra improvement is obtained on the results of the previous works. Numerical results are presented for different configurations of rectangular microstrip patch antenna and compared to data available in the literature. The radiation pattern of rectangular microstrip patch antenna of suspended-composite substrates is also investigated.

The bandwidths of single layer of rectangular microstrip patch for the fundamental mode TM_{01}, computed by the present approach are depicted in Table 1. It is clear from Table 1 that, the calculated results bandwidths from the present approach are very close to experimental and theoretical values [13, 14].

In Table 2, we have compared our computed resonant frequencies values with theoretical and experimental values [9] available in the open literature for a rectangular patch without air gap layer having different parameters of antenna. The results of our approach show good consistency with both experimental and theoretical values.

Table 1: Comparison of measured and calculated bandwidth of rectangular microstrip patch antenna on single substrate, $\varepsilon_{r2} = 2.55$

Input Parameters (mm)			Bandwidth *BW* (%)		
			Measured	Calculated	
a	*b*	d_2	[13]	[14]	Present
7.76	10.8	3.3	17.50	18.48	13.10
9.87	14.5	4.5	17.90	19.17	13.18
9.74	26.20	9.52	20.60	27.17	25.7

Table 2: Comparison of calculation and measured resonant frequencies for rectangular microstrip antenna on single substrate

Input Parameters				Resonant Frequency f_r^{01} (GHz)		
				Measured	Calculated	
a (mm)	*b* (mm)	d_2 (mm)	ε_r	[15]	[9]	Present
30	20	1.27	10.2	2.26	2.29	2.29
29.83	19	2.54	10.2	2.18	2.32	2.33
40	25	0.79	2.22	3.92	3.93	3.91

In Table 3, effects of air gap layer on the resonant frequencies have been tabulated for various thickness of air gap layer. This can be obtained by having $d_1 = 0$, and $\varepsilon_{r1} = 1$.

Table 3: Computed values of resonant frequency of rectangular microstrip patch with different air gap heights, $\varepsilon_{r2} = 2.33$, $d_2 = 1.575$ mm, $a = b = 30$ mm

Air Gap Thickness d_1 (mm)	Resonant Frequency f_r^{01} (GHz)		
	Calculated [9]	Simulated [9]	Present
0	3.11	3.10	3.13
1	3.58	3.51	3.61
2	3.64	3.50	3.68

The results of the present approach show the closest agreement with calculated and simulated values [9]. In order to observe the effects suspended and composite substrates on the resonant frequencies, bandwidth and radiation pattern of rectangular microstrip antenna shown in Fig. 1, some results are presented and investigated in this section. The effect of the composite substrate to the resonance frequency and the bandwidth of the rectangular microstrip antenna are studied. In Fig. 2, we present results for resonant frequencies versus the variation of thickness d_2 of layer II of a rectangular microstrip patch on suspended-composite substrates. It is observed that the resonant frequency is increased for a composite substrate and deceased for a suspended substrate with the increase of d_2. The effect of the suspended-composite substrate to the half-power bandwidth is shown in Fig. 3. Note that the bandwidth of rectangular microstrip patch antenna increased for composite and suspended substrates, substrate with increase of d_2.

We show in Fig. 4 the equivalent relative permittivity of the composite two-layer structure, computed from [16], Equation (21), versus air separation for the structures considered in Fig. 4.

It is seen that when d_2 increases, the equivalent relative permittivity decreases rapidly for composite substrate, and increases for suspended substrate.

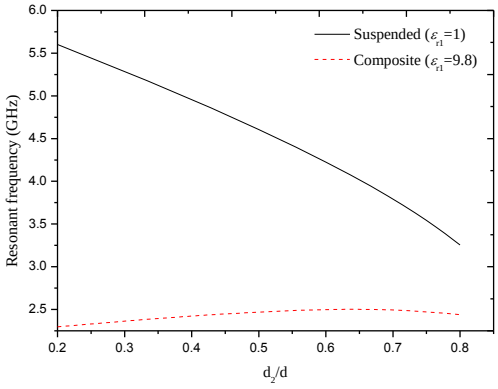

Fig. 2. Variation of the resonant frequency on suspended-composite substrates with the variation of thickness of layer II; ($d_1 = 1.27$ mm, $a = 27$ mm, $b = 22$ mm, $\varepsilon_{r2} = 5.4$).

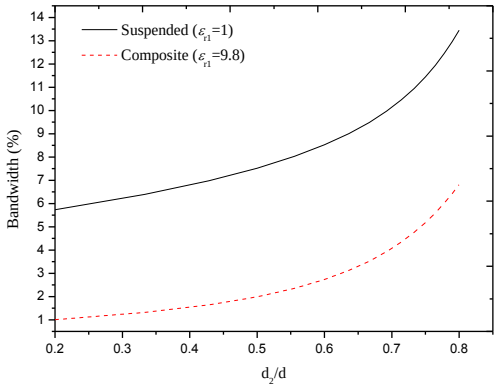

Fig. 3. Variation of the half-power bandwidth on suspended-composite substrates with different thicknesses of layer II, (parameters as in Fig. 2).

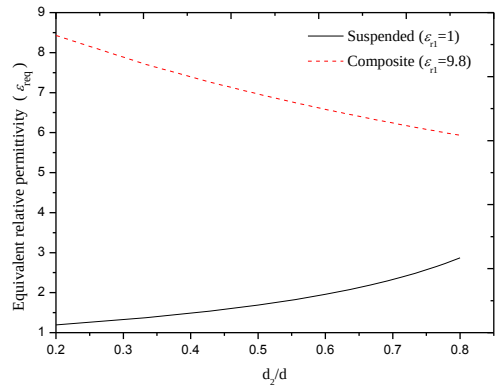

Fig. 4. Variation equivalent relative permittivity on suspended-composite substrates with different thicknesses of layer II, (parameters as in Fig. 2).

This observation can well justify the very fast decrease in the resonant frequency shown in Fig. 2. These behaviors agree with those discovered theoretically for resonant frequency and bandwidth of triangular and circular patch antenna [5, 16].

The radiation pattern of rectangular patch printed on suspended and composite substrates is investigated using the analytical technique explained in the previous section. In Figs. 5 (a) and 5 (b), we plot the variation of the normalized radiation pattern in the E-plane ($\phi = 0$) and H-plane ($\phi = \pi/2$), respectively, as function of permittivity and thickness of substrate in region II.

The three cases of single, suspended, and composite substrates are illustrated. From the results in Fig. 5 (a), it is seen that the E-plane radiation pattern is insensitive to the variation of thickness (d_2) of substrate in region II. However, the H-plane pattern show in Fig. 5 (b) exhibits important decreases (increases if $\varepsilon_{r1} = 9.8$) with increasing thickness (d_2) of substrate in region II. Thus, the directivity of the antenna increases (decreases

if $\varepsilon_{r1} = 9.8$) with the thickness (d_2) of substrate in region II.

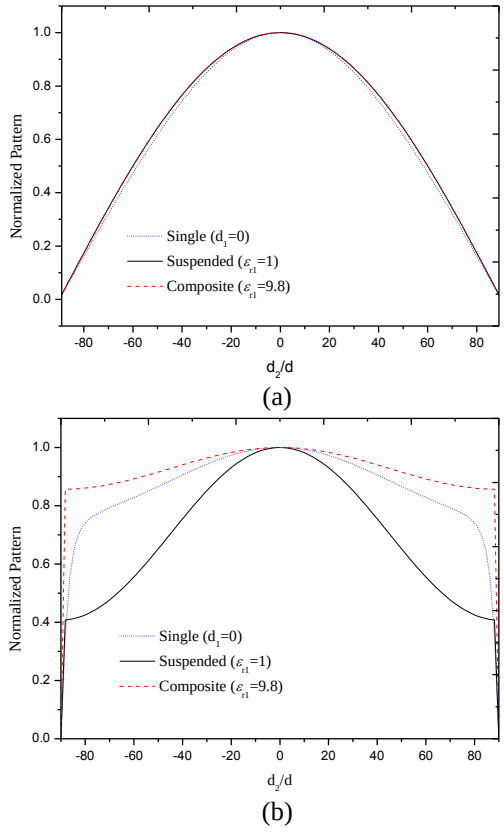

Fig. 5. Normalized radiation pattern of rectangular microstrip antennas for various configurations in the E-plane (a) and H-plane (b); a = 27 mm, b = 22 mm, d_2 = 1.27 mm, d_1 = 1.27 mm, ε_{r2} = 5.4.

To explain these results, we determine an equivalent permittivity of the composite two-layer structure by first deriving a simple approximate formula for the resonant frequency. Using (7), the spectral dyadic Green's function of the composite two-layer structure shown in Fig. 1, when d_1 and d_2 are quite thin electrically, takes the form [7]:

$$\overline{\mathbf{G}}(\mathbf{k}_s) \underset{d_1+d_2\to 0}{\to} diag\left[G^e, G^h\right]$$

$$\overline{\mathbf{G}}(\mathbf{k}_s) \underset{d_1+d_2\to 0}{\to} diag\left[k_0^2 - \frac{\varepsilon_{r1}\cdot\varepsilon_{r2}\cdot(d_1+d_2)}{\varepsilon_{r1}\cdot d_2 + \varepsilon_{r2}\cdot d_1} k_s^2, k_0^2\right] \quad (21)$$

The basis functions for the following numerical calculations are selected to be sinusoidal functions of:

$$J_{xk}(x,y) = \sin\left[\frac{k_1\pi}{a}(x+\frac{a}{2})\right] + \cos\left[\frac{k_2\pi}{b}(y+\frac{b}{2})\right], \quad (22)$$

$$J_{xk}(x,y) = \cos\left[\frac{m_1\pi}{a}(x+\frac{a}{2})\right] + \sin\left[\frac{m_2\pi}{b}(y+\frac{b}{2})\right]. \quad (23)$$

Because one sinusoidal basis function in the y direction is sufficient to give excellent convergent results, the characteristic Equation (19) reduces to:

$$\int_{-\infty}^{+\infty}\int_{-\infty}^{+\infty} \overline{\mathbf{Q}}_{yy}\tilde{\mathbf{J}}_{y1}(-\mathbf{k}_s)\,\tilde{\mathbf{J}}_{y1}(\mathbf{k}_s)\,dk_x dk_y = \mathbf{0}. \quad (24)$$

The function J_{y1} corresponds to (m_1, m_2) = (0, 1) in (23). It possesses closed-form Fourier transform, given by:

$$\tilde{J}_{y1}(\mathbf{k}_s) = \pi b \frac{\sin(k_x a/2)}{k_x} \frac{\cos(k_y b/2)}{(\pi/2)^2 - (k_y b/2)^2}. \quad (25)$$

Using the asymptotic expression of $\boldsymbol{G}$ given by Eq. (21) together with Eq. (10) and Eq. (25), and after performing some algebraic operations, Equation (24) reduces to:

$$\varepsilon_{r1}\cdot\varepsilon_{r2}\cdot(d_1+d_2)b^2k_0^2 I_1 - 4(\varepsilon_{r1}\cdot d_2 + \varepsilon_{r2}\cdot d) I_2 = 0, \quad (26)$$

where

$$I_1 = \int_0^\infty \frac{\cos^2 k_y}{\left(k_y^2 - (\pi/2)^2\right)^2 - \left(k_y b/2\right)^2} dk_y,$$

$$I_2 = \int_0^\infty \frac{k_y^2 \cos^2 k_y}{\left(k_y^2 - (\pi/2)^2\right)^2 - \left(k_y b/2\right)^2} dk_y. \quad (27)$$

Using contour integration, the integrals in Eq. (27) can be evaluated explicitly giving $I_1 = 1/\pi$ and $I_2 = \pi/4$. On using the values of I_1 and I_2 in Eq. (26), we obtain the following expression for the resonant frequency:

$$f_r = \frac{C}{\left(2b\sqrt{\varepsilon_{req}}\right)}, \quad (28)$$

where C is the velocity of light in free space, and ε_{req} is the equivalent relative permittivity of the composite two-layer structure given by:

$$\varepsilon_{req} = \frac{\varepsilon_{r1}\cdot\varepsilon_{r2}\cdot(d_1+d_2)}{\varepsilon_{r1}\cdot d_2 + \varepsilon_{r2}\cdot d_1}. \quad (29)$$

IV. CONCLUSION

In this paper, a full-wave analysis has been applied to investigate the effect of suspended and composite substrates on the radiation pattern of a rectangular microstrip antenna. The spectral-domain integral equations in conjunction with stationary phase method have been used to calculate the complex resonant frequency and radiation pattern of various antenna structures. In order to test the validity of the analysis, the numerical results obtained via Galerkin's method in the Fourier transform domain have been compared with theoretical and experimental data, and good agreement has been found. Numerical results show that the resonant frequency is increased, for suspended substrate and decreases for composite substrate, so the air separation can be adjusted to have a maximum operation frequency of the antenna.

The bandwidth, on other hand, decreases for composite, and the bandwidth is increased for suspended substrate, the E-plane radiation pattern is significantly affected, so that an enhancement in the directive gain of the antenna is achieved. The present approach is also well suited for single substrate. No experimental and theoretical values are available for a rectangular patch printed on composite substrate, only the theoretical results of suspended substrate are compared with experimental data. Note that, the theoretical results of rectangular patch microstrip antenna need to be further validated with experimental works.

REFERENCES

[1] R. Bedra, S. Bedra, S. Benkouda, and T. Fortaki, "Efficient full-wave analysis of resonant modes of circular microstrip antenna printed on isotropic or uniaxially anisotropic substrate," *Wireless Personal Communications*, vol. 81, no. 1, pp. 239-251, 2015.

[2] S. Bedra, R. Bedra, S. Benkouda, and T. Fortaki, "Efficient full-wave analysis of inverted circular microstrip antenna," *Microwave and Optical Technology Letters*, vol. 56, no. 10, pp. 2422-2425, 2014.

[3] S. Chattopadhyay, M. Biswas, J. Y. Siddiqui, and D. Guha, "Rectangular microstrips with variable air gap and varying aspect ratio: improved formulations and experiments," *Microwave and Optical Technology Letters*, vol. 51, no. 1, pp. 169-173, 2009.

[4] S. Bedra, R. Bedra, S. Benkouda, and T. Fortaki, "Full-wave analysis of anisotropic circular microstrip antenna with air gap layer," *Progress In Electromagnetics Research M*, vol. 34, pp. 143-151, 2014.

[5] M. Biswas and M. Dam, "Characteristics of equilateral triangular patch antenna on suspended and composite substrates," *Electromagnetics*, vol. 33, no. 2, pp. 99-115, 2013.

[6] V. Losada, R. R. Boix, and M. Horn, "Resonant modes of circular microstrip patches in multilayered substrate," *IEEE Trans. Antennas Propagat*., vol. 47, no. 4, pp. 488-497, 1999.

[7] T. Fortaki, D. Khedrouche, F. Bouttout, and A. Benghalia, "A numerically efficient full-wave analysis of a tunable rectangular microstrip patch," *International Journal of Electronics*, vol. 91, no. 1, pp. 57-70, 2004.

[8] F. Abboud, J. P. Damino, and A. Papiernik, "Accurate model for the input impedance of coax-fed rectangular microstrip antenna with and without air gaps," *Proc. Int. Conf. Antennas Propag*., pp. 102-106, 1989.

[9] S. Chattopadhyay, M. J. Biswas, Y. Siddiqui, and D. Guha, "Input impedance of probe-fed rectangular microstrip antennas with variable air gap and varying aspect ratio," *IET Microw. Antennas Propag*., vol. 3, no. 8, pp. 1151-1156, 2009.

[10] H. I. Kang and J. T. Song, "Electrically tunable rectangular microstrip antenna," *Electron. Lett.*, vol. 46, no. 1, pp. 18-19, 2009.

[11] I. Wolff and N. Knoppik, "Rectangular and circular microstrip disk capacitors and resonators," *IEEE Trans. Microwave Theory Tech*., vol. 22, no. 10, pp. 857-864, 1974.

[12] E. Chang, S. A. Long, and W. F. Richards, "Experimental investigation of electrically thick rectangular microstrip antennas," *IEEE Trans. Antennas Propag*., vol. 34, no. 6, pp. 767-772, 1986.

[13] M. Kara, "A novel technique to calculate the bandwidth of rectangular microstrip antenna elements with thick substrates," *Microwave and Optical Technology Letters*, vol. 12, no. 2, pp. 59-64, 1996.

[14] I. J. Bahl and P. Bhartia, *Microstrip Antennas*, Artech House, Canton, MA, 1980.

[15] D. Schaubert, D. Pozar, and A. Adrian, "Effect of microstrip antenna substrate thickness and permittivity: comparison of theories and experiment," *IEEE Trans. Antennas Propag.*, vol. 37, no. 6, pp. 677-682, 1989.

[16] N. Nasimuddin, K. Esselle, and A. K. Verma, "Fast and accurate model for circular microstrip antennas on suspended and composite substrates," *IEEE Trans. Antennas Propag*., vol. 53, no. 9, pp. 3097-3100, 2005.

Combined PSO-FDFD Optimization of Rectangular Ridged Waveguides

Marco Simone, Alessandro Fanti, Giorgio Montisci, Giovanni Andrea Casula, and Giuseppe Mazzarella

Dipartimento di Ingegneria Elettrica ed Elettronica
Università di Cagliari, Cagliari, Italy
marco.simone@diee.unica.it, alessandro.fanti@diee.unica.it, giorgio.montisci@unica.it, a.casula@diee.unica.it, mazzarella@diee.unica.it

Abstract ─ Finite-difference frequency-domain technique in conjunction with the particle swarm optimization algorithm is presented as an effective procedure for ridged waveguides design optimization. A suitable objective function is furthermore able to deal with the conflicting requirements of wide bandwidth and high power handling capability. Different configurations have been analyzed, and the influence of the algorithm parameters on the optimized structure has been investigated.

Index Terms ─ Cutoff frequency, finite-difference frequency-domain, microwave components, microwave filters, optimization, PSO, ridged waveguides, waveguide modes.

I. INTRODUCTION

In RF engineering, a large number of applications require very intense fields, thus devices with high power handling capabilities and low losses are required. Metallic hollow waveguides (WGs) represent the structures more suitable to satisfy such strict requirements. WG modal propagation is high-pass and dispersive [1], so WGs can be used only in the frequency range characterized by single-mode propagation. Such a useful bandwidth (BW) is relatively narrow. Ridged waveguide (R-WG) structures have been proposed to increase significantly the BW, retaining all the useful WG properties [2].

The first approach to the electromagnetic analysis of rectangular R-WG [3,4] is the transverse resonance technique (TRT) [5]. TRT is able to compute, in an approximate way, the cut-off frequencies of the first few modes of a R-WG and their attenuation. Moreover, Hopfer [4] was able to compute also the power handling capability (PHC) taking also into account, in an approximate way, the singular behaviour of the field at the wedges.

Despite of the reduced accuracy, TRT is still a useful tool for the "back-to-envelope" evaluation of the cut-off frequency of the fundamental mode [6]. But, of course, numerical techniques such as finite-difference frequency-domain (FDFD) [7] or finite element method (FEM) [8] allow to compute the cut-off frequencies and the modal distribution of a R-WG with a far better accuracy. On the other hand, the accuracy of TRT is sufficient to compute the PHC of a R-WG [4].

In practical applications, the increase in BW comes together with a reduced PHC of R-WGs which can limit their use. In other words, we have to deal with two conflicting requirements. Suitable optimization procedures are therefore needed in order to obtain an effective trade-off. Such procedures are based on a synergic work of a time-effective EM analysis program of the structure and of a suitable optimization algorithm.

In this work, an effective in-house FDFD-TRT procedure has been developed to compute eigenvalues, mode distribution and PHC of different R-WG configurations, whereas the optimization problem has been solved by using the particle swarm optimization (PSO) algorithm. In the following section the procedure is described in detail.

We have considered different ridged configurations with different design specifications, extending therefore the results presented in [9].

II. FDFD

The R-WG analysis procedure is realized using a FDFD strategy [7], which can be applied both to scalar [10]-[12] and vector [13] problems. As a matter of fact, the FDFD approach, namely the direct discretization of the differential eigenvalue problem, is the simplest numerical strategy to compute eigenvalues and modes of metallic hollow WGs [14]. Therefore, it is well tailored to be used in PSO, but it is useful also in the procedures based on method of moments (MoM) [15]-[16] or mode-matching (MM) [17]. The WG section is partitioned in a set of regular discretization cells, and the differential eigenvalue problem [18] is replaced by a finite difference one, using suitable Taylor approximations of second [7] or fourth [19] order. The standard FDFD approach, using two Cartesian sampling grids (one for

Submitted On: October 15, 2014
Accepted On: January 9, 2016

TE modes and the other for TM, due to the different boundary conditions), allows a very effective solution for rectangular WGs or, more generally, for WGs with piecewise rectangular boundaries, since in these cases the boundary is perfectly fitted to the grid, either uniform or non-uniform. The FDFD has been suitably generalized [20] to evaluate all modes (either TE or TM) on a single grid. The discretization results in a matrix eigenvalue problem, which is sparse, so a very effective computation is possible. Once the eigenvalue problem is solved, the smallest two eigenvalues give directly the BW.

III. PSO

PSO is an iterative algorithm designed to find out the solution of optimization problems, very efficient in solving multidimensional problems in a large variety of applications. It has been proposed first by Kennedy and Eberhart [21] for non-linear functions optimization and neural network training. Later on, it has been introduced in electromagnetic research for antenna design [22]-[25], and subsequently it has been applied to artificial ground plane for surface wave antennas [26], microstrip antennas [27]-[29], linear and planar array geometry [30]-[31], log-periodic array dipole antennas, aperture antennas, and so on.

PSO takes inspiration from the animal kingdom, in particular from the group movement in search of a common objective. The algorithm consists of a swarm randomly initialized inside a predetermined solution space, which represents the set of the admissible solutions for the problem. The quality of the solution is measured through a suitable objective function, associated with each position in the solution space. The choice of the objective function is a key point of every PSO procedure, since it must be accurately defined to well describe the requests of the problem. The group of particles moves iteratively inside the solution space, trying to reach the position which represents the optimal solution, corresponding to the minimum value of the objective function. The movement of each individual is based on its own instinct, on the memory of its path and on the iterations with the other individuals. Each particle is described by a vector of variables x, which are the coordinates of the solution space and, at the same time, the parameters to be optimized. In the j-th iteration, the i-th particle is characterized by its position $x_{i,j}$ (1) and velocity $v_{i,j}$ (2). Next position, direction and velocity of the single particle are updated according to its position and velocity at the previous step, the best solution found by the particle in its path (personal best, *p*), and the best solution found by the whole swarm (global best, *g*).

Therefore,

$$x_{i,j} = x_{i,j-1} + v_{i,j}, \tag{1}$$

$$v_{i,j} = w \cdot v_{i,j-1} + c_1 \cdot r_1 \cdot (p_{i,j} - x_{i,j-1}) + \\ + c_2 \cdot r_2 \cdot (g_{i,j} - x_{i,j-1}), \tag{2}$$

wherein, *w* scales the velocity component in the same direction of the previous step (inertia weight), r_1, r_2 are two random numbers between 0.0 and 1.0 which simulate the random component of the swarm behaviour, c_1, c_2 provide a weight between the pull of *g* and *p*: low values allow particles to roam far from target positions before being attracted to, whereas high values provide movements more strongly orientated towards the target. Eberhart suggested that the best choice for c_1 and c_2 is 2.0 [32] for most of applications. In general, velocity is applied to position updating for a time-step Δt which is set to 1 in this work.

The main steps of the algorithm can be indentified in the following (Fig. 1):

1. Initialization of swarm position and velocity;
2. Systematic particles movement in the solution space. For each particle:
   a) Objective function fitness evaluation (*g*, *p* update)
   b) Velocity update
   c) Position update (swarm movement);
3. Iteration of point 2 until a stop criterion (convergence or maximum number of iterations) is reached.

The objective function shown in Fig. 1 is relative to the model proposed in this paper and evaluates the performance of the R-WG, whose geometrical parameters constitute the *x* vector components, and therefore the dimensions of the solution space.

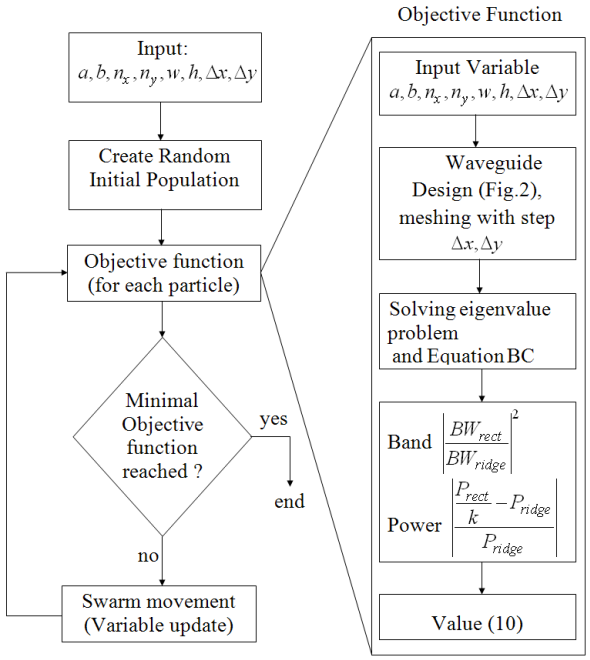

Fig. 1. PSO block diagram.

IV. WG DESIGN

The implementation of an optimization algorithm starts from the definition of the optimization variables, which define the solution space through their constraints. In our case, the variables are the geometrical dimensions of all the ridges (width w and height h) and the horizontal spacing s between them. However, use of FDFD requires the WG section be discretized. As a consequence, the variables can assume only values that are multiples of the discretization steps (D_x, D_y) of the WG section. The solution space of the PSO is therefore a discrete one, and its constraints are set to prevent all singular configurations. Four different R-WG configurations have been considered, with either equal or unequal ridges, and are shown in Fig. 2.

V. EVALUATION OF POWER HANDLING CAPABILITY

The PHC depends on both the WG shape and, for hollow WGs, the dielectric capability of the air. In order to compare different R-WGs, the maximum value of $|E|$ has been set to 1. Following Hopfer [4], we start from the well known relation between the power flux P and the total energy for unit length W_{EM}:

$$P = W_{EM}\frac{\beta c}{k_0}, \tag{3}$$

wherein β is the propagation constant, c and k_0 are respectively the speed of light and the wavenumber in vacuum. Then we obtain:

$$P = \frac{1}{\sqrt{\varepsilon_0\mu_0}}\frac{\lambda_0}{\lambda_g}\left[2\left(\frac{1}{2}CV^2\right)+\frac{\varepsilon_0}{2}\int E^2 dS\right], \tag{4}$$

where V is the fundamental mode voltage at the ridge edge, and C is the capacitance equivalent to each discontinuity:

$$C = \frac{2\varepsilon_0}{\pi}\ln\left[\csc\left(\frac{\pi d}{2b}\right)\right], \tag{5}$$

wherein b is the height of the waveguide, and d is the height of the ridged area.

The total energy can be evaluated on the transmission-line equivalent circuit used for TRT. Since the details of the configurations 1 (Fig. 2 (a)) and 2 (Fig. 2 (b)) are discussed in an appendix of [4], we add here some considerations for the six-ridges case (shown in Fig. 2 (c)), since the generalization is not trivial. Figure 3 represents the transmission line model (TLM) of only half of the transversal section of a six-ridge WG, so it stores half of the total energy. The antipodal case (shown in Fig. 2 (d)) can be dealt with in the same way.t

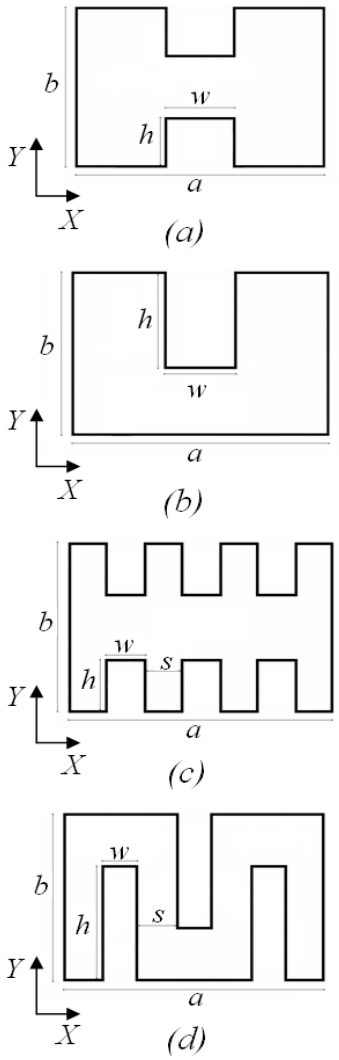

Fig. 2. (a) Configuration 1: a standard R-WG with two ridges centred along the widths of a rectangular WG; (b) configuration 2: a standard R-WG with a ridge centred along a width of a rectangular WG; (c) configuration 3: a standard R-WG with six ridges with equispaced centres; (d) configuration 4: a three-symmetric-antipodal R-WG.

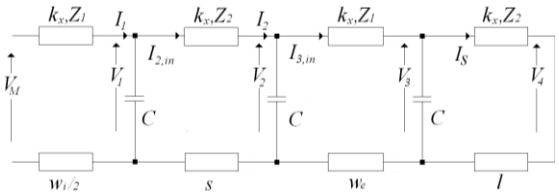

Fig. 3. Transmission line model for a six ridges geometry.

The TRT starts by considering the transversal section of the R-WG as a resonator. The propagation constant is the same for each line (representing a parallel plate section of the R-WG) and it is equal to the transverse propagation constant k_c, while the impedance is proportional to the WG height. To evaluate the PHC, a voltage V_M corresponding to the maximum electric field is set at the open-circuit (i.e., at the WG center), and an unknown current I_S at the short circuit end (i.e., at the WG lateral wall).

Letting $l_1 = w_i/2$, $l_2 = s$, we have:

$$\begin{aligned} V_1 &= A_1 \cos(k_x x) \\ V_2 &= A_2 \cos\left[k_x\left(x-l_1\right)\right] - jB_2 \sin\left[k_x\left(x-l_1\right)\right] \\ V_3 &= A_3 \cos\left[k_x\left(x-\left(l_1+l_2\right)\right)\right] + \\ &\quad - jB_3 \sin\left[k_x\left(x-\left(l_1+l_2\right)\right)\right] \\ V_4 &= B_4 \sin(k_x x') \end{aligned} \quad , \quad (6)$$

where k_x is the propagation constant in the x direction at cutoff and is given by $k_x = k_c = 2\pi/\lambda_c$ and,

$$\begin{aligned} A_1 &= V_M \\ A_2 &= V_1\left(w_i/2\right) \\ A_3 &= V_2\left(w_i/2+s\right) \\ B_2 &= -jZ_2 I_{2,in} \\ B_3 &= -jZ_1 I_{3,in} \\ B_4 &= -jZ_2 I_S \end{aligned} \quad , \quad (7)$$

$I_{2,in}$, $I_{3,in}$ are the input currents at the lines after the capacitors nodes:

$$\begin{aligned} I_1\left(w_i/2\right) &= I_{2,in} - CV_1\left(w_i/2\right) \\ I_2\left(w_i/2+s\right) &= I_{3,in} - CV_2\left(w_i/2+s\right). \end{aligned} \quad (8)$$

The unknown current I_S can be obtained by imposing the continuity of the voltages at the steps. The electric field is described from the (6) as:

$$\begin{aligned} E_1 &= G_1 V_1 \\ E_2 &= G_2 V_2 \\ E_3 &= G_3 V_3 \\ E_4 &= G_4 V_4 \end{aligned} \quad , \quad (9)$$

the constants G_1, G_2, G_3, G_4 can be obtained by imposing the voltage continuity at the steps.

VI. RESULTS

A. FDFD and PSO parameters

A 6x2 cm WG has been considered for all cases of Fig. 2. The WG cross-section has been discretized using a TE grid with steps $(D_x, D_y) = 0.1$ *mm*. It follows that the dimensions *w*, *h*, and *s* are expressed in terms of number of nodes in the grid. The structure has been tested for different values of acceleration coefficient and number of particles *np* (i.e., the swarm size), and it has been verified whether different PSO parameters modify or not the results. In all the tests, a varying inertia weight is applied by linearly changing its value from 0.9 at the beginning of the iterations to 0.4 towards the end (a smaller inertia weight encourages the local search [33]). We will show the optimal bandwidth $BW = f_{c2} - f_{c1}$, and the ratio BW_N between the bandwidth of the optimal R-WG and of the rectangular one with the same external size. f_{c1}, f_{c2} are the cut-off frequencies of the first two R-WG modes.

B. Objective functions

An appropriate objective function must be defined to obtain the solution best suited to the required application. It has been selected an objective function able to optimize the BW with a constraint on the power. More precisely, the following objective function:

$$f(k) = \left|\frac{P_{rect}/k - P_{ridge}}{P_{ridge}}\right| + \left|\frac{BW_{rect}}{BW_{ridge}}\right|^2 , \quad (10)$$

maximizes the BW with a constraint on the power decrease (k-time reduction with respect to the rectangular WG). P_{ridge}, BW_{ridge} are the values for the R-WG at hand, whereas P_{rect}, BW_{rect} are the values for the host rectangular WG [34]. In the following, it has been usually chosen $k = 2.0; 3.0$, so that the objective function tries to optimize the BW with a maximum power reduction equal to 50% or 66%.

C. Convergence test

The behaviour of a R-WG in terms of BW is rather well-known. Some preliminary optimization of $f(\infty)$ (i.e., BW-only optimization) have been then performed to evaluate the convergence properties of our approach. Since the solution space is discrete, we assume as convergence criterion the equality of the best and worst fitness values of the swarm.

A test on configuration 1 leads to the result that the largest BW requires the highest possible ridges ($h = 99$) with a large width ($w = 192$). This optimum is always obtained using different c_1, c_2, *np* values and starting point, since no traps are present. The smaller c_i's, the more rapid the convergence: for $np = 5$, the convergence require about 80 steps for $c_1 = c_2 = 1.5$, and about 100 steps for $c_1 = c_2 = 2$. A similar behaviour has been obtained for larger *np*. On the other hand, a larger c_i's allow to better explore the solution space, and therefore to escape more easily from traps. The increase in the computational cost is quite small and, since the introduction of the PHC constraints modifies the topology of the solution space and can introduce some local minima (i.e., traps) we have, in the following, chosen $c_1 = c_2 = 2$.

Then, we have tested the dependence of the number of particles of the swarm. A typical value for *np*

is 1.5 to 2 times the number of optimization variables. Of course, for the simple cases involving only two variables, we have taken $np \geq 5$. It appears that a significant increase of *np* introduces no reduction in the number of iterative steps. Even worse, this number usually increases a little bit (10-30% in the cases we have tested). Therefore, we conclude that the typical value of *np* quoted above is also the more effective, since we need, at each step, *np* evaluation of eigenvalues and mode distributions.

D. Optimization results

The objective functions *f(2)* and *f(3)* have been chosen to constraint the ratio P_{ridge}/P_{rect} to 50% or 33% respectively. The tests confirm the effectiveness of the objective function: the constraint on PHC is fulfilled with a smaller discrepancy.

The optimized geometries of the configuration 1 have been obtained with *np = 5* for equal ridges (2 optimization variables) and *np = 10* for different ridges (4 variables), and they are shown in Table 1. Actually, the optimum is always with equal ridges, so that only this case is shown. The optimum BW should be compared with the best one obtained with no PHC constraints, which is equal to 6.7726 GHz (i.e., $BW_N = 2.711$), but in this case the maximum power flux is very small respect to P_{rect}.

Table 1: Results configuration 1

k	$\frac{w}{a}$	$\frac{h}{b}$	BW (GHz)	BW_N (GHz)
2	0.35	0.20	3.07	1.23
3	0.33	0.27	3.42	1.37

Similarly, the Table 2 presents the performance of the configuration 2. A single ridge presents a lower improvement in terms of bandwidth with respect to the 2-ridges case.

Table 2: Results configuration 2

k	$\frac{w}{a}$	$\frac{h}{b}$	BW (GHz)	BW_N (GHz)
2	0.28	0.37	3.00	1.20
3	0.26	0.52	3.29	1.32

The configurations 3, and 4 investigate the effect of the side ridges. The configuration 3 does not work for the equal ridges case: as expected, large side ridges prevent the BW improvement, so the algorithm tends to remove them and the geometry tends toward rectangular WG without ridges. Regarding the case with different ridges, the symmetry of the fundamental mode allows to simplify the problem to a symmetric structure with respect to its two axes: it has been considered a geometry whose central ridges (w_C, h_C) vary independently of the side ones (w_S, h_S), and the spacing between the ridges *s* is chosen as another parameter to be optimized. The solution space has therefore 5 dimensions and the optimized geometries (obtained with *np = 20* particles in the swarm) are shown in Table 3. A comparison with Table 1 shows a significant BW improvement (for a given PHC) due to the additional (optimized) side ridges.

Table 3: Results configuration 3

k	$\frac{w_c}{a}, \frac{h_c}{b}$	$\frac{w_s}{a}, \frac{h_s}{b}$	$\frac{s}{a}$	BW (GHz)	BWN (GHz)
2	0.32, 0.38	0.32, 0.24	0.01	3.48	1.39
3	0.29, 0.36	0.32, 0.15	0.03	3.67	1.47

As a further analysis of the side ridges effect, we consider an antipodal geometry (configuration 4), where the two external ridges are equal and equally spaced from the central one. Such configuration can also be obtained by adding two lateral ridges to configuration 2 on the un-ridged side. Since the ridge spacing is also an optimization variable, the solution space has again 5 dimensions, and we have used *np = 20* in the tests. Table 4 displays the performance of this geometry.

Table 4: Results configuration 4

k	$\frac{w_c}{a}, \frac{h_c}{b}$	$\frac{w_s}{a}, \frac{h_s}{b}$	$\frac{s}{a}$	BW (GHz)	BWN (GHz)
2	0.19, 0.46	0.03, 0.16	0.35	3.25	1.300
3	0.12, 0.47	0.03, 0.05	0.34	3.27	1.307

In both cases, the lateral ridges are small and distant from the central one and, unlike the configuration 2, the central ridge does not cross the horizontal axis of the WG. It is apparent from Table 4 that the antipodal configuration allows a BW improvement when a relatively loose constraint on PHC is set. For the tested case, a constraint of 50% reduction in power gives an improvement in BW around 10%. On the other hand, when a small PHC is required, the single ridge geometry is preferable.

VII. CONCLUSIONS

In this paper, the effectiveness of PSO in the geometrical optimization of a guiding structure has been illustrated. It has been shown how a suitable objective function allows to make a trade-off between two conflicting requests: the BW of a R-WG has been maximized for a determined power decrease respect to the un-ridged geometry. Among the different geometries presented, the 6-symmetric ridge geometry results to be the best solution in terms of bandwidth.

ACKNOWLEDGMENT

Marco Simone gratefully acknowledges Sardinia Regional Government for the financial support of his Ph.D. scholarship (P.O.R. Sardegna F.S.E. Operational Programme of the Autonomous Region of Sardinia, European Social Fund 2007-2013 - Axis IV Human Resources, Objective l.3, Line of Activity l.3.1.).

Alessandro Fanti gratefully acknowledges Sardinia Regional Government for the financial support (P.O.R. Sardegna F.S.E. Operational Programme of the Autonomous Region of Sardinia, European Social Fund 2007-2013 - Axis IV Human Resources, Objective l.3, Line of Activity l.3.1 Avviso di chiamata per il finanziamento di Assegni di Ricerca).

This work was supported in part by Regione Autonoma della Sardegna under contract CRP-49231 (CUP C45E120000200002).

The authors would like to thank George Evers for making freely available its MATLAB PSO Research Toolbox which has been used for simulations.

REFERENCES

[1] R. E. Collin, *Field Theory of Guided Waves*, 2nd ed., New York, IEEE Press, 1991.

[2] J. Helszajn, *Ridge Waveguides and Passive Microwave Components*, London, IEE, 2000.

[3] S. B. Cohn, "Properties of ridged waveguide," *Proceedings of the IRE*, vol. 35, pp. 783-788, Aug. 1947.

[4] S. Hopfer, "The design of ridge waveguide," *IRE Transactions on Microwave Theory and Techniques*, vol. MTT-3, pp. 20-29, Oct. 1955.

[5] R. Sorrentino, *Transverse Resonance Technique*, in Numerical Techniques for Microwave and Millimeter Wave Passive Structures, Chapter 11, New York, John Wiley, 1989.

[6] J. Helszajn and M. McKay, "Voltage-current definition of impedance of double ridge waveguide using the finite element method," *IEE Proc.-Microw. Antennas Propagation*, vol. 145, no. I, Feb. 1998.

[7] A. Fanti and G. Mazzarella, "Curvilinear finite difference approach to the computation of modes of circular and elliptic waveguides," *IEEE Proc. Int. Conf. on Applied Electromagnetics and Communications, (ICECom 2010)*, Dubrovnik, Croazia, Sep. 20-23, 2010.

[8] A. M. Svedin, "Propagation analysis of chiro waveguides using the finite element method," *IEEE Trans. on Microwave Theory Tech.*, vol. 38, no. 10, pp. 1488-1496, Oct. 1990.

[9] M. Simone, A. Fanti, G. Mazzarella, and G. Montisci, "Band optimization of ridge waveguides using PSO," *30th International Review of Progress in Applied Computational Electromagnetics*, Jacksonville, Florida, Mar. 23-27, 2014.

[10] A. Fanti, L. Deias, G. A. Casula, and G. Montisci, "A fourth order FDFD approach for the analysis of sectorial elliptic waveguides," *Applied Computational Electromagnetics Society (ACES) Journal*, vol. 30, no. 5, pp. 488-495, May 2015.

[11] C. S. Lavranos and G. A. Kyriacou, "Eigenvalue analysis of curved waveguides employing FDFD method in orthogonal curvilinear co-ordinates," *IEE Electronics Letters*, vol. 42, no. 12, pp. 702-704, June 2006.

[12] C. S. Lavranos and G. A. Kyriacou, "Eigenvalue analysis of curved waveguides employing an orthogonal curvilinear frequency-domain finite-difference method," *IEEE Transactions on Microwave Theory and Techniques*, vol. 57, iss. 3, pp. 594-611, Mar. 2009.

[13] A. Fanti, G. Mazzarella, G. Montisci, and G. A. Casula, "VFD approach to the computation TE and TM modes in elliptic waveguide on TM grid," *Applied Computational Electromagnetics Society (ACES) Journal*, vol. 28, pp. 1205-1212, 2013.

[14] Y. J. Zhao, K. L. Wu, and K. K. M. Cheng, "A compact 2-D full-wave finite-difference frequency-domain method for general guided wave structures," *IEEE Transactions on Microwave Theory and Techniques*, vol. 50, iss. 7, pp. 1844-1848, 2002.

[15] G. Mazzarella and G. Montisci, "Accurate characterization of the interaction between coupling slots and waveguide bends in waveguide slot arrays," *IEEE Trans. Microw. Theory Tech.*, vol. MTT 48, pp. 1154-1157, Sep. 2000.

[16] T. Hirano, J. Hirokawa, and M. Ando, "Method of moments analysis of a waveguide crossed slot by using the eigenmode basis functions derived by the edge-based nite-element," *Proc. Inst. Elect. Eng. Microwaves, Antennas Propagation*, vol. 147, no. 5, pp. 349-353, 2000.

[17] J. Bornemann and F. Taringou, "Mode-matching analysis of substrate-integrated waveguide circuits," *Proc. Canadian Conf. Elec. Comp. Engr.*, pp. 579-582, Niagara Falls, Canada, May 2011.

[18] K. W. Morton and D. F. Mayers, *Numerical Solution of Partial Differential Equations, An Introduction*, Cambridge University Press, 2005.

[19] A. Fanti, M. Simone, and G. Mazzarella, "High order FDFD computation of all waveguide modes using a single grid," *IEEE Int. Proc. 2013 Loughborough Antennas and Propagation Conference*, Loughborough, UK, 2013.

[20] A. Fanti and G. Mazzarella, "Finite difference single grid evaluation of TE and TM modes in metallic waveguides," *IEEE Proc. Int. Conf. Loughborough Antennas and Propagation Conference*, UK, pp. 517-520, Nov. 8-9, 2010.

[21] J. Kennedy and R. Eberhart, "Particle swarm

optimization," *Proceedings of IEEE International Conference on Neural Networks*, vol. 4, pp. 1942-1948, Perth Wash, Australia, Nov. 1995.

[22] J. Robinson, S. Sinton, and Y. Rahmat-Samii, "Particle swarm, genetic algorithm, and their hybrids: optimization of a profiled corrugated horn antenna," *IEEE Antennas and Propagation Society International Symposium 2002*, vol. 1, pp. 314-317, San Antonio, Texas, June 2002.

[23] J. Robinson and Y. Rahmat-Samii, "Particle swarm optimization in electromagnetics," *IEEE Transactions on Antennas and Propagation*, vol. 52, iss. 2, pp. 397-407, Feb. 2004.

[24] N. Jin and Y. Rahmat-Samii, "Particle swarm optimization for antenna designs in engineering electromagnetics," *Journal of Artificial Evolution and Applications*, vol. 2008, no. 9, 2008.

[25] H. Wu, J. Geng, R. Jin, J. Qiu, W. Liu, J. Chen, and S. Liu, "An improved comprehensive learning particle swarm optimization and its application to the semiautomatic design of antennas," *IEEE Transactions on Antennas and Propagation*, vol. 57, iss. 10, pp. 3018-3028, Oct. 2009.

[26] E. Carrubba, A. Junge, F. Marliani, and A. Monorchio, "Particle swarm optimization for multiple dipole modeling of space equipment," *IEEE Transactions on Magnetics*, vol. 50, iss. 12, pp. 1-10, Dec. 2014.

[27] Y. Choukiker, S. K. Behera, D. Mishra, and R. K. Mishra, "Optimization of dual band microstrip antenna using PSO," *Applied Electromagnetics Conference (AEMC)*, Kolkata, India, pp. 1-4, Dec. 2009.

[28] A. A. Minasian and T. S. Bird, "Particle swarm optimization of microstrip antennas for wireless communication systems," *IEEE Transactions on Antennas and Propagation*, vol. 61, iss. 12, pp. 6214-6217, Dec. 2013.

[29] A. Deb, J. S. Roy, and B. Gupta, "Performance comparison of differential evolution, particle swarm optimization and genetic algorithm in the design of circularly polarized microstrip antennas," *IEEE Transactions on Antennas and Propagation*, vol. 62, iss. 8, pp. 3920-3928, Aug. 2014.

[30] M. M. Khodier and C. G. Christodoulou, "Linear array geometry synthesis with minimum side lobe level and null control using particle swarm optimization," *IEEE Transactions on Antennas and Propagation*, vol. 53, iss. 8, part 2, pp. 2674-2679, Aug. 2005.

[31] D. Cao, A. Modiri, G. Sureka, and K. Kiasaleh, "DSP implementation of the particle swarm and genetic algorithms for real time design of thinned array antennas," *IEEE Antennas Wireless Propagation Letter*, vol. 11, pp. 1170-1173, 2012.

[32] R. C. Eberhart and Y. Shi, "Particle swarm optimization: development, applications and resources," *Proceedings of the 2001 Congress on Evolutionary Computation*, COEX Seoul, Korea, vol. 1, pp. 81-86, May 2001.

[33] Y. Shi and R. Eberhart, "Empirical study of particle swarm optimization," *Proceedings of the IEEE Congress on Evolutionary Computation*, vol. 3, pp. 1945-1950, 1999.

[34] M. Simone, A. Fanti, and G. Mazzarella, "Ridge waveguide optimization with PSO algorithm," *Journal of Electromagnetic Waves and Applications*, vol. 2, iss. 29, pp. 199-209, Feb. 2015.

Marco Simone received the bachelor's degree in Electronics Engineering from the University of Cagliari in 2007. In 2011, he received the master's degree from the University of Cagliari. In 2012, he did an internship at Vitrociset about Radar Systems, Radar Signal and Data Processing. From 2013 to 2015, he worked as Ph.D. student (scholarship winner) at Doctoral School of Electronic and Computer Engineering (DRIEI) at the Department of Electrical and Electronic Engineering (DIEE) of University of Cagliari. He's currently writing his Ph.D. thesis (to be discussed in March). In 2015, he spent 6 months at Queen Mary University of London to achieve the Doctor Europaeus qualification. From January 2016, he is employed as Postdoctoral Research Assistant in the School of Electronic Engineering and Computer Science at Queen Mary University of London, under the supervision of Prof. Yang Hao. His research activity involves the use of optimization techniques for microwave devices.

Alessandro Fanti received the Laurea degree in Electronic Engineering and Ph.D. degree in Electronic Engineering and Computer Science from the University of Cagliari in 2006 and 2012, respectively. He currently holds a post-doc scholarship for design of microwave components. His research activity involves the use of numerical techniques for modes computation of guiding structures, optimization techniques, analysis and design of waveguide slot arrays, analysis and design of patch antennas.

Giorgio Montisci received the Laurea degree (summa cum laude) in Electronic Engineering and Ph.D. degree in Electronic Engineering and Computer Science from the University of Cagliari, Cagliari, Italy, in 1997 and 2000, respectively. In November 2000, he became Assistant Professor, and since October 2015 he is Associate Professor of Electromagnetic Fields at the Dipartimento di Ingegneria Elettrica ed Elettronica, University of Cagliari, teaching courses in electromagnetics and microwave engineering. His research activity is mainly focused on analysis and design of waveguide slot arrays, microwave holographic techniques for the diagnostic of large reflector antennas, numerical methods in electromagnetics, and printed antennas. He is author or co-author of about 50 papers in international journals and Reviewer for EM Journals.

Giovanni Andrea Casula received the Laurea degree (summa cum laude) in Electronic Engineering and Ph.D. degree in Electronic Engineering and Computer Science from the University di Cagliari, Cagliari, Italy, in 2000 and 2004, respectively. Since March 2006, he is an Assistant Professor of Electromagnetic Field and Microwave Engineering at the Dipartimento di Ingegneria Elettrica ed Elettronica, University of Cagliari. His current research interests are in the field of synthesis, analysis and design of wire, patch, and slot antennas. Casula serves as Reviewer for several international journals and is a Member of the Italian Electromagnetic Society (SIEm).

Giuseppe Mazzarella graduated Summa with Laude in Electronic Engineering from the Università "Federico II" of Naples in 1984 and obtained the Ph.D. in Electronic Engineering and Computer Science in 1989. In 1990, he became Assistant Professor at the Dipartimento di Ingegneria Elettronica at the Università "Federico II" of Naples. Since 1992, he is with the Dipartimento di Ingegneria Elettrica ed Elettronica of the Universit di Cagliari, first as Associate Professor and then, since 2000, as Full Professor, teaching courses in Electromagnetics, Microwave, Antennas and Remote Sensing. His research activity has focused mainly on: efficient synthesis of large arrays of slots, power synthesis of array factor, microwave holography techniques for the diagnostic of large reflector antennas, use of evolutionary programming for inverse problems solving. He is author (or co-author) of about 50 papers in international journals, and is a Reviewer for many EM journals.

Narrow-band Bandpass Filters with Improved Upper Stopband Using Open/Shorted Coupled Lines

Wenjie Feng, Meiling Hong, and Wenquan Che

Department of Communication Engineering
Nanjing University of Science and Technology, Nanjing, 210094, China
fengwenjie1985@163.com, merlin_hon@163.com, yeeren_cher@163.com

Abstract **–** Two transversal narrow-band bandpass filters with improved stopband based on open/shorted coupled lines and transversal signal-interaction concepts are proposed in this paper. By utilizing the stopband transmission characteristic of the open/shorted coupled lines, three transmission zeros can be easily achieved to suppress the second harmonic for the first bandpass filter. To further reduce the circuit size of the first filter, unequal open stubs and transmission lines are used for the second bandpass filter with six transmission zeros in the upper stopband. The transmission zeros near the passband can be adjusted conveniently by only changing the electrical length of the open/shorted stubs when the ratio of characteristic impedance is fixed. To verify the presented concepts, two prototypes ($\varepsilon_r = 2.65$, $h = 0.508$ mm, $tan\delta$ = 0.003) with 3-dB fractional bandwidths (FBWs) of 4.3% (1.78-1.86 GHz), 2.8% (1.76-1.81 GHz) are designed and fabricated. Good agreements are observed for the theoretical and measured results, indicating good in-band filtering performances and high selectivity.

Index Terms **–** Bandpass filter, fractional bandwidth (FBW), narrowband, open/shorted coupled lines, transversal signal-interaction concepts.

I. INTRODUCTION

With the rapid growth of modern wireless communication systems [1]-[2], the bandpass filters with the features of planar structure, easy fabrication, low cost and easiness of integration into passive or active microwave components have attracted great attention. For conventional half-wavelength resonators bandpass filter, lowpass and bandstop networks are demanded to improve the rejection levels and harmonic suppression due to the unwanted periodic harmonics; however, the filter size and the passband insertion loss will enlarge [1].

In the past few years, different approaches have been applied to suppress harmonics of bandpass filters. Phase velocities compensation for the even- and odd-mode of the coupled lines using corrugated lines, substrate suspension and lumped-elements to remove the harmonics have been introduced in [3]-[4]. Stepped-impedance resonators with different characteristic impedance are capable of pushing the second harmonic to higher frequencies [5], cascaded different SIR structures with the same fundamental resonant and various high-order frequencies can be utilized to design high-order bandpass filters with wide upper stopband [6]-[8]. In addition, discriminating coupling, which blocks unwanted signals at certain frequency and allows the transmission of signals at other frequencies, can be used to suppress the harmonics without extra circuits [9]. Dual-behavior resonators (DBRs) with two stopband structures which bring two transmission zeros on either side of the passband can be used also to design high performance narrow-band bandpass filters [10], but low-pass structures and capacitive-coupled dual-behavior resonator are needed to suppress spurious resonances on both sides of the bandpass response [11].

Recently, wideband bandstop/bandpass filters based on transversal signal-interaction concepts have drawn a lot of attention [12]-[15]. By introducing intentionally a passband constructive interference and out-of-band signal energy cancellations to produce power transmission zeros, high-selectivity filtering responses and harmonic suppression can be achieved in this kind of filter structures. However, little research has described the application of transversal signal-interaction concepts in the high performance narrow-band bandpass filters. In this paper, two transversal narrow-band bandpass filters with improved upper stopband based on open/shorted coupled lines and transversal signal-interaction concepts are proposed. Three transmission zeros can be easily realized by the two transmission paths consisting of two open/shorted coupled lines for the two narrowband bandpass filters, another three more transmission zeros are realized for the second bandpass filter with two asymmetric transmission paths. The transmission zeros for the two transversal narrowband bandpass filters can be adjusted conveniently by changing the electrical length of the open/shorted stubs when the ratio of characteristic impedance is fixed. Detailed theoretical design, simulation and experimental results are demonstrated and discussed. The organization and

Submitted On: September 16, 2015
Accepted On: December 5, 2015

framework of this paper should be given here.

II. ANALYSIS OF PROPOSED NARROW-BAND FILTERS

A. Bandpass filter with three zeros in upper stopband

Figure 1 (a) shows the first proposed bandpass filter with three zeros in upper stopband. Similar as the wideband filters in [12]-[15], two similar transmission paths are introduced to realize the signal transmission from Port 1 to Port 2. The characteristic impedance of the two pairs of open/shorted stubs is Z_2 (electrical length θ_1, even/odd-mode characteristic impedance Z_{oe}, Z_{oo}) with two attached transmission lines (characteristic impedance Z_1, electrical length θ_1). For calculation simplicity, $Z_1 = Z_2$ are chosen, and the input admittance Y_{in1} of Fig. 1 (b) can be illustrated as [1]:

$$Y_{in1} = -j\cot(\theta_1+\theta_2)/Z_1 + j\tan\theta_2/Z_1. \quad (1)$$

As discussed in [6], [16], the external quality factor Q_{e1} of Fig. 1 (b) can be calculated as:

$$Q_{e1} = R_{L1}\frac{\omega_0}{2}\frac{dY_{in1}}{d\omega}\bigg|_{\omega_0}, \quad (2)$$

where R_{L1} is the load impedance for the open/shorted stubs, ω_0 is the operation frequency, and after further calculation, Q_{e1} can be illustrated as:

$$Q_{e1} = 0.5R_{L1}[(\theta_1+\theta_2)\csc^2(\theta_1+\theta_2)/Z_1 + \theta_2\sec^2\theta_2/Z_1]. \quad (3)$$

When $Y_{in1} = 0$, the resonant condition of open/shorted stubs can be obtained; meanwhile the external quality factor Q_{e1} of the bandpass filter can be selected from the required value of filter specification, then the two unknown variables θ_1 and θ_2 can be solved when the ratio of Z_1/Z_2 are fixed. The open/shorted stubs using the conditions (1) = 0 and (2) to solve the two remnant unknown variables (θ_1, θ_2) is similar to the method used in [16], which can avoid the use of additional impedance transformers. The transmission zeros and the external quality factor Q_{e1} versus θ_2 and the simulated frequency responses of the filter are shown in Figs. 2 (a)-(c). We may notice that, each desired transmission zero frequency of the open/shorted stubs is equal to quarter/half-wavelength, respectively [1], and the two transmission zeros created by the open/shorted stubs can be freely chosen to locate in both sides of the passband. Besides the transmission zeros (f_{01}, f_{s1}) of the open/shorted stubs, the transmission zero ($2f_{01}$) created by the bandstop transmission characteristic of the open/shorted coupled lines [1] and the transmission zeros ($2f_{s1}$) of the shorted stubs can be also used to further improve the upper stopband of the narrow-band bandpass filter, and the frequencies of four transmission zeros decrease as θ_1, θ_2 increase.

Moreover, the desired external quality factor Q_{e1} of the filter can be obtained by changing the electrical length θ_2 of the open stub when $Z_1 = Z_2$. If we want to adjust the frequencies of the transmission zeros (f_{01}, f_{s1}) with similar Q_{e1} value for the narrow-band bandpass filter, the R_{L1} value ($Z_1 \neq Z_2$) can be altered correspondingly to keep the Q_{e1} value unchanged, if the R_{L1} does not equal to 50 Ω. In addition, the quarter-wavelength transformer should be employed to perform as the impedance transformation, as discussed in [6]. To further reduce the circuit size and improve the harmonic suppression of the narrow-band bandpass filter with three transmission zeros in upper stopband, a narrow-band bandpass filter with six transmission zeros in upper stopband will be proposed and investigated next.

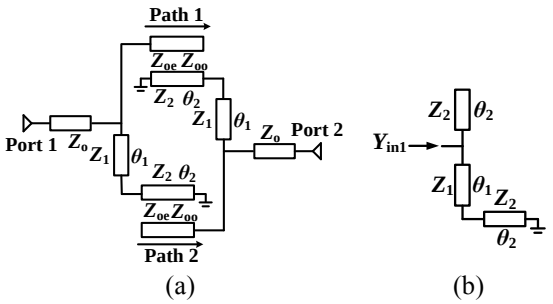

Fig. 1. (a) Bandpass filter with three transmission zeros in upper stopband, and (b) the input admittance of the open/shorted stubs.

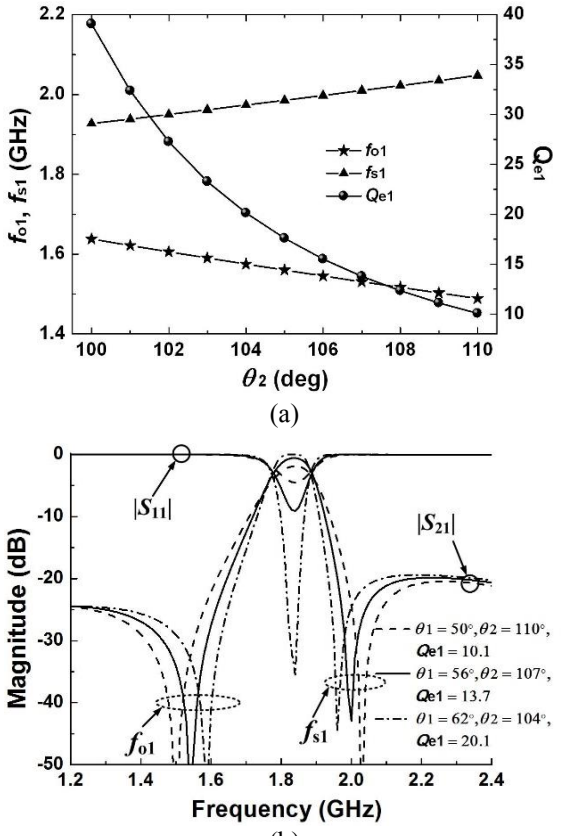

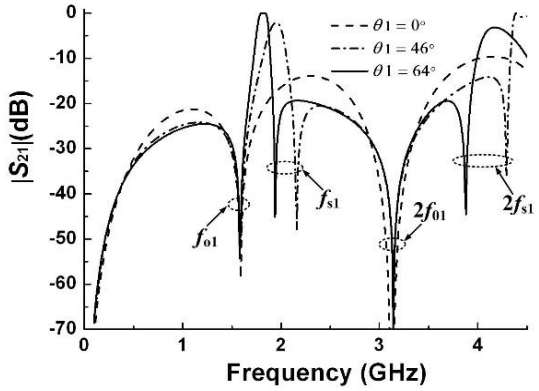

(c)

Fig. 2. (a) Transmission zeros and external quality factor Q_{e1} versus θ_2, θ_1 = 270°-2θ_2, (b) simulated frequency responses of the filter, and (c) simulated frequency responses versus θ_1, θ_2= 103°. (Z_o = 50 Ω, Z_1 = Z_2 = 100 Ω, Z_{oe} = 141 Ω, Z_{oo} = 74 Ω, f_0 = 1.82 GHz).

B. Bandpass filter with six zeros in upper stopband

The bandpass filter with six transmission zeros in the upper stopband is shown in Fig. 3 (a). Different from the bandpass filter with three transmission zeros in the upper stopband, there is only a pair of open/shorted stubs in Path 1, the transmission line with characteristic impedance Z_1 and electrical length θ_1 has been removed for Path 1; the Path 2 is same as the filter of Fig. 1 (a), and a shunt-connected stub (characteristic impedance Z_3, electrical length θ_3) are connected in Port 2. As discussed in *Part A*, $Z_1 = Z_2$ are chosen for simplicity, and the input admittance Y_{in21}/Y_{in22} of Fig. 3 (b) can be illustrated as:

$$Y_{in21} = -j\cot(\theta_1+\theta_2)/Z_1 + j\tan\theta_2/Z_1, \quad (4)$$

$$Y_{in22} = -j\cot\theta_2/Z_1 + j\tan\theta_2/Z_1 + j\tan\theta_3/Z_3. \quad (5)$$

The external quality factor Q_{e21}/Q_{e22} of Fig. 3 (b) can be calculated as:

$$Q_{e21} = 0.5R_{L21}[(\theta_1+\theta_2)\csc^2(\theta_1+\theta_2)/Z_1 + \theta_2\sec^2\theta_2/Z_1], \quad (6)$$

$$Q_{e22} = 0.5R_{L22}[(\theta_2\csc^2\theta_2/Z_1 + \theta_2\sec^2\theta_2/Z_1 + \theta_3\sec^2\theta_3/Z_3]. \quad (7)$$

When Y_{in21} = Y_{in22} = 0, the resonance condition of open/shorted stubs of Fig. 3 (b) can be also obtained, and the external quality factor Q_{e21} should be equal to Q_{e22} to meet the required value of filter specification, and then the three unknown variables θ_1, θ_2 and θ_3 can be solved when the ratio of Z_1/Z_2, Z_1/Z_3 are fixed. In addition, it can be deduced that the shunt-connected stub θ_3 is a requirement condition for the Equation (5) to have real roots. The transmission zeros and the external quality factor Q_{e21}/Q_{e22} versus θ_3 and the simulated frequency responses of the filter with six transmission zeros in upper stopband are shown in Figs. 4 (a)-(c). As the filter originally has three transmission zeros in upper stopband, besides the transmission zeros (f_{01}, f_{03}, f_{s1}) of the open/shorted stubs (θ_1, θ_2, θ_3), the transmission zero ($2f_{01}$, $3f_{01}$) created by the bandstop transmission characteristic of the open/shorted coupled lines [1] and the transmission zeros ($2f_{s1}$) of the shorted stubs can be also used to improve the upper stopband of the narrow-band bandpass filter. In addition, the simulated transmission coefficients of the two paths at the frequency of f_{tsc} (4.18 GHz, tsc-transversal signal-interaction concepts) are 0.13∠81.8° and 0.13∠-98.7°, respectively. Thus, the signals transmitted from the two paths have the same magnitude but out-of-phase and are thus cancelled out, resulting in the generation of f_{tsc} [14]-[15]. Moreover, in Fig. 4 (b), for same external quality factor Q_{e21}/Q_{e22}, the passband responses are nearly unchanged and the locations of the transmission zeros (f_{01}, f_{03}, f_{s1}) for the open/shorted stubs (θ_1, θ_2, θ_3) can be freely chosen to locate in either both of the stopbands, leading to a quasi-elliptic function that improves the passband and out-of-band performances for the filter.

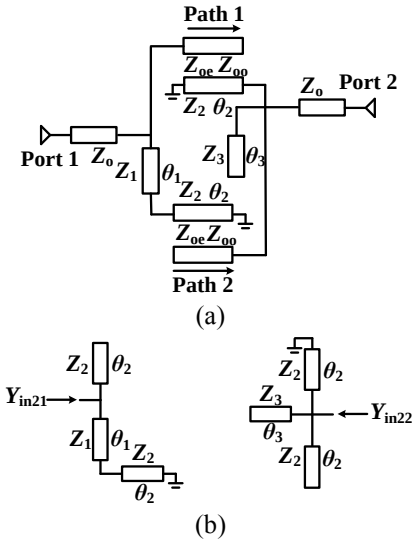

(a)

(b)

Fig. 3. (a) Bandpass filter with six zeros in upper stopband, and (b) the input admittance of the open/shorted stubs.

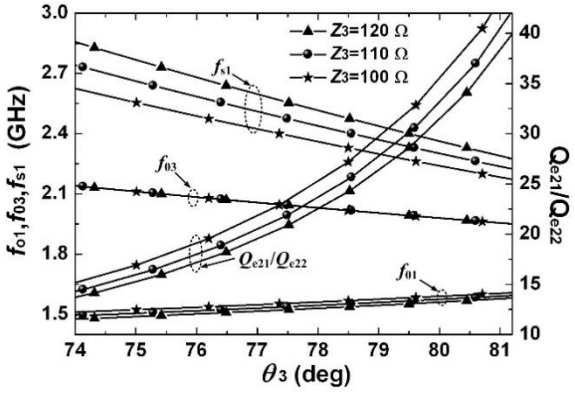

(a)

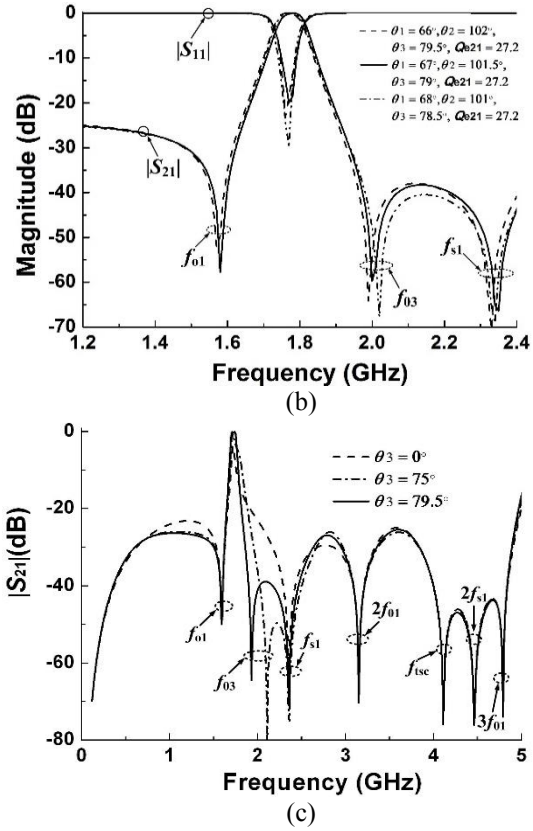

Fig. 4. (a) Transmission zeros and external quality factor Q_{e21}/Q_{e22} versus θ_3, $\theta_1 = 270°\text{-}2\theta_2$, (b) simulated frequency responses of the filter for same Q_{e21}/Q_{e22}, and (c) simulated frequency responses versus θ_3, $\theta_1 = 66°$, $\theta_2 = 102°$. ($Z_o = 50\ \Omega$, $Z_1 = Z_2 = 100\ \Omega$, $Z_{oe} = 127\ \Omega$, $Z_{oo} = 85\ \Omega$, $f_0 = 1.76$ GHz).

III. FILTERS DESIGN AND MEASURED RESULTS

A. Design procedures

In order to demonstrate the proposed concepts, two experimental Chebyshev bandpass filters with three and six transmission zeros in upper stopband are implemented with center frequency of 1.82 GHz and 1.76 GHz, fraction bandwidths of 4.2% and 3.1% and ripple of 0.1 dB. Based on the required responses, the lumped element values of the second-order prototypes filter are selected to be: $g_0 = 1$, $g_1 = 0.8431$, $g_2 = 0.6220$, $g_3 = 1.3554$. The required coupling coefficient and external quality factor can be obtained based on [1]:

$$Q_e = \frac{g_0 g_1}{FBW}, \quad k = \frac{FBW}{\sqrt{g_1 g_2}}. \tag{8}$$

It can be calculated that $Q_{e1} = 20.1$, $k_1 = 0.058$; $Q_{e21} = Q_{e22} = 27.2$, $k_2 = 0.043$. The Q_e factors and the coupling coefficients are extracted based on:

$$Q_e = \frac{f_0}{\Delta f_{\pm 90°}}, \quad k = \frac{f_2^2 - f_1^2}{f_2^2 + f_1^2}, \tag{9}$$

where f_0 is resonant frequency, and $\Delta f_{\pm 90°}$ is the bandwidth over which the phase shifts ±90º with respect to the absolute phase at f_0; f_1 and f_2 are the two resonant frequencies of the open/shorted coupled lines. Figure 5 shows the extracted k at f_2 against the gap (g_1) of the open/shorted coupled lines.

Based on the above discussion and the theoretical analysis in *Section II*, the final parameters for the two bandpass filters are: $Z_0 = 50\ \Omega$, $Z_1 = 100\ \Omega$, $Z_2 = 100\ \Omega$, $\theta_1 = 62°$, $\theta_2 = 104°$, $Q_{e1} = 20.1$, $k_1 = 0.058$, $Z_{oe} = 137\ \Omega$, $Z_{oo} = 73\ \Omega$, $f_0 = 1.82$ GHz; $Z_0 = 50\ \Omega$, $Z_1 = 100\ \Omega$, $Z_2 = 100\ \Omega$, $Z_3 = 120\ \Omega$, $\theta_1 = 66°$, $\theta_2 = 102°$, $\theta_3 = 79.5°$, $Q_{e21} = Q_{e22} = 27.2$, $k_2 = 0.043$, $Z_{oe} = 127\ \Omega$, $Z_{oo} = 85\ \Omega$, $f_0 = 1.76$ GHz. The final structure parameters for two bandpass filters shown in Figs. 6 (a)-(b) are: $l_1 = 20.9$ mm, $l_2 = 13.4$ mm, $l_3 = 20.4$ mm, $l_4 = 12.6$ mm, $l_5 = 19.9$ mm, $w_0 = 1.37$ mm, $w_1 = 0.35$ mm, $d = 0.5$ mm, $g_1 = 0.20$ mm, 52 mm × 34 mm, $\varepsilon_r = 2.65$, $h = 0.5$ mm, tan $\delta = 0.003$; $l_1 = 10.3$ mm, $l_2 = 23.3$ mm, $l_3 = 12.35$ mm, $l_4 = 22.3$ mm, $l_5 = 10.95$ mm, $l_6 = 22.65$ mm, $l_7 = 20.95$ mm, $m_1 = 2.5$ mm, $m_2 = 3.3$ mm, $m_3 = 10.2$ mm, $m_4 = 10.0$ mm, $w_0 = 1.37$ mm, $w_1 = 0.35$ mm, $w_2 = 0.25$ mm, $g_1 = 0.40$ mm, 42 mm × 40 mm, $\varepsilon_r = 2.65$, $h = 0.5$ mm, tan $\delta = 0.003$.

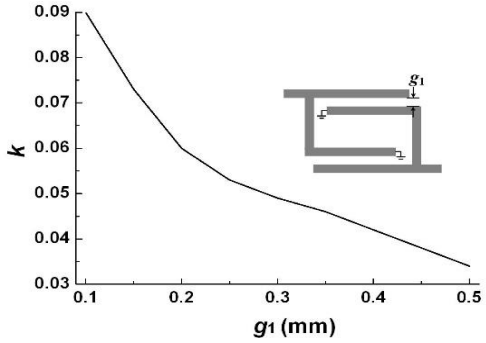

Fig. 5. Variation of k against the coupling gap (g_1) of the open/shorted coupled lines.

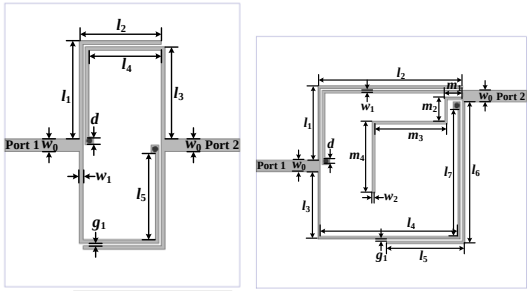

Fig. 6. Geometries of the two narrow bandpass filters: (a) three zeros in upper stopband, and (b) six zeros in upper stopband.

B. Measured and simulated results

The photographs, measured and simulated results of the two bandpass filters are shown in Fig. 7. For the filter

with three transmission zeros in upper stopband, four measured zeros are located at 1.55, 1.99, 3.36 and 3.98 GHz, respectively, the 3-dB bandwidth of the bandpass filter is approximately 4.3% (1.78-1.86 GHz) with 20-dB upper stopband from 1.96 to 4.85 GHz (2.66f_0); for the filter with six transmission zeros in upper stopband, seven measured transmission zeros are located at 1.56, 2.0, 2.73, 3.46, 3.89, 4.95 and 5.2 GHz, respectively, a passband with return loss greater than 12 dB is realized (3-dB fractional bandwidth is approximately 2.8% (1.76-1.81 GHz)) with 25-dB upper stopband from 1.97 to 5.4 GHz (3.07f_0). Compared with the bandpass filter with three zeros in upper stopband, the circuit size has been reduced and the harmonic suppression has been much improved. However, the in-band insertion loss for the second bandpass filter is a little big. Some better dielectric substrate such as Rogers 5880 with $\varepsilon_r = 2.65$, $h = 0.508$ mm, and $tan\delta = 0.0009$ can be chosen to realize higher-order bandpass filter with low insertion loss. In addition, the slight frequency discrepancies of the transmission zeros in the upper stopband and larger insertion loss for the passband between the measured and simulated results are mainly caused by the imperfect soldering skill of the shorted stubs and folded transmission line of the filter, and the even and odd mode phase velocities of the microstrip coupled line also affect the positioning of the transmission zeros of the filters; some slots located in the shorted/coupled lines can be considered to extend the electrical path of the odd mode, and the effective phase velocity of odd mode will be reduced [17].

For the purpose of comparison, Table 1 illustrates the measured results for some bandpass filters. Compared with other bandpass filters [4]-[16], the core circuit size of the filter with six zeros in the upper stopband is very compact, which is only 0.040λ^2_0, and seven transmission zeros with wide upper stopband (3.07f_0, $|S_{21}| > 25$ dB) are realized for the narrow bandpass filter. Moreover, the upper stopband of the two proposed filters can be further extended by using stepped impedance resonator stubs as [18].

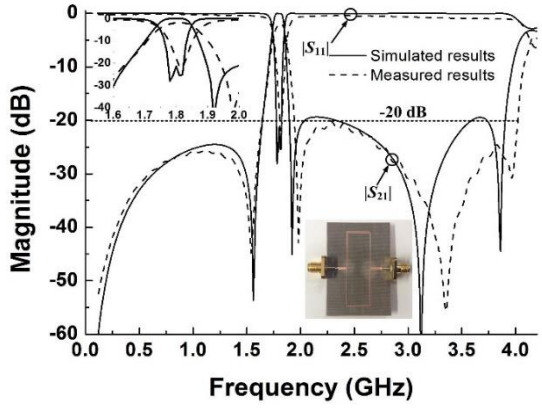

(a)

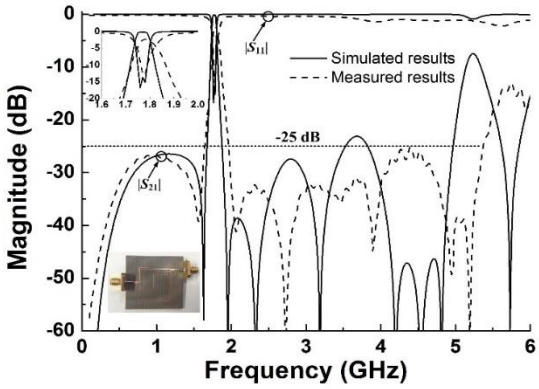

(b)

Fig. 7. Photographs, measured and simulated results of the two narrow bandpass filters: (a) three zeros in upper stopband, and (b) six zeros in upper stopband.

Table 1: Comparisons of some bandpass filters

Filters	TZs, (f_0)	3-dB Bandwidth	In-band $\|S_{11}\|$, dB	Circuit Size, (λ^2_0)	Upper Stopband, $\|S_{21}\|$, dB
Ref. [4]	3 (1.57 GHz)	1.80%	> 15.0	0.3*0.22	> 20 (2.67f_0)
Ref. [10]	6 (5.00 GHz)	4.50%	> 15.0	0.8*0.50	> 20 (2.60f_0)
Ref. [16]	8 (2.00 GHz)	6.00%	> 15.0	0.5*0.25	> 27 (2.88f_0)
This work	4 (1.82 GHz)	4.30%	> 15.0	0.23*0.2	> 20 (2.66f_0)
	7 (1.78 GHz)	2.80%	> 13.0	0.2*0.2	> 25 (3.07f_0)

IV. CONCLUSION

In this paper, two transversal high selectivity narrow-band bandpass filters with improved upper stopband using open/shorted couple lines based on transversal signal-interaction concepts are proposed. Four and seven transmission zeros can be adjusted conveniently by only changing the electrical length of the open/shorted stubs when the ratio of characteristic impedance of the stubs are fixed. The proposed bandpass filters have advantages of compact effective circuit size, simpler design theory and wideband harmonic suppression. Good agreements between simulated and measured responses of the filters are demonstrated, which will make the proposed filters suitable for wireless applications.

ACKNOWLEDGMENT

This work is supported by the 2012 Distinguished Young Scientist awarded by the National Natural Science Foundation Committee of China (61225001), and by National Natural Science Foundation of China (6140010914, 61571231), Natural Science Foundation of Jiangsu Province (BK20140791) and the 2014 Zijin

Intelligent Program of Nanjing University of Science and Technology.

REFERENCES

[1] J. S. Hong and M. J. Lancaster, *Microstrip Filters for RF/Microwave Applications*, New York: Wiley, 2002.

[2] M. Soer, E. Klumperink, P. deBoer, F. vanVliet, and B. Nauta, "Unified frequency domain analysis of switched-series-RC passive mixers and samplers," *IEEE Trans. Circuits Syst. I, Reg. Papers*, vol. 57, no. 10, pp. 2618-2631, Oct. 2010.

[3] J.-T. Kuo, W. H. Hsu, and W. T. Huang, "Parallel coupled microstrip filters with suppression of harmonic response," *IEEE Microw. Wireless Compon. Lett.*, vol. 12, no. 10, pp. 383-385, Oct. 2002.

[4] A. Gorur, "A novel dual-mode bandpass filter with wide stopband using the properties of microstrip open-loop resonator," *IEEE Microw. Wireless Compon. Lett.*, vol. 12, no. 10, pp. 386-388, Oct. 2002.

[5] M. Makimoto and S. Yamashita, "Bandpass filters using parallel-coupled stripline stepped impedance resonators," *IEEE Trans. Microwave Theory Techn.*, vol. 28, no. 12, pp. 1413-1417, Dec. 1980.

[6] H. J. Orchard and A. N. Willson, "Elliptic functions for filter design," *IEEE Trans. Circuits Syst. I, Fundam. Theory Appl.*, vol. 44, no. 4, pp. 273-287, Apr. 1997.

[7] A. Genc, R. Baktur, and R. J. Jost, "Dual-bandpass filters with individually controllable passbands," *IEEE Trans. Compon., Packag. Manuf. Technol*., vol. 3, no. 1, pp. 105-112, Jan. 2014.

[8] S. C. Lin, P. H. Deng, Y. S. Lin, C. H. Wang, and C. H. Chen, "Wide-stopband microstrip bandpass filters using dissimilar quarter-wavelength stepped-impedance resonators," *IEEE Trans. Microw. Theory Techn*., vol. 54, no. 3, pp. 1011-1018, Mar. 2006.

[9] Y. C. Li, X. Y. Zhang, and Q. Xue, "Bandpass filter using discriminating coupling for extended out-of-band suppression," *IEEE Microw. Wireless Compon. Lett.*, vol. 20, no. 7, July 2010.

[10] C. Quendo, E. Rius, and C. Person, "Narrow bandpass filters using dual behavior resonators," *IEEE Trans. Microw. Theory Techn.*, vol. 51, no. 3, pp. 734-743, Mar. 2003.

[11] C. S. Ahn, Y. J. Sung, and Y. S. Kim, "Miniaturization and spurious suppression of dual-behavior resonator bandpass filter using compact microstrip resonant cell," presented at the *Asia–Pacific Microw. Conf.*, New Delhi, Dec. 2004.

[12] M. K. Mandal and P. Mondal, "Design of sharp-rejection, compact, wideband bandstop filters," *IET Microw. Antennas Propag.*, vol. 2, no. 4, pp. 389-393, July 2008.

[13] R. Gómez-García, M. Sánchez-Renedo, B. Jarry, J. Lintignat, and B. Barelaud, "A class of microwave transversal signal-interference dual passband planar filters," *IEEE Microw. Wireless Compon. Lett.*, vol. 19, no. 3, pp. 158-160, Mar. 2009.

[14] W. J. Feng, W. Q. Che, Y. M. Chang, S. Y. Shi, and Q. Xue, "High selectivity fifth-order wideband bandpass filter with multiple transmission zeros based on transversal signal-interaction concepts," *IEEE Trans. Microw. Theory Techn*., vol. 61, no. 1, pp. 89-97, Jan. 2013.

[15] W. J. Feng, W. Q. Che, and Q. Xue, "Overview of high performance wideband bandpass filters based on transversal signal-interaction concepts," *IEEE Microw. Magazine*, vol. 15, no. 2, pp. 84-96, Mar. 2014.

[16] P. H. Deng and J.-T. Tsai, "Design of microstrip cross-coupled bandpass filter with multiple independent designable transmission zeros using branch-line resonators," *IEEE Microw. Wireless Comp. Lett.*, vol. 23, no. 5, pp. 249-251, May 2013.

[17] M. A. Sánchez-Soriano, E. Bronchalo, and G. Torregrosa-Penalva, "Compact UWB bandpass filter based on signal interference techniques," *IEEE Microw. Wireless Compon. Lett.*, vol. 19, no. 11, pp. 692-694, Nov. 2009.

[18] K. X. Ma, S. X. Mou, K. P. Wang, and K. S. Yeo, "Embedded transformed radial stub cell for BPF with spurious-free above ten octaves," *IEEE Trans. Compon., Packag. Manuf. Technol*., vol. 3, no. 9, pp. 1597-1603, Sep. 2013.

Wenjie Feng was born in Shangqiu, Henan Province, China, in 1985. He received the B.Sc. degree from the First Aeronautic College of the Airforce, Xinyang, China, in 2008, the M.Sc. and Ph.D. degrees from the Nanjing University of Science and Technology (NUST), Nanjing, China, in 2010, 2013.

From November 2009 to February 2010, he was a Research Assistant with the City University of Hong Kong. From October 2010 to March 2011, he was an exchange student with the Institute of High-Frequency Engineering, Technische Universität München, Munich, Germany. He is currently a Teacher with the Nanjing University of Science and Technology, Nanjing, China. He has authored or co-authored nearly 100 internationally referred journal papers and conference papers. His research interests include ultra-wideband (UWB) circuits and technologies, substrate integrated components and systems, planar microstrip filters and power dividers,

LTCC circuits etc.

Feng is a Reviewer for over ten internationally referred journal and conference papers, including four IEEE Transactions and three IEEE Letters. He serves as an Associate Editor for the *International Journal of Electronics* from 2015.

Meiling Hong was born in Nantong, Jiangsu Province, China, in 1991. She received the B.E. degree from the Nanjing University of Science and Technology (NUST), Nanjing, China, in 2014. From September 2014, she went to Nanjing University of Science and Technology (NUST), Nanjing, China, for further study as a postgraduate. Her research interests include passive device and circuit.

Wenquan Che received the B.Sc. degree from the East China Institute of Science and Technology, Nanjing, China, in 1990, the M.Sc. degree from the Nanjing University of Science and Technology (NUST), Nanjing, China, in 1995, and the Ph.D. degree from the City University of Hong Kong (CITYU), Kowloon, Hong Kong, in 2003.

In 1999, she was a Research Assistant with the City University of Hong Kong. From March 2002 to September 2002, she was a Visiting Scholar with the Polytechnique de Montréal, Montréal, QC, Canada. She is currently a Professor with the Nanjing University of Science and Technology, Nanjing, China. From 2007 to 2008, she conducted academic research with the Institute of High Frequency Technology, Technische Universität München. During the summers of 2005–2006 and 2009–2012, she was with the City University of Hong Kong, as Research Fellow and Visiting Professor. She has authored or co-authored over 200 internationally referred journal papers and international conference papers. She has been a Reviewer for IET Microwaves, Antennas and Propagation. Her research interests include electromagnetic computation, planar/coplanar circuits and subsystems in RF/microwave frequency, microwave monolithic integrated circuits (MMICs) and medical application of microwave technology.

Che is a Reviewer for the IEEE Transactions on Microwave Theory and Techniques, IEEE Transactions on Antennas and Propagation, IEEE Transactions on Industrial Electronics, and IEEE Microwave and Wireless Components Letters. She was the recipient of the 2007 Humboldt Research Fellowship presented by the Alexander von Humboldt Foundation of Germany, the 5th China Young Female Scientists Award in 2008 and the recipient of Distinguished Young Scientist awarded by the National Natural Science Foundation Committee (NSFC) of China in 2012.

A New Design of Very Compact UWB Band-Stop Filter Using Coupled W-Shaped Strips

Houman Akbarzadeh [1], N. Ojaroudi [2], and Y. Ojaroudi [3]

[1] Electrical Engineering Department
Shahid Sattari Aeronautical University of Science and Technology, Tehran, Iran

[2] Young Researchers and Elite Club, Ardabil Branch
Islamic Azad University, Ardabil, Iran
n.ojaroudi@yahoo.com

[3] Young Researchers and Elite Club, Germi Branch
Islamic Azad University, Germi, Iran

Abstract ─ In this paper, a compact microstrip band-stop filter (BSF) with 3-18 GHz bandwidth for radar applications is proposed. The microstrip filter configuration consists of a transmission line with a pair of coupled W-shaped strips as a stub, and a ground plane. Operation frequencies of the filter can be easily controlled by changing the size of W-shaped strips. The proposed band-stop filter has a very wide bandwidth from 3 to 18 GHz that can be used in C-band (4-8 GHz), X-band (8-12 GHz) and Ku-band (12-18 GHz) applications. An excellent agreement between measured and simulated was obtained. The proposed microstrip filter fabricated on a *Rogers* RT/Duroid 5880 substrate with a relative dielectric constant of 2.2 and has a very small size of 10×15 mm^2. The proposed antenna configuration is simple, easy to fabricate and can be integrated into any radar system.

Index Terms ─ Band-stop filter, radar systems, W-shaped strip.

I. INTRODUCTION

In modern communications, one of the important parameter is isolation between channels in a given bandwidth. Filters with different configurations are essential components in communication systems and these are generally used as signal rejection for unwanted signals and simultaneously allow the wanted signals in required bands [1]. In recent times, the design of filters has become an active research area as filtering is important when used in close proximity to other circuit components, like power amplifiers in the transmitter part and low noise amplifiers in receiver part, for various RF applications [2].

Conventionally, the microwave band-stop filter (BSF) is implemented either by all shunt stubs or by series connected high-low stepped-impedance microstrip line sections. However, generally these are not easily available in microwave band due to the high impedance microstrip line and the spurious pass-bands. To remove these disadvantages, defected ground structures for microstrip lines have been presented in recent years. They have been presented in a number of different shapes for filter applications [3-5]. The DGS applied to a microstrip line causes a resonant character of the structure transmission with a resonant frequency controllable by changing the shape and size of the slot. This technique is suitable for periodic structures, and for both band-stop and band-pass filters, e.g., [6-14].

This paper work deals with design and development of a microstrip band-stop filter for radar application. In this structure, the resonant behaviors of the W-shaped strips are used here introduces transmission zeroes to the filter response and consequently improves its band-stop performance. Also, the reason for the choice of coupled W-shaped configuration is that it provides an almost constant tight coupling, which is important to generate a good frequency response. The designed filter has a small dimension of 10×15×0.635 mm^3.

II. FILTER DESIGN

The proposed microstrip filter configuration is shown in Fig. 1. This band-stop filter was designed on a Rogers RT/Duroid 5880 substrate with 0.635 mm in thickness and with a relative dielectric constant of 2.2. For the input/output connections 50-Ohm microstrip lines are used. The microstrip band-stop filter was designed on both substrate sides by opening aperture in the ground metallization under the low-impedance transmission line.

As shown in Fig. 1, a pair of W-shaped resonators

Submitted On: December 1, 2013
Accepted On: December 11, 2014

is embedded to the microstrip transmission line. The gap between them is used as the coupling structure. The characteristic impedance of the transmission line is chosen to be 50-Ohm to obtain good stop-band matching in wideband.

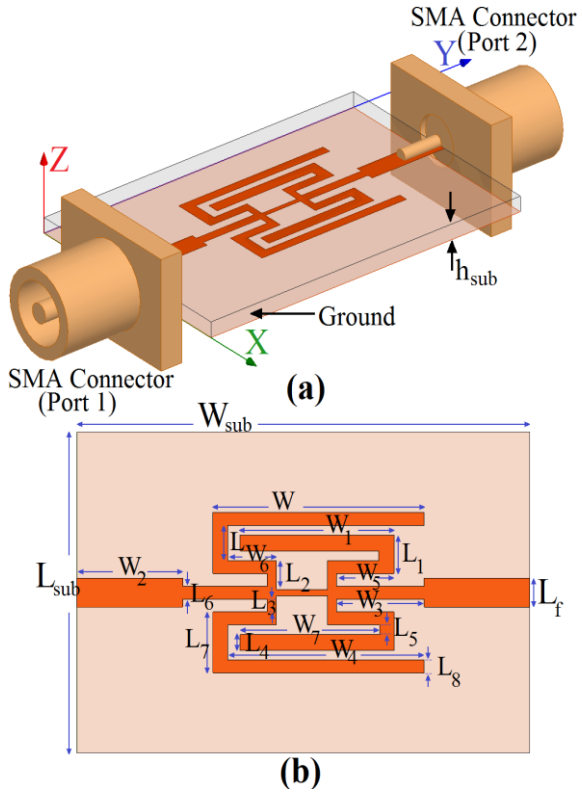

Fig. 1. Geometry of the proposed BSF: (a) side view and (b) top view.

To realize the desired capacitive and inductive values of the filter elements by the stubs of high/low impedance transmission lines, the characteristic impedance and effective dielectric constant of these transmission lines have to be determined. The resonant frequencies of the W-shaped resonators could be easily extracted using the odd-even modes analysis. In the odd excitation case, an electric wall could be added to the symmetric line of the whole structure. Thus, a quasi-quarter wavelength resonator of W-shaped trips could be extracted. In the even case, the electric wall is replaced by a magnetic wall and the resonator can be equivalent to a folded quasi half wavelength resonator.

The BSF's working frequency is dependent on the odd-mode resonant frequency, which could be modified by the pair of C-shaped strips as a microstrip-stub (L_2, L_3, W_5, and W_6). The relative working bandwidth is determined by distance of the odd-even mode frequencies, which could be easily adjusted by the size of W-shaped strips (W, W_1, L, L_1, L_5, and L_7). The matching strength is controlled by L_6, while matching balance is controlled by the bend rate Lf. The widths of the lines (W_2) have smaller impact on frequency tuning than the sizes (W_3).

Another adjustable parameter is the notch of resonator's arm (W_6). The BSF will look simpler without notches. However, without notches, the coupling between feeding line and resonator will be weakest in odd mode, whereas strongest in even mode according to the coupled line theory [15].

As shown in Fig. 2, results in unbalanced coupling or single mode in the working band. Figure 4 illustrates the reflection responses of E-shaped dual mode BSFs with different bend rates. From the curves we could find that two balanced rejection zeros is realized under proper widths of the W-shaped strips. In addition, the gap between feedline and resonator dominates the coupling in both odd-even cases. As shown in Fig. 5, it is quite sensitive. The coupling is stronger with smaller gap size. Final values of the presented band-stop filter design parameters are specified in Table 1.

Table 1: Final parameter values of the proposed band-stop filter

Parameter	W_{sub}	W_{sub}	h_{sub}	W	L_f
Value (mm)	10	15	0.635	7	0.9
Parameter	W_1	L_1	W_2	L_2	W_3
Value (mm)	5.1	1.2	3.5	0.9	2.9
Parameter	L_3	W_4	L_4	W_5	L_5
Value (mm)	0.4	6.5	0.5	1.9	0.3
Parameter	W_6	L_6	W_7	L_7	L_8
Value (mm)	1.6	0.4	4.6	1.9	0.4

III. RESULTS AND DISCUSSIONS

The proposed microstrip band-stop with various design parameters was constructed, and the experimental results of the S-parameter characteristics are presented and discussed. The simulated results are obtained using the Ansoft simulation software high-frequency structure simulator (HFSS) [16].

The structure of the various filters used for simulation studies were shown in Fig. 2. S-parameter characteristics for the microstrip filter with a pair of C-shaped strips (Fig. 2 (a)), the filter with left-side W-shaped and C-shaped strips (Fig. 2 (b)), and the proposed filter structure (Fig. 2 (c)) are compared in Fig. 3. As illustrated in Fig. 3, by using a pair of C-shaped strips as a microstrip-stub, two transmission zeroes at the upper frequencies can be achieved by converting the left-side C-shaped strip to the W-shaped structure, a new transmission zero at the low frequency is generated. Finally, with proposed structure (Fig. 2 (c)), good impedance matching for return loss/insertion (S_{11}/S_{21}) characteristics with 3-18 GHz bandwidth can be achieved [2-5].

In Fig. 4, the surface current distribution of the proposed filter is depicted. In this figure, the current distributions at four different frequencies are presented. The first lower transmission zero is at 3.8 GHz, the upper transmission zero is at 15.5 GHz and the mid-frequencies in the pass-band are at 8.3 and 10.1 GHz. In Fig. 4 (a), the current is mainly located at the left-side W-shaped strip. This implies that the lower transmission zero is mainly due to the bigger W-shaped strip. In Fig. 4 (b), the current is mainly located at transmission line. In Fig. 4 (c) and 4 (d), it can be seen that two sides of the W-shaped strips have effect on the overall performance of the filter because of acting as a half-wave resonant structure [17-19].

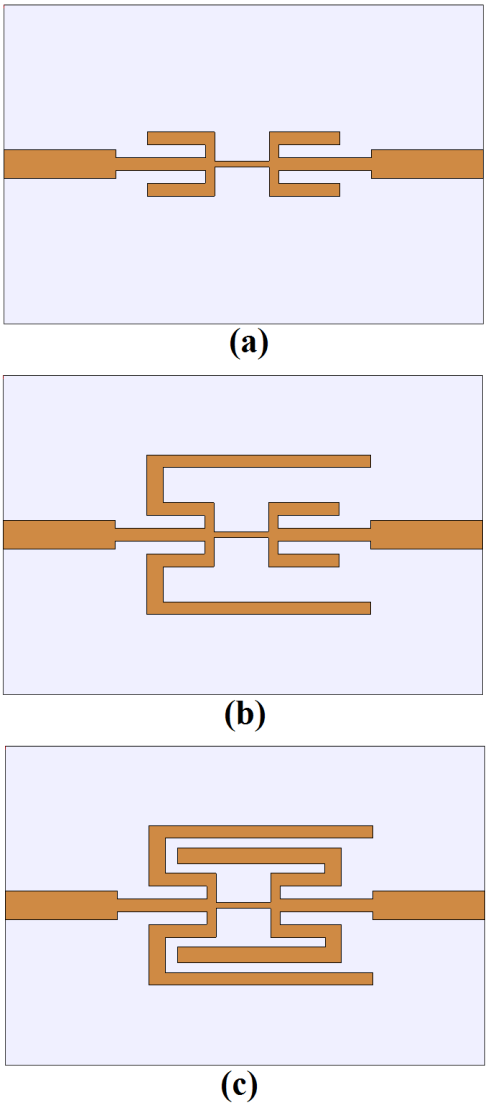

Fig. 2. (a) Microstrip filter with a pair of C-shaped strips, (b) the filter with left-side W-shaped and C-shaped strips, and (c) the proposed filter structure.

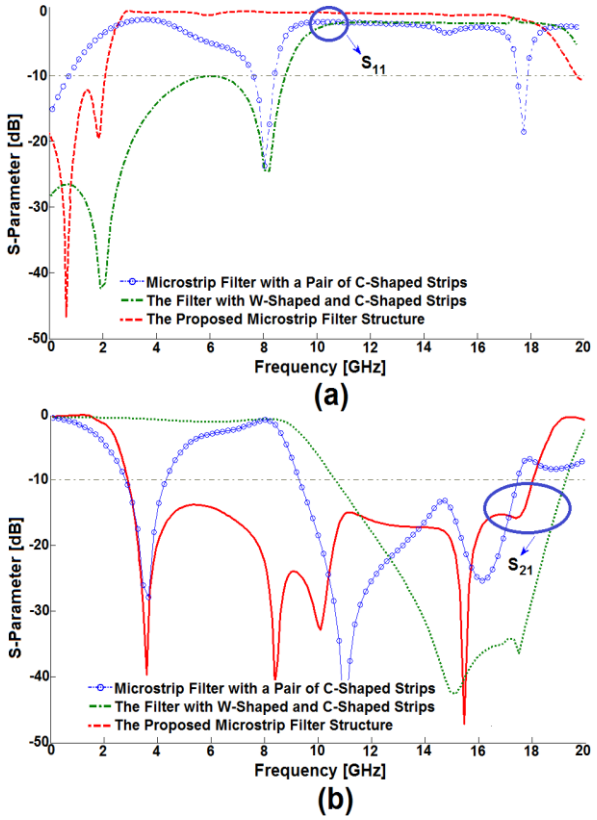

Fig. 3. Simulated S-parameter characteristics for the various structures shown in Fig. 2.

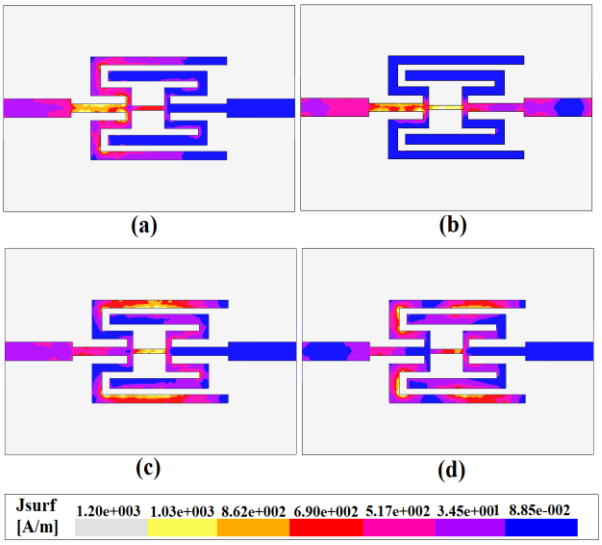

Fig. 4. Simulated surface current distribution of the proposed filter at transmission zeroes frequency: (a) 3.8 GHz, (b) 8.3 GHz, (c) 10.1 GHz, and (d) 15.5 GHz.

The simulated VSWR curves with different values are plotted in Fig. 7. As shown in Fig. 5, when the

interior widths of the W-shaped strips increase from 6.3 and 4.7 mm to 7.7 and 5.3 mm respectively, the lower stop-band frequency is increases from 1.7 GHz to 3.6 GHz and also the upper stop-band frequency is increased from 14 GHz to 19 GHz. From these results, we can conclude that the stop-band operation is controllable by changing the size of the embedded W-shaped strips. As illustrated in Fig. 5, the microstrip filter with W=7.7 mm and W_1=5.3 mm has a coefficient and wider stop-band bandwidth.

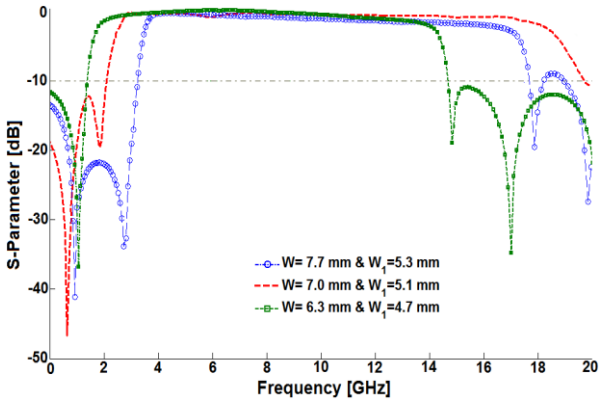

Fig. 5. Simulated and measured insertion and return loss characteristics of the filter.

The proposed filter with final design as shown in Fig. 6, was fabricated and tested that has a good insertion loss (S_{11}) and return loss (S_{21}) are introduced to the filter response from 2.82 to 18.05 GHz. Figure 7 shows the simulated and measured insertion and return loss of the filter. As shown in Fig. 7, a flat insertion and return losses are introduced to the filter response. Consequently, a very wide band-stop characteristic was achieved.

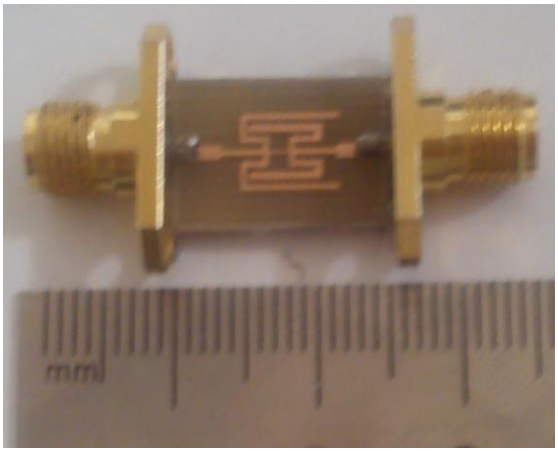

Fig. 6. Photograph of the fabricated microstrip filter.

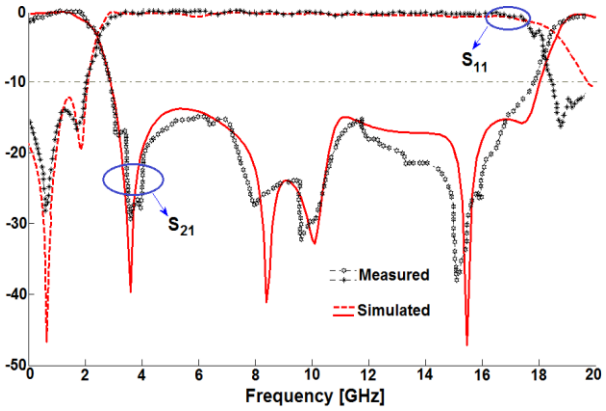

Fig. 7. Simulated and measured return and insertion loss (S_{11}/S_{21}) characteristics of the filter.

IV. CONCLUSION

In this paper, a novel design of band-stop microstrip filter that covers frequency bandwidth of 3-18 GHz has been presented. Configuration of the presented filter consists of a transmission line with a pair of coupled W-shaped strips .The measured results have shown that the fabricated filter has a band-stop characteristic that extends from 2.082 to 18.05 GHz, with an insertion loss (S_{21}) which is larger than 20 dB and a return loss (S_{11}) which is less than 0.5 dB at the center of the band-stop frequency range. The proposed filters are promising for use in radar wireless technologies for UWB communications due to their simple structure, compact size, and excellent performance.

ACKNOWLEDGMENT

The authors are thankful to Microwave Technology (MWT) Company staff for their beneficial and professional help (www.microwave-technology.com).

REFERENCES

[1] J. A. Kong, *Electromagnetic Wave Theory*, EMW Publishing, Cambridge, 2000.

[2] K. L. Finch and N. G. Alexopoulos, "Shunt posts in microstrip transmission lines," *IEEE Trans. Microwave Theory Tech.*, vol. MMT.-38, pp. 1585-1594, 1990.

[3] D. S. La, Y. H. Lu, S. Y. Sun, N. Liu, and J. L. Zhang, "A novel compact band stop filter using defected microstrip structure," *Microw. Opt. Technol. Lett.*, vol. 53, pp. 433-435, Feb. 2011.

[4] X.-H. Wang, B.-Z. Wang, H. Zhang, and K. J. Chen, "A tunable band-stop resonator based on a compact slotted ground structure," *IEEE Trans Microwave Theory Tech.*, vol. 55, pp. 1912-1918, 2007.

[5] W. D. Yan and R. R. Mansour, "Compact tunable

bandstop filter integrated with large deflected actuators," *IEEE MTT-S International Microwave Symposium*, Honolulu, HI, pp. 1611-1614, 2007.

[6] R. Habibi, Ch. Ghobadi, J. Nourinia, M. Ojaroudi, and N. Ojaroudi, "Very compact broad band-stop filter using periodic L-shaped stubs based on self-complementary structure for X-band application," *Electron. Lett.*, vol. 48, no. 23, pp. 1483-1484, 2012.

[7] L. H. Weng, Y. C. Guo, X. W. Shi, and X. Q. Chen, "An overview on defected ground structure," *Progress In Electromagnetics Research* B, vol. 7, pp. 173-189, 2008.

[8] M Ojaroudi and N. Ojaroudi, "Microstrip low-pass filters by using novel defected ground structure slot with a pair of protruded T-shaped strips inside the slot," *Advanced Electromagnetic Symp., (AES)*, 2012.

[9] N. Ojaroudi, M. Ojaroudi, and R. Habibi, "Design and implementation of very compact band-stop filter with petal-shaped stub for radar applications," *Microw. Opt. Technol. Lett*., vol. 55, pp. 1130-1132, 2013.

[10] N. Ojaroudi, H. Ojaroudi, and Y. Ojaroudi, "Very low profile ultra-wideband microstrip band-stop filter," *Microw. Opt. Technol. Lett*., vol. 56, pp. 709-711, 2014.

[11] N. Ojaroudi, Y. Ojaroudi, and S. Ojaroudi, "Novel design of UWB band-stop filter (BSF) based on Koch fractal structures," *Applied Computational Electromagnetics Society (ACES) Journal*, vol. 30, no. 1, pp. 576-581, 2015.

[12] M. Pourbagher, N. Ojaroudi, Ch. Ghobadi, and J. Nourinia, "A novel design of compact board band-stop filter for use in X-band transceivers," *Applied Computational Electromagnetics Society (ACES) Journal*, vol. 30, no. 4, pp. 423-427, 2015.

[13] S. Ojaroudi, Y. Ojaroudi, and N. Ojaroudi, "Compact planar microstrip-fed printed antenna with double band-filtering for UWB application," *Applied Computational Electromagnetics Society (ACES) Journal*, vol. 30, no. 4, pp. 457-462, 2015.

[14] N. Ojaroudi, "Novel design of low-profile microstrip band-stop filter (BSF) with Koch fractal RSLRs," *22nd Telecommunications Forum, TELFOR 2014*, Belgrade, Serbia, Nov. 25-27, 2014.

[15] N. Ojaroudi, "Application of protruded Γ-shaped strips at the feed-line of UWB microstrip antenna to create dual notched bands," *International Journal of Wireless Communications, Networking and Mobile Computing*, vol. 1, no. 1, pp. 8-13, 2014.

[16] Ansoft High Frequency Structure Simulator (HFSS), ver. 13, Ansoft Corporation, Pittsburgh, PA, 2010.

[17] N. Ojaroudi, "A modified compact microstrip-fed slot antenna with desired WLAN band-notched characteristic," *American Journal of Computation, Communication and Control*, vol. 1, no. 3, pp. 56-60, 2014.

[18] N. Ojaroudi, "An UWB microstrip antenna with dual band-stop performance using a meander-line resonator," *22nd International Conference on Software, Telecommunications and Computer Networks (SoftCOM)*, Split, Croatia, 2014.

[19] N. Ojaroudi, "A new design of Koch fractal slot antenna for ultra-wideband applications," *21st Telecommunications Forum, TELFOR 2013*, Belgrade, Serbia, Nov. 27-28, 2013.

Electromagnetic Beam Position Monitoring Model for Particle Energy Linear Accelerator

Sabir Hussain, Alistair Duffy, and Hugh Sasse

School of Engineering and Sustainable Development, Faculty of Technology
De Montfort University, Gateway, Leicester LE1 9BH, UK
shussain95@yahoo.co.uk, apd@dmu.ac.uk, hgs@dmu.ac.uk

Abstract ─ Beam position monitoring (BPM) systems are crucial in particle acceleration facilities such as linear and circular accelerators. They are used to maintain a stable and precise beam position to achieve a high level of beam quality. BPMs are also essential for accelerator commissioning, performance optimisation, and fault analysis. Beam functional properties information, such as displacement from the desired axis, information about synchrotron oscillations and betatron movements can be derived from data gathered in BPM systems. Medical linear accelerators (linacs) also employ beam position measurements to ensure optimal generation of treatment radiation. The most common form of analysis is to use a multi-physics based approach and model the beam as a stream of electrons, often involving Monte Carlo implementation – an accurate but computationally expensive approach. This paper presents a simple, but robust and efficient, CST microwave model of the linear accelerator (linac) beam, generated using a simplified approach to beam modeling that uses a conducting filament in place of the particle. This approach is validated by comparison with published work. An approach to BPM using the method applied in this paper opens up opportunities to further analyze the overall design and that of components of particle accelerator systems using commonly available full-wave electromagnetic simulators without the need to include specific particle solutions.

Index Terms ─ Beam position monitoring, BPM, electromagnetic, linear accelerators, particle accelerators, pickup electrode.

I. INTRODUCTION

A. Linear accelerators

A linear accelerator (linac) is a device that accelerates electrons to high energies through a waveguide [1]. Figure 1 represents an overview of the structure of a medical linear accelerator, typically up to 22 MeV, which is the sufficient energy for practical radiotherapy.

The big challenge to the application of a linac is the production of a monoenergetic high current electron beam of a small focal spot, ensuring a production of sharply focused X-rays [2]. There are two main classes of accelerators: electrostatic and cyclic. The following discussion concentrates on the cyclic type of accelerator, which is widely used in radiotherapy. The electric fields used in cyclic accelerators are variable and non-conservative, associated with a variable magnetic field, resulting in some closed paths along which the kinetic energy gained by the particle differs from zero. If the particle is made to follow such a closed path many times, a process of gradual acceleration is obtained that is not limited to the maximum voltage drop existing in the accelerator. Thus, the final kinetic energy of the particle is achieved by submitting the charged particle to the same relatively small potential difference a large number of times, each cycle adding a small amount of energy to the kinetic energy of the particle [3].

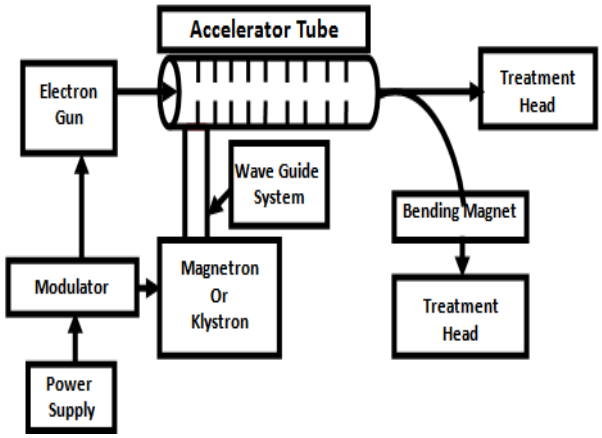

Fig. 1. A block diagram of medical linear accelerator [1].

This cyclic process of acceleration provides an increase in the electron energy. This is then made to imping on a tangsten target for the production of high energy X-rays, typically for tumour treatment. Moreover, the critical performance optimisation of particle accelerators of any kind depends on particle energy beam position monitoring (BPM). For the linear accelerator to be applied successfully in radiotherapy, particularly for

Submitted On: March 24, 2015
Accepted On: January 9, 2016

intensity modulated and image guided radiotherapy processes, the delivery of the dose to encompass the target volume must be done with great accuracy. The divergence of the beam from the desired position within the waveguide and at the point of striking the tangsten target will diminsh the dose profile of the particle beam. This may result in missing the target volume, leading to an unwanted dose to the healthy tissues and structures surrounding the target volume. To overcome this problem, correct positioning of the beam within the linac waveguide is critical for successful radiotherapy outcomes.

The rest of the paper is organized as follows: within the introduction, Subsection B introduces some of the relevant background, including information on energy beams for radiotherapy dose optimization. Subsection C discusses BPM in linear accelerators and Subsection D contains information on the use of the transducer for beam position monitoring. Section II also comprises Subsections A, B, C, D and E in which A introduces the methodology adopted, with specific discussions on simple principles of electromagnetic based simulation of the model. B explains meshing and solver setting for BPM model, C discusses computational experiments made by applying a current carrying wire for beam position monitoring model, and E explains the probability density function and the cumulative distribution function applied for BPM. Section III concerns the results and analysis including the principles applied for the determination of cumulative density function for the BPM model and final section concludes the paper.

B. Energy beams for radiotherapy dose optimization

Considerable effort has been expended to analyse the components of linear accelerators for the assessment of beam quality for high precision intensity modulated radiotherapy (IMRT) dose optimisation [4] and for image guided radiotherapy. These have the aim of enabling the irradiation process to deliver the most effective dose to the target volume, while the radiation is as low as reasonably achievable (ALARA) [5] to the tissues and structures surrounding the target volume. Therefore, the process of optimized dose delivery in photon radiotherapy is performed by establishing treatment-planning models according to the knowledge of energy beam parameters such as energy beam spectra and variations in the distribution of photons incident on the surface of the target volume [6].

Various methods, particularly Monte Carlo (MC), have been considered for many years as the successful techniques for modeling the beam energy components of the linear accelerator for improving accuracy of the dose delivery process in radiotherapy to overcome the speed issues in performing this analysis. Approximation and simplifications may be necessary which compromise the advantages of Monte Carlo dose calculations [7]. This has provided a motivation to investigate full-wave electromagnetic simulation for the optimization of the critical components of the linac instead of multiphysics simulators to solve the dosimetric problems in radiotherapy.

C. Beam position monitoring in linear accelerators

The main goal of this paper is to establish a non-invasive transverse beam position monitoring model for linear accelerator electromagnetic simulation instead of applying special particle solutions. Beam position monitoring systems (BPMs) has critical role for any particle acceleration facilities such as linear and circular accelerators. They are applied to maintain a stable and precise beam position to achieve a high level of beam quality critical for the accelerator performance. For synchrotron accelerators and storage rings, precise and stable beam position becomes necessary during the thousands of revolutions of the beam. The efficiency of the BPMs depends upon its ability to measure small displacements of the beam, compared to its absolute position resolution. Typically the resolution of a system is much better than the accuracy. In most cases, good resolution is much more important than good accuracy. However, it is often appropriate to know the absolute beam position to a fraction of a millimeter, even though the beam motion needs to be known to a few micrometres [8].

Therefore, it is required to constraint the accelerating bunches of electrons throughout the central axis of the waveguide, particularly in the buncher section, otherwise their mutual repulsion will lead the electron beam to diverge. This would ultimately produce losses in the beam current as well as serious damage to waveguide structure [2].

For the beam position measurement, BPM can be calibrated by bench measurement by simulating the field generated by the beam by an rf antenna. However, the EM field generated by the current carrying wire is different from the field induced by the particle beam. Therefore, it is necessary to determine the EM field induced by a beam in a BPM both to calculate its sensitivity and to be able to predict its influence on the stability of the beam. The electric field produced by an ultra-relativistic beam is Lorentz contracted in longitudinal direction which can be considered as established by a line charge of infinite length. This allows one to deal it as a simple electrostatic problem [15].

D. Pickup for beam position monitoring

Pickup electrodes have been used in particle accelerators for determining the displacement of the energy beam from the desired position in the waveguide. For achieving information about the energy beam

position in electron accelerators, several different approaches are present in the literature. Interceptive techniques such as fluorescent screens, wire grids or wire scanners are useful during accelerator installation but cannot be used during accelerator machine operation as they destroy the characteristics of the beam [9]. Even though the electromagnetic pickups are not 'ideal' instruments, they are essential for the operation of the beam. They are still the simplest, fastest and most precise measurement of the beam centre [10].

In a running linac system, the beam must not be disrupted. However, the technique most commonly used to collect information about the spectral content of bunched particle beams is to couple gently to the electromagnetic field of the beam [11]. To comply with this condition, our model of BPM consists of two symmetrically arranged electrode/pickups spaced at 180 degrees, as shown in Fig. 2. Which is in accordance with the conventional technique of using one or two pairs of electrodes, for the measurement of beam offset (i.e., along horizontal and vertical dimention) from its desired position [8]. The pickup electrodes detect the electromagnetic field generated by the conducting filament and convert it to a voltage signal. In order to mimic the real situation of the operating linear accelerator, the use of a current carrying wire in the model is considered as an analogue to the line charge flowing through the centre of the waveguide. Since the electron beam passing through a BPM induces a charge on the pickup electrode, which uniquely depends on the position of the beam and, due to absence of longitudinal variations, the electron beam appears to be essentially a line of moving charge. Measuring the voltage at the pickups can provide the position of the electron beam [12]. This paper verifies the appropriateness of the approach of using a current carrying wire instead of particle beam for beam position monitoring.

E. Probability density function in application of cumulative density function for BPM data

For the beam position monitoring system, the disadvantage of the peak detection method is that the signal peak voltage is very sensitive to the shape of the pulse, and very sensitive due to attenuation in the cable and also due to signal dispersion in lengthy cables [8]. This situation could be resolved by applying a probability density function (PDF) approach for cumulative distribution function (CDF) in calculating the variations in the measured signal. The approach used in this paper is a 'maximum likelihood' approach obtained from the 50% CDF level, its calculation process can be explained in the following paragraphs.

The probability density function of a continuous valued random variable X is traditionally defined in terms of its PDF, f(x), from which probabilities associated with X can be determined using the Equation (1) [13]:

$$P(a < X \leq b) = \int_a^b f(x)dx. \quad (1)$$

This means the probability that X has a value in the interval [a; b] is the area above this interval and under the graph of the density function. The method for PDF employed in this study is continuous probability density functions based on a normal kernel function described in detail in [13] and given in Equation (2):

$$f(x) \equiv \frac{d}{dx}F(x) \equiv \lim_{n\to\infty}\left(\frac{F(x+h)-F(x-h)}{2h}\right). \quad (2)$$

In Equation (2), F(x) is the cumulative distribution function of the random variable x and h is the 'bandwidth'. For a random sample of size n from the density f, X: {x1, x2, … xn}, its empirical cumulative distribution function (ECDF) has this expression:

$$F'^{(x)} = \frac{N\{X \leq x\}}{n}. \quad (3)$$

In Equation (3) N{X ≤ x} shows the number of elements of value less than or equal to x in X. By substituting this to Equation (2) it takes the form:

$$f'(x) = \frac{N\{(x-h)<x\leq(x+h)\}}{2nh}. \quad (4)$$

This equation can be expressed as (5):

$$\hat{f}(x) = \frac{1}{nh}\sum_{i=1}^{n} K\left(\frac{x-xi}{h}\right), \quad (5)$$

where as,

$$K(u) = \begin{cases} -\frac{1}{2}, -1 < u < 1, \\ 0, \ otherwise. \end{cases} \quad (6)$$

The Equation (6) is a kernel density estimator having a uniform kernel function K. Note this kernel function is a uniform function for the data elements interval of -1 to 1. The kernel bandwidth, *h*, controls the smoothness of the probability density curve, its explanation is given in [13]. In this study the Gaussian kernel function is chosen to achieve much smother PDF which has the following form:

$$KGaussian = \begin{cases} (2\pi)^{-\frac{1}{2}} e^{-\frac{u^2}{2}}, -1 < u < 1, \\ 0, otherwise. \end{cases}$$

II. METHODOLOGY

A. Simulations

By using a 3D electromagnetic solver [14], the electron beam position was modelled by creating a perfectly conducting cylinder as a waveguide. A current carrying wire of thickness 2 mm was placed in the centre of the modelled waveguide as an electron beam (around 2 mm being a typical size for the electron beam). It was initially placed at the center of the cylindrical waveguide and its position was calculated using data from the pick-ups. The waveguide length is 160 mm as shown in Fig. 2. The beam termination offset is 150 mm for the setup of lumped element ports on both sides of the cavity. The outer radius of the main cavity is 55 mm and this is also called the beam line radius or waveguide radius. The pick-up electrodes based on the description given in the CST particle studio [14], were modeled as coaxial

systems in which the output voltage was measured.

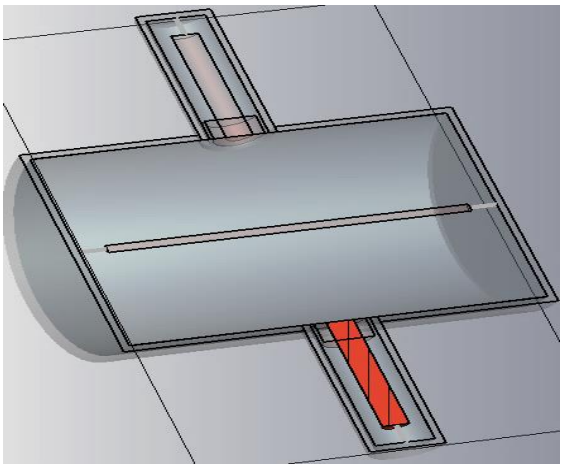

Fig. 2. Cut plane view of the pickup beam position monitoring model.

We have taken a difference-over-sum approach used in [8], and the voltage signal processing is not performed in hardware or electronics instead an excel spread sheet was used. The variations in the measured voltage of various positions of the 'beam' away from the centre provide the information about its displacement from desired position. The BPM data was noted using a CST commercial solver. The variations in the beam position due to its offsets in the transverse plane and with the shift in beam phase from the central axis of the waveguide were determined by time-domain simulations. The outer radius of each pickup was 9.5 mm having height of 18 mm and of inner conductor of the coaxial system was 5 mm with length of 59 mm. These symmetrically arranged electrodes/pickups, as shown in Fig. 2, were connected with two discrete ports with an impedance of 50 Ohm each, were used to detect the electromagnetic field generated by the current carrying wire as a voltage signal.

The behaviour of the electrode was modelled by measuring the voltage signal at the upper port marked as port 2 and the lower port marked as port 3. The beam positional variations are only taken in the transverse direction (i.e., along the Y axis) and, for phase analysis, in the XY plane, which is diagonal to the XY plane in this experiment. For the extraction of the signal from the pickup button, a difference-over-sum scheme was used. One benefit of the difference-over-sum procedure is that it can also be performed in the time domain by using a peak detector to collect the peak voltage in the bipolar signal from the individual electrodes. The disadvantage of peak detection method is that the peak voltage is very sensitive to the pulse shape and also very sensitive to the measurement system attenuation and dispersion [8]. In order to overcome this situation a probability density approach to cumulative distribution function (CDF) to determine the variation in the measured signal at its 50% level was used, as previously described in Subsection E in Section I. The results presented are in good agreement with the trend of data in the published work as shown on page 28 in Ref. [8], redrawn in Fig. 3.

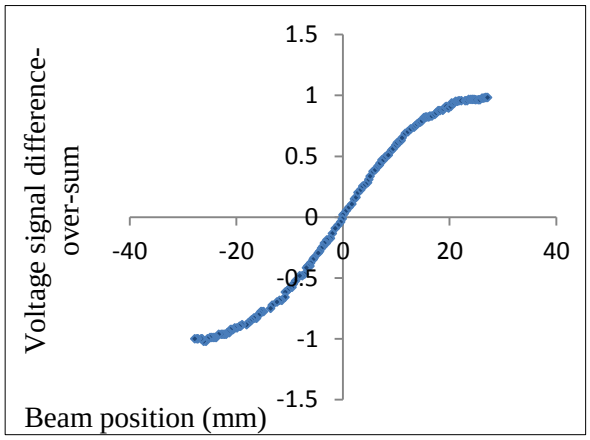

Fig. 3. Beam position monitoring data, redrawn from the reference [8].

B. Meshing and solver parameters settings for the model

Defining the meshing parameters is an important and critical step for the simulation of any model. For this purpose, hexahedral meshing was used, which is very robust even for most complex imported geometries. The hexahedral mesh in the commercial software [14] used 30 lines per wavelength, a mesh limit of 20 and a meshing line ratio of 15 with a smallest mesh limit of 0.15. After applying this mesh setting, the automatic meshing option provided the total 324,131 mesh cells as sketched in Fig. 4.

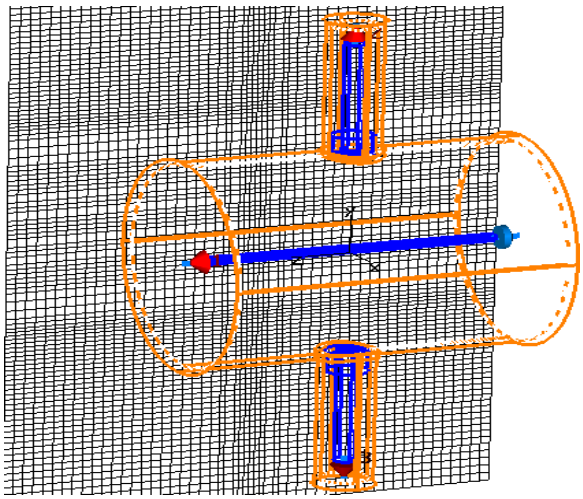

Fig. 4. BPM model with wire frame activated.

The robustness and accuracy of the model was further increased by applying enhance fast perfect boundary approximation (FPBA). This is because the internally used representation of the model geometries is limited regarding the resolution of the geometrical details if the mesh type "FPBA" is used. For the background material, the density points, fixing points option was also applied. Also for the advanced meshing, the option of 'convert geometry data after meshing' was used for model singularity in case of PEC and lossy metal edges. Due to use of different materials in the model, the material based refinement and consideration of surrounding space for lower mesh limit was also used. All these above important mesh setting provided the necessary requirements for the model to obtain the optimal results with a reasonable simulation time. The transient solver with an accuracy limit of -30 dB was used. For the waveguide setting, inhomogeneous port accuracy enhancement (QTM (Quasi-TM) modes) was used and twenty frequency samples were taken. The accuracy of 1% with maximum passes 4 for the line impedance adaptive solver run was implemented.

The mode calculation frequency during the simulation was 2.856 GHz. In order to meet the steady state criteria, 200 pulses for solver setting were implemented. This parameter needs to be selected with much care since without its optimum selection, the solver will not run.

C. Computational experiments for beam position monitoring

The energy beam, as a current carrying wire, was displaced in the transverse direction to mimic the real situation of beam displacement.

The voltage signal from the displaced beam along the various transverse positions was determined at the upper and lower ports. The voltage signal V2 at upper port marked as port 2 and V3 at the lower port marked as port 3 were noted for the tranverse offsets of the beam and the difference over sum of signals from these ports were calculated by using following equation:

$$\frac{\Delta V}{\Sigma} = \frac{(V2-V3)}{(V2+V3)}. \quad (7)$$

The data of voltage signals at the origin and at various offsets with an increment of 1 mm up to 23 mm was calculated and variations in the voltage signal were determined by computing the difference/sum for each displacement. A kernel density estimator is used to smooth the data and the cumulative distribution function is then obtained as in [13]. This is to overcome the drawback of detecting the signal peak method [8]. The CDF values were calculated for different beam offsets in the transverse plane in the +ve and –ve directions. The changes in the voltage signals due to change in the positions of the beam were simulated by determining the variations at 50% of the cumulative density level. 50% was selected simply because of it being a mid-range value and, in general, the turning point for the probability density function: i.e., the peak probability. The results were analysed which showed the values of the voltage signals at 50% CDF for various offsets of the beam at 2 mm with an increment of 1 mm up to 23 mm from the beam origin.

III RESULTS AND ANALYSIS

A. Beam position monitoring results with cumulative density function

The data obtained by simulation was analysed to obtain voltage signals on the pickup. The energy beam positions simulated at various displacements were determined with respect to the central axis. The CDF curve shown in Fig. 5 is representative of the cumulative distribution function for the beam offset at 11 mm from the beam central axis. Similarly, this distribution was calculated for all beam positions by displacing the beam away from the central axis. The CDF data was obtained for beam offsets in the transverse direction, i.e., on +ve and –ve Y axis and for 45 degrees shift in phase of the beam along the diagonal of the XY plane on the +ve and –ve dimention, the proceeding paragraph and Subsections B, and C further analyse these results.

The combined graph of 50% CDF values was obtained for all the beam offsets in the range 0 to 23 mm and is presented in the following figures. For illustration purposes, the trend of the CDF plotted values is examined in Fig. 6 by taking only the extremes of maximum and minium beam displacements in the +ve and -ve Y axis. These CDF values of beam offset illustrate the symmetric pattern of the data. To observe the variations in the voltage signals due to a shift in the beam phase of 45 degrees (i.e., on the diagonal of the XY plane), CDF values were calculated in both XY +ve and –ve planes.

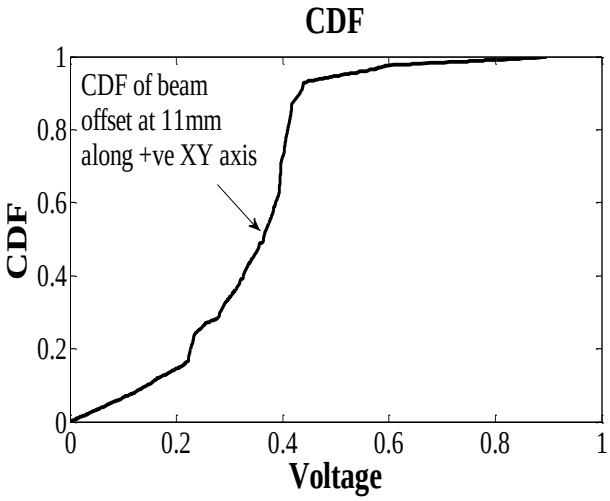

Fig. 5. CDF data verses voltage at 11 mm beam offset.

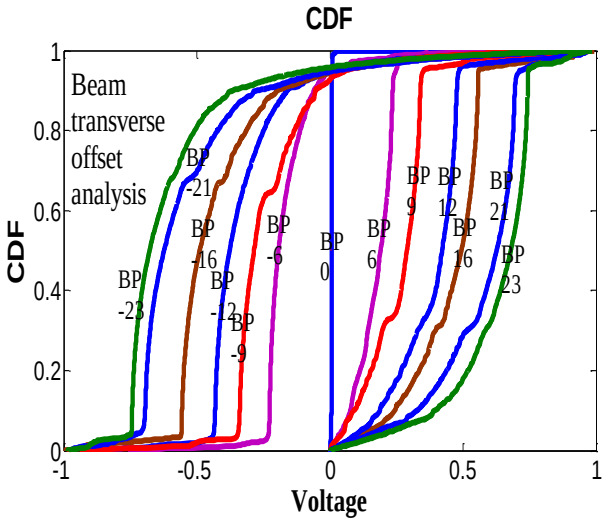

Fig. 6. Combine CDF curves for beam position offsets in transverse plane from beam central axis.

The trend of the data and their combined symmetric pattern can be observed from Fig. 8. Figures 7 and 9 represent all the numerical values at the 50% CDF levels for various beam positions (BP). In Fig. 6, curve BP0 refers to the beam position at the origin and curve BP3 refers the beam at displacement of 3 mm in the transverse plane in +ve Y axis and curve BP-3 referred as beam position at the distance of 3 mm in the –ve Y axis and for the beam offsets ranging 4 mm to 23 mm same pattern was used. Similarly, for the beam position phase analysis in Fig. 8, CDF curve BP0 refers to the beam at the origin, BP3 referred beam position at 3 mm in the XY plane with the phase angle of 45 degrees and in the –ve XY plane the same position referred as BP-3 for -3 mm. The same pattern of beam position representation was used for the beam offsets ranging 4 mm to 23 mm.

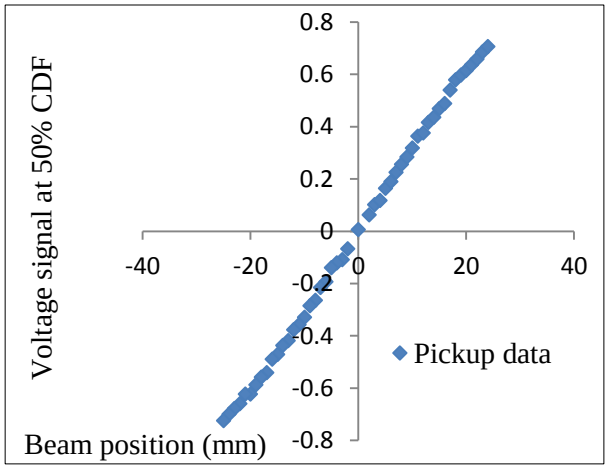

Fig. 7. CDF data for beam position in transverse directions (i.e., along +ve and –ve Y axis).

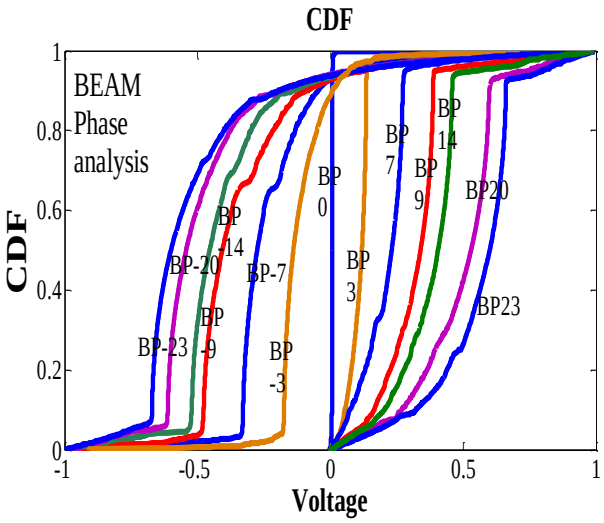

Fig. 8. Combine CDF curves for beam offsets at 45 degrees in XY plane from beam central axis.

B. Beam position due to transverse offsets

The transverse offsets of the beam positions were determined from the CDF data taken on linear scale. The values of the voltage signals are graphed in Figs. 6 and 7. In Fig. 6, the curve BP0 referred to beam at the origin which is considered as an ideal beam position. The data was further analysed for the simulated approach to observe any changes that might be present in the linearilty of the data due to the establishment of the current carrying wire approach compared to the particle beam consisting of electron bunches. This has also validated the approach described in Section I. The cumulative distribution functions of the voltage signals were simulated at various displacements with an increment of 1 mm, from 2 to 23 mm and also in negative directions for same displacements from the central axis. The combined graph of Fig. 6 for various cumulative density functions has shown variations in the voltage signal at 50% of CDF. This means that the signal value changes with respect to beam displacement from its central position considered as the desired beam axis.

C. Beam phase analysis

The beam phase analysis given in Fig. 9 of the combined CDF data shows the computation of the voltage signal variations for the BPM at 45 degrees with respect to its position at 90 degrees. It shows that a change in the signal appeared as the beam phase angle varies from 90 to 45 degrees with respect to Z axis, it could be observed by comparing the Figs. 7 and 9. The data obtained with change in phase angle of 45 degrees along the +ve and –ve XY plane is drawn in Fig. 9. The graph trend shows that the major effect is due to beam offset in the transverse plane (along Y axis), specially with the shift in the beam phase of 45 degrees (i.e., on

the diagonal of the XY plane). A change in the linearity of the graph also appears particularly with the shift of 45 degrees in the beam phase. It has observed that the BPM data obtained from our proposed approach is similar in trend with the data presented in Fig. 3.

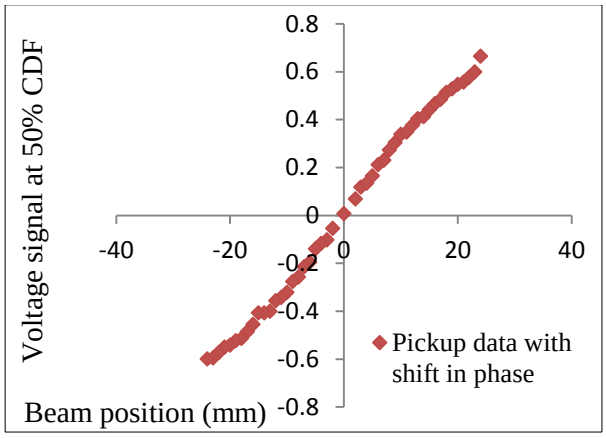

Fig. 9. CDF data for beam phase, phase analysis.

IV. CONCLUSION

A simple and robust model of beam position monitoring (BPM) for the linear accelerator (linac) was obtained using full-wave electromagnetic simulation. A brief review was also presented about electron beam characteristics, beam position monitoring (BPM) concepts and beam parameter processing methods used in particle accelerators. The BPM data was generated through the application of CST 3D electromagnetic software.

The analysis of the data was performed by using a cumulative distribution function. The CDF has provided close approximation to the real situation of the BPM. The simulated results showed the variations in the voltage signal generated at the pickup electrode due to displacement from its central axis and a single numerical value of this voltage signal is obtained from the 50% of the CDF level. The analysis of the model was also made by taking into account the effects of variations in the phase on beam position and its effects on the voltage signal due to displacement of the beam along the horizontal direction. The simulated data of the BPM model was compared with published work, which demonstrates that the behavior of the proposed approach is similar to the data published in [8]. This has validated the approach applied in our study and demonstrates the potential to use a full wave electromagnetics solver to analyse such systems with the result that studies such as probe design and analysis can be undertaken without the need to use Monte Carlo methods and multiphysics/particle simulation software.

REFERENCES

[1] F. M. Khan, *The Physics of Radiation Therapy*, 3rd ed., Lippincott & Wilkins, Q 2003.

[2] L. Loverock, *Linear Accelerators*, ch. 11, Taylor & Francis Group, LLC, 2007.

[3] E. E. B. Podgorsak, *Review of Radiation Oncology physics: A Handbook for Teachers and Students*, Department of Medical Physics, McGill University Health Centre Montréal, Québec, Canada, 2005.

[4] S. Hussain, et al., *Modeling of Linear Accelerator MLC for the Assessment of Beam Quality Dependence in IMRT*, M.Sc. Thesis, School of Physics and Astronomy, The University of Birmingham, Birmingham B15 2TT, UK, Dec. 2004.

[5] ICRP 26, *Recommendations of the International Commission on Radiological Protection*, Annals of the ICRP 1, 3, 1977.

[6] S. Hussain, "Artificial neural network model for spectral construction of a linear accelerator megavoltage photon beam," *UKSim/AMSS IEEE 1st International Conference on Intelligent Systems, Modelling and Simulation*, Liverpool, England, UK, pp. 86-91, 2010.

[7] N. Reynaert, et. al., *Monte Carlo Treatment Planning an Introduction*, Report 16 of the Netherlands Commission on Radiation Dosimetry, 2006.

[8] R. E. Shafer, "Beam position monitoring," *American Institute of Physics (AIP) Conference Proceedings*, vol. 212, pp. 26-58, 1989.

[9] C. Peschke, *Higher-Order-Mode Dampfer als Strahllagemonitore*, Ph.D. Thesis, Johann Wolfgang Goethe-Universit_t Frankfurt am Main, 2006.

[10] P. Strehl, *Beam Instrumentation and Diagnostics*, Berlin: Springer-Verlag Berlin Heidelberg, 1st ed., 2006.

[11] I. Podadera, *Tutorial on Electromagnetic Beam Position Monitors for Low-β High Intensity Linacs*, Sep. 27, 2011.

[12] C. D. Chan, *Beam Position Monitor Test Stand*, Department of Physics and Astronomy, the Johns Hopkins University, Baltimore, MD, 21218, 2004.

[13] J. S. Simonoff, *Smoothing Methods in Statistics*, New York: Springer Verlag, 1996.

[14] CST, Microwave Studio® (CST MWS) and Particle Studio (PS).

[15] B. W. Zotter, et al., *Impedances and Wakes in High-Energy Particle Accelerators*, pp. 364, ISBN: 978-981-281-738-9, Published: Jan. 1, 1998.

Design and Electromagnetic Analysis of a New Rotary-Linear Switched Reluctance Motor in Static Mode

M. M. Nezamabadi, E. Afjei, and H. Torkaman

Faculty of Electrical Engineering
Shahid Beheshti University, G.C., Tehran, Iran
{m_nezamabadi, e-afjei, h_torkaman}@sbu.ac.ir

Abstract ─ A newly designed rotary-linear switched reluctance (RLSRM) motor is presented and electromagnetically analyzed in this paper. The motor has an integrated structure and can control both linear and rotary motions. It is mainly designed to control the engagement of a rotating gear. For this purpose a two-section motor comprised of a rotary and a linear SRM is designed. In the middle part of the motor assembly, a three-phase rotary SRM with 6 stator and 4 rotor poles creates rotary motion. The linear section which is a transverse flux two-phase SRM is composed of two parts placing at each side of the rotary section. The cylindrical translators inside the linear stator poles provide short magnetic flux paths which reduce the core losses and increase the force per volume. The motor parameters derived from the motor design procedure are evaluated using 3-dimensional finite element analysis (3DFEA). The motor performance indices such as flux linkages, flux density, mutual flux, static torque and force for various loads are obtained and assessed for rotary and linear motions. Finally, a comparative study is performed and 3DFEA results are compared with two different RLSRM structures. The comparison shows that the proposed structure has the highest force per motor volume.

Index Terms ─ Electromagnetic analysis, finite element analysis, rotary-linear motion, switched reluctance motor.

I. INTRODUCTION

Switched reluctance motors have become a popular alternative for variable speed drives in recent decade. Simple structure, lack of magnetic material or coil on the moving part, fault tolerance, and low manufacturing and maintenance costs have changed it to a serious competitor for induction and brushless DC motors [1-5]. In contrast with many of the DC and AC motors, SRMs need a control system for normal operation. This requirement restricted its utilization but appearing low cost power semiconductors accelerated its application in recent years. Rotary and linear structures have been developed for SRMs with a variety of applications. For rotary type, different variable speed applications such as home appliances, electric and hybrid electric vehicles have been introduced. Linear SRM has been used in elevators and electrical trains [6-9].

Rotary and linear motions are needed together in several applications. Power transmission systems in automatic or electrical vehicles, robots, wire winding machines, weaving equipment, and component insertion systems are among the known applications [10]. Usually, two or more motors or combination of pneumatic, hydraulic, and electric systems are needed to provide the motions required in these applications. Conventional systems for rotary-linear motion control are often accompanied by some mechanical parts such as gears or belts. These systems require frequent maintenance and adjustment that decrease the whole system reliability [11]. Less mechanically complicated and more electronically controllable solutions for rotary-linear motion control are highly demanded. Rotary-linear electrical motors providing both rotary and linear motions in an integrated structure are a good alternative for conventional electro-hydraulic systems [12]. These rather newly appeared motors can bring more controllability and precision, faster response and higher efficiency with less cost and space [13].

Several structures for rotary-linear motors based on SRM technology have been reported in the literature in recent years [14-19]. In [14], a RLSRM consisting of two separate stators and a rotor-translator is proposed. The rotary and linear motions are controlled by the optical sensors inside the motor and the linear position sensor mechanically coupled to the shaft, respectively. The motor operation depends on the precision and adjustment of two sensor types which impose cost and complexity to the system and reduce the reliability. For this structure, a control strategy based on the multiphase excitation method has been reported in [15,16]. A torque and force distribution function is proposed for the RLSRM to decouple the two axes of motion. The control strategy is still dependent to the sensors information.

Another RLSRM with two different structures for rotary and linear stators is introduced in [17]. Due to the

Submitted On: July 20, 2015
Accepted On: December 5, 2015

encoder coupling to the motor, the shaft is only accessible from one side. The long rotor creates magnetic interference for rotary and linear motion control.

Two different RLSRM structures with their electromagnetic simulations are exposed in [18,19]. Using position sensors and the interference of rotary and linear motions control have increased the complexity in all of the proposed RLSRMs.

In the structures that utilize multi-stacks of slotted rotor [14-18], excitation of the linear phases produce torque and the motor has combined rotary-linear motion instead of pure linear motion. So at least they need a decoupling strategy to decouple rotary and linear motion control [15,16]. In multi-stack RLSRMs the number of rotor poles are less than the number of stator poles. So it is not possible to utilize all of the rotor and stator cores capacity for linear force production as only one stator phase poles are in rotationally aligned position at each time and can be used for linear motion without torque production.

The main purpose of this paper is proposing a new RLSRM for independent control of the rotary and linear motions. The completely separated magnetic flux paths decouple the motor operation in rotary and linear modes and give the possibility to control two-axis motion both simultaneously and separately.

In this research, the new RLSRM is capable of working in three different modes: 1- Rotary, 2- Linear, 3- Rotary-linear (RL). For solving the problems originated from slotted translators, two cylindrical translators have been used. Also, the hybrid motion control by the constructed RLSRM does not need any decoupling control algorithm, which is an important issue in the other rotary-linear motors. The decoupled rotary and linear motion control and simple integrated structure are the advantages of the proposed RLSRM.

In the following, after a discussion about the design procedure of the motor in Section 2, the design verification by 3DFEA is presented in Section 3. For design verification, static analysis is performed by 3DFEM. Based on the available information for the other RLSRMs structures, a comparative study has been performed at the end of Section 3. Finally, the consequences of this research are described in Section 4.

II. DESIGN AND THEORETICAL ANALYSIS OF THE NEW RLSRM

The motor is designed to engage and disengage a rotating gear in a wire winding machine. It is comprised of two sections, each one responsible for one axis motion control. The rotary section which is a radial field rotary SRM is in the middle part of the motor assembly. It has 6 salient poles on the stator and 4 on the rotor. The coils on the stator opposite poles are serially connected and form a phase. Therefore, the motor has 3 phases that should be excited sequentially to rotate the rotor. Since the motor shaft has both rotary and linear motions, the rotor stack length has been considered as the half of the stator stack length. The linear section is a two phase transverse flux LSRM with active stators and passive translators. Each phase is comprised of a six-pole stator and a cylindrical translator situated at both sides of the rotary section. For the sake of simplicity, the linear and rotary stators have the same structures. The structure of the new RLSRM is illustrated in Fig. 1.

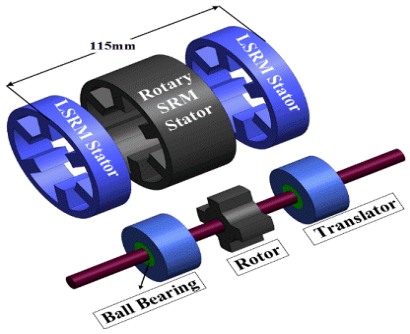

Fig. 1. The proposed structure for RLSRM.

All of the coils in each linear stator phase are serially connected and excited together. The coils are wrapped around the poles in a way that make opposite magnetic poles in two neighbor stator poles. Therefore by exciting a phase coils the magnetic flux finds short paths inside the translator. The short magnetic flux paths increase the motor efficiency by reducing the magnetic core losses. During a phase excitation 6 magnetic circuits are established by the translator, stator pole windings, and two air gaps. The translator moves toward more overlap with the stator poles in order to create the magnetic circuit with minimum reluctance. The configuration of the linear section facing the front view is depicted in Fig. 2.

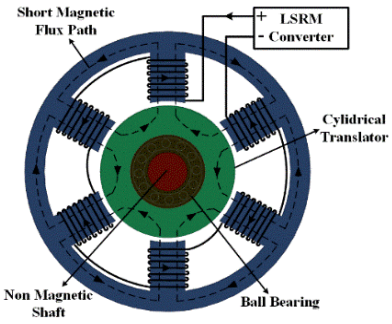

Fig. 2. The front view of the linear section.

If the translator rotates while the linear phase coils are energized, the magnetic field induced in the translator produces undesirable negative torque. Therefore, each translator is coupled to the shaft by a pair of ball bearings. The bearings are fixed on the shaft so that the

coupled translator can rotate freely while it cannot move linearly relative to the shaft. In this way, the translators can have linear motion while the shaft is rotating inside the bearings. For retaining the shaft so that it can move linearly while rotating, one slide-rotary bush (SRB) couples the shaft to the motor cap at each side. The structure of the SRB is shown in Fig. 3.

(a)

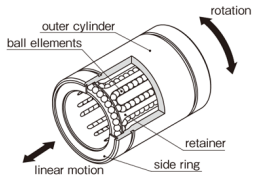

(b)

Fig. 3. (a) The used slide-rotary bush, and (b) the internal structure of the slide-rotary bush [20].

The SRBs retain the shaft at the center of rotation axis while the shaft can rotate and slide freely on the SRB ball elements.

A. Design procedure-rotary section

For decoupling the control of rotary and linear motions, separate structures are considered for each kind of motion. The motor design starts with selecting parameters for a radial field 3-phase, 6/4 rotary SRM. The output equation of a SRM is given by:

$$P_o = K_m B A_s D^2 L N, \quad (1)$$

in which P_o is the output power, A_s is the specific electric loading, D is the bore diameter, and N is the rotor speed in RPM. K_m is a factor depends on several parameters such as the motor efficiency, duty cycle, and saturated and unsaturated inductances [3]:

$$D = \sqrt[3]{\frac{P_o}{K_m k B A_s N}}. \quad (2)$$

The rotor stack length is calculated by:

$$L = kD, \quad (3)$$

in which k is a parameter that depends on the nature of the application. The range of k for non-servo applications is:

$$0.25 < k < 0.7. \quad (4)$$

Assuming β_s and β_r as the stator and rotor pole arcs, the width of stator and rotor poles t_s and t_r can be calculated as:

$$t_s = D \sin\left(\frac{\beta_s}{2}\right), \quad (5)$$

$$t_r = D \sin\left(\frac{\beta_r}{2}\right). \quad (6)$$

The range of stator and rotor yoke thicknesses, S_y and R_y are given by:

$$0.5t_s < S_y < t_s, \quad (7)$$

$$0.5t_r < R_y < 0.75t_r. \quad (8)$$

The magnetic field intensity in the air gap is obtained from (9):

$$H_g = \frac{B}{\mu_0}. \quad (9)$$

The number of turns per phase for a peak current of I_p is:

$$N_{ph} = \frac{H_g \times 2g}{I_p}. \quad (10)$$

The cross section of the conductor is calculated from (11) in which J is the conductor current density:

$$A_c = \frac{I_p}{J\sqrt{q}}. \quad (11)$$

For obtaining the stator pole height, h_s it is required to calculate the stator coil width, C_w and height C_h. Subtracting the stator pole arc lengths and the distances between adjacent coils from the bore periphery, the coil width can be calculated from (12):

$$C_w = \frac{\pi D - P_s\left[\beta_s \cdot \frac{D}{2} + C_g\right]}{2P_s}, \quad (12)$$

in which P_s is the number of stator poles and C_g is the gap between the stator adjacent coils. The stator coil height is achieved from (13):

$$C_h = \frac{a_c N_{ph}}{2C_w}. \quad (13)$$

The stator pole height is specified considering the span given in (14):

$$C_h < h_s < 1.4C_h. \quad (14)$$

The rotor pole height, h_r is obtained by applying the calculated parameters in the previous steps to (15):

$$h_r = \frac{D - 2(g + R_{sh} + R_y)}{2}, \quad (15)$$

in which R_{sh} is the shaft radius.

Table 1 shows the final parameters of the rotary SRM obtained from theoretical formulation.

Table 1: Specifications of rotary SRM

Parameter	Value	Parameter	Value
Rated power	80 W	Rotor pole width	10 mm
Rated speed	3000 RPM	Stator pole width	8.8 mm
Air gap	0.25 mm	Rotor yoke thickness	5.4 mm
Supply voltage	48 V	Stator yoke thickness	5 mm
Phase peak current	2.5 A	No. of turns/coil	120
No. of stator poles	6	Rotor stack length	17.5 mm
No. of rotor poles	4	Stator stack length	35 mm
Specific elec. loading	28500 A/m	Rotor pole height	7.3 mm
Rotor pole arc	32 Deg.	Stator Pole height	13 mm
Stator pole arc	28 Deg.	Rotor pole width	9.8 mm
Shaft radius	5 mm	Stator pole width	8.7 mm
Current density	5 A/m^2	Bore diameter	36 mm
k	0.48	Conductor cross section	0.3 mm^2

B. Design procedure-linear section

For controlling the engagement of a rotating gear a

two-phase transverse flux LSRM is designed to create forward-backward movement. Before designing the LSRM several assumptions should be considered. The required linear force and displacement are 14 N and 17.5 mm, respectively. For having simple and uniform structure the linear stator is considered the same as the rotary stator with less stack length. The motor structure side view is illustrated in Fig. 4.

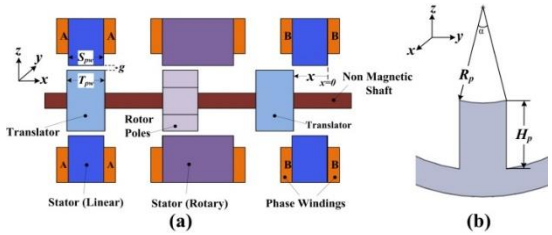

Fig. 4. (a) The structure of the RLSRM facing the side view, and (b) the linear stator structure.

Considering a linear phase, the variation of magnetic energy in the air gap as a result of translator movement can be calculated by:

$$dW_f = \frac{1}{2} B_{ag} H \; dV, \tag{16}$$

in which B_{ag} is the magnetic flux density in the air gap, H is the magnetic field intensity and dV is the air gap volume variation. The air gap volume variation as a result of translator movement along the x-axis will be:

$$dV = dA_{tp}\, g = R_p\, \alpha \left(S_{pw} - x\right) g, \tag{17}$$

where A_{tp} is the overlapping area of the translator and one stator pole, g is the air gap, R_p is the bore radius, α is the stator pole angle, x is the axial translator displacement, and S_{pw} is the stator pole width. The linear force, f_L for a constant exciting current can be calculated as:

$$f_L = \frac{\partial W_f}{\partial x} = \frac{1}{2} \frac{B_{ag}^{\;2}}{\mu_0} \left(-R_p \alpha\right) g. \tag{18}$$

By neglecting the translator and stator core reluctances against the air gap reluctance the magneto motive force (mmf) is achieved:

$$\Im \cong \frac{B_{ag}}{\mu_0} g. \tag{19}$$

Considering (17) and (18) reveals that the force is only a function of mmf, stator pole circumferential length ($R_p\alpha$) and air gap:

$$f_L = -\frac{1}{2} \mu_0 \Im^2 \frac{R_p \alpha}{g}. \tag{20}$$

By utilizing variable equivalent air gap permeance model for SRM [21], it is possible to develop an equation for the linear force produced by one phase excitation:

$$f = \frac{6}{\mu_0} \frac{P_c}{K_c K_s} B_{ag}^{\;2} . g . \alpha . R_p, \tag{21}$$

in which K_c is Carter's factor and P_c is the permeance coefficient. K_s is saturation coefficient depended to the core material magnetic characteristics and the length of magnetic flux path in the core and air gap. The required slot area A_w for winding as a function of air gap flux density B_{ag}, current density J, and fill factor K_w is obtained:

$$A_w = \frac{2g\, B_{ag}}{\mu_0 J\, K_w}. \tag{22}$$

For designing the linear section the following parameters are considered initially: air gap length g, air gap flux density B_{ag}, stator slot fill factor K_w, saturation coefficient K_c, Carter's coefficient K_s, permeance coefficient P_c, and current density J. The winding area obtained from (23). Applying (19), the required mmf per coil is achieved. So for the peak current value the number of turns per coil can be calculated. The required 14 N linear force gives the stator pole circumferential length from (20) $R_p.\alpha$. Since the rotary and linear stator structures are the same, the optimized R_p and α are calculated, respectively. The prior assumptions and the calculated parameters for the linear section are summarized in Table 2.

Table 2: Specifications of the linear SRM

Parameter	Value	Parameter	Value
Air gap	0.25 mm	Peak current	4 A
B_{ag}	1.6 T	Slot area (A_w)	3 cm^2
Slot fill factor	0.4	mmf/coil ($\Im$)	300 A.t
Saturation coeff.	1.6	No. of turns/coil	75
Carter's coeff.	1.4	Bore radius	18 mm
Permeance coeff.	1.3	Stator pole arc	28 Deg.
Current density	5×10^6 A/m^2		

Considering the motor whole volume V, the motor force per volume, F_v is:

$$F_v = \frac{F_{lmax}}{Motor\,Volume} = \frac{14}{\pi \times (40)^2 \times 140 \times 10^{-9}} = 19894 \left[N/m^3 \right]. \tag{23}$$

For design verification, the proposed structure completely analyzed with 3DFEM and the results are given in the following section.

III. ELECTROMAGNETIC ANALYSIS OF RLSRM USING 3DFEM

Complete and accurate modeling of the designed motor is a necessary step in verifying the obtained parameters from analytical calculations. Finite element method is a precise and efficient solution for modeling and analyzing magnetic circuits. Although it is more complex and time consuming, 3DFEA of the machine has remarkable advantages over 2D. Some practical parameters such as the motor length effects cannot be

considered in 2D analysis. For starting the analysis geometric and magnetic model of the motor are specified then the boundary conditions and polynomial order are set. Based on the input information, the initial 3D meshing is performed and the magnetic field distribution is calculated inside and around the motor layout. Based on the achieved magnetic field distribution, some other parameters such as flux linkage, core losses, and torque (force) can also be obtained. Figure 5 shows the initial 3D mesh layout of the designed RLSRM in Magnet CAD package for analysis [22].

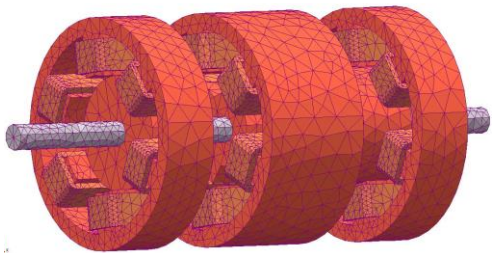

Fig. 5. 3D finite element meshing of the designed RLSRM.

Both stator and rotor cores are made up of non-oriented silicon steel laminations, while the shaft is from non-magnetic material. Static analysis is performed by 3DFEM and the results are given in the following.

A. Static electromagnetic analysis of RLSRM

For static analysis after determining the geometric model, the parameters of 3DFEA are set. For the rotary SRM, the coils of one phase are energized and the magnetic field distribution is calculated from unaligned to the next unaligned positions.

Fig. 6Figure 6 illustrates the magnetic flux density and flux path with the motor poles in unaligned and aligned positions. The coils of phase A are energized with 2A constant current and the rotor rotates with mechanical resolution of 0.5 degree. In each step, the magnetic field distribution is calculated and recorded. The flux density of the rotor pole is about 0.97 and 0.1 Tesla for aligned and unaligned positions.

The variation of flux linkage with refer to the rotor pole position is shown in Fig. 7, for various excitations. Regarding to four times excitation of phase A in one rotation, its flux linkages are raised according to the rotor position. As shown in this figure, the maximum amplitude of flux linkage is about 33, 25, 17 and 8 mWb at aligned rotor position for 2, 1.5, 1 and 0.5 A, respectively.

The angular position is measured between the center of two adjacent rotor poles and the center of the excited stator pole. By starting the rotor and stator poles overlap the magnetic circuit would have the maximum inductance variation versus rotor position. In Fig. 7, the rotor and stator poles overlap starts at 15°. Since the rotor can move linearly inside the stator, the analysis of the flux linkage is performed in 3 different linear positions with 1 A excitation current. The results of the analysis with the rotor at the sides and middle of the stator are exposed in Fig. 8.

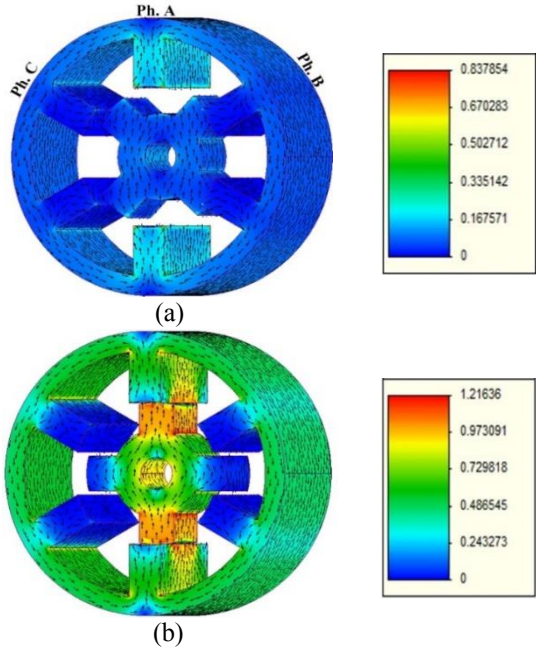

Fig. 6. Flux density and flux path of the rotary section at: (a) unaligned, and (b) aligned positions.

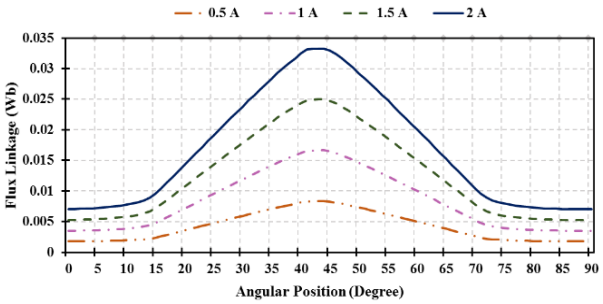

Fig. 7. Variation of flux linkage versus the rotor pole angular position in rotary motion mode.

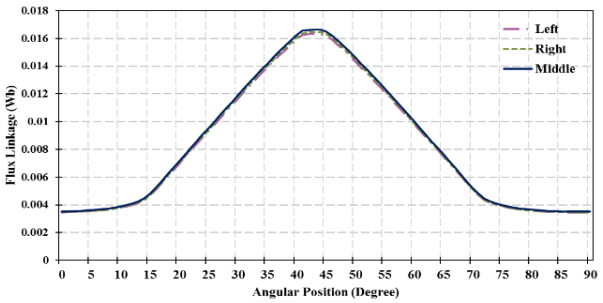

Fig. 8. The effect of the rotor linear motion on flux linkage.

Figure 8 reveals that the linear movement of the rotor does not have considerable effect on the rotary SRM performance.

The amount of magnetic flux that closes its path from two idle phases is considered as the mutual flux. This portion of the magnetic flux does not cooperate in torque production and should be as low as possible. Figure 9 shows the mutual flux of two idle phases as a result of a phase excitation.

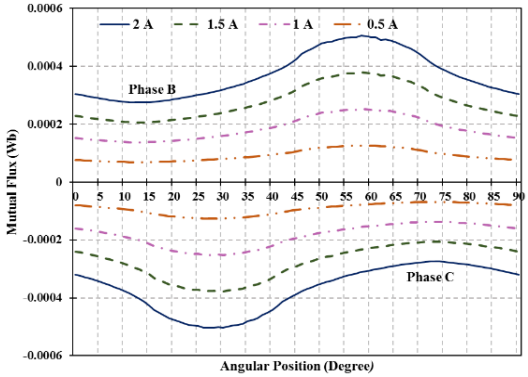

Fig. 9. Mutual flux of two idle phases in rotary motion mode.

The maximum leakage is about 0.5 mWb, which is 1.25% of the maximum flux linkage. This phenomenon helps to minimize the power losses.

The torque in a SRM can be obtained from:

$$T = \frac{\partial W'_f(i,\theta)}{\partial \theta}\Big|_{i=constant} \cong \frac{1}{2}\frac{dL(\theta,i)}{d\theta}\, i^2, \qquad (24)$$

where $W'_f(i,\theta)$ is the magnetic circuit co-energy, θ is the rotor pole angle, L and i are the phase inductance and current, respectively. The static torque as a result of 90° rotor rotation is depicted in Fig. 10. Based on Equation (24) as shown in Fig. 10, the static torque is raised when the excitation current goes up, in which the torque of the motor reaches to 0.25 N.m in the rated current.

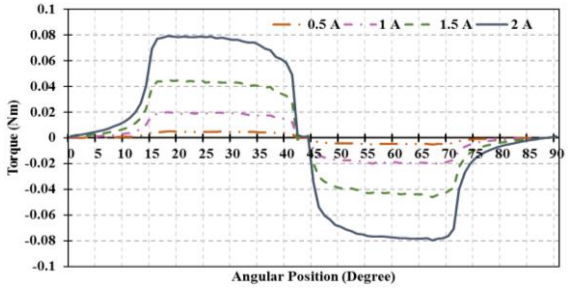

Fig. 10. The static torque from unaligned to the next unaligned position rotary motion mode.

The motor linear operation analysis is performed via 3DFEM while all of coils in one phase are energized. The magnetic field distribution is calculated from the translator unaligned to aligned positions. The magnetic flux path and the magnetic field distribution in stator and translator are depicted in Fig. 11 for linear motion mode. All of the stator windings are excited with 2 A current. The flux density of the translator is about 1 and 0.25 Tesla for aligned and unaligned positions. Each magnetic circuit comprised of two stator poles, two air gaps, translator, and stator back iron, which creates a short magnetic flux path in the translator. The analysis is performed with 0.5 mm step from unaligned up to full aligned position.

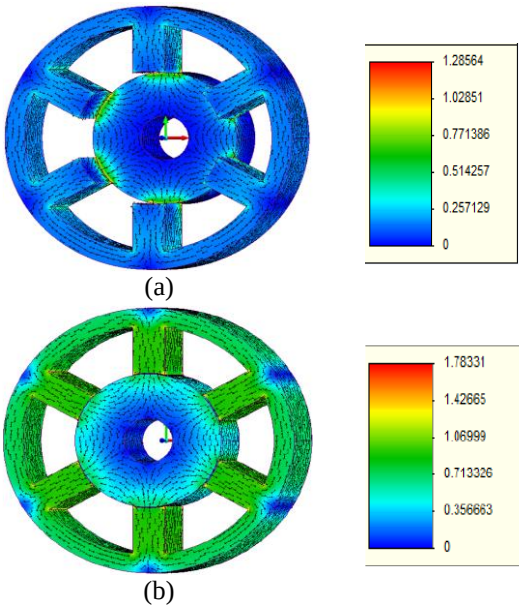

Fig. 11. Flux density and flux path of the motor in linear motion mode at: (a) unaligned, and (b) aligned positions.

The shape of flux linkage during one linear stroke is illustrated in Fig. 12. The flux linkage analysis has been performed for 4 different current values. As shown in Fig. 12, flux linkage of the coil in phase A has 13, 23, 32 and 37 mWb maximum amplitudes when the motor is excited with 1, 2, 3 and 4A, respectively, in the linear motion mode.

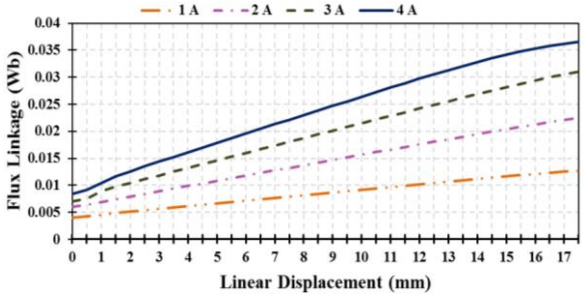

Fig. 12. Flux linkage of a phase during one stroke for linear motion mode.

Energizing the phase coils brings the translator to a position with less reluctance and hence more overlap with the stator. The position of the translator is measured between the edges of the stator pole and the translator.

Linear force is analyzed statically with the translator movement in 0.5 mm step. The analysis results for 4 different current magnitudes are given in Fig. 13. As shown in this figure, when the excitation current goes up from 1 A to 2, 3 and 4 A, the amplitude of produced motion force in RLSRM is increased by 4, 8.5, and 14 times higher.

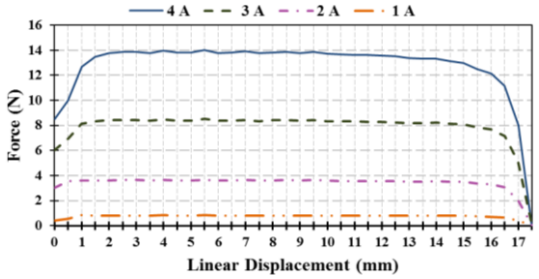

Fig. 13. The linear force for different excitation currents during one stroke.

The core losses decrease as a result of short flux paths in the translator. Energizing 6 stator coils together and the short magnetic flux paths increases the motor force per volume, which will be discussed in the next section.

B. Comparative study

After verification of the obtained parameters from the design procedure and FEM verification, a prototype is fabricated in the laboratory. Figure 14 shows the structure of different parts of the constructed motor.

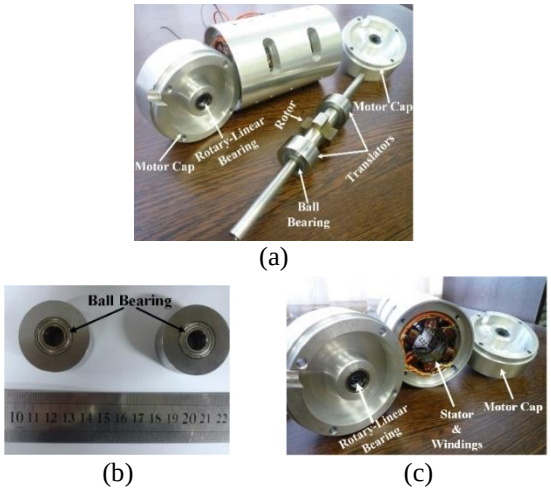

Fig. 14. Constructed RLSRM structure: (a) motor parts, (b) translator structure, and (c) motor cap, stator and windings.

In order to show any improvement in the motor performance, it is required to compare the motor output parameters with the parameters of the similar structures. The motor parameters are compared with the parameters of two RLSRMs found in the literature. The RLSRMs presented in [14] and [16] are based on a same structure. They have two identical 6-pole stators and an extended 4-pole rotor. Based on the given information the following parameters can be extracted: 1- Force and torque per mmf per volume for the motor in [14], 2- Force and torque per mmf per mass for the motors in [16], [17]. Table 3 shows the parameters of the constructed RLSRM and the other comparable structures in the literature.

Table 3: Comparison of the motor parameters with other RLSRMs

Parameter	Proposed RLSRM	RLSRM [14]	RLSRM [16]	RLSRM [17]
Force per volume ($N/m^3.A.t$)	11.05	8.92	DNA*	DNA
Force permass ($N/kg.A.t$)	2.88×10^{-3}	DNA	2.53×10^{-3}	2.13×10^{-3}
Torque per volume ($N.m/m^3.A.t$)	0.59	0.44	DNA	DNA
Torque per mass ($N.m/kg.A.t$)	1.19×10^{-4}	DNA	1.33×10^{-4}	1.01×10^{-4}

*Data not available

The constructed motor has the highest linear force among the studied structures. The normalized force and torque per volume show 23% and 34% increase with reference to the motor in [14], respectively. The normalized force per mass is 14% more than its corresponding value in [16]. The normalized torque per mass is 11% less than the value of [16]. This reduction can be interpreted as the constructed motor does not utilize a considerable part of the motor volume for rotary motion. This can be considered as the main disadvantage of the proposed structure. It should be noted that this special structure decouples rotary and linear motion control. Although the rotary section does not have any contribution in linear motion, the short magnetic flux paths give the highest force to the constructed motor. Therefore, the motor operation in rotary, linear and rotary-linear modes is applicable with improved characteristics in comparison with the other ones. As shown experimentally, the compound rotary-linear motion control by the constructed RLSRM does not need any decoupling control algorithm which is an important issue in the other rotary-linear motors [15,16]. The decoupled rotary and linear motion control and simple integrated structure are the advantages of the proposed RLSRM that make it a good competent for the other rotary–linear motors.

IV. CONCLUSION

A new structure for rotary-linear motion control based on SRM technology has been presented. The parameters of the RLSRM are calculated from rotary and linear SRM design equations. Verification of the calculated values is performed by the model analysis via 3D-FEM. The static electromagnetic analysis of the motor gives the static torque, linkage and leakage fluxes and linear force. The achieved flux linkage was about 40 mWb with minimum leakage about 0.5 mWb, which proves the low motor loss. Also, the power of flux density was 0.97 and 1 Tesla in rotary and linear motion modes, respectively. A prototype has been fabricated based on the design parameters. The comparative study has been performed and shows that the motor has the highest force per volume among the studied RLSRM structures (i.e., the normalized force and torque per volume show 23% and 34% increase in comparison with other ones). These achieved results show the applicability of the proposed motor in different applications for rotary, linear and rotary-linear modes of operation.

REFERENCES

[1] L. Xiang, S. Zuo, L. He, M. Zhang, J. Hu, and G. Long, "Optimization of interior permanent magnet motor on electric vehicles to reduce vibration caused by the radial force," *Applied Computational Electromagnetics Society Journal*, vol. 29, 2014.

[2] E. Afjei, M. Tavakoli, and H. Torkaman, "Eccentricity compensation in switched reluctance machines via controlling winding turns/stator current: theory, modeling, and electromagnetic analysis," *Applied Computational Electromagnetics Society Journal*, vol. 28, 2013.

[3] R. Krishnan, *Switched Reluctance Motor Drives: Modeling, Simulation, Analysis, Design, and Applications*, CRC Press, 2010.

[4] H. Torkaman, N. Arbab, H. Karim, and E. Afjei, "Fundamental and magnetic force analysis of an external rotor switched reluctance motor," *Applied Computational Electromagnetics Society Journal*, vol. 26, 2011.

[5] E. Aycicek, N. Bekiroglu, I. Senol, and Y. Oner, "Rotor configuration for cogging torque minimization of the open-slot structured axial flux permanent magnet synchronous motors," *Applied Computational Electromagnetics Society Journal*, vol. 30, 2015.

[6] C. He, H. Chen, and Y. Zhou, "Design indicators and structure optimisation of switched reluctance machine for electric vehicles," *Electric Power Applications, IET*, vol. 9, pp. 319-331, 2015.

[7] J. Lin, K. W. E. Cheng, X. Xue, N. C. Cheung, and Z. Zhang, "Estimation of inductance derivative for force control of linear switched reluctance actuator," *IEEE Transactions on Magnetics*, vol. 50, pp. 1-4, 2014.

[8] A. Labak and N. C. Kar, "Design and prototyping a novel 5-phase pancake shaped axial flux SRM for electric vehicle application through dynamic FEA incorporating flux-tube modeling," *IEEE Transactions on Industry Applications*, vol. 49, pp. 1276-1288, 2013.

[9] R. Madhavan and B. G. Fernandes, "Axial flux segmented SRM with a higher number of rotor segments for electric vehicles," *IEEE Transactions on Energy Conversion*, vol. 28, pp. 203-213, 2013.

[10] T. Yano, *Actuator with Multi Degrees of Freedom*, in Next-Generation Actuators Leading Breakthroughs, ed: Springer, pp. 279-290, 2010.

[11] G. Krebs, A. Tounzi, B. Pauwels, D. Willemot, and F. Piriou, "Modeling of a linear and rotary permanent magnet actuator," *IEEE Transactions on Magnetics*, vol. 44, pp. 4357-4360, 2008.

[12] M. Bertoluzzo, P. Bolognesi, O. Bruno, G. Buja, S. Castellan, V. Isastia, et al., "A distributed driving and steering system for electric vehicles using rotary-linear motors," in *Power Electronics Electrical Drives Automation and Motion, 2010 International Symposium on*, pp. 1156-1159, 2010.

[13] K. Meessen, J. Paulides, and E. Lomonova, "Analysis of a novel magnetization pattern for 2-DoF rotary-linear actuators," *IEEE Transactions on Magnetics*, vol. 48, pp. 3867-3870, 2012.

[14] Y. Sato, "Development of a 2-degree-of-freedom rotational/linear switched reluctance motor," *IEEE Transactions on Magnetics*, vol. 43, pp. 2564-2566, 2007.

[15] J. Pan, F. Meng, and G. Cao, "Decoupled control for integrated rotary–linear switched reluctance motor," *Electric Power Applications, IET*, vol. 8, pp. 199-208, 2014.

[16] J. F. Pan, Z. Yu, and N. C. Cheung, "Performance analysis and decoupling control of an integrated rotary-linear machine with coupled magnetic paths," *IEEE Transactions on Magnetics*, vol. 50, pp. 761-764, 2014.

[17] J. Pan, N. Cheung, and G.-Z. Cao, "Investigation of a rotary-linear switched reluctance motor," *XIX International Conference on Electrical Machines*, pp. 1-4, 2010.

[18] I. Bentia, L. Szabo, and M. Ruba, "On a rotary-linear switched reluctance motor," in *Power Electronics, Electrical Drives, International Symposium on Automation and Motion*, pp. 507-510, 2012.

[19] J. Cao, "A rotary-linear switched reluctance motor," in *2009 3rd International Conference on Power Electronics Systems and Applications*, pp. 1-4, 2009.

[20] *Slide Rotary Bush*. Available: http://www.nb-linear.co.jp/english/product/lineup/strokebush/sre.

html/, June 2015.

[21] J. Chang, D. Kang, I.-A. Viorel, and S. Larisa, "Transverse flux reluctance linear motor's analytical model based on finite-element method analysis results," *IEEE Transactions on Magnetics*, vol. 43, pp. 1201-1204, 2007.

[22] *Magnet CAD Package User Manual*, Infolytica Corporation Ltd., Montreal, Canada, 2007.

Design and Non-Linear Modeling of a Wide Tuning Range Four-Plate MEMS Varactor with High Q-Factor for RF Application

M. Moradi [1], R. S. Shirazi [1], and A. Abdipour [2]

[1] Microwave Measurement Lab., Department of Electrical Engineering
[2] Institute of Communication Technology & Applied Electromagnetics
Amirkabir University of Technology (Tehran Polytechnic), Tehran, 158754413, Iran
mehrdad_moradi@aut.ac.ir, sarraf@aut.ac.ir, abdipour@aut.ac.ir

Abstract ─ In this study, a micro-electromechanical variable capacitor that can achieve a wide tuning range is presented. The mechanical behaviors such as squeezed film damping and modal analysis are investigated. Also, scattering parameters, electromagnetic properties, and linear and nonlinear circuit models are presented for MEMS varactors. The four-plate tunable capacitor has nominal capacitance of 0.055 pF, a Q-factor of 175 at 10 GHz, and a tuning range of 2.59:1. The presented four-plate MEMS varactor has a suspended plate with the ability of moving downward and upward in order to increase the tuning range. The results were obtained by using simulation software. For the mechanical analyses, FEM in COMSOL Multiphysics software was used, and Ansoft HFSS and Agilent ADS were used for the electromagnetic analyses.

Index Terms ─ Linear model, MEMS varactor, nonlinear model, tuning range.

I. INTRODUCTION

In wireless communication systems, VCOs and tunable filters need high quality factor components. This can lead to low phase noise and low power in voltage-controlled oscillators (VCO) and low insertion loss in the band pass filters. High quality factor variable capacitors (varactors) with common p-n junction are off-chip [1,2]. There are problems with off-chip passive components such as packaging complexity, high cost and large system area. These problems have increased the need for a new technology to realize high performance on-chip passive elements which can be monolithically integrated with active circuitry.

Recent investigations into micromachining proposed RF MEMS (microelectromechanical system) varactors with an adequate Q-factor. MEMS varactors are fabricated in either an aluminum [3] or a polysilicon [4] surface micromachining technology. MEMS varactors provide high quality factor, wide tuning range, low phase noise and small chip size and are compatible with the standard IC fabrication [5-8]. MEMS varactors have a high Q-factor and wide tuning range due to the unique capabilities enabled by micromechanical tuning and the low loss materials used in the construction of RF MEMs devices. Since their mechanical resonance frequency is normally around 10-100 KHz, the MEMS varactors will not resonate mechanically in response to the RF frequencies.

Parallel plate configuration of MEMS varactors is the most common configuration that has been used because of its simplicity in fabrication and high Q-factor. The parallel plate MEMS varactors consist of a suspended metal plate over a bottom fixed metal plate. By applying a DC voltage between two plates, the suspended metal plate moves toward the bottom plate, and this being the case, displacement between two plates results in the variation of the capacitance. A two parallel plate MEMS varactor with a Q-factor on the order of 60 and a measured tuning range of 16% were reported in [3]. It was shown that the measured tuning range of MEMS varactors are less than their theoretical calculation. The foremost limitation of MEMS varactors is their actual tuning range being less than their theoretical one. To overcome this problem, Young et al. [3], Dec et al. [4], and Chen et al. [11] have offered some solutions and innovative efforts. Furthermore, a different structure with seven supporting beams is presented in [16], which its capacitance ranges from 0.064pF for a single beam structure to 0.448 pF for a seven beam structure.

This paper presents a four parallel plate MEMS varactor that offers a large tuning range on the order of 2.59:1 with a high Q-factor of 175 at 10 GHz. For mechanical and electrostatic calculation, we used COMSOL Multiphysics 3.5a. The electromagnetic behaviors were simulated by Ansoft HFSS and Agilent ADS. A linear circuitry model is proposed by scattering parameters extracted from HFSS simulation outcomes. Finally, a new nonlinear circuitry model was prepared for MEMS varactors devices. Using this nonlinear circuitry model in circuit simulators to simulate circuits consisting MEMS varactors is possible. Only by

Submitted On: June 25, 2015
Accepted On: December 5, 2015

changing some input parameters of the model, the nonlinear model can be applied to RF MEMS varactors. The principle of its operation is described in Section II. The varactor design including electrostatic activation, pull-in effect, computation of spring constant, squeezed film damping and modal analysis is discussed in Section III. The static electrostatic analysis and electromagnetic simulation are presented in Section IV and V, respectively, and finally, the linear and nonlinear circuitry models are elaborated in Section VI.

II. PRINCIPLE OF OPERATION

A two parallel plate MEMS varactor is shown in Fig. 1. The top plate is suspended by cantilever beams and the bottom metal plate is fixed. The overlapping area and the initial spacing between the two plates are called A and d_0, respectively. When a bias voltage is applied across the two plates, it induces an electrostatic force on them and causes the suspended plate to move towards the bottom plate until the electrostatic and spring forces become equal. This displacement increases the value of the capacitance.

The value of the capacitance (C) between two plates can be calculated by the following equation:

$$C = \frac{\varepsilon A}{d}, \tag{1}$$

where d is the distance between two plates. If V_{DC} is applied across the two plates, an attractive electrostatic force is generated between them. The electrostatic force can be derived as [9,10]:

$$F_e = \frac{1}{2}\frac{\partial C(d)}{\partial d}V_{DC}^2 = -\frac{1}{2}\frac{\varepsilon_0 A V_{DC}^2}{d^2}, \tag{2}$$

where A is the overlapping surface between the two plates. The suspended plate moves downward to reach an equilibrium between electrostatic force and the mechanical restoring force. The mechanical restoring force is given by Equation (3), where k_m is the spring constant of the suspended plate. By equating these two forces, we find:

$$\frac{1}{2}\frac{\varepsilon_0 A V_{DC}^2}{h^2} = k_m (d_0 - d). \tag{3}$$

Increasing applied voltage leads to decrease distance between top and bottom plates until d reaches $d_0/3$. The corresponding voltage at $d=d_0/3$ is called pull-in voltage. If V_{DC} increases beyond pull-in voltage, the suspended plate collapses down onto the bottom plate at $d=2d_0/3$. The increase in the electrostatic force is greater than the increase in the restoring force and no equilibrium position can be reached between the two forces; consequently, the suspended beam position becomes unstable. This event is called pull-in effect. Pull-in effect limits capacitance tuning range to 1.5:1. To solve this problem, a new design is proposed in [11].

Presented in [11], Fig. 2, illustrates the novel design of two parallel MEMS capacitor. As shown in Fig. 2, the plate E_1 is a suspended plate with the ability of moving down. E_2 and E_3 are fixed on the bottom substrate. In this design, actuated beams and capacitor beams are separated. E_1 and E_2 form a variable capacitor. The electrostatic actuation is provided by plate E_3 (the plate that surrounds E_2) and E_1. The distance between E_1 and E_2 that is called d_1 is designed to be smaller than d_2. Pull-in effect occurs between plates E_1 and E_3 at $d=d_2/3$ that makes further change in the capacitance between E_1 and E_2. The relative tuning range is calculated by:

$$\frac{C - C_0}{C_0} = \frac{\varepsilon A/(d_1 - d) - \varepsilon A/d_1}{\varepsilon A/d_1} = \frac{d}{d_1 - d}. \tag{4}$$

When d reaches $d_2/3$, the maximum tuning range can be obtained. Replacing d with $d_2/3$ in Equation (4) results in a maximum tuning range of $d_2/(3d_1-d_2)$. By choosing $d_1=2\ \mu m$ and $d_2=3\ \mu m$ in [11], the tuning range of 1:1 is achieved.

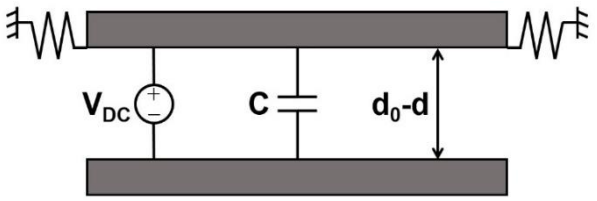

Fig. 1. Cross-section of two-parallel plate micromachined varactor.

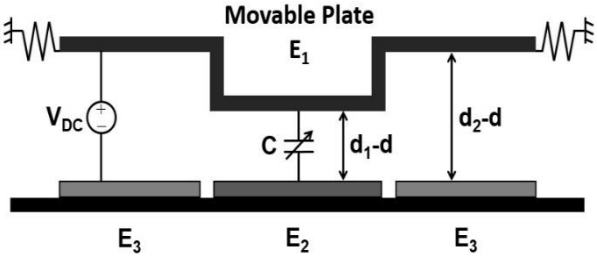

Fig. 2. A schematic model of the MEMS tunable capacitor using different gap spacing [11].

III. A NEW DESIGN OF THE PARALLEL PLATE MEMS VARACTOR

Using the configuration idea presented in [11] and [5], we achieved a novel design that increases the tuning range of the three plate varactor proposed in [11]. Figure 3 illustrates schematic model of our design. The fourth plate (E_4) is used to move the suspended plate (E_1) upward. The 3D configuration and career beams of E_1 are shown in Fig. 4. When a bias voltage is applied between E_1 and E_4, electrostatic force is generated on plates and E_1 moves toward E_4. E_4 is suspended by high stiffness beams and its displacement due to the applied voltage can be neglected. When the biasing voltage is

applied between E_1 and E_3, the maximum value of capacitance will be $\varepsilon A/(d_1-d_2/3)$. Due to the DC voltage applied across E_1 and E_4, E_1 moves upward and capacitance value decreases until pull-in effect occurs between E_1 and E_4. The minimum value of capacitance is derived as $\varepsilon A/(d_1+d_2/3)$. By choosing d_1 and d_2 as in [11] and $d_3=2\ \mu m$, tuning range of 3:1 is accomplished. It must be noticed that this wide tuning range is completely controlled by biasing voltage. Another advantage of adding E_4 to the structure is protecting other plates using a firm and bulky plate. Gold is chosen for E_1, E_2 and E_3. Nickel for E_4, and silicon for substrate. Plates E_1 and E_4 thickness are respectively *2* and *15 µm*. Plates E_2 and E_3 thickness is *0.5 µm*, which can be thermally evaporated on the substrate. Silicon with *1 mm* thickness is used as the substrate.

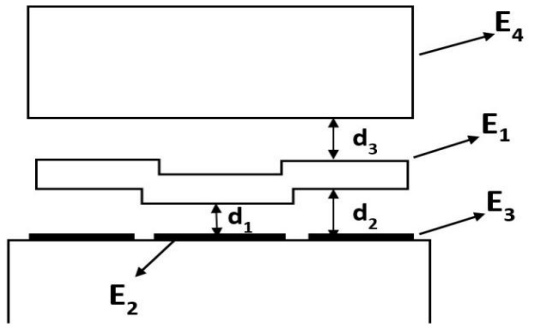

Fig. 3. A schematic model of the novel wide-tuning-range tunable capacitor.

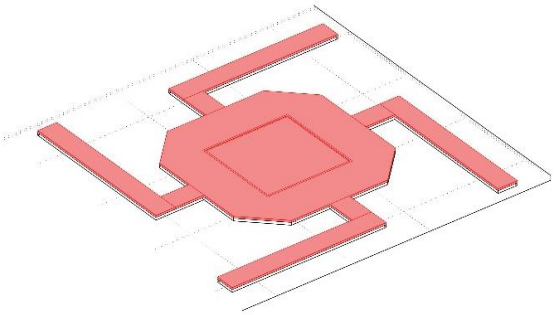

Fig. 4. The suspended plate E_1 and its beams.

IV. STATIC ELECTROMECHANICAL SIMULATION

Electrical and mechanical physical domains must be considered among simulation of RF MEMS devices. Accordingly, the relation between electrical and mechanical parameters should be taken into account. The simulations, were performed in a 3D domain, and used the finite element method (FEM) in the COMSOL Multiphysics 3.5a.

Career beams of E_1 plate are designed in order to make tradeoff between low control voltage and low sensitivity due to the external forces. E_1 spring coefficient is 6.5 which is calculated by simulation. Pull-in effect between E_1 and E_2 plates occurs about 15.6V and between E_4 and E_1 plates occurs about 7.3V.

Figures 5 (a) and 5 (b) show varactor capacitance variations with and without the fourth plate (E_4) respectively. As it was expected, adding the fourth plate has no effect on maximum capacitance value, but it decreases minimum capacitance value via increasing air gap between E_1 and E_2. The tuning range of the varactor's capacitance is presented here as:

$$\frac{C_{max}-C_{min}}{C_{min}}=\frac{0.109-0.04214}{0.04214}=1.587. \qquad (5)$$

So, simulated varactor tuning range is 2.587:1, which is less than calculated theoretical value (3:1) due to fringing capacitance.

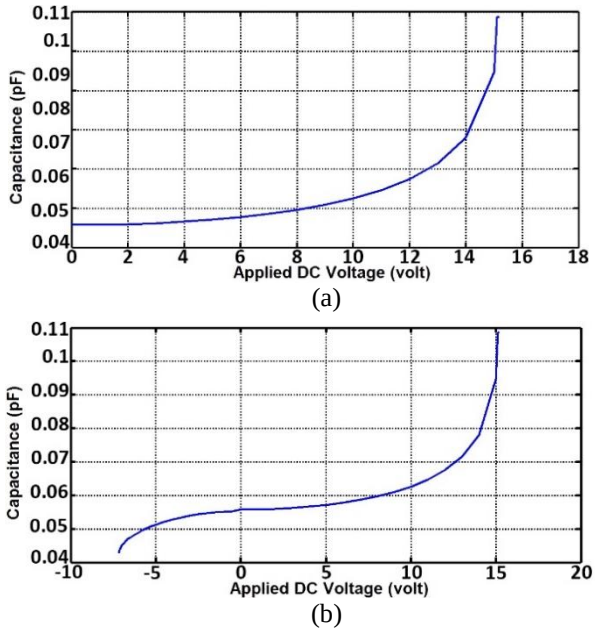

Fig. 5. The capacitance of the wide tuning range varactor vs. applied DC voltage: (a) without E4, and (b) with E4.

V. MICROWAVE SIMULATION

The RF behavior of the variable capacitor is simulated using HFSS software [12]. The simulated S_{11} parameter on smith chart is plotted from 1 GHz to 20 GHz, as shown in Fig. 6.

The calculated Q-factor is obtained as $1/\omega RC$. R and C are extracted by simulated S_{11} parameter, Fig. 6. The Q-factor of the proposed capacitor, from the simulated data at 10 GHz, is found to be 175. The Q-factor of the capacitor is shown in Fig. 7, over the frequency range 1-20 GHz.

Using S_{11} parameter calculated in HFSS, the linear equivalent circuit of the four-plate varactor can be presented as in Fig. 8, which offers a linear circuitry

model to describe the steady state behavior of varactor. *C5*, *L5* and *R5* represent plates E_1 and E_2. Coupling between the silicon substrate and the top plate is modeled by *C4*, *L4* and R4. *C1*, *L1*, *L2*, and *R1* are the capacitance, inductance and resistance associated with the attached supporting beams that are connected to the top plate. The anchors located around the varactor can be represented by *C2* and *R2*. The inductance and the capacitance of the wires forming a connection between the center RF pad and the beams' anchors are represented by *C4* and *L3*. Finally, *C3* and *L3* represent RF pads. These elements are determined by parameter extraction from the HFSS simulations at zero dc bias voltage [13]. As shown in Figs. 9 (a) and 9 (b), magnitude and phase of S_{11} calculated by linear circuitry model are in satisfying agreement with HFSS results.

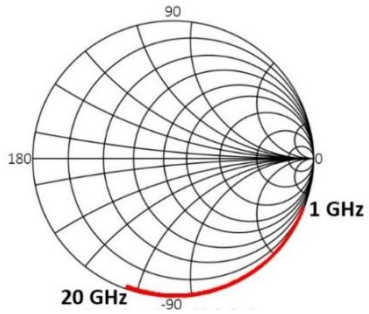

Fig. 6. S_{11} parameter for four-plate varactor proposed in this paper.

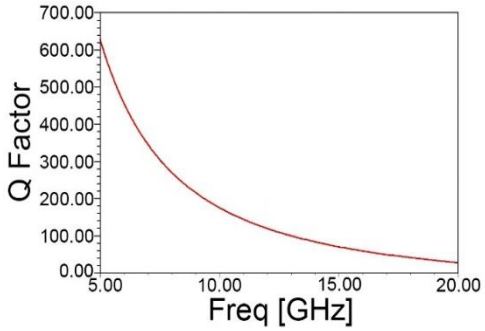

Fig. 7. The quality factor for four-plate variable capacitor over frequency range from 1 GHz up to 20 GHz.

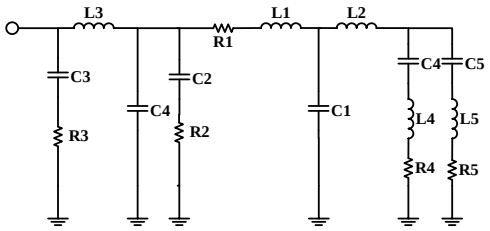

Fig. 8. The equivalent circuit of the simulated proposed varactor as a one-port network.

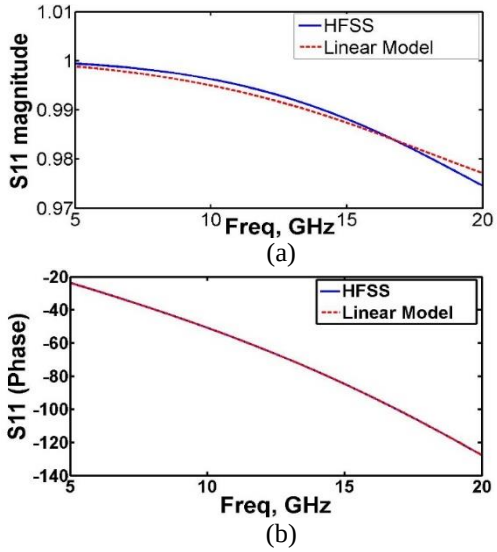

Fig. 9. The comparison between HFSS results and linear model results: (a) magnitude of S_{11} vs. frequency, and (b) phase of S_{11} vs. frequency.

VI. DYNAMIC ELECTROMECHANICAL SIMULATION (NONLINEAR CAD MODEL OF A MEMS VARACTOR)

A second-order system can mathematically describe the electromechanical dynamic behavior of the tunable capacitor [14]. In this second-order system viscous damping, inertia and spring force are considered as:

$$m\frac{d^2x}{dt^2}+b\frac{dx}{dt}+kx=f_{ext}, \tag{6}$$

where m is the mass of the movable plate E_1, b is the damping coefficient, the damping force (F_D) determined by bdx/dt, kx is the spring force and f_{ext} denotes the electrostatic force applied on E_1 which is calculated by Equation (2). The frequency response can be achieved by Fourier transferring of Equation (6):

$$\frac{X(j\omega)}{F(j\omega)}=\frac{1}{k}\left(\frac{1}{1-\left(\omega/\omega_0\right)^2+j\omega/\left(Q\omega_0\right)}\right), \tag{7}$$

where $\omega_0=\sqrt{k/m}$ is the mechanical resonance frequency and $Q=k/\omega_0 b$ is the mechanical quality factor.

The squeezed air-film underneath the E_1 produces a damping force that opposes the downward motion of the E_1. The behavior of the squeezed air film between the closely spaced E_1 and the bottom plates is governed by Reynold's equation [15]:

$$\frac{\partial}{\partial x}\left[\left(\frac{\rho h^3}{\mu}\right)\frac{\partial P}{\partial x}\right]+\frac{\partial}{\partial y}\left[\left(\frac{\rho h^3}{\mu}\right)\frac{\partial P}{\partial y}\right]=12\frac{\partial(\rho h)}{\partial t}, \tag{8}$$

where p denotes the pressure in the film, μ is the coefficient of the air viscosity, ρ is density, and h is the thickness of the air. The small geometry of the MEMS devices causes negligible temperature variation. Under isothermal condition, ρ is directly proportional to the P, and Reynold's equation is simplified as:

$$\frac{\partial}{\partial x}\left[\left(\frac{Ph^3}{\mu}\right)\frac{\partial P}{\partial x}\right]+\frac{\partial}{\partial y}\left[\left(\frac{Ph^3}{\mu}\right)\frac{\partial P}{\partial y}\right]=12\frac{\partial(Ph)}{\partial t}. \quad (9)$$

In order to determine the damping coefficient (b) in Equation (1), the simplified Reynold's equation is used by the COMSOL Multiphysics 3.5a. The simulated damping coefficient (b) is 1.38×10^{-4} *kg/s*. This damping coefficient leads to a settling time of *500 μsec*. A specific pattern for perforating E_1, illustrated in Fig. 10, is used to reduce the settling time.

Equations (1), (2) and (7) are coupled together. These equations describe the relationship between the electrical and mechanical domain. Finite-difference method is used to solve these equations in MATLAB. A third order polynomial is used to fit capacitance as a function of the E_1's displacement. The simulated displacement of E_1 and varactor capacitance vs. time are shown in Fig. 11, when DC voltage of 8 volts is applied between E_1 and E_3. Perforating of E_1 results in damping coefficient of $b = 5e^{-5}$. In downward motion, the squeezed film damping on E_1 is simulated by the COMSOL Multiphysics 3.5a, Fig. 10.

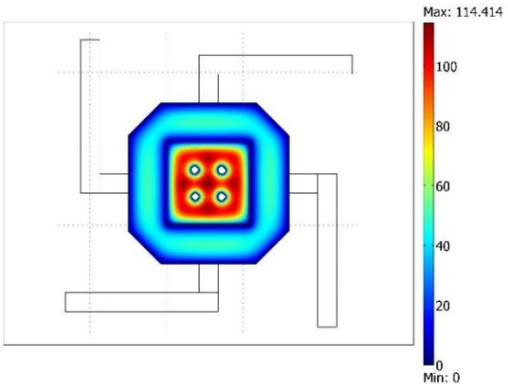

Fig. 10. The perforated E_1 plate in order to reach $b = 5e^{-5}$ when V_{DC} is applied between E_1 and E_3.

As shown in Fig. 11, damping coefficient of $b = 5e^{-5}$ leads to a settling time of *55 μsec*.

In order to demonstrate the nonlinear behavior in circuits using MEMS varactors, a nonlinear model of the MEMS device is implemented, Fig. 12. Capacitance is modeled by module 3 that is calculated by Equation (1). The E_1's displacement is calculated from the electrostatic force by module 2 which uses Equation (6).

The electrostatic force is calculated by module 1 from voltage V_{DC} (module 3's output) and the displacement x. This module generates an output voltage f equivalent to the electrostatic force, Equation (3). For implementing the nonlinear model described in Fig. 12, SDD tool is used from Agilent ADS, Fig. 13. Applying V_{DC} causes changing in the capacitance value (C). Using the concept of analogues systems, the value of C is calculated by the electrical system, Fig. 13. Following this, using SDD in ADS, the relation between current and voltage of the output port is defined as a capacitance.

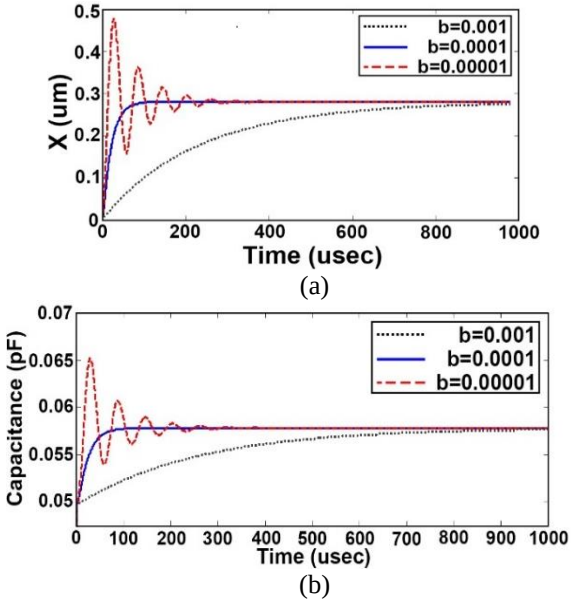

Fig. 11. The transient behavior of the proposed MEMS varactor at different damping coefficients: (a) E_1's displacement vs. time, and (b) the value of capacitance vs. time.

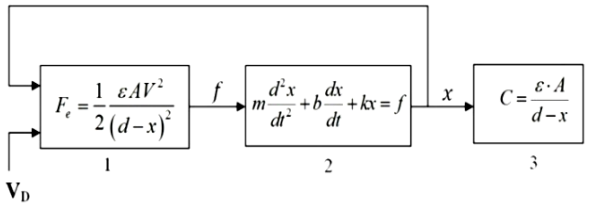

Fig. 12. Modeling of the proposed MEMS varactor's nonlinear behavior.

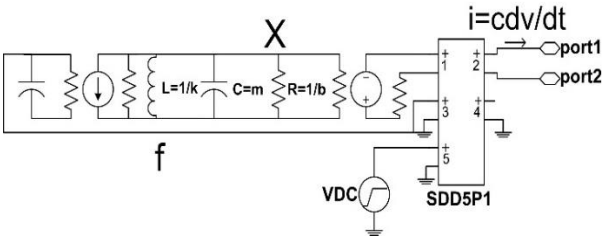

Fig. 13. The nonlinear model for simulation of MEMS varactor's transient behavior.

The proposed four-plate MEMS varactor's response to a step voltage with rise time of 1 psec is obtained by using the nonlinear model, Fig. 14. Comparing the results of the nonlinear model with numerical solution, reveals that nonlinear model is not only reliable but also can help adequate modeling of the varactor's transient behavior. Furthermore, varacor variation via applying sawtooth voltage is shown in Fig. 15.

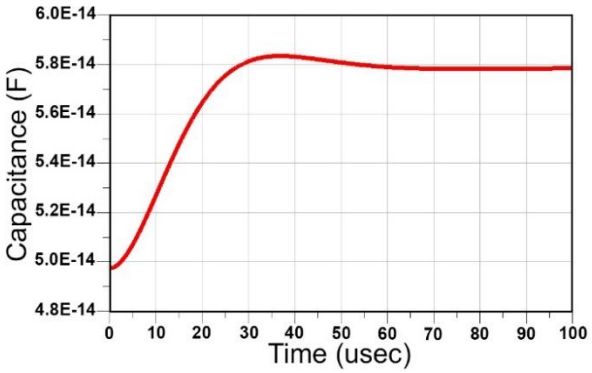

Fig. 14. The simulated capacitance vs. time when subject to a step voltage.

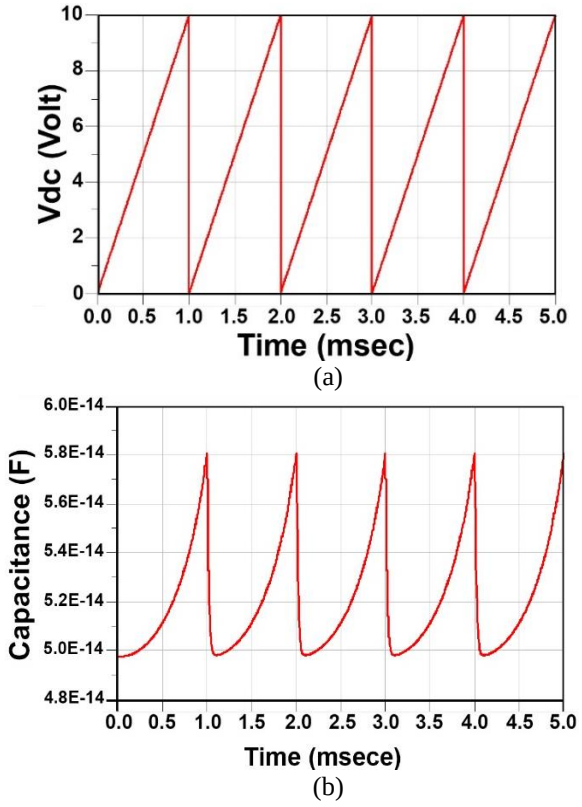

Fig. 15. (a) The sawtooth input voltage applied to the varactor as a tuning voltage. (b) The periodic response of the presented MEMS varactor to the periodic sawtooth input.

VII. CONCLUSION

In this paper, a high-Q varactor with wide tuning range was presented. This novel structure consists of four plates, two suspended plates and two fixed plates. The fourth plate was used to increase the distance between capacitance's plates in order to decrease the varactor's capacitance. Therefore, adding E_4 to three plate varactor led to the wider tuning range. The novel structure gained a tuning range of 2.587:1 (158.7%). Also, the proposed MEMS varactor in this paper showed a Q of 175 at 10 GHz.

Electromechanical behaviors of the varactor were also characterized. We studied both dynamic and static behaviors of the MEMS varactor. A perforated pattern for E_1 was chosen to achieve a proper damping coefficient leading to a fast transient behavior.

Microwave parameters were also studied by the simulation software. An equivalent circuit of the presented varactor was obtained by simulated *S*-parameters. The dynamic behavior of the varactor was modeled in this research work in order to study transient responses of the varactor.

ACKNOWLEDGMENT

We would like to thank Rahmat Jesri for his helpful suggestions and comments.

REFERENCES

[1] N. Nguyen and R. Meyer, "Si IC-compatible inductors and LC passive filters," *IEEE J. Solid-State Circuits*, vol. 25, pp. 1028-1031, Aug. 1990.

[2] M. Soyuer, K. Jenkins, J. Burghartz, and M. Hulvey, "A 3 V 4 GHz nMOS voltage-controlled oscillator with integrated resonator," *IEEE ISSCC Dig. Tech. Papers*, pp. 394-395, Feb. 1996.

[3] D. J. Young and B. E. Boser, "A micro-machined variable capacitor for monolithic low-noise VCOs," *IEEE Solid-State Sensor and Actuator Workshop Dig.*, pp. 86-89, June 1996.

[4] A. Dec and K. Suyana, "Micromachined varactor with a wide tuning range," *Electronics Letters*, vol. 33, no. 11, pp. 922-924, May 1997.

[5] A. Dec and K. Suyana, "Micromachined capacitors and their application to RF IC's," *IEEE Transactions on Microwave Theory and Techniques*, vol. 46, no. 12, pp. 2587-2596, 1998.

[6] A. Dec and K. Suyana, "2.4 GHz CMOS LC VCO using micromachined variable capacitors for frequency tuning," *Microwave Symposium Dig.*, 1999 IEEE MTT-S International, vol. 1, pp. 79-82, 1999.

[7] T. Clark, C. Nguyen, L. P. B. Katehi, and G. M. Rebeiz, "Micromachined devices for wireless communications," *Proceeding of the IEEE*, vol. 86, no. 8, pp. 1756-1767, 1998.

[8] E. Abbaspour-Sani, N. Nasirzadeh, and G.

Dadashzadeh, "Two novel structures for tunable MEMS capacitor with RF applications," *Progress In Electromagnetics, PIER 68*, pp. 169-183, 2007.

[9] M. Zahn, *Electromagnetic Field Theory: A Problem Solving Approach*, John Wiley & Sons, New York, 1979.

[10] G. M. Rebeiz, *RF MEMS Theory, Design, and Technology*, John Wiley & Sons, 2003.

[11] J. Chen, J. Zou, C. Liu, J. E. Schutt-Ainé, S.-M. K. Kang, "Design and modeling of a micromachined high-Q tunable capacitor with large tuning range and a vertical planar spiral inductor," *IEEE Transactions on Eelectron Devices*, vol. 59, no. 3, pp. 730-739, Mar. 2003.

[12] Ansoft High Frequency Structure Simulation (HFSS), ver. 11, Ansoft Corporation, Pittsburgh, PA, 2005.

[13] M. Bakri-Kassem, Novel RF MEMS Varactors Realized in Standard MEMS and CMOS Processes, *Doctoral Dissertation, University of Waterloo*, Ontario, Canada, 2007.

[14] W. Weaver, Jr., S. P. Timoshenko, and D. H. Young, *Vibration Problems in Engineering*, John Wiley & Sons, New York, 1990.

[15] W. A. Gross, L. A. Matsch, V. Castelli, A. Eshel, J. H. Vohr, and M. Wildmann, *Fluid Film Lubrication*, John Wiley & Sons, New York, 1980.

[16] S. Lakshmi, S. Rao, P. Manohar, and P. N. Sayanu, "Design and simulation of multi-beam RF MEMS varactor," *Circuits, Communication, Control and Computing (I4C), International Conference on*, vol. 1, pp. 308-311, Nov. 2014.

Mehrdad Moradi received the B.S. degree from the Isfahan University of Technology, Iran, and the M.S. degree from the Tehran Polytechnic, Iran, in 2008 and 2011, respectively. He is currently Faculty Member of the Islamic Azad University, Iran.

His major research interest lines in the RF MEMS devices and their application. In addition, RF and microwave circuits and applied electromagnetics are his research interests.

Reze Sarraf Shirazi received the B.S., M.S., and Ph.D. degrees from the Amirkabir University of Technology (Tehran Polytechnic), Iran, in 1980, 1993, and 2006, respectively. He is currently an Associate Professor at the Amirkabir University of Technology, where he is Director of the Wave Propagation & Microwave Measurement Lab.

His interest fields are wave propagation, numerical methods in electromagnetic and radio link design. In addition, he has published two papers in ACES Journal.

Abdolali Abdipour received the B.S. from University of Tehran, Iran, in 1988, and M.S. degree from University of Limoges, France, 1992. He received the Ph.D. degree from the University of Paris XI(Orsay), France, 1996. He is currently a Professor at the Amirkabir University of Technology. He is currently the Director of Institute of Communication Technology and Applied Electromagnetic at Amirkabir University of Technology, 2012-Present.

His research interests include RF/Microwave/ Millimeter-Wave/THz Circuits and Systems Design, and Linear and Nonlinear Modeling of Microwave/ Millimeter-wave Circuits and Devices. In addition, he has published two papers in ACES Journal.

Characterization of Surface Cracks Using Eddy Current NDT Simulation by 3D-FEM and Inversion by Neural Network

B. Helifa [1], M. Féliachi [2], I. K. Lefkaier [1], F. Boubenider [3], A. Zaoui [4], and N. Lagraa [5]

[1] Laboratoire de Physique des Matériaux
Université de Laghouat, BP 37G, Laghouat 03000, Algérie
helifa@yahoo.fr, lefkaier_ik@yahoo.fr

[2] IREENA-IUT
Université de Nantes – L'UNAM, CRTT, BP 406, 44602 Saint-Nazaire cedex, France
mouloud.feliachi@univ-nantes.fr

[3] Laboratoire de Physique des Matériaux
USTHB, Bab-Ezzouar, Alger 016000, Algérie
fboubenider@hotmail.com

[4] EMP
BP 17 Bordj El Bahri 16100 Alger, Algérie
zaoui_abdelhalim@yahoo.fr

[5] Laboratoire d'Informatique et de Mathématique
Université de Laghouat, BP 37G, Laghouat 03000**,** Algérie
nasrlag@gmail.com

Abstract ─ In this work, we suggest an approach of signal inversion from sensors used in eddy current (EC) nondestructive testing (NDT). The aim is to characterize surface cracks from the EC signal. A methodology that combines 3D finite element (FEM) simulation and a data inversion by neural networks (NN) is proposed. We show that the use of a set of numerical measurements representing the EC signature of surface crack enables to remedy of the unicity problem. The obtained results show that the developed approach leads to the quantification of the crack.

Index Terms ─ 3D finite element simulation, eddy current NDT, neural network, surface cracks.

I. INTRODUCTION

Non-destructive testing by eddy currents is a powerful tool for testing the quality and reliability. Its exploiting in real-time has become a capital necessity, and it is essential to have a fast mean for the inversion of eddy current signals.

Usually, this inversion is carried out through an experimental investigation by plotting the standard curves, which is efficient but costly investigation [1], or through an optimization algorithm leading to a computation time that can easily become prohibitively high [2], [3], [4] and [5].

In this context, 3D finite element simulation is performed in order to construct a database relating the sensor impedance variation and the crack geometry, which will be used instead of experimental measurements. After that, data inversion by means of neural networks is performed and enables us to fully characterize the surface crack. In this approach, the obtained signal represents the no perturbed crack one. Therefore, the use of wavelet and IFT techniques cannot give any addition, since they are usually performed in perturbed environment [6], [7], [8] and [9]. In this work, we test the validity of obtained results by comparing them with experimental ones in "Team Workshop Problem 15" [10].

II. MODELING

Eddy current NDT system can be modeled by the scheme represented in Fig. 1. A material representing the critical part and containing the crack is subjected to the action of an electromagnetic field produced by a coil forming the EC sensor where a time-changing current density is imposed.

The aim is to evaluate the eddy currents in the

Submitted On: January 4, 2015
Accepted On: December 6, 2015

defective part and the change in impedance of the coil.

Our simulation of the EC NDT devices is carried out in the context of harmonic quasi-stationary regime.

Crack:
length: ***l***
width: ***w***
depth: ***d***

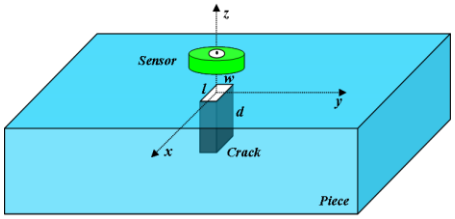

Fig. 1. Sensor-crack system.

Amongst the usual formulations in use for the EC problem, the « $\vec{A}V-\vec{A}$ » nodal formulation is the most popular due to its generality, robustness and ease of implementation without any restriction on continuity conditions [11].

The adopted formulation of the 3D electromagnetic model is:

$$\begin{cases} \vec{\nabla}\times\nu\vec{\nabla}\times\vec{A}-\vec{\nabla}\nu\vec{\nabla}\cdot\vec{A}+\sigma\left(\dfrac{\partial\vec{A}}{\partial t}+\vec{\nabla}\cdot V\right)=\vec{J}_s \\ \vec{\nabla}\cdot\sigma\left(\dfrac{\partial\vec{A}}{\partial t}+\vec{\nabla}\cdot V\right)=0. \end{cases} \quad (1)$$

The geometry and the meshing are developed using GMSH mesher [12].

Figure 2 shows a part of the meshing of the system.

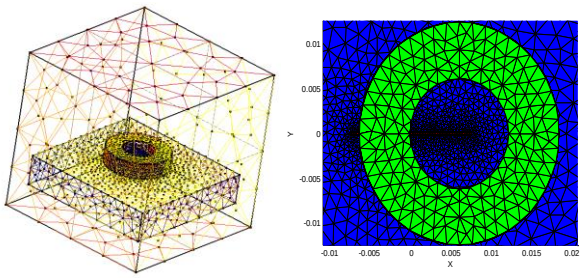

Fig. 2. Top view of the meshing of the system generated by GMSH.

Our study is based on data analysis of scans, carried out by small displacements of the sensor with 0.5 mm or 1 mm steps, parallel and perpendicular to the crack on the surface of the material. In order to simulate the movement of the sensor, while keeping the same mesh topology, we use the 3D band geometry method [13]. The obtained results will be compared to experimental data of the academic benchmark configuration [10].

III. EDDY CURRENT REPRESENTATION

In every position of the sensor on the surface of material, we calculate both the impedance of the system with and without the crack. The impedance variation ΔZ is given by:

$$\Delta Z=\frac{j\omega}{I^2}\int_{\Omega_s}\left(\vec{A}-\vec{A}_0\right)\cdot\vec{J}_s d\Omega_s, \quad (2)$$

where $\vec{A}$ and $\vec{A}_0$ are the magnetic vector potentials with and without the crack respectively; I and ω are respectively the intensity and the frequency of the current in the coil; Ω_s is the volume of the coil. We note here that, the integral in the above equation corresponds to the electromagnetic energy difference in the coil with and without the crack, so the simulation of the case "zero" (no cracks) is always included.

Figure 3 shows the EC signals, namely the variation in the resistance and reactance of the sensor for a surface crack using system of TEAM Workshop Benchmark problem, Pb. No. 15-1 (Table 1) [10]. These signals represent the signatures of crack.

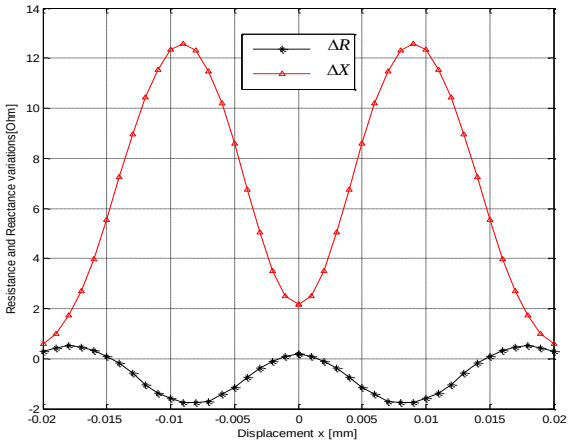

Fig. 3. Signature of the crack: the variation of resistance and reactance of the impedance of the system as function of displacement of the sensor.

IV. THE EC-NDT SIMULATION

The study of the crack size effect on the EC signal will enable us to identify the EC-NDT device sensitivity. This sensitivity allows us to define accessible parameters necessary for the inverse problem. In this respect, it will be possible to predict which relevant parameters can be calculated by the simulation.

We purposely chose to work with the same system of TEAM Workshop Benchmark problem, Pb. No. 15-1 [10]. The characteristics of this system are presented in Table 1.

Table 1: Parameters of test experiment system of TEAM Workshop Benchmark [10]

The Coil	
Outer radius	12,40 ± 0,05 mm
Inner radius	6,15 ± 0,05 mm
Height	6,15 ± 0,1 mm
Number of turns	3790
Lift-off	0,88 mm
The Test Specimen	
Conductivity	$(30,6 \pm 0,20)10^6$ S/m
Thickness	12,22 ± 0,02 mm
The defect	
Length	12,6 ± 0,02 mm
Depth	5,00 ± 0,05 mm
Width	0,28 ± 0,01 mm
Others Parameters	
Frequency	900 Hz
Skin depth at 900 Hz	3,04 mm

A. Crack width effect on the EC signal

Most of previous works known to the authors were concerned with the depth effect of the crack on the EC signal, but few studies were concerned with the width effect [1] and [15].

Figure 4 depicts EC signatures of three different cracks having the identical length and depth with different widths: 0.30 mm, 0.25 mm and 0.15 mm.

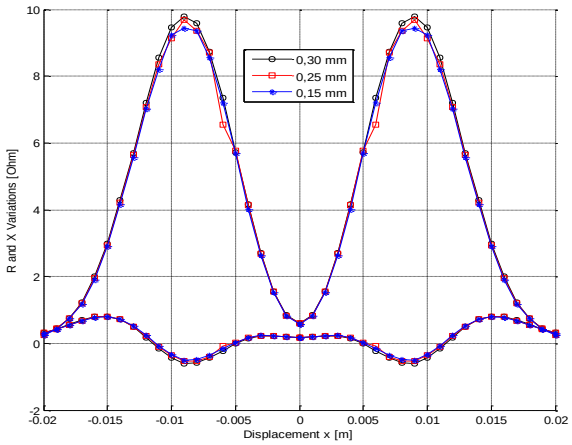

Fig. 4. EC signatures of cracks with 0.30 mm, 0.25 mm and 0.15 mm width having the identical length and depth.

Thus, a change from 0.15 to 0.30 mm in width will have no effect on the EC signals. This result is in good agreement with the work of Chen et al. and Helifa et al. on the electro-eroded slots [1] and [15]. This can be explained by the fact that the amplitude of the crack signal depends on the ratio defect volume/scanned volume. In this interval, the increase of the width raises the volume of the defect, but the volume ratio stays weak. The sensor is then insensitive to this change. We can conclude, that for thin cracks (<0.3 mm), the change in width has no effect on the EC signal; probably, this is a reason that researchers do not speak about this parameter.

B. Crack length effect on the EC signal

Figures 5 and 6 present EC signatures of the resistance and reactance variations with respect to the sensor displacement produced by cracks of identical width (0.20 mm) and depth (5 mm) having different lengths.

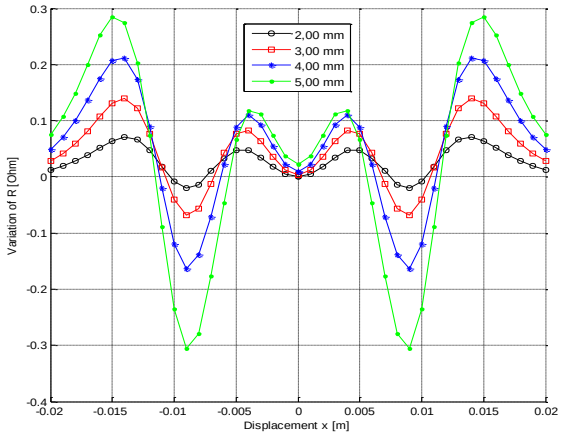

Fig. 5. Resistance vs. sensor displacement of cracks with identical width (0.20 mm) and depth (5 mm) having different lengths.

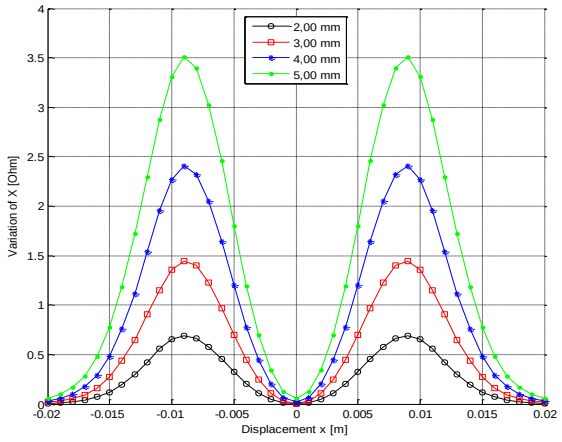

Fig. 6. Reactance vs. sensor displacement of cracks with identical width (0.20 mm) and depth (5 mm) having different lengths.

Thus, the crack length effect on the EC signal is clearly apparent contrary to the crack width. Hence, one can conclude that for thin cracks the EC signal strongly

depends on crack length.

C. Crack depth effect on the EC signal

Figures 7 and 8 show EC signatures of the resistance and reactance variations with respect to the sensor displacement produced by cracks of identical width (0.20 mm) and length (9 mm) having different depths.

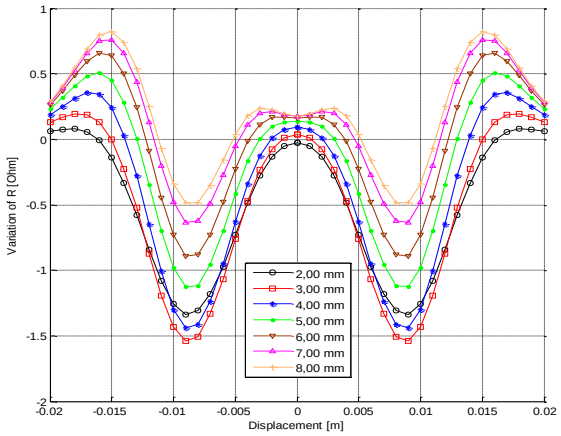

Fig. 7. Resistance vs. sensor displacement of cracks with identical width (0.20 mm) and length (9 mm) having different depths.

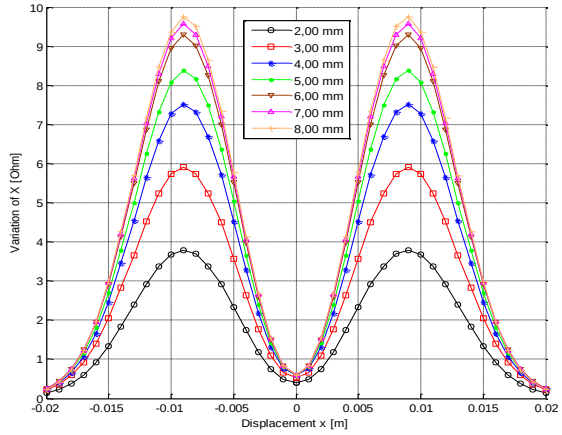

Fig. 8. Reactance vs. sensor displacement of cracks with identical width (0.20 mm) and length (9 mm) having different depths.

Thus, the crack depth effect on the EC signal is also apparent as the length effect. On the other hand, we notice that the curves of reactance vs. sensor displacement are no longer evident over a certain depth. This point will be discussed in the following paragraph.

D. EC signal and the depth limit

Figure 9 shows a zoom of three EC signatures representing the reactance variations with respect to the sensor displacement produced by cracks of identical width (0.20 mm) and length (9 mm) having different depths.

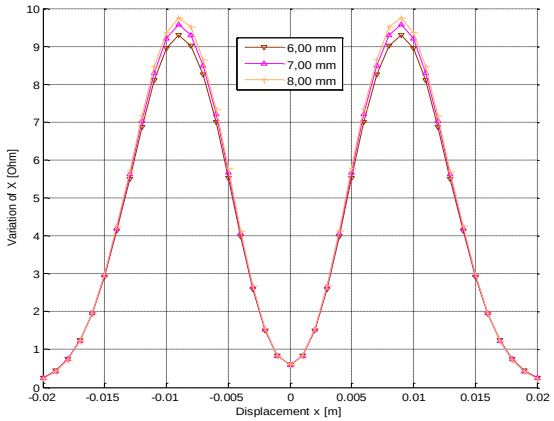

Fig. 9. Zoom on the reactance variations with respect to the sensor displacement produced by cracks of identical width (0.20 mm) and length (9 mm) having different depths.

We note in Fig. 9 that, over 6 mm depth, the curves of reactance vs. sensor displacement are no longer evident over a certain depth that we name depth limit. In consequence, we are not able to estimate the real depths of cracks exceeding these depth limit. This result corroborates the work of Helifa et al. [1].

We can also show this depth limit by plotting the reactance variations with respect to the depth of cracks at one position of sensor (Fig. 10).

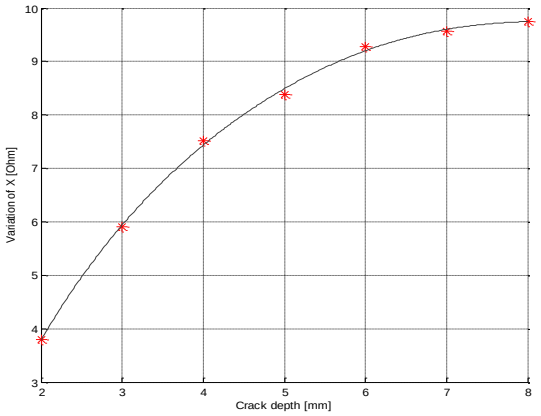

Fig. 10. Reactance vs. depth of cracks with identical width (0.20 mm) and length (9 mm) at one position of sensor.

We must note here that, this depth limit is not related to the skin depth. Indeed, the depth limit in our case is estimated at 6 mm while the skin depth is 3 mm. This can be explained by the fact that for a surface

crack, which is open to the surrounding, and as the probe radiates to an extent of many times its diameter, the electromagnetic field can, therefore, diffuse deeply inside this surface crack at distances well over than the skin depth. Eddy currents always occur at equal effective skin depth in both surface and internal walls of this crack.

We can show the same result for the resistance variations; however, the depth limit is not the same as defined for the reactance variations. Indeed, Fig. 11 shows that the curves representing the resistance variations with respect to the sensor displacement are always discernible even beyond the depth limit previously set for the reactance variations.

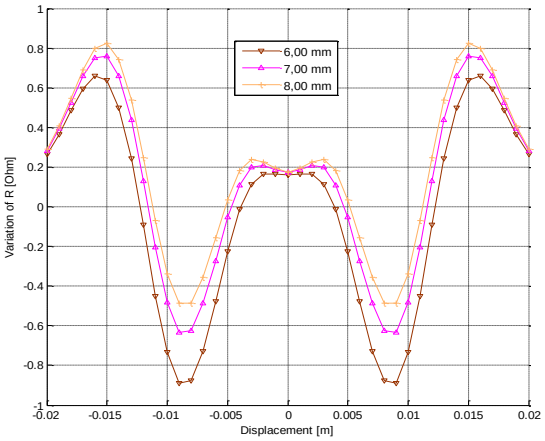

Fig. 11. Zoom on the resistance variations with respect to the sensor displacement produced by cracks of identical width (0.20 mm) and length (9 mm) having different depths.

Figure 12 shows the resistance variations with respect to the depth of cracks at one position of sensor.

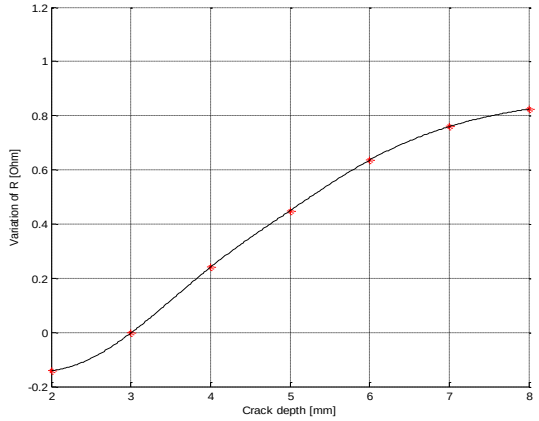

Fig. 12. Resistance vs. depth of cracks with identical width (0.20 mm) and length (9 mm) at one position of sensor.

Thus, Figs. 9, 10, 11 and 12 show that the depth limit is not the same for the resistance and reactance variations.

In conclusion, and in spite of the fact that signals corresponding to resistance variations are much less intense than those of the reactance variations, the resistance variations are more sensitive to the crack depth than the reactance ones.

V. DATA INVERSION

The next step consists of inversion of data results, using neural networks (NN) based MLP (*MultiLayer Perceptron*) model. There are two reasons to this choice. The first one is that, NN are able to approximate any function with a finite number of discontinuities to any required precision, they are "universal parcimonial approximators". The second reason is that, NN are known to be fast in finding quasi-instantly the solution of nonlinear problems.

To solve the inverse problem, it is necessary to achieve the Hadamard conditions [14]. Instead of using one numerical measurement only corresponding to a single position, we will use the crack signature which contains a whole set of numerical measurements corresponding to a set of sensor positions. We choose as input of NN a vector containing 21 numerical measurements of the resistance variation related to 21 different sensor positions through the surface crack. Indeed, the shapes of curves in Fig. 13 cannot be represented by only 2 or 3 values of the resistance variation. Thus, with this approach we can overcome the unicity problem of solution. Indeed, a cross over points in Fig. 13 are a tangible proof of the fact that the input vector NN containing 2 or 3 values is not sufficient to define completely a single crack as is often done in many works [2].

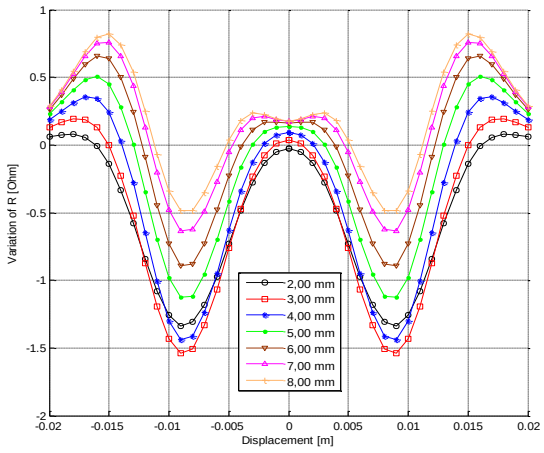

Fig. 13. Resistance vs. sensor displacement of cracks with identical width (0.20 mm) and length (9 mm) having different depths.

A. NN MLP inversion

Behavioral laws of EC sensors are strongly non-linear. There are NN structures able to model these types of problems. Among these structures, the multilayer neural networks MLP (or Multilayer Perceptron) are the most common and widely used in the EC NDT [2] and [16]. We use the algorithm of back-propagation gradient of Levenberg-Marquardt, adopted for multilayer networks with a supervised learning [2].

Since all our input parameters have the same physical unit (impedance), we do not need preconditioning. This is also the case for output parameters (length). Furthermore, the EC crack signature is already centered and does not need any further centering.

B. Characterization of surface cracks

The objective consists of simultaneously estimating the two main crack parameters: length and depth. The response of EC sensor simulated by 3D Finite elements is the data base for the NN.

The structure of NN application is made of hidden layer with hyperbolic tangent activation function and an output layer with a linear activation function (Fig. 14). The number of neurons in the hidden layer is equals to 80.

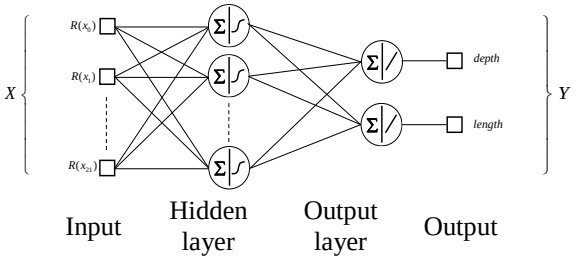

Fig. 14. Implementation of the MLP NN.

C. Result validation

The last step is to test the model's ability to be generalized. In this phase, we will test the network capacity to find the target parameters (crack depth and length) corresponding to examples of impedances in the learning domain. These examples are different from those used in the two basis previously used for learning and evaluation.

The relative error between the real parameters and the estimated ones is characterized for each P parameter using the following relationship:

$$ER(P) = \sqrt{\frac{1}{N}\sum_{i=1}^{N}\left(\frac{P_i - P_i}{P_i}\right)^2}, \qquad (3)$$

where N, P_i and P_i are respectively the number of examples over the test basis, the desired parameters and the estimated parameters of the NN.

Table 2 shows the relative errors in estimating the crack parameters (length and depth) by the NN MLP method.

Table 2: Relative errors by the NN MLP method

	Depth	Length
Relative error by NN MLP	2,50%	2,00%

When using NN, the training phase determines the limitations. That means following the interval values [min, max] of inputs and outputs sets, the performance of NN depends on this interval. For larger intervals the limitations will evolve.

According to the obtained results, we can conclude that the inverse model by MLP NN is able to generalize and gives results with good accuracy. This aptitude of generalizing is illustrated in Figs. 15 and 16.

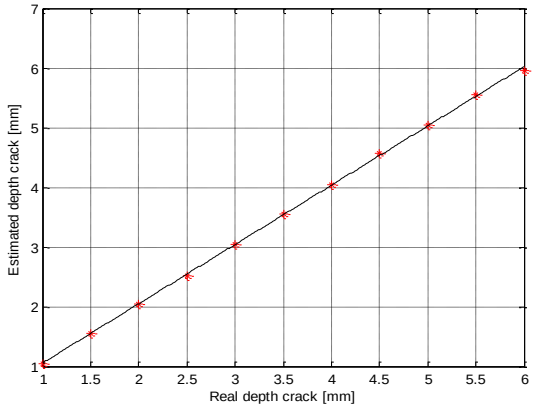

Fig. 15. Estimated depth vs. real depth of crack.

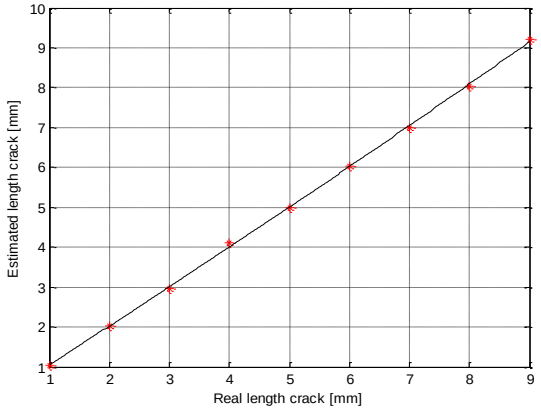

Fig. 16. Estimated length vs. real length of crack.

VI. CONCLUSION

During this work, the 3D finite element simulation of the EC NDT for a surface crack was conducted. The simulation results were validated and compared to those given by the Team Workshop Benchmark problem, Pb. No. 15-1. This study shows that for thin cracks, the EC

signal is independent of the crack width. However, it strongly depends on its length and depth. Nevertheless, beyond a certain depth limit, the sensor becomes insensitive beyond this limit. The depth limit is not related to the skin depth and can reach much higher values than that of skin depth.

The inverse problem is solved using an MLP neural networks. The application consists to simultaneously estimate the two parameters of the crack: depth and length. The use of a range of variation values of resistance or reactance (signature of the crack) is taken as input vector for MLP NN. The generalized approach that we developed can estimate with good accuracy the crack required geometric parameters.

REFERENCES

[1] B. Helifa, A. Oulhadj, A. Benbelghit, I. K. Lefkaier, F. Boubenider, and D. Boutassouna, "Detection and measurement of surface cracks in ferromagnetic materials using eddy current testing," *NDT&E International, Elsevier*, vol. 39, issue 1, pp. 384-390, Mar. 2006.

[2] Y. Le Bihan, J. Pavo, and C. Marchand, "Characterization of small cracks in eddy current testing," *Eur. Phys. J. Appl. Phys*., 43, pp. 231-237, 2008.

[3] D. Prémel and A. Baussard, "Eddy-current evaluation of three-dimensional flaws in flat conductive materials using a Bayesian approach," *Institute of Physics Publishing*, Inverse Problems 18, pp. 1873-1889, 2002.

[4] G. Rubinacci, A. Tamburrino, and S. Ventre, "Regularization and numerical optimization of a fast eddy current imaging method," *IEEE Transactions on Magnetics*, vol. 42, no. 4, pp. 1179-1182, Apr. 2006.

[5] B. Helifa, A. Zaoui, M. Feliachi, I. K. Lefkaier, F. Boubenider, and A. Cheriet, "Simulation du CND par courants de Foucault en vue de la caractérisation des fissures débouchantes dans les aciers austénitiques," *6ème Conférence Européenne sur les méthodes numériques en Electromagnétisme NUMELEC*, Liège – Belgique, Déc. 2008.

[6] X. Qiu, P. Zhang, J. Wei, X. Cui, C. Wei, and L. Liu, "Defect classification by pulsed eddy current technique in con-casting slabs based on spectrum analysis and wavelet decomposition," *Sensors and Actuators A: Physical*, 20, pp. 272-281, 2013.

[7] R. Smid, A. Docekal, and M. Kreidl, "Automated classification of eddy current signatures during manual inspection," *NDT&E International*, vol. 38, pp. 462-470, 2005.

[8] L. Udpa, P. Ramuhalli, J. Benson, and S. Udpa, "Automated analysis of eddy current signals in steam generator tube inspection," *16th WCNDT World Conference on NDT*, Montreal, Aug. 30 – Sep. 3, 2004.

[9] G. Chen, Y. Yoshida, K. Miya, and M. Uesaka, "Application of eddy current testing inspection to the first wall of fusion reactor with wavelet analysis," *Fusion Engineering and Design*, 29, pp. 309-316, 1995.

[10] Team Workshop Problem 15, *Rectangular Slot in a Thick Plate: a Problem in Nondestructive Evaluation*, http://www.compumag.org/jsite/images/stories/TEAM/problem15.pdf.

[11] M. Rachek and M. Féliachi, "3-D movement simulation techniques using FE-methods: application to eddy current non-destructive testing," *NDT&E international, Elsevier*, vol. 40, issue 1, pp. 35-42, Jan. 2007.

[12] C. Geuzaine, *Meshing Software*, www.geuz.org/gmsh.

[13] B. Bendjima, K. Srairi, and M. Féliachi, "A coupling model for analysing dynamical behaviors of an electromagnetic forming system," *IEEE Transactions on Magnetics*, vol. 33, no. 2, pp. 1638-1641, Mar. 1997.

[14] Z. Chen, M. Rebican, N. Yusa, and K. Miya, "Fast simulation of ECT signal due to a conductive crack of arbitrary width," *IEEE Transactions on Magnetics*, vol. 42, no. 4, pp. 683-687, Apr. 2006.

[15] Ph. Beltrame and N. Burais, "Generalization of the ideal crack model in eddy-current testing," *IEEE Transactions on Magnetics*, vol. 40, no. 2, pp. 1366-1379, Mar. 2004.

[16] N. Yusa, W. Cheng, Z. Chen, and K. Miya, "Generalized neural network approach to eddy current inversion for real cracks," *NDT&E International 35*, pp. 609-614, 2002.

Bachir Helifa received the degree of High Studies (Master of Science) in Physics from USTHB University of Algiers and the Magister in Materials Sciences from Laghouat University and the Ph.D. in Materials Physics from USTHB University of Algiers. His research interests include the Materials Sciences, Non-destructive Testing, Magnetism and Electromagnetism.

Mouloud Feliachi received the Engineering degree in Electrical Engineering from the National Polytechnic School of Algiers and the Doctor Engineer degree from the Conservatoire National des Arts et Métiers of Paris and the Ph.D. in Physical Sciences from

the National Polytechnic Institute of Grenoble. His research interests include Modelling of Electromagnetic Systems, Non-destructive Testing and Magnetic materials.

Ibn Kheldoun Lefkaier received the degree of High Studies (Master of Science) in Physics from Ferhat Abas University of Setif-Algeria and the Ph.D. in Solid Physics from Kabarino Balkarie University of Nalchik-Russia. His research interests include the Materials Sciences, thermodynamics of solid and Non-destructive Testing.

Nonlinear Modelling Approach for Linear Switched Reluctance Motor and its Validation by Two Dimensional FEA

I. Mahmoud, M. Fathallah, and H. Rehaoulia

Department of Electrical Engineering
National High School of Engineers of Tunis (ENSIT)
Tunisia University 5 av. Taha Hussein BP 56 – 1008 Tunis, Tunisia
Mahmoud.Imed@issatm.rnu.tn, Habib.Rahaoulia@esstt.rnu.tn

Abstract ─ This paper exposes two procedures in order to develop a refined analytical model which describes the behaviour of a linear switched reluctance motor. The first approach is based on the flux linkage and the second on the inductance, both versus position and current. Taking into account the non-linearity of the magnetic circuit, models are expressed by either Fourier series or polynomials where the only first three components are considered. Results of these analytical approaches are compared with those obtained using finite element methods (FEM) where a good agreement is observed.

Index Terms ─ Actuator, analytical model, computer simulation, electromagnetic force.

I. INTRODUCTION

Nowadays, linear switched reluctance machines are widely used. Unfortunately, in order to generate a high-propulsion force the LSRM must be operated in the saturation zone. In saturation conditions, main magnetic characteristics, such as flux linkage, inductance and propulsion force, are highly nonlinear. Consequently, the analytical methods based on some hypotheses are not very accurate to determine system performances and to elaborate control strategies. Regarding their modelling, there are many approaches such as lookup-table techniques, magnetic equivalent-circuit analysis, cubic-spline interpolations and finite-element methods (FEM), [3-4].

In a linear switched reluctance machine, the phase inductances and flux linkages vary with rotor position due to stator and rotor saliencies. The phase inductances and flux linkages at any rotor position also vary with the instantaneous phase currents because of magnetic saturation. However, these variations can be modelled analytically using the data obtained through FEM or through experiments. These analytical expressions are used to represent the linear switched reluctance machine dynamics and hence, the machine performance can be obtained, [1-2].

In order to determine a refined model which describes the behaviour of a saturated reluctant structure, there are basically two ways to represent the static LSRM characteristics. The first way is to plot the flux linkage versus rotor position and different phase currents. In this section, two approaches will be developed. The second way is to plot the phase inductance as function of rotor position and different phase currents, [5-8].

The paper is organized as follows. Taking apart the introduction and the conclusion, in Section 2, two approaches based on flux linkage model are developed. Section 3 gives the second method based on inductance model. Finally, Section 4 is reserved to determine the dynamic performances with and without saturation for the LSRM.

II. FLUX-LINKAGE-BASED MODEL OF LSRM

As previously stated, in a linear switched reluctance machine, the magnetic flux depends on both the relative stator and rotor position and winding current. Using Fourier series, the stator-phase flux linkage of the LSRM limited to the second harmonic order is:

$$\varphi(i,x)=\varphi_0+\varphi_1\cos\left(\frac{2\pi}{\lambda}x\right)+\varphi_2\cos\left(\frac{4\pi}{\lambda}x\right). \quad (1)$$

For a given phase current, coefficients φ_0, φ_1 and φ_2 can be derived as functions of the aligned position flux linkage φ_c; the unaligned position flux linkage φ_{op} and the flux linkage at the midway φ_i, as follows, [9-10]:

$$\varphi_0=\frac{1}{2}\left[\frac{1}{2}\left(\varphi_c+\varphi_{op}\right)+\varphi_i\right], \quad (2)$$

$$\varphi_1=\frac{1}{2}\left(\varphi_c-\varphi_{op}\right), \quad (3)$$

$$\varphi_2=\frac{1}{2}\left[\frac{1}{2}\left(\varphi_c+\varphi_{op}\right)-\varphi_i\right]. \quad (4)$$

Based on the above description, the proposed analytic modelling can be developed by using three curves: the aligned, the unaligned and the midway-position curves. The unaligned position curve, as shown in Fig. 1, is approximated by a straight line and can be described by:

$$\varphi_{op}=L_{op}i, \quad (5)$$

Submitted On: October 30, 2013
Accepted On: October 22, 2015

where L_{op} is a constant.

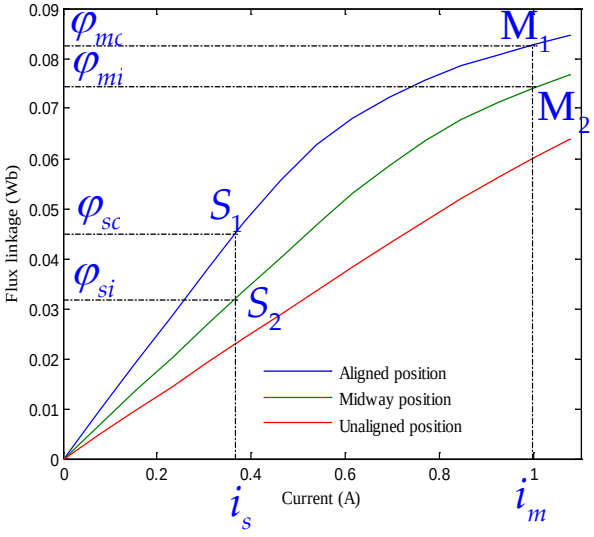

Fig. 1. Flux linkage against phase current for different mover positions.

To determine φ_c and φ_i and consequently the coefficients of the Fourier series φ_0, φ_1 and φ_2, two approaches have been developed.

A. First approach

Obviously, there is no linear relationship between the flux linkage and current in the saturated region for both aligned and midway positions, as shown in Fig. 1. At aligned and midway positions, the flux linkage may be approximated by an arctangent function:

$$\varphi_c = \frac{\arctan(a_1 i)}{a_2}, \tag{6}$$

$$\varphi_i = \frac{\arctan(m_1 i)}{m_2}, \tag{7}$$

where a_1, a_2, m_1 and m_2 are constants to be evaluated in the following sequence of steps.

- Step1: Choose two points φ_{mc} and φ_{sc} on the aligned position, Fig. 1. φ_{sc} is the flux linkage at the threshold saturated current i_s, and φ_{mc} is the flux linkage at the value of the triple to quadruple of i_m.
- Step 2: Constant a_1 is evaluated by using curve-fitting so that:

$$\frac{\varphi_{mc}}{\varphi_{sc}} = \frac{\arctan(a_1 i_m)}{\arctan(a_1 i_s)}. \tag{8}$$

- Step 3: Constant a_2 is calculated by:

$$a_2 = \frac{\varphi_{sc}}{\arctan(a_1 i_s)}. \tag{9}$$

- Step 4: Proceed the same way for m_1 and m_2.

Specifications of the designed prototype of the LSRM are shown in Fig. 2 and Table 1.

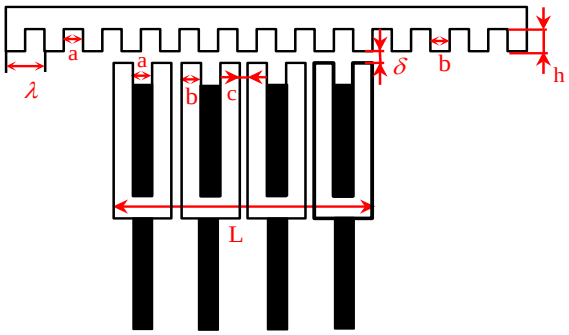

Fig. 2. Main dimensions of the conceived actuator.

Table 1: Motor mechanical and electrical parameters

Number of modules	4
Tooth width (b)	3 mm
Slot width (a)	3 mm
Tooth pitch (λ)	6 mm
Phase separation (c)	1.5 mm
Mover length	135 mm
Stator length (L)	40.5 mm
Air gap width (δ)	0.1 mm
Step size	1.5 mm
Number of turns per phase	520
Height of the mover teeth (h)	4 mm

Figure 3 shows the comparison of flux linkage versus phase current for different positions. We notice that the flux linkage versus current with different positions characteristics obtained by the proposed model closely match those obtained by FEM in the saturated region. However, the deviation in the linear region, as shown in Fig. 4, is obvious. Consequently, it is necessary to develop a new method to solve this problem.

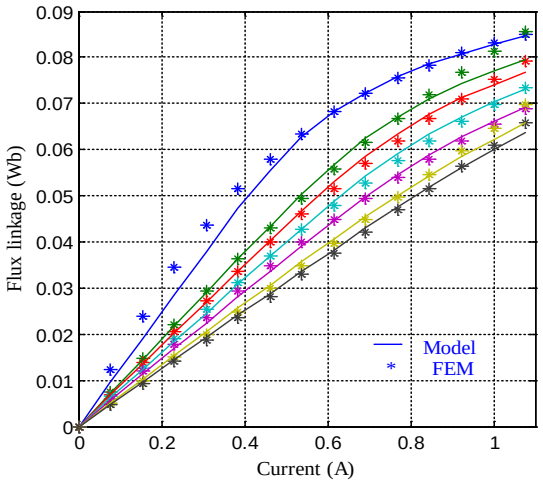

Fig. 3. Extreme left phase: comparison of flux linkage versus current with different positions (-Model, *FEM).

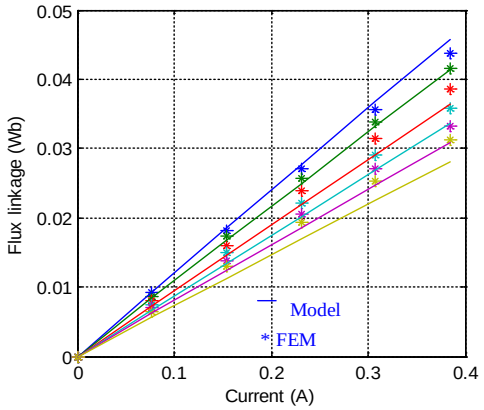

Fig. 4. Extreme left phase: comparison of flux linkage versus current with different positions in the linear region (-Model, *FEM).

B. Second approach

The flux linkage of the aligned position, shown in Fig. 1, can be expressed as, [11-17]:

$$\varphi_c = \begin{cases} L_c\, i & i \prec i_s \\ a_1 - \dfrac{a_2}{i} & i \geq i_s \end{cases}, \tag{10}$$

with

$$L_c\, i_s = a_1 - \frac{a_2}{i_s}. \tag{11}$$

In a similar way, we get for the midway position:

$$\varphi_i = \begin{cases} L_i\, i & i \prec i_s \\ m_1 - \dfrac{m_2}{i} & i \geq i_s \end{cases}, \tag{12}$$

with

$$L_i\, i_s = m_1 - \frac{m_2}{i_s}, \tag{13}$$

where L_c and L_i are also constants.

Constants a_1, a_2, m_1 and m_2 are evaluated by using respectively points M_1, S_1 and M_2, S_2 in Fig. 1.

Figure 5 gives the comparison of flux linkage produced by the left extreme phase versus current for different positions. It can be observed that results obtained by the proposed analytical model closely match those obtained by finite element methods.

The force produced by an LSRM is proportional to the rate of change of co-energy as the rotor moves from one position to another, as follows:

$$F(i,x) = \frac{\partial W_c(i,x)}{\partial x}, \tag{14}$$

$$W_c(i,x) = \int_0^i \varphi(i,x)di, \tag{15}$$

Using (14) and (15), we get:

$$F(i,x) = \int_0^i \frac{\partial \varphi(i,x)}{\partial x}di. \tag{16}$$

As shown previously, the electromagnetic force of the conceived motor is formulated by Equation (16). Now, the flux linkage is limited to the second order Fourier model as indicated by (1) and its related relations (2), (3) and (4). After necessary mathematical manipulations, it is not difficult to get, [18-19]:

$$F = -\frac{1}{2}\left[\frac{2\pi}{\lambda}\sin\left(\frac{2\pi}{\lambda}x\right)\right]\left[\int_0^i \varphi_c di - \int_0^i \varphi_{op} di\right] - \left[\frac{2\pi}{\lambda}\sin\left(\frac{4\pi}{\lambda}x\right)\right]\left[\frac{1}{2}\int_0^i \varphi_c di + \frac{1}{2}\int_0^i \varphi_{op} di - \int_0^i \varphi_i di\right]. \tag{17}$$

Electromagnetic force Equation (17) is a highly nonlinear function with respect to the mover position and current. Figure 6 represents the comparison of the thrust force produced by the left extreme phase as function of mover position. Characteristics are calculated via the proposed model and respectively by FEM. Evidently, the main difference comes from the choice of the mathematical model, specifically the linkage flux model, Equation (1). We expect that the accuracy may be improved by introducing higher order harmonics in Equation (1) and eventually by correctly choosing the number of Fourier terms.

Figure 6 shows a reasonable coincidence between the proposed analytical model with those obtained by the finite element method (FEM) which attests to the truth of the approach. Therefore, the second order of Fourier series is sufficient to achieve the desired results.

The flux linkage based model has larger error, but basically the results cover satisfactory in the second order of Fourier series. In order to improve these results, it was essential to develop a more realistic approach, [20-21].

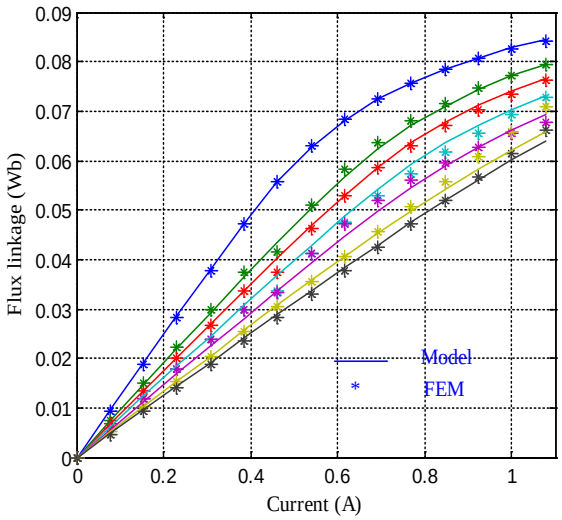

Fig. 5. Extreme left phase: comparison of flux linkage versus current with different positions (-Model, *FEM).

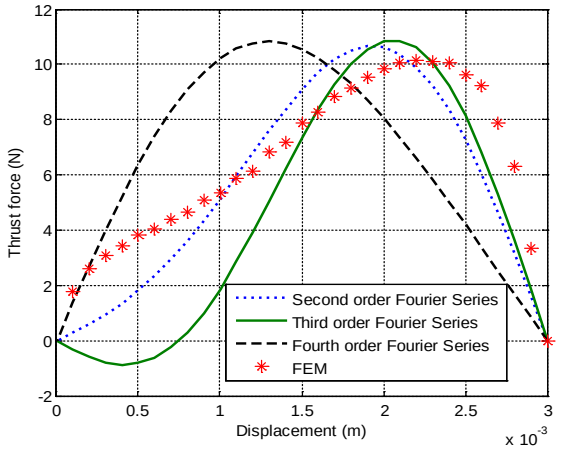

Fig. 6. Extreme left phase: comparison of the thrust force as function of mover position for different order of Fourier series (-Model, *FEM).

III. INDUCTANCE-BASED MODEL OF LSRM

In LSRM, the reluctance of the magnetic path in a given phase changes with rotor movement. The reluctance is maximum in unaligned position and minimum in the aligned position. As a consequence, phase inductance changes periodically as function of the rotor position. At any given rotor position, the phase inductance also varies with the instantaneous phase current. Therefore, the phase inductance versus mover position will be represented by Fourier series (18) and the nonlinear variation of its coefficients with current will be expressed by polynomial functions (20, 21), [22-23]:

$$L(x,i)=\sum_{k=0}^{m}L_k(i)\cos kN_r x\,, \tag{18}$$

where i, x and m are respectively the phase current, the position of the mover and the number of terms in the Fourier series.

The accuracy and stability of numerical simulations are the main challenges which should be met. To simplify expression (18), only the first three terms of the Fourier series are considered. The inductance expression is given by Equation (19), [24-25]:

$$L(x,i_j)=L_0(i_j)+L_1(i_j)\cos\left(N_r\left(x-(j-1)\frac{2\pi}{NN_r}\right)\right) + L_2(i_j)\cos\left(2N_r\left(x-(j-1)\frac{2\pi}{NN_r}\right)\right), \tag{19}$$

with $L(x, i_j)$ and N are respectively the inductance associate to the phase j in the position x of the mover for the current i_j and the number of phase.

To determine the three coefficients L_0, L_1 and L_2, we use the inductance at three positions: aligned position L_c (i_j), unaligned position L_{op} (i_j) and midway position between the above two positions L_i (i_j). Note that, L_{op} (i_j) can be treated as a constant but, L_c (i_j) and L_i (i_j) are functions of the phase current i_j and can be approximated by the polynomials, [25-26]:

$$L_c(i_j)=\sum_{n=0}^{p}a_n i^n{}_j\,, \tag{20}$$

$$L_i(i_j)=\sum_{n=0}^{p}b_n i^n{}_j\,, \tag{21}$$

where p is the order of the polynomials and a_n, b_n are the coefficients.

In our research, p = 6 is chosen after we compare the fitting results of different p values, (p = 3, p = 4, p = 5 and p = 6 have been tried and compared). As a result the inductance of the aligned position L_c (i_j) and midway position L_i (i_j) are approximated respectively by the Equations (22) and (23). Figure 7 shows the good agreement between the FEM and the proposed curve fitting methods. FEM results are obtained by Magnet 2D software. Analytical calculations were performed by means of curve-fitting matlab toolbox:

$$L_c(i)=a_1i^6+a_2i^5+a_3i^4+a_4i^3+a_5i^2+a_6i+a_7$$
$$\begin{aligned} a_1 &= -0.4883 & a_2 &= 1.356\\ a_3 &= -1.153 & a_4 &= 0.1993\\ a_5 &= 0.06603 & a_6 &= -0.02222\\ a_7 &= 0.1253 \end{aligned}, \tag{22}$$

$$L_i(i)=b_1i^6+b_2i^5+b_3i^4+b_4i^3+b_5i^2+b_6i+b_7$$
$$\begin{aligned} b_1 &= -0.3227 & b_2 &= 1.186\\ b_3 &= -1.609 & b_4 &= 0.9716\\ b_5 &= -0.2766 & b_6 &= 0.03345\\ b_7 &= 0.09355 \end{aligned}. \tag{23}$$

Consequently, the three coefficients for the Fourier series can be computed as, [27-29]:

$$L_0=\frac{1}{2}\left[\frac{1}{2}\left(L_c+L_{op}\right)+L_i\right], \tag{24}$$

$$L_1=\frac{1}{2}\left(L_c-L_{op}\right), \tag{25}$$

$$L_2=\frac{1}{2}\left[\frac{1}{2}\left(L_c+L_{op}\right)-L_i\right]. \tag{26}$$

The stator phase inductance at the aligned position is very affected by the stator phase current variations. On the contrary, the unaligned inductance is practically constant due to the large reluctance that characterizes this position.

It is worth mentioning that, found analytical model remains valid for any position x and any current i as illustrated by Figs. 8 and 9.

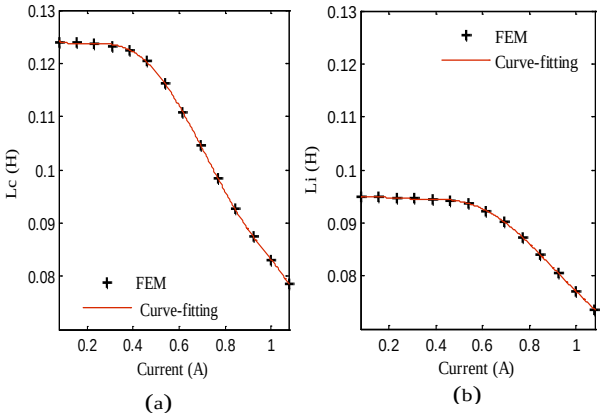

Fig. 7. Evolution of the winding inductance versus current: (a) aligned position, and (b) midway position.

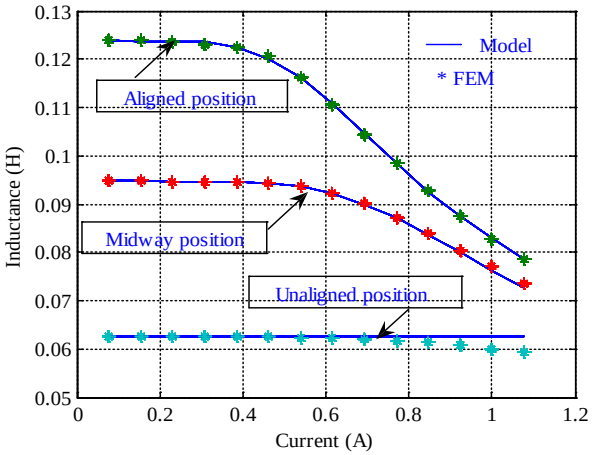

Fig. 8. Extreme left phase: comparison of inductance versus current with three positions (-Model, *FEM).

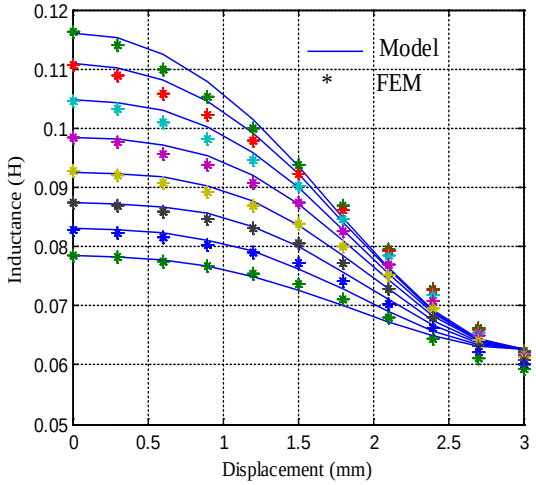

Fig. 9. Extreme left phase: comparison of inductance versus position with different currents (-Model, *FEM).

Multiplying the expression of inductance by the current (i), it gives the expression of linkage flux, [30-32]:

$$\varphi(i,x) = iL(i,x). \tag{27}$$

Figure 10 gives the comparison of linkage flux produced by the left extreme phase versus current for different positions. It can be observed that the linkage flux versus current for different position characteristics which are obtained by the proposed model closely match those obtained by finite element methods. These results prove the effectiveness of the proposed model.

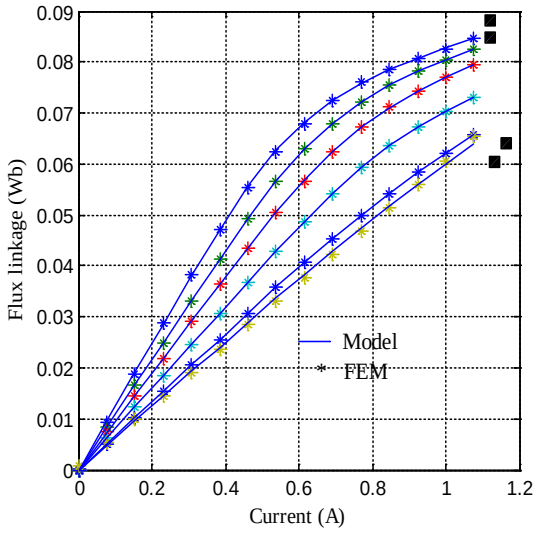

Fig. 10. Extreme left phase: comparison of linkage flux versus current with different positions (-Model, *FEM).

Furthermore, it is well known that the total electromagnetic force is given by the following expression:

$$F = \sum_{j=1}^{N} F_j(i,x), \tag{28}$$

where N is the number of phase, F_j the force of phase j and i_j the phase current. Consequently, the force F_j can be described by the following equation:

$$F_j(i,x) = \frac{\partial W_{c,j}}{\partial x} = \frac{\partial\left(\int_0^i L(x,i_j) i_j di_j\right)}{\partial x}, \tag{29}$$

$L(x, i_j)$ is the inductance associate to the phase j in the position x of mover for the current i_j.

For a given current, Equation (29) becomes:

$$F_j(i,x) = \frac{1}{2}\frac{\partial L_j(x)}{\partial x} i_j^{\,2}\Big|_{[i]=cte}. \tag{30}$$

Figure 11 shows also a reasonable coincidence between the curve obtained by the proposed model and that taken via the finite element method (FEM).

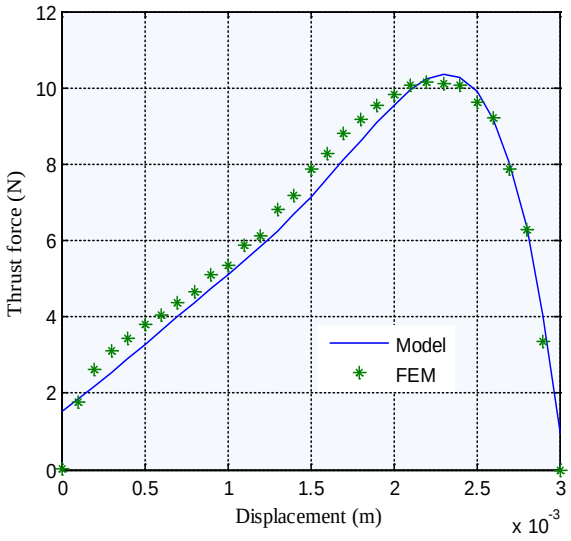

Fig. 11. Extreme left phase: comparison of the thrust force as function of mover position (-Model, *FEM).

IV. DYNAMIC PERFORMANCES OF LSRM

We plan to study the dynamic behavior of the all biomedical system. Dynamic electric equations of the four phases are:

$$U_A = Ri_A + \left(L(x,i_A) + \frac{\partial L(x,i_A)}{\partial i_A} i_A \right) \frac{d\,i_A}{dt} + \frac{\partial L(x,i_A)}{\partial x} i_A \frac{dx}{d\,t}, \quad (31)$$

$$U_B = Ri_B + \left(L(x,i_B) + \frac{\partial L(x,i_B)}{\partial i_B} i_B \right) \frac{d\,i_B}{dt} + \frac{\partial L(x,i_B)}{\partial x} i_B \frac{dx}{d\,t}, \quad (32)$$

$$U_C = Ri_C + \left(L(x,i_C) + \frac{\partial L(x,i_C)}{\partial i_C} i_C \right) \frac{d\,i_C}{dt} + \frac{\partial L(x,i_C)}{\partial x} i_C \frac{dx}{d\,t}, \quad (33)$$

$$U_D = Ri_D + \left(L(x,i_D) + \frac{\partial L(x,i_D)}{\partial i_D} i_D \right) \frac{d\,i_D}{dt} + \frac{\partial L(x,i_D)}{\partial x} i_D \frac{dx}{d\,t}. \quad (34)$$

The mechanical equation relating the rotor acceleration, speed, position and load force is:

$$m_c \frac{dx^2}{dt^2} = F(x) - \xi \frac{dx}{dt} - F_0 signe\left(\frac{dx}{dt}\right) - F_r, \quad (35)$$

parameters m_c, ξ, F_0 and F_r designate the actuator mass, the viscous friction force, the dry friction force and the load force.

In order to validate the accuracy of the proposed model, Matlab/Simulink was used to perform the simulation with this model. This last, has been tested and compared by the linear model to predict the dynamic performance of the LSRM. Dynamic behaviour of position, thrust force and speed are resumed in Fig. 12. Note that, the excitation of phase A allows positioning the translator on the first step corresponding to 1.5 mm. Successive excitation of other phases are needed for next steps.

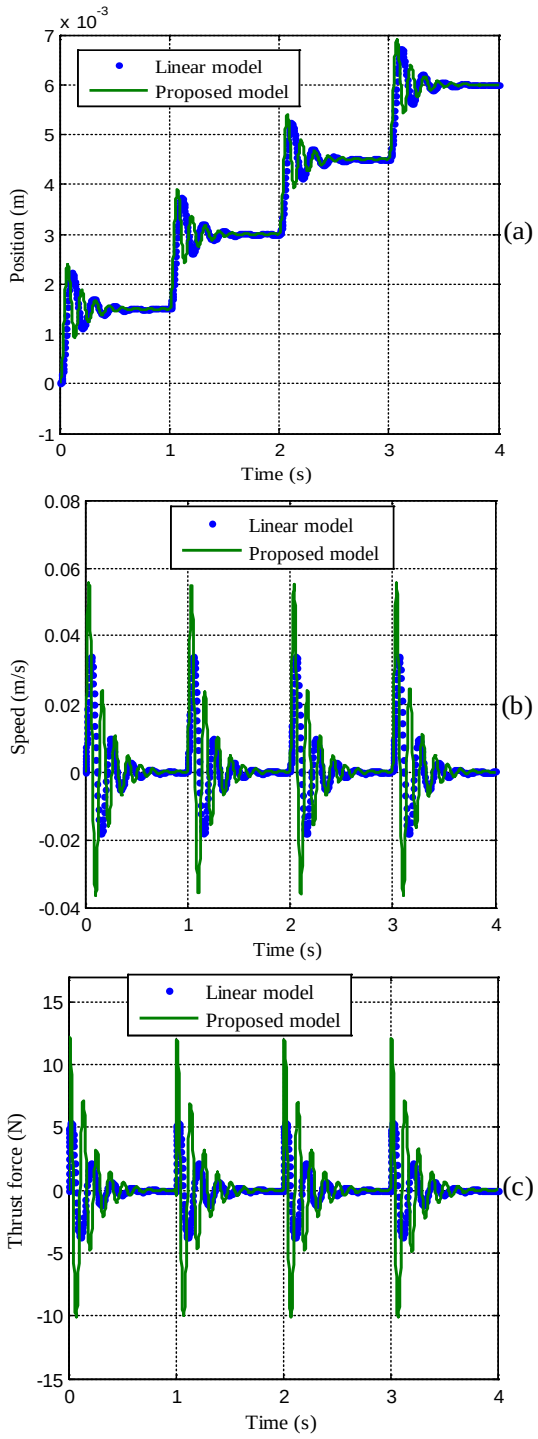

Fig. 12. (a) Position, (b) speed, and (c) thrust force evolution during four steps (*linear model, -proposed model).

The proposed model of the LSRM is characterized by a strongly oscillatory translation compared to the linear model. These oscillations are expected to disturb

the accuracy of the position and the constancy speed often required by many industrial applications and especially in the medical fields. This problem often leads to losses of synchronism, [33-36].

V. CONCLUSION

It is essential to have an accurate model of a linear switched reluctance motor that describes its static characteristics. It has been shown in this paper that there are different ways of modelling static characteristics of an LSRM. The developed analytical models consider the variation of either the phase flux linkage or the phase inductance with rotor position accounting for magnetic saturation. Results are compared to those obtained via the 2D-FEM. The comparison shows a reasonable agreement, proving the validity of the proposed approaches.

REFERENCES

[1] G. Singh, "Modelling and dynamic simulation of multiple-stack variable-reluctance step motors," *Comput. and Elect. Engng*., vol. 1, pp. 481-500, 1974.

[2] M. Feyrouz, "Contribution à l'Etude d'une Génératrice à Réluctance Variable," *Magistère en Electrotechnique*, Université Mentouri de Constantine, 2009.

[3] F. R. Salmasi, "Virtual auto-tuning position and torque sensors for switched reluctance motor drives," *IEEE Transactions on Industry Applications*, pp. 1355-1361, 2004.

[4] H. P. Chi, "Simplified flux-linkage model for switched-reluctance motors," *IEE Proc. - Electr. Power Appl.*, vol. 152, no. 3, pp. 577-583, May 2005.

[5] S. W. Zhao, "A self-tuning regulator for high-precision position control of linear switched reluctance motor," *IEEE Transactions on Industrial Electronics*, vol. 54, no. 5, Oct. 2007.

[6] J. Nicholas, "Modeling of a saturated switched reluctance motor using an operating point analysis and the unsaturated torque equation," *IEEE Transactions on Industry Applications*, vol. 36, no. 3, May/June 2000.

[7] M. Imed and R. Habib, "Development of analytical approach for linear switched reluctance motor and its validation by two dimensional FEA," *International Conference on Control, Engineering & Information Technology (CEIT'14)*, Monastir – Tunisia, Mar. 22-25, 2014.

[8] J. Hur, "Modeling of switched reluctance motor using Fourier series for performance analysis," *Journal of Applied Physics*, 2003.

[9] V. Ioan-Adrian, "Analytical flux linkage model of switched reluctance motor," *Rev. Roum. Sci. Techn. – Électrotechn. et Énerg*., vol. 54, no. 2, pp. 139-146, Bucarest, 2009.

[10] I. A. Viorel, "Speed-thrust control of a double sided linear switched reluctance motor (DSL-SRM)," *Proceedings of the 2008 International Conference on Electrical Machines*, Paper ID 879, 978-1-4244-1736-0/08 ©2008 IEEE, 2008.

[11] L. Lawler, "A simulation model for the four phase switched-reluctance motor," *Thesis, The University of Tennessee*, Knoxville, May 2003.

[12] Z. Haijuin, "Static characteristic and vibration dynamic response analysis of switched reluctance motor system," *International Conference on Mechatronics and Automation, Proceeding of IEEE*, Aug. 2009.

[13] H. Jin, "Modelling of switched reluctance motor using Fourier series for performance analysis," *Journal of Applied Physics*, vol. 93, no. 10, 15, May 2003.

[14] H. P. Chi, "Flux-linkage based models for switched-reluctance motors," *Ph.D. Philosophy, National Cheng Kung University*, Dec. 2005.

[15] A. O. Khalil, "Modeling and analysis of four quadrant sensorless control of a switched reluctance machine over the entire speed range," *The Graduate Faculty of the University of Akron, Ph.D. Thesis*, Aug. 2005.

[16] J. Lee, "Structural design optimization of electrical motors to improve torque performance," *Ph.D. Thesis, University of Michigan*, 2010.

[17] I. G. Sirbu, "Novel approach for electromagnetic actuators analysis in transient behaviour," *Advances in Electrical and Computer Engineering*, vol. 12, no. 1, 2012.

[18] E. Pădurariu, "Switched reluctance motor analytical models, comparative analysis," *The International Conference on Optimization of Electrical and Electronic Equipment, OPTIM 2010*, IEEE, 2010.

[19] R. M. Schupbach, "Modeling switched reluctance motors under multi-phase excitation," *University of Arkansas*, Department of Electrical Engineering 3217 Bell Engineering Center Fayetteville, AR 72701 – 1201 (501) 575-3005, Second Annual Report - Part 1 (AR2.1).

[20] A. Espírito Santo, "Static simulation of a linear switched reluctance actuator with the flux tube method," *Advances in Electrical and Computer Engineering*, vol. 10, no. 2, 2010.

[21] N. C. Lenin, "Force profiles of a linear switched reluctance motor having special pole face shapes," *Advances in Electrical and Computer Engineering*, vol. 10, no. 4, 2010.

[22] S. Song, "A comparative study on modeling methods for switched reluctance machines," *Computer and Information Science*, vol. 3, no. 2, May 2010.

[23] K. Ha, "Position estimation in switched reluctance

motor drives using the first switching harmonics of phase voltage and current," *Ph.D. Thesis, Virginia Polytechnic Institute and State University*, 2008.

[24] B. Fahimi, "A new approach to model switched reluctance motor drive application to dynamic performance prediction, control and design," C*onference IEEE 1998*, 0-7803-4489-8/98, 1998.

[25] W. Lu, "Modelling and control of a switched reluctance machine for electro-mechanical brake systems," *Ph.D. Thesis, Ohio State University*, 2005.

[26] J. Maridor, "Design, optimization, and sensorless control of a linear actuator," *Ph.D. Thesis, école Polytechnique Fédérale de Lausanne*, 2011.

[27] H. Gao, "Inductance model-based sensorless control of the switched reluctance motor drive at low speed," *IEEE Transactions on Power Electronics*, vol. 19, no. 6, Nov. 2004.

[28] K. I. Hwu, "Applying Powersys and Simulink to modeling switched reluctance motor," *Tamkang Journal of Science and Engineering*, vol. 12, no. 4, pp. 429-438, 2009.

[29] H. Torkaman, "Comprehensive detection of eccentricity fault in switched reluctance machines using high frequency pulse injection," *IEEE Transactions on Power Electronics*, vol. 28, no. 3, 1382{1390, 2013.

[30] E. K. Beser, "Design and analysis of an axially laminated reluctance motor for variable-speed applications," *Advances in Electrical and Computer Engineering*, vol. 13, no. 1, 2013.

[31] H. Torkaman, "Comprehensive detection of eccentricity fault in switched reluctance machines using high frequency pulse injection," *IEEE Transactions on Power Electronics*, vol. 28, no. 3, 1382{1390, 2013.

[32] I. G. Sirbu, "Novel approach for electromagnetic actuators analysis in transient behavior," *Advances in Electrical and Computer Engineering*, vol. 12, no. 1, 2012.

[33] A. Mosallanejad and A. Shoulaie, "Inductance profile calculation of step winding structure in tubular linear reluctance motor using three dimensional finite element method," *Euro. Trans. Electr. Power*, vol. 22, pp. 721-732, 2012.

[34] S. Méndez, "Design, characterization, and validation of a 1-kW AC self-excited switched reluctance generator," *IEEE Transactions on Industrial Electronics*, vol. 61, no. 2, Feb. 2014.

[35] J. F. Pan, Y. Zou, and G. Cao, "Adaptive controller for the double-sided linear switched reluctance motor based on the nonlinear inductance modelling," *IET Electr. Power Appl.*, vol. 7, iss. 1, pp. 1-15, 2013.

[36] S. Song, "Accurate measurement and detailed evaluation of static electromagnetic characteristics of switched reluctance machines," *IEEE Transactions on Instrumentation and Measurement*, vol. 64, no. 3, Mar. 2015.

Imed Mahmoud was born in Mahdia, Tunisia, on March 4, 1982. He received the Diploma of Baccalaureate in Applied Science degree in 2002 at Secondary School Souassi Mahdia, the M.Sc. degree in 2006, in Electrical Engineering option Electrical Engineering and Power Electronics and Master degree in Electrical Engineering and Systems Industrial 2008 all from the ESSTT (High School of Sciences and Technology of Tunis), University of Tunis, Tunisia. He joined the teaching staff of the ESSTT in 2008. His main research interests are study, design, modelling and control of linear actuators.

Mourad Fathallah Assistant Professor in Electrical Engineering at the ENISO. He is a doctor in Electrical Engineering INSA Lyon. He has five years experience in Consulting in Parisian society (Speech at multiple clients: VALEO, Barco, Philips etc.). Projects in Electronics (databases, design of control modules fluorescent lamps (subject to patent), size of losses in power lamps.

Habib Rehaoulia received the B.S. degree in 1978, the M.S. degree in 1980 and the Doctoral degree in 1983, all from the ENSET (Institute of Technical Sciences), University of Tunis, Tunisia. He joined the teaching staff of the ENSET in 1978. Since 1995, he is with the ESSTT (Institute of Sciences and Technology of Tunis), where he obtained the Habilitation degree in 2007.

During his career, he was on leave for several months at WEMPEC (University of Madison Wisconsin USA), ENSIEG (University of Grenoble France), "Lab. d'électrotechnique" (University of Paris VI France), and the CREA (University of Picardie France). His main research interests are analysis, modeling and simulation of electrical machines.

Rehaoulia is a Member of SIME (Signal, Image and Energy Management), ASET (Association for Tunisian Electrical Specialists), ATTNA (Tunisian Association for Numerical Techniques and Automatics) and IEEE (region 8, France section).

Utilization of Protruded Strip Resonators to Design a Compact UWB Antenna with WiMAX and WLAN Notch Bands

J. Mazloum [1] and N. Ojaroudi [2]

[1] Electrical Engineering Department
Shahid Sattari Aeronautical University of Science and Technology, Tehran, Iran

[2] Young Researchers and Elite Club, Ardabil Branch
Islamic Azad University, Ardabil, Iran
n.ojaroudi@yahoo.com

Abstract ─ In this paper, a new design of ultra-wideband (UWB) microstrip monopole antenna is presented. The main novelty of the proposed structure is the using of protruded strips as resonators to design an UWB antenna with dual band-stop property. In the proposed design, by cutting the rectangular slot with a pair of rotated Y-shaped strips in the ground plane, additional resonance is excited and much wider impedance bandwidth can be achieved. To make a single band-notched function, the square radiating patch is converted to the square-ring structure with a pair of protruded fork-shaped strips. Finally, by cutting a rectangular slot with a protruded M-shaped strip at the feed line, a desired dual band-notched function is achieved. The measured results reveal that the presented dual band-notched antenna offers a very wide bandwidth from 2.8 to 11.6 GHz, with two notched bands, around of 3.3-3.7 GHz and 5-6 GHz covering all WiMAX and WLAN bands.

Index Terms ─ Dual band-notched antenna, protruded strip resonators, UWB system.

I. INTRODUCTION

UWB communication systems usually require smaller antenna size in order to meet the miniaturization requirements of the radio-frequency (RF) units [1]. It is rapidly advancing as a high data rate wireless communication technology. The Federal Communication Commission (FCC) has released a bandwidth of 7.5 GHz (from 3.1 GHz to 10.6 GHz) for ultra wideband wireless communications. Due to its high bandwidth and very short pulses, UWB radio wave propagation provides very high data rate which may be up to several hundred Megabits per seconds (Mbps), and it is difficult to tract the transmitting data, which highly ensures the data security. The UWB technology has another advantage from the power consumption point of view. Due to spreading the energy of the UWB signals over a large frequency band, the maximum power available to the antenna as part of UWB system will be as small as in order of 0.5 mW according to the FCC spectral mask. This power is considered to be a small value and it is actually very close to the noise floor compared to what is currently used in different radio communication systems. It is a well-known fact that planar antennas present really appealing physical features, such as simple structure, small size, and low cost. Due to all these interesting characteristics, planar antennas are extremely attractive to be used in emerging UWB applications, and growing research activity is being focused on them. Consequently, a number of planar microstrip antennas have been experimentally characterized [2-4].

The frequency range for UWB systems between 3.1–10.6 GHz [5] will cause interference to the existing wireless communication systems, for example the wireless local area network (WLAN) for IEEE 802.11a operating in 5.15–5.35 GHz and 5.725–5.825 GHz bands, the worldwide interoperability microwave access (WiMAX) operating in 3.3–3.7 GHz and 5.35-5.65 GHz, so the UWB antenna with a band-notched function is required. Lately to generate the frequency band-notched function, several band-notched microstrip antennas have been reported [6-11].

All of the above methods are used for rejecting a single band of frequencies. However, to effectively utilize the UWB spectrum and to improve the performance of the UWB system, it is desirable to design the antenna with dual band rejection. It will help to minimize the interference between the narrow band systems with the UWB system. Some methods are used to obtain the dual band rejection in the literature [12-15].

In this paper, a new monopole antenna with dual band-notched characteristic for UWB applications has been proposed. The proposed antenna consists of a square-ring radiating stub with a pair of protruded fork-shaped strips, a feed-line with an M-shaped strip

Submitted On: February 23, 2014
Accepted On: October 22, 2015

protruded inside the rectangular slot, and a ground plane with a pair of protruded Y-shaped strips inside the slot.

II. ANTENNA DESIGN

The presented small monopole antenna fed by a microstrip line as shown in Fig. 1, is printed on an FR4 substrate of thickness 1.6 mm, permittivity 4.4, and loss tangent 0.018.

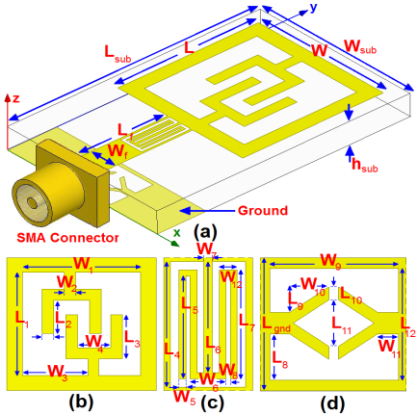

Fig. 1. Geometry of the proposed monopole antenna: (a) side view, (b) radiating patch, (c) feed-line, and (d) modified DGS.

The basic monopole antenna structure consists of a square patch, a feed line, and a ground plane. The square patch has a width W. The patch is connected to a feed line of width W_f and length L_f. On the other side of the substrate, a conducting ground plane is placed.

Regarding defected ground structures (DGS) theory, the creating slots in the ground plane provide additional current paths. Moreover, these structures change the inductance and capacitance of the input impedance, which in turn leads to change the bandwidth [16]. Therefore, by cutting a rectangular slot with a pair of rotated Y-shaped strips in the ground plane, much enhanced impedance bandwidth may be achieved. In the proposed design, protruded Y-shaped strips in the ground plane are used to make an additional resonance and increase the bandwidth.

This work started by choosing the dimensions of the designed antenna. Hence, the essential parameters for the design are: f_0 = 4.5 GHz (first resonance frequency), ε_r = 4.4 and h_{sub} = 0.8 mm. The dimensions of the patch along its length have now been extended on each end by a distance ΔL, which is given as:

$$\Delta L = 0.412\, h_{sub} \frac{(\varepsilon_{eff} + 0.3)\left(\frac{W_{sub}}{h_{sub}} + 0.264\right)}{(\varepsilon_{eff} - 0.258)\left(\frac{W_{sub}}{h_{sub}} + 0.8\right)}, \quad (1)$$

where h_{sub} is the height of dielectric, W_{sub} is the width of the microstrip monopole antenna and ε_{reff} is the effective dielectric constant. Then, the effective length (L_{eff}) of the patch can be calculated as follows:

$$L_{eff} = L + 2\Delta L. \quad (2)$$

For a given resonant frequency f_0, the effective length is given as:

$$L_{eff} = \frac{C}{2 f \sqrt{\varepsilon_{reff}}}. \quad (3)$$

For a microstrip antenna, the resonance frequency for any TM_{mn} mode is given by as:

$$\varepsilon_{eff} = \frac{(\varepsilon_r + 1)}{2} + \frac{(\varepsilon_r - 1)}{2}\left[1 + 12\frac{h_{sub}}{W_{sub}}\right]^{-\frac{1}{2}}. \quad (4)$$

The width W_{sub} of microstrip antenna is given:

$$W_{sub} = \frac{C}{2 f_0 \sqrt{\frac{(\varepsilon_r + 1)}{2}}}. \quad (5)$$

The last and final step in the design is to choose the length of the resonator and the band-stop filter elements. In this design, the optimized length $L_{resonance}$ is set to resonate at $0.25\lambda_{resonance}$, where $L_{resonance}=L_9+L_{12}-L_8+W_{11}+0.5W_{10}$. $\lambda_{resonance}$ corresponds to the extra resonance frequency (12 GHz), respectively. Also, the optimized length L_{notch} is set to band-stop resonate at $0.5\lambda_{notch}$, where $L_{notch1}=L_5+W_5+W_{12}+0.5(L_4+L_6+W_6)$, and $L_{notch2}=0.5(L_1+W_1)+L_2+W_2+W_4$. λ_{notch1} and λ_{notch2} correspond to first band-notched frequency (3.5 GHz) and second band-notched frequency (5.5 GHz), respectively. The final values of proposed design parameters are specified in Table 1.

Table 1: Final dimensions of antenna parameters

Parameter	W	L	W_1	L_1
Value (mm)	10	10	8	8
Parameter	W_2	L_2	W_3	L_3
Value (mm)	0.5	3.1	4.5	3.6
Parameter	W_4	L_4	W_5	L_5
Value (mm)	2	3.5	0.2	3
Parameter	W_6	L_6	W_7	L_7
Value (mm)	1	3.1	0.2	3.1
Parameter	W_8	L_8	W_9	L_9
Value (mm)	0.15	1.25	4	0.75
Parameter	W_{10}	L_{10}	W_{11}	L_{11}
Value (mm)	1.25	0.3	0.75	2.8
Parameter	W_{12}	L_{12}	W_f	L_f
Value (mm)	0.55	3	7	2
Parameter	W_{sub}	L_{sub}	h_{sub}	L_{gnd}
Value (mm)	12	18	1.6	3.5

In the square-ring stub, two fork-shaped strips protruded inside the ring have been used for generating

a single band-stop performance that's playing an important role in the broadband characteristics of this antenna, because by using it, the band-notch performance can be controlled such as band-rejections range and variable function. The modified M-shaped strip protruded inside rectangular slot at feed-line causes a second band-notched performance which finally a multi-resonance antenna with desired dual band-notched function to suppress interferences from WLAN, WiMAX, and C-bands can be achieved [11].

III. RESULTS AND DISCUSSIONS

The planar monopole antenna with various design parameters was constructed, and the numerical and experimental results of the input impedance and radiation characteristics are presented and discussed. The analysis and performance of the proposed antenna is examined by using Ansoft simulation software high-frequency structure simulator (HFSS) [17], for better impedance matching.

VSWR characteristics for the ordinary monopole antenna [Fig. 2 (a)], the antenna with a pair of rotated Y-shaped strips protruded inside the slot at ground plane [Fig. 2 (b)], the square-ring antenna with pairs of protruded Y-shaped and fork-shaped strips [Fig. 2 (c)], and the proposed antenna structure [(Fig. 2 (d)] are compared in Fig. 3.

As shown in Fig. 3, by using the pair of rotated Y-shaped strips at the ground plane, a new resonance at the higher frequency (10.7 GHz) is generated and the usable upper frequency of the antenna is extended from 10.3 GHz to 11.9 GHz. To generate a single frequency band-notched function, the square radiating patch was converted to the square-ring structure with a pair of protruded fork-shaped strips, and also by using an M-shaped strip inside the rectangular slot at feed-line, the good dual band-notched function can be achieved which is covering the 3.5/5.5 GHz WiMAX/WLAN bands [11-13].

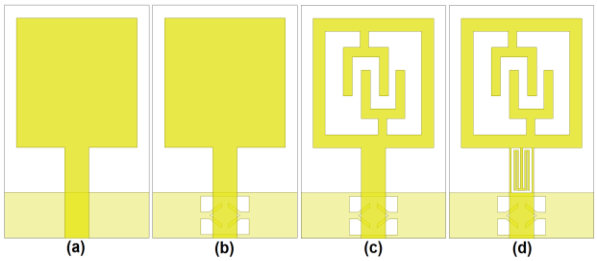

Fig. 2. (a) Ordinary monopole antenna, (b) antenna with pair of Y-shaped strips, (c) antenna with pairs of Y-shaped and fork-shaped strips, and (d) the proposed monopole antenna.

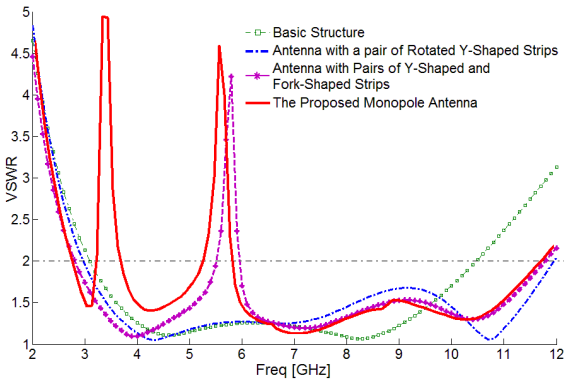

Fig. 3. Simulated VSWR characteristics for the various structures shown in Fig. 2.

To understand the phenomenon behind the multi resonance and dual band-notched performances, the simulated current distribution for the proposed antenna at the new resonance frequency (9.5 GHz) and notched frequencies (3.5 & 5.5 GHz) is presented in Fig. 4. It can be observed on Fig. 4 (a), at 10.5 GHz the current concentrated on the edges of the interior and exterior of the Y-shaped strips protruded inside the slot. Therefore, the antenna impedance changes at these frequencies due to the resonance properties of the proposed structure.

Figures 4 (a) and 4 (b) present the simulated current distributions on the top layer at the notched frequencies (3.7 and 5.5 GHz). As illustrated in Figs. 4 (b) and 4 (c), at the notched frequencies, the current flows are more dominant around of the fork-shaped and M-shaped strips. As a result, the desired high attenuation near the notched frequencies can be produced [18-19]. As seen in these figures, the current direction on the reject structures is opposite to each other, so the far fields produced by the currents on the reject structures cancel out each other in the reject band.

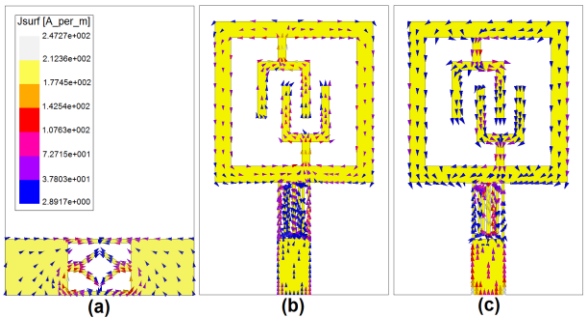

Fig. 4. Simulated surface current: (a) at 10.7 GHz (first extra resonance frequency), (b) at 3.5 GHz (first notched frequency), and (c) at 5.5 GHz (second notched frequency).

The proposed antenna with final design as shown in Fig. 5, was built and tested. The VSWR characteristic of the antenna was measured using the HP 8720ES network analyzer in an anechoic chamber. The radiation patterns have been measured inside an anechoic chamber using a double-ridged horn antenna as a reference antenna placed at a distance of 2 m. Also, two-antenna technique using an Agilent E4440A spectrum analyzer and a double-ridged horn antenna as a reference antenna placed at a distance of 2 m is used to measure the radiation gain in the z axis direction (x-z plane). Measurement set-up of the proposed antenna for the VSWR, antenna gain and radiation pattern characteristics are shown in Fig. 6.

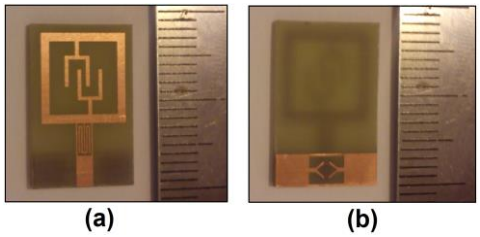

Fig. 5. Fabricated antenna: (a) top view, and (b) bottom view.

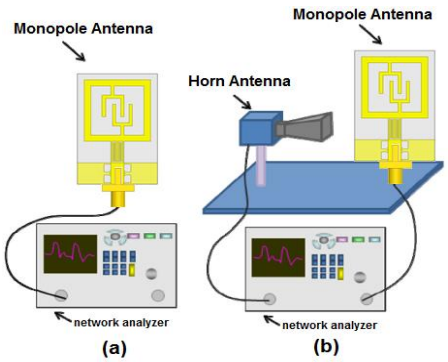

Fig. 6. Measurement set-up of the antenna: (a) VSWR, and (b) antenna gain and radiation patterns.

Figure 7 shows the measured and simulated VSWR characteristics of the proposed antenna. The antenna has the frequency band of 2.8 to 11.8 GHz with two rejection bands around 3.3.-3.7 and 5-6 GHz.

Figure 8 depicts the measured and simulated radiation patterns of the proposed antenna including the co-polarization and cross-polarization in the H-plane (x-z plane) and E-plane (y-z plane). It can be seen that quasi-omnidirectional radiation pattern can be observed on x-z plane over the whole UWB frequency range, especially at the low frequencies. The radiation patterns on the y-z plane display a typical figure-of-eight (8), similar to that of a conventional dipole antenna. The radiating patterns indicated at higher frequencies have more ripples in both E- and H-planes, owing to generation of higher-order modes [20-21]. Measured and simulated maximum gains of the proposed antenna are shown in Fig. 9. Two sharp decrease of maximum gains in the notched frequencies bands at 3.5 and 5.5 GHz are shown in Fig. 9. For other frequencies outside the notched frequencies, the antenna gains has a flat property which increases by the frequency. As illustrated, the proposed antenna has sufficient and acceptable gain level in the operation bands [22].

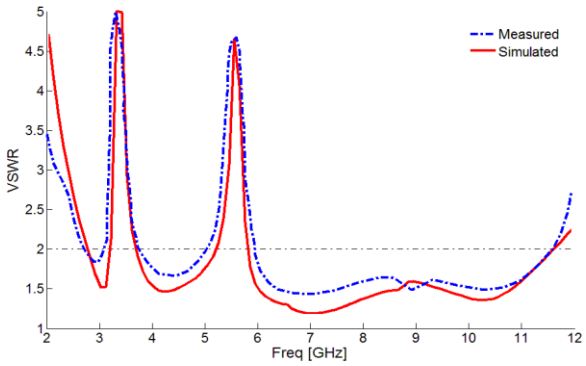

Fig. 7. Measured and simulated VSWR characteristics of the proposed antenna.

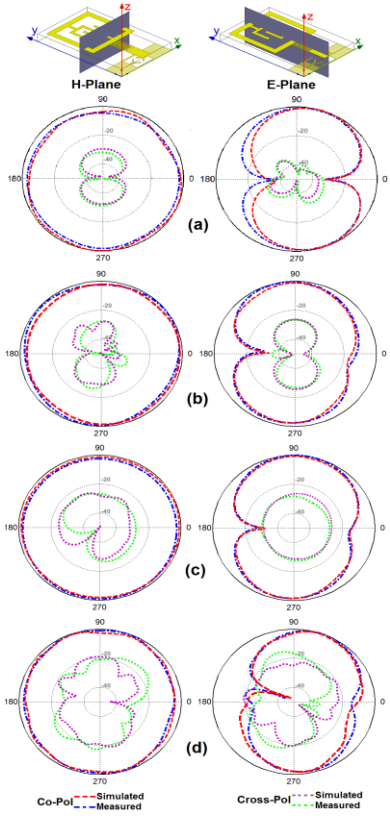

Fig. 8. Measured and simulated radiation patterns: (a) 3 GHz, (b) 4.5 GHz, (c) 7 GHz, and (d) 11 GHz.

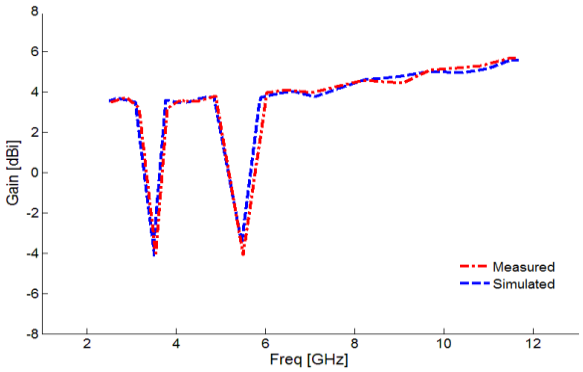

Fig. 9. Measured and simulated gains of the proposed antenna.

The measured and simulated radiation efficiency characteristic of the proposed antenna is shown in Fig. 10. The efficiency measurement was conducted using the reverberation chamber a cavity-technique and based approach, called the source-stirred method. Measured and also simulated results of the calculations using the software HFSS indicated that the proposed antenna features a good efficiency, being greater than 87% across the entire radiating band except in two notched bands [23]. On the other hand, the radiation efficiencies of the proposed dual band-notched antenna at 3.5 and 5.5 GHz, are only about 29 and 31%, respectively.

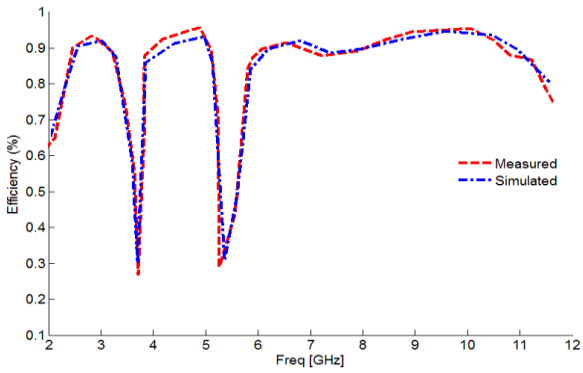

Fig. 10. Measured and simulated radiation efficiency characteristic of the proposed antenna.

IV. CONCLUSION

In this paper, a novel small monopole antenna with WiMAX/WLAN band-stop characteristic for UWB applications is proposed. In this design, the proposed antenna can operate from 2.8 to 11.8 GHz with two rejection bands around 3.3 to 3.7 GHz and 5 to 6 GHz. The designed antenna has a small size of 12×18×1.6 mm^3. Good VSWR and radiation pattern characteristics are obtained in the frequency band of interest.

REFERENCES

[1] D. Cheng, *Compact Ultra Wideband Microstrip Resonating Antenna*, US Patent 7872606, Jan. 2011.

[2] N. Ojaroudi, M. Ojaroudi, and N. Ghadimi, "UWB omnidirectional square monopole antenna for use in circular cylindrical microwave imaging systems," *IEEE Antennas Wireless Propag. Lett.*, vol. 11, pp. 1350-1353, 2012.

[3] N. Ojaroudi, "Compact UWB monopole antenna with enhanced bandwidth using rotated L-shaped slots and parasitic structures," *Microw. Opt. Technol. Lett.*, vol. 56, pp. 175-178, 2014.

[4] N. Ojaroudi, "Bandwidth improvement of monopole antenna using π-shaped slot and conductor-backed plane," *International Journal of Wireless Communications, Networking and Mobile Computing*, vol. 1, no. 2, pp. 14-19, 2014.

[5] FCC News Release, FCC NEWS (FCC 02-48), Feb. 14, 2002.

[6] N. Ojaroudi, "Application of protruded strip resonators to design an UWB slot antenna with WLAN band-notched characteristic," *Progress in Electromagnetics Research C*, vol. 47, pp. 111-117, 2014.

[7] H. Mardani, C. Ghobadi, and J. Nourinia, "A simple compact monopole antenna with variable single-and double-filtering function for UWB applications," *IEEE Antennas and Wireless Propagation Letters*, vol. 9, pp. 1076-1079, 2010.

[8] N. Ojaroudi, "A modified compact microstrip-fed slot antenna with desired WLAN band-notched characteristic," *American Journal of Computation, Communication and Control*, vol. 1, no. 3, pp. 56-60, 2014.

[9] N. Ojaroudi and M. Ojaroudi, "An UWB slot antenna with band-stop notch," *IET Microw. Antennas Propag.*, vol. 10, pp. 831-835, 2013.

[10] N. Ojaroudi, S. Amiri, and F. Geran, "A novel design of reconfigurable monopole antenna for UWB applications," *Applied Computational Electromagnetics Society (ACES) Journal*, vol. 28, no. 6, pp. 633-639, July 2013.

[11] N. Ojaroudi, "Frequency reconfigurable microstrip antenna integrated with PIN diodes for cognitive radio," *22nd Telecommunications Forum, TELFOR 2014*, Belgrade, Serbia, Nov. 25-27, 2014.

[12] N. Ojaroudi, "Microstrip monopole antenna with dual band-stop function for UWB applications," *Microw. Opt. Technol. Lett.*, vol. 56, pp. 818-822, 2014.

[13] N. Ojaroudi, "Application of protruded Γ-shaped strips at the feed-line of UWB microstrip antenna to create dual notched bands," *International Journal of Wireless Communications, Networking*

and Mobile Computing, vol. 1, no. 1, pp. 8-13, 2014.

[14] N. Ojaroudi, "An UWB microstrip antenna with dual band-stop performance using a meander-line resonator," *22nd International Conference on Software, Telecommunications and Computer Networks (SoftCOM)*, Croatia, 2014.

[15] N. Ojaroudi, "Design of small reconfigurable microstrip antenna for UWB-CR applications," *19th International Symposium on Antenna and propagation, ISAP2014*, Kaohsiung, Taiwan, Dec. 2-5, 2014.

[16] N. Ojaroudi, "Microstrip-fed antenna design for use in circular cylindrical microwave imaging applications," *22nd Telecommunications Forum, TELFOR 2014*, Belgrade, Serbia, Nov. 25-27, 2014.

[17] Ansoft High Frequency Structure Simulator (HFSS), ver. 13, Ansoft Corporation, Pittsburgh, PA, 2010.

[18] N. Ojaroudi, "Small microstrip-fed slot antenna with frequency band-stop function," *21st Telecommunications Forum, TELFOR 2013*, Belgrade, Serbia, Nov. 27-28, 2013.

[19] N. Ojaroudi, "Novel design of low-profile microstrip band-stop filter (BSF) with Koch fractal RSLRs," *22nd Telecommunications Forum, TELFOR 2014*, Belgrade, Serbia, Nov. 25-27, 2014.

[20] N. Ojaroudi, "New design of multi-band PIFA for wireless communication systems," *19th International Symposium on Antenna and propagation, ISAP 2014*, Kaohsiung, Taiwan, Dec. 2-5, 2014.

[21] N. Ojaroudi, "Design of ultra-wideband monopole antenna with enhanced bandwidth," *21st Telecommunications Forum, TELFOR 2013*, Belgrade, Serbia, Nov. 27-28, 2013.

[22] N. Ojaroudi, "Design of microstrip antenna for 2.4/5.8 GHz RFID applications," *German Microwave Conference, GeMic 2014*, Germany, 2014.

[23] N. Ojaroudi and M. Ojaroudi, "Novel design of dual band-notched monopole antenna with bandwidth enhancement for UWB applications," *IEEE Antennas Wireless Propag. Lett.*, vol. 12, pp. 698-701, 2013.